University of Louisville

ThinkIR: The University of Louisville's Institutional Repository

Electronic Theses and Dissertations

1-2022

Structural, charge transport, gas sensing, magnetic, pseudocapacitive, and electrocatalytic properties of perovskite oxides.

Surendra Bahadur Karki
University of Louisville

Follow this and additional works at: https://ir.library.louisville.edu/etd

Part of the Catalysis and Reaction Engineering Commons, Inorganic Chemistry Commons, Materials Chemistry Commons, Materials Science and Engineering Commons, Sustainability Commons, and the Transport Phenomena Commons

Recommended Citation

STRUCTURAL, CHARGE TRANSPORT, GAS SENSING, MAGNETIC,

PSEUDOCAPACITIVE, AND ELECTROCATALYTIC PROPERTIES OF

PEROVSKITE OXIDES

By

Surendra Bahadur Karki
M.S., University of South Carolina, 2016
M.Sc., Tribhuvan University, 2009

A Dissertation
Submitted to the Faculty of the
College of Arts and Sciences of the University of Louisville
in Partial Fulfilment of the Requirements
for the Degree of

Doctor of Philosophy in Chemistry

Department of Chemistry
University of Louisville
Louisville, Kentucky

May 2022

STRUCTURAL, CHARGE TRANSPORT, GAS SENSING, MAGNETIC,

PSEUDOCAPACITIVE, AND ELECTROCATALYTIC PROPERTIES OF

PEROVSKITE OXIDES

By

Surendra Bahadur Karki

A   Dissertation Approved on

April 20, 2022

by the following Dissertation Committee:

_____

Dissertation Director- Dr. Farshid Ramezanipour

_____

Dr. Robert M. Buchanan

_____

Dr. Richard P. Baldwin

_____

Dr. Sumanasekera Gamini

DEDICATION

This work is dedicated to my parents, children (Subrisha Karki and Subhav Karki), and my beloved wife, Sabrina Karki Adhikari for all the support, love, inspiration, and motivation. Lastly, I dedicate this work to my high school teachers, faculties of Tribhuvan University, University of South Carolina, and University of Louisville for illuminating me with their knowledge and academic support to drive my career toward the Doctor of Philosophy degree.

ACKNOWLEDGMENTS

Firstly, I am thankful to my research advisor, Dr. Farshid Ramezanipour. For me, it's a matter of pride and the highest honor to be his student and contribute to the field of material science. Dr. Ramezanipour has always been supportive, caring, and motivation throughout my graduate studies. His availability, counsel, relentless support, patience, and guidance will be a lifetime favor for me. Therefore, I would like to put my sincere gratitude to Dr. Ramezanipour, who has been an irreplaceable mentor to me. I appreciate him for shaping me not only into a better scientist but also a good human being. It has been an honor to be a part of the Ramezanipour research group.

I am thankful to my family members for the support they gave me to achieve my dream to become a PhD scholar. They have always helped, supported, and motivated me in many difficult situations while achieving all the milestones of the PhD degree. My immense gratefulness to my wife; Mrs. Sabrina Karki Adhikari for not only the encouragement throughout my life, but also taking care of me and the kids. Her contribution to take care and raise my children during my PhD career, will be the most beautiful memories to cherish in future. I am lucky and honored to have such great, amazing, loving, and caring people in my life.

I would like to sincerely acknowledge Dr. Robert Buchanan, Dr. Richard Baldwin, and Dr. Gamini Sumanasekera for serving on my research and dissertation committees. I appreciate their constructive criticism, advice, and guidance to complete my graduate degree. I would

ABSTRACT

STRUCTURAL, CHARGE TRANSPORT, GAS SENSING, MAGNETIC,

PSEUDOCAPACITIVE, AND ELECTROCATALYTIC PROPERTIES OF

PEROVSKITE OXIDES

Surendra Bahadur Karki

April 20, 2022

Perovskites are functional materials with the general formula ABO_3 (A = alkali, alkaline earth or lanthanoid cations and B = transition metal or main group cations). These materials are marked by a variety of crystal structures and interesting properties such as colossal magnetoresistance, ferroelectricity, multiferroicity, superconductivity, pseudocapacitance, gas sensing, charge transport, and electrocatalytic properties. The formula of perovskite can be written as $AA'BB'O_6$, when there is ordering between two cations over A and B-sites. Such compounds are called double perovskite oxides. Some amount of oxygen could be lost from crystal structure without decomposition of the phase. Such class of materials are termed oxygen deficient perovskites (ODPs). In this study, several double perovskite oxides and ODPs are utilized for systematic study of magnetic, charge transport, pseudocapacitive, and electrocatalytic properties.

The magnetic and electrical properties of $BaSrMMoO_6$ (M = Mn, Fe, Co, Ni) double perovskite oxides show an interesting property trend. $BaSrFeMo_6$ shows a ferrimagnetic ordering of moments of Fe along with metallic behavior in variable temperature conductivity studies. However, Mn, Co, and Ni containing materials show an antiferromagnetic ordering of moments and semiconducting features from 25 – 800 ℃.

The oxygen deficient perovskite (ODP) in this study is explored to understand the high temperature gas interaction properties. Structurally stable $Ca_2Fe_2O_5$ shows an outstanding gas sensing behavior that could be utilized in systems that operate at elevated temperature. Similarly, ODPs can be explored to understand hydroxide intercalation based pseudocapacitance. Two novel ODPs namely $Ca_3GaMn_2O_8$ and $SrCa_2GaMn_2O_8$, have shown great promise for energy devices with at least 5000 charge/discharge cyclability.

Another focus of our research is to solve problems and issues of energy conversion process that is involved with an electrochemical water splitting to generate hydrogen gas for fuel. Water splitting has two half reactions namely oxygen evolution reaction (OER) and hydrogen evolution reaction (HER). Both reactions have significant amounts of overpotential and require catalysts to lower the overpotential and enhance the reaction kinetics. Overpotential has been reduced by catalyzing both OER and HER using commercial RuO_2, IrO_2, and Pt/C However, such catalysts are expensive, use precious metals, and some of them have stability issues in acidic condition. Our approach involves development of economic perovskite oxide-based catalysts that contain earth abundant metals.

The main tools for the problem-solving approach of our research involved both A and B-sites modification, conductivity enhancement, structural transformation, and control

of the oxygen content in perovskite structure. For example, A-site substitution strategy is adopted by substituting Sr with Ca in $Sr_2FeCoO_{6-\delta}$ and $LaSr_2Fe_3O_8$. This leads to significant enhancement of OER/HER activity in structurally ordered compounds namely $Ca_2FeCoO_{6-\delta}$ and $LaCa_2Fe_3O_8$. The B-site modification, on the other hand, is also utilized by systematically varying the Mn content in the series $CaSrFe_{1-x}Co_{1-x}Mn_{2x}O_{6-\delta}$ (x = 0-1). This helped to identify a material with formula $CaSrFe_{0.75}Co_{0.75}Mn_{0.5}O_{6-\delta}$ (CSFCM), that has an e_g occupancy of near unity, as required for optimized activity. Additionally, upon using both experimental and computation methods, we have studied the electronic structure of several materials, including CSFCM. This has led to the discovery of a new descriptor, namely free e_g carrier. This could be a universal descriptor for both OER and HER for bifunctional catalysts. Similarly, we have discovered several other oxide catalysts such as $CaSrFeMnO_{6-\delta}$, $BaSrCoMoO_6$, Sr_3FeMnO_6, $Ca_2Sr_2Mn_2CoO_{10-\delta}$, and $La_3Co_3O_8$, which have remarkably low overpotentials, as low as 0.25 V in both acidic and basic media. In most of these oxides, electrocatalytic properties arise from the combination of structure, enhanced electrical conductivity, and higher amount of oxygen vacancies.

TABLE OF CONTENTS

xi

LIST OF FIGURES

CHAPTER 1

INTRODUCTION

1. BACKGROUND

Solid-state materials, i.e., non-molecular solids, have been utilized due to their interesting properties and chemistry that involve the structural, chemical, and physical properties. They have been explored for their dielectric, piezoelectric, charge transport, magnetic, gas sensing, pseudocapacitive, and electrocatalytic properties, to name a few. [1-5] However, these area of studies still face some issues/problems that need to be addressed for improving the performance in several devices. Most importantly, a careful material choice and design strategy allows modification of the operating cost of such devices.

Devices such as batteries, supercapacitors, and fuel cells require a wise and economic choice of materials. Such devices are important to the utilization and storage of clean energy. Minimizing the usage of fossil fuel energy to mitigate energy crisis in near future and developing cleaner energy technologies, have been a focal point in past decades.[6] Novel alternative renewable energy technologies that involve water, wind power and solar energy have great economic and social impact. Some efficient systems for energy storage involve batteries, pseudocapacitors, water electrolyzers, and fuel cells. One example of materials that have been studied for such devices is perovskite oxide that contain network of atoms.

1.1 PEROVSKITE OXIDES

Mixed oxides contain two or more metal cations and charges in the unit formulae of such compound are balanced by oxide ions. There are many possible crystal structures of such materials. Mixed oxides having the crystal structure similar to that of a well-known mineral calcium titanate ($CaTiO_3$) are called perovskite oxides. $CaTiO_3$ was discovered in the Ural Mountains of Russia by Gustav Rose in 1839, and the term 'Perovskite' was coined after Russian mineralogist, Lev Perovski. The crystal structure of perovskite was first described by Victor Goldschmidt.[7] Helen Dick Megaw published the crystal structure later in 1945 AD, which was based on X-ray diffraction data of Barium Titanate ($BaTiO_3$).[8] Perovskite oxide is represented by the general chemical formula ABO_3, where A represents metal cations of s and f block and B is usually transition metal or p block metal cation. As shown in Figure 1.1, perovskite structures have at least three different crystallographic positions, where each unit cell has the A and B-site cations in 12 and 6-fold coordinations, respectively.[1] For the sake of visualization, cuboctahedralon and octahedral coordination geometry are drawn for the A and B-site cations, respectively.

Perovskite oxides (ABO_3) are considered ionic crystals, where there is a relation between unit cell axis (a) and radii of A, B, and O^{2-} ions. In case of an ideal cubic perovskite oxide, the relation is:[1]

$$a = \sqrt{2}(r_A + r_O) = 2\ (r_B + r_O) \tag{1.1}$$

where, a = cell length, r_A, r_B, and r_O are radii of A, B, and O^{2-} ions, respectively. However, it is possible for such cubic structures to distort and produce lower symmetry structures such as hexagonal, tetragonal, orthorhombic, triclinic, etc. The distortion directly affects

the properties. Therefore, understanding of such deviations can be done by tolerance factor (*t*) as calculated from the following equation.[1]

$$t = \frac{(r_A + r_O)}{\sqrt{2}(r_B + r_O)}$$ (1.2)

where, *a* is the cell length, and r_A, r_B, and r_O are radii of A, B, and O^{2-} ions, respectively. In an ideal cubic structure, $t = 1$, whereas the *t* values range between ~0.80 and 1.10 for structures with other types of symmetry. For example, perovskites with *t* near 0.85 have orthorhombic or rhombohedral structures and those with *t* >1 have hexagonal or tetragonal structures.[1] The, *t* values can be tuned by A or B cation substitution in the perovskite structure that not only changes the crystal symmetry but also creates oxygen defects which produce several interesting properties.

Oxygen

A-site atom in cuboctahedron

A-site atom

B-site atom

B-site atom in octahedron
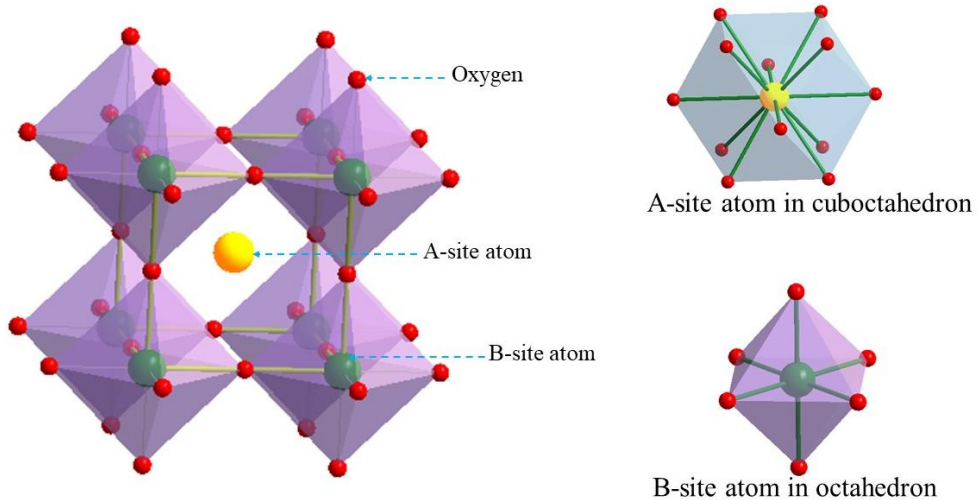
Figure 1.1: Unit cell of perovskite structure showing A-and B-site cations coordination.

1.1.2 OXYGEN DEFICIENT PEROVSKITE OXIDES

Oxygen deficient perovskites (ODPs) are sub-class of perovskite oxide family, where the structure is marked by the loss of some amount of oxygen that result on the crystal defects. ODPs are represented by general formula $ABO_{3-\delta}$ or $A_2B_2O_{6-\delta}$, where δ

represents amount of oxygen deficiency per unit formula. In these $ABO_{3-\delta}$ type materials, oxygen-deficiencies result in different coordination geometries for the B-site cations, ranging from octahedral (BO_6) to tetrahedral (BO_4) and square pyramidal (BO_5).[9, 10] As shown in Figure 1.1.2, the oxygen-vacancies are sometimes distributed randomly (represented by small squares in the scheme).[11] There are also situations where the arrangement of oxygen-vacancies is ordered.[10] One of the common types of ordering results in the so-called brownmillerite structure, named after mineral Ca_2AlFeO_5.[9] The structure consists of sequential layers of tetrahedra (T) and octahedra (O), forming TOTOT…, with A-site cation residing between the layers. The tetrahedra form chains that are twisted in either left-handed or right-handed orientation to yield several orthorhombic structural variants adopting space groups such as *Ibm2*, *Pnma*, *Pbcm* or *Icmm*.[10, 12]

While the brownmillerite type ordering is commonly observed, there is also a similar, but less common ordering scheme with ideal formula $A_3B_3O_8$ ($ABO_{3-(1/3)}$), sometimes called Grenier phase.[13] This structure consists of bilayer stacks of octahedra alternating with a single layer of tetrahedra, i.e., TOOTOOT…, often adopting orthorhombic space groups such as *P2₁ma*, *Pbma*, *Pmma*, *Pb2₁m*.[14-17]

There is a direct correlation between the structure and functional properties of perovskite oxides, particularly ODPs. The modification of cations on both A and B-sites is known to affect the structure of oxygen-deficient perovskites. Following section briefly discusses some of the properties of perovskite oxides that have been expanded and studied thoroughly in recent years.

No vacancies

ABO₃

Perovskite

Random   Ordered   Ordered OTOTOTO…   Ordered OOTOOTOO..

Brownmillerite   Bilayer Brownmillerite

Oxygen Deficient Perovskites, ODPs (ABO$_{3-\delta}$)

T = Tetrahedron
O = Octahedron
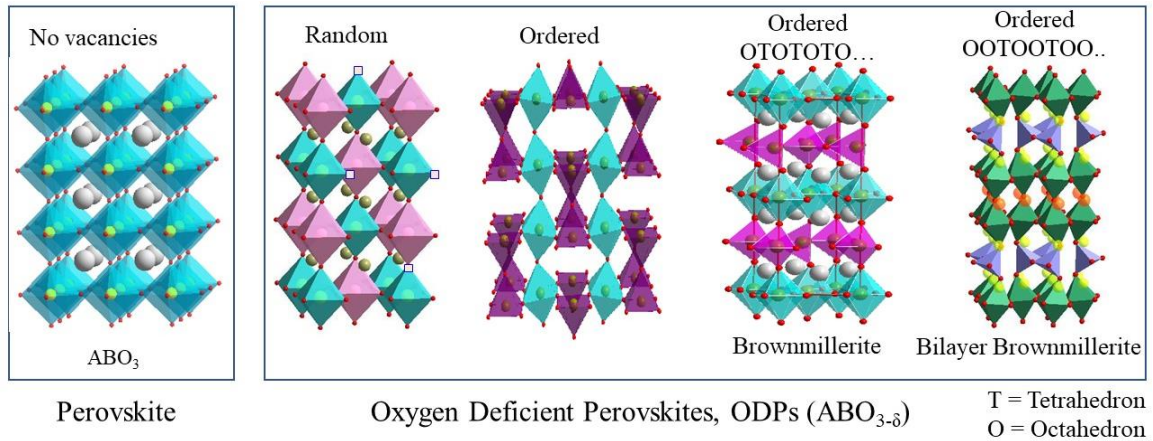
Figure 1.1.2: Vacancy ordering schemes in oxygen deficient perovskites.

1.1.3 PROPERTIES OF PEROVSKITE OXIDES

As discussed above, variations of structural architectures in perovskite oxides by controlling the oxygen defect concentration allow this class of materials to be used for energy devices to address energy-related challenges. A myriad of exciting properties such as photovoltaics, magnetism, gas sensor, pseudocapacitance, electrocatalysis, electrical charge transport, etc., could be studied. Recently, their use in energy devices such as electrode materials for batteries, water electrolyzers, and fuel cells has attracted a lot of attention from interdisciplinary researchers.

1.1.3.1 ELECTRICAL CHARGE TRANSPORT PROPERTY

The electrical charge transport properties of perovskite oxides can be studied by using alternating (AC) and direct current (DC) conductivity measurement. For AC measurement that allows to understand the ionic conduction process, both two and four-probe techniques are used.[18, 19] However, four probe technique by applying certain voltage, is mostly preferred during the DC conductivity measurements because this technique prevents the contribution from contacts and wires to the total resistance.[5, 19] Many

perovskite oxides, including ODPs show mixed conduction properties, where conductivity arises because of oxide ionic and electronic conduction processes. When ODP structures are furnished with transition metals with variable oxidation states at the B-site, dominance of electronic transport takes place through holes.[20, 21] This process is often called the polaron mechanism.[11, 22] A scheme of polaron mechanism is shown in Figure 1.1.3.1. Since the electron hopping takes place with a fast speed, it looks like the positive charge is moving. So, it is considered as positive charge or hole movement or p-type conductivity. During this process, the electrons hop through $B^{n+}-O-B^{m+}$ bond pathway. For instance, the electron hopping in $Sr_2Fe_2O_{6-\delta}$ material has been described to occur via $Fe^{3+}-O-Fe^{4+}$ where the Fe^{3+} oxidizes to Fe^{4+}.[23] Then, a reverse route $Fe^{4+}-O-Fe^{3+}$ for back-hopping of electron takes place, causing the reduction.
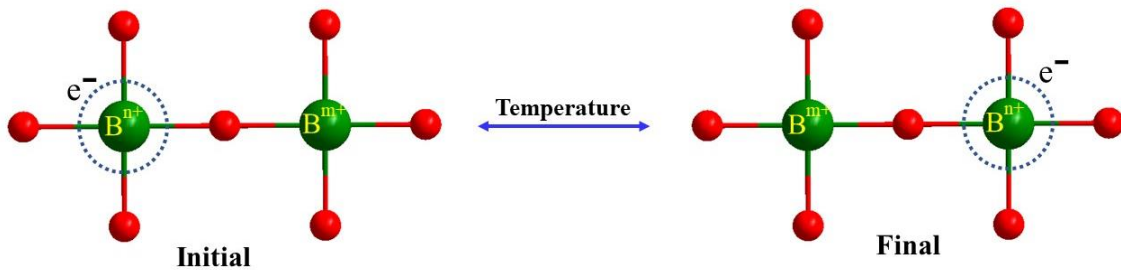
Figure 1.1.3.1: Electron hopping mechanism through B^{n+}-O-B^{m+} pathway in perovskite.

There are several governing factors for electronic charge transport in ODPs. They include hole concentration, B-site cation bond lengths (B-O), and bond angles (B-O-B). If the hole concentration (polarons) increases in a material, the electronic transport and electrical conductivity is also enhanced.[20, 24] Similarly, shorter B-O bond length and the larger B-O-B bond angle provide a better orbital overlap and electronic transport and hence, the conductivity increases.[25, 26] Overall semiconducting feature is observed when

conductivity increases as a function of increasing temperature in variable temperature conductivity measurement and the opposite trend indicates the metallic property of ODPs.

Substitution of Fe in the B-site of the double perovskite series $BaSrMMoO_6$ (M = Mn, Co, Ni) shows a transformation of metallic to semiconducting conductivity features in the three compounds. Similarly, most ODPs which will be discussed in several chapters show semiconducting charge transport properties in the studied temperature range of 25 – 800 °C. Therefore, understanding the charge transport properties in these functional materials allows to enhance other related properties such as electrocatalytic performance.

1.1.3.2 GAS SENSING PROPERTY

Gaseous emissions from industries and automobiles are the main contributors to human health issues, acid rain, ozone depletion, and the greenhouse effect. Gas sensors are important to monitoring the environmental pollution, which ultimately assist in preventing the damage to the environment and quality of life.[27, 28] High-temperature gas sensors are also required in industries associated with the combustion process. Generally, optical, chromatography and spectroscopy method-based gas sensors are in use to detect the gases at various concentration levels. However, these analytical techniques are not versatile methods as they are expensive to use and pose challenges for in-situ monitoring of gases at high temperature.

CeO_2, Ga_2O_3, TiO_2, Nb_2O_5, SnO_2-TiO_2 composites etc. are some of the semiconducting type gas sensors.[29-32] Semiconductor-based gas sensors have been categorized into p-type and n-type gas sensors. The response and behavior of the p-type and n-type semiconductors toward oxidizing (O_2, NO_2, CO_2, NO, etc.) and reducing gases (CO, NH_3, SO_2, CH_4, etc.) have been well studied in various reports.[32-36] On the other hand,

perovskite-type structure based transition metal oxides have the potential to be used for sensing different gases. A lot of these oxides have displayed an excellent detection of reducing gases like H_2,[4] CO[37] and oxygenic gases like CO_2[38] and NO_x.[39] Such types of solid-state sensors can operate in wide ranges of temperatures, for example, oxygen sensor in high temperature automotive exhaust emission control [40] and temperature independent resistive oxygen sensors.[41]

1.1.3.3 MAGNETIC PROPERTY

Magnetic dipole moment of an electron is generated by electron spin and orbital magnetic moments. As result of orientation of magnetic dipole moments of unpaired d electrons, magnetic behaviors such as paramagnetism, diamagnetism, and ferromagnetism are observed in materials. In perovskite oxides, B-site cations having unpaired d-electrons such as Fe^{3+}, Mn^{3+}, and Co^{3+}, could result in magnetic ordering. However, phenomena such as antiferromagnetism and ferromagnetism occur due to super and double exchange.[1] The antiferromagnetic system has antiparallel alignment of the neighboring moments.

The oxygen vacancy can affect the magnetic properties of perovskite oxides.[1] Additionally, the nature of the B-site cation plays a crucial role in structural phase transition and disparities in electrical and magnetic properties. For instance, dominance of antiferromagnetic ordering in double perovskite oxide series Sr_2LnMoO_6 (Ln = Eu, Gd, Dy, Ho, Er, Yb)[2] and ferrimagnetism[42] in $CaLaMnMoO_6$, has been observed. It is evident that double perovskites which host two different transition metal cations on B-site may allow the introduction of two different types of magnetic sublattices. They can also host a magnetic and a nonmagnetic sublattice, leading to different types of magnetic order. For example, the interplay between magnetic 3d cations with non-magnetic 4d or 5d ions have

8

led to ferrimagnetic metallic ordering in Sr_2FeMoO_6, Sr_2CrWO_6 and Sr_2CrReO_6.[43] It is interesting to explore the effect of varying the magnetic ion in such system, where a nonmagnetic sublattice (Mo^{6+}) is fixed. In $Sr_2Fe_2O_{6-\delta}$ an incommensurate magnetic structure is observed, where moments are in spin-density wave state, and are oriented perpendicular to the body diagonal of the unit cell. However, $CaSrFe_2O_{6-\delta}$ shows long-range antiferromagnetic order, where the moments align in 001 direction.

1.1.3.4 PSEUDOCAPACITIVE ENERGY STORAGE PROPERTY

Another property of the ODP materials is their pseudocapacitive capability. Supercapacitors have been extensively researched because of their significant advantages in power density and cycling stability. However, they suffer from low energy density, and their charge storage capability is limited. Unlike traditional electric double layer capacitors that rely on non-Faradaic electrostatic charge storage, pseudocapacitors operate based on Faradaic processes, and therefore show greater charge storage capacity. However, since the Faradaic charge transfers in pseudocapacitors occur on or near the surface, they are not limited by bulk diffusion, leading to cyclic voltammetry (CV) and galvanostatic charge-discharge (GCD) behavior similar to traditional capacitors. Pseudocapacitors in theory can possess both high power density of capacitors and high energy density of batteries.[44] Intercalation-based pseudocapacitors involve Faradaic electron transfer that occurs upon intercalation and de- intercalation of ions.[44]

The intercalation of oxygen anion was first observed in 1975 in perovskite oxide, $Nd_{1-x}Sr_xCoO_3$, in alkaline solution.[45] Further utilization of this phenomenon for pseudocapacitive energy storage was shown several decades later in 2014.[44] Since then, several other pseudocapacitive materials based on oxygen anion intercalation have been

studied. Examples of the materials that have been investigated are $La_{1-x}Sr_xMnO_3$,[3, 44, 46] $La_{1-x}Ca_xMnO_3$,[47] $SrCo_{0.9}Nb_{0.1}O_3$,[48] and $LaNi_{1-x}Fe_xO_{3-\delta}$.[49]

1.1.3.5 ELECTROCATALYTIC PROPERTY

Hydrogen production via water splitting has garnered attention as an environmentally benign and economic approach to the generation of hydrogen fuel.[50, 51] As shown in Figure 1.1.3.5.1, the electrochemical water-splitting proceeds via two half-reactions, hydrogen evolution reaction (HER) and oxygen evolution reaction (OER).[52] Figure 1.1.3.5.2 shows the thermodynamics of both OER and HER processes, where hydrogen evolution takes place ideally at the potential of 0 V vs reversible hydrogen electrode (RHE) and oxygen evolution is thermodynamically favorable at 1.23V vs RHE. However, both HER and the OER are sluggish processes due to the high activation barrier and several intermediate steps that involve electron transfer.[53, 54] This results in the significant overpotential. Similarly, the polarization curve as shown in the I-V curve of Figure 1.1.3.5.2, also shows some parameters such as onset potential (potential at which Faradaic current evolves). Such parameters including overpotential at 10 mA/cm^2 current density, Tafel slopes, and electrochemically active surface area will be thoroughly discussed in several chapters.
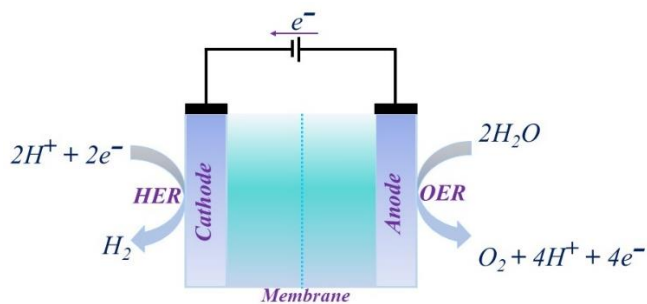
Figure 1.1.3. 5.1: A schematic representation of electrochemical water splitting.

The generally accepted mechanism for HER involves Volmer reaction, followed by either Heyrovsky or Tafel reaction, as shown below:[55, 56]

Volmer reaction in acidic condition:

$$H_3O^+ + M + e^- \rightleftharpoons M–H* + H_2O \qquad (1.3)$$
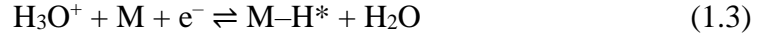
Volmer reaction in alkaline condition:

$$H_2O + M + e^- \rightleftharpoons M–H* + OH^- \qquad (1.4)$$

Heyrovsky reaction in acidic condition:

$$M–H* + H_3O^+ + e^- \rightleftharpoons M + H_2 + H_2O \qquad (1.5)$$
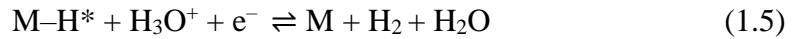
Heyrovsky reaction in alkaline condition:

$$M–H* + H_2O + e^- \rightleftharpoons M + H_2 + OH^- \qquad (1.6)$$
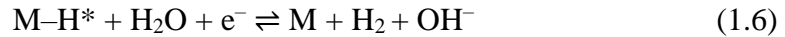
Tafel reaction in both acidic and alkaline conditions:

$$2M–H* \rightleftharpoons 2M + H_2 \qquad (1.7)$$

Similarly, the OER mechanism at the surface of the catalyst is expected to proceed via the adsorbate evolution mechanism (AEM).[57] Generally, the AEM takes place through four single electron charge transfer steps in alkaline medium, involving adsorption and desorption of a sequence of reaction intermediates as shown below.[57, 58] The overall response begins with the adsorption of OH⁻ and finishes with the desorption of the OH⁻.

$$M + OH^- \rightleftharpoons M–OH + e^- \qquad (1.8)$$

$$M–OH + OH^- \rightleftharpoons M–O + H_2O + e^- \qquad (1.9)$$

$$M–O + OH^- \rightleftharpoons M–OOH + e^- \qquad (1.10)$$

$$M\text{–}OOH + OH^- \rightleftharpoons M + O_2 + H_2O + e^- \qquad\qquad (1.11)$$
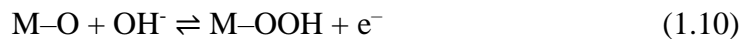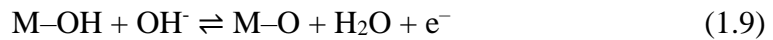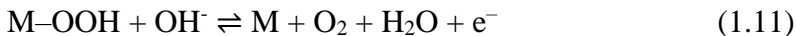
Similarly, OER mechanism in acidic medium involves following steps:

$$M + H_2O \rightleftharpoons M\text{–}OH + H^+ + e^- \qquad\qquad (1.12)$$

$$M\text{–}OH \rightleftharpoons M\text{–}O + H^+ + e^- \qquad\qquad (1.13)$$

$$M\text{–}O + H_2O \rightleftharpoons M\text{–}OOH + H^+ + e^- \qquad\qquad (1.14)$$

$$M\text{–}OOH \rightleftharpoons M + O_2 + H^+ + e^- \qquad\qquad (1.15)$$
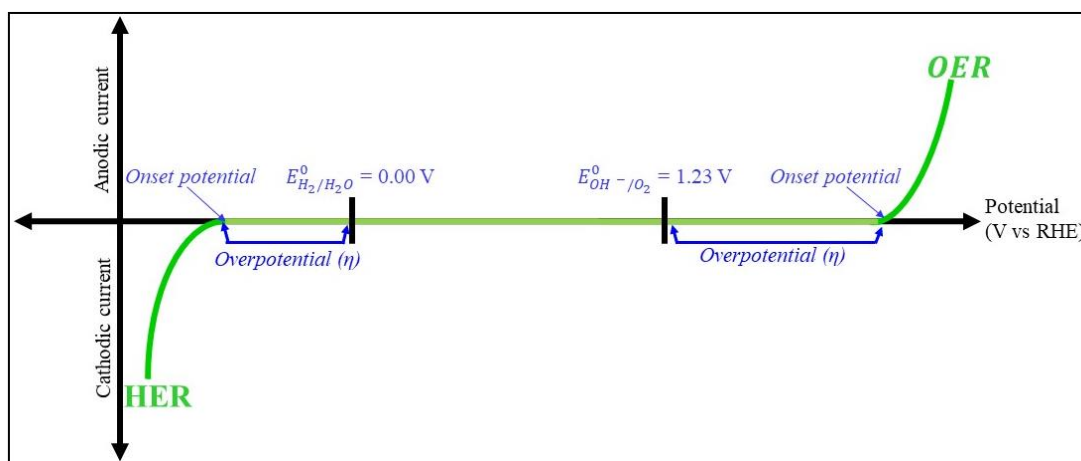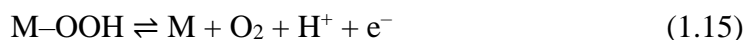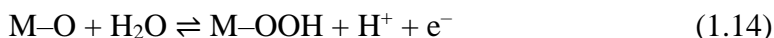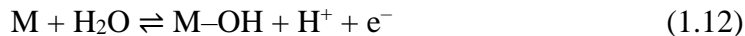
Figure 1.1.3.5.2: Half reactions of water splitting process.

Therefore, efficient electrocatalysts are required for these half reactions to facilitate the electron transfer as discussed above, which ultimately lower the overpotential. In particular, the OER is often considered the bottleneck for the overall water splitting. The traditional HER and OER catalysts are based on precious metals, including platinum,[59] iridium dioxide,[60, 61] and ruthenium dioxide.[62] The high cost of precious metals is clearly a prohibitive factor.[63] Therefore, considerable effort has been made in recent years to develop inexpensive and efficient catalysts for both OER and HER.[64-67]

Among different classes of materials, perovskite oxides have been pursued as robust, stable, and economic electrocatalysts for water splitting in recent years.[68-70] In particular, oxygen-deficient perovskites (ODPs) are promising candidates for replacing precious metal catalysts, given their structural diversity and flexibility of their functional properties.[64, 65] A number of oxygen-deficient perovskites have been investigated as OER electrocatalysts in alkaline media, such as $SrNb_{0.1}Co_{0.7}Fe_{0.2}O_{3-\delta}$,[66] $SrCo_{0.9}Ti_{0.1}O_{3-\delta}$,[71] $La_{0.5}Sr_{0.5}Co_{0.8}Fe_{0.2}O_{3-\delta}$,[72] $La_{0.7}(Ba_{0.5}Sr_{0.5})_{0.3}Co_{0.8}Fe_{0.2}O_{3-\delta}$,[73] and $Ba_{0.5}Sr_{0.5}Co_{0.8}Fe_{0.2}O_{3-\delta}$ (BSCF)[74]. There have also been studies on the HER activity of some oxygen-deficient perovskites in alkaline environment, such as $(Gd_{0.5}La_{0.5})BaCo_2O_{5.5+\delta}$,[75] $Pr_{0.5}(Ba_{0.5}Sr_{0.5})_{0.5}Co_{0.8}Fe_{0.2}O_{3-\delta}$,[76] and $SrNb_{0.1}Co_{0.7}Fe_{0.2}O_{3-\delta}$.[77] Some materials have been used as part of a composite with a precious metal catalyst, such as $K_{0.469}La_{0.531}TiO_3$ decorated by Ru cations on the surface, where nucleation growth of Ti-doped RuO_2 nanoparticles occurs.[78] This composite has better performance than Pt/C composite,[78] but it still uses a precious metal.

1.2 GENERAL OVERVIEW

This thesis contains fourteen chapters, where detailed information on perovskite oxides from synthesis to characterization to property studies, are presented. Chapter 1 describes the perovskite oxide family and its subclasses such as double perovskites, and oxygen deficient perovskites, along with basics of several properties that are studied in upcoming chapters. Chapter 2 explains the experimental aspects such as synthesis methodologies, characterization techniques, oxygen content analysis, device fabrication, and electrochemical measurement for perovskite oxides and related structures. Solid state and sol gel synthesis methods were utilized for the synthesis of materials. Similarly, this

chapter briefly discusses the characterization techniques of materials using powder X-ray diffraction, neutron diffraction, scanning electron microscopy, X-ray photoelectron spectroscopy, iodometric titration, etc. A detailed description of electrochemical measurements from catalyst ink preparation method to working electrode preparation to data analysis methods are also explained.

Chapter 3 explains the interesting magnetic and electrical property transformation of double perovskite series $BaSrMMoO_6$ (M = Mn, Fe, Co, Ni). $BaSrFeMoO_6$ has ferrimagnetic ordering of the moments of Fe ions and metallic behavior while measuring DC conductivity from 25 – 800 °C. However, Mn, Co, and Ni-containing materials have antiferromagnetic ordering and semiconducting behavior in the same temperature range.

Chapter 4 describes the results of O_2, CO_2, and CO gas interactions at 700 °C of four ODPs namely $Ca_2Fe_2O_5$, Ca_2FeMnO_5, Sr_2FeMnO_5, and Sr_2FeMnO_5. Among four materials, $Ca_2Fe_2O_5$ shows an outstanding sensing property for those three gases due to its structural stability. Chapter 5 describes detailed characterization and property studies of two novel ODPs $Ca_3GaMn_2O_8$ and $SrCa_2GaMn_2O_8$. Charge transport, magnetic, pseudocapacitive, and electrocatalytic hydrogen evolution activity in 0.5 M H_2SO_4 for the two compounds are thoroughly explained.

Chapters 6 through 13 explain the electrocatalysis of several perovskite oxides and their related structures toward OER and HER of water splitting. The best performing materials out of many electrocatalysts that have been considered for the study are $CaSrFeMnO_{6-\delta}$ (Chapter 6), $LaCa_2Fe_3O_8$ (Chapter 7), $Ca_2Sr_2Mn_2CoO_{10-\delta}$ (Chapter 8), $CaSrFe_{0.75}Co_{0.75}Mn_{0.5}O_{6-\delta}$ (Chapter 9), Sr_3FeMnO_6 (Chapter 10), $Ca_2FeCoO_{6-\delta}$ (Chapter 11), $BaSrCoMoO_6$ (Chapter 12), and $La_3Co_3O_8$ (Chapter 13). Our goal in these studies is

to find good electrocatalysts for lowering the overpotential. Finally, Chapter 14 presents an overall conclusion of this thesis, which will provide a summary of results and discussion of the interesting properties.

CHAPTER 2

SYNTHESIS, CHARACTERIZATION, AND FABRICATION METHODS

2.1 GENERAL OVERVIEW

One of the crucial aspects of materials chemistry is the synthesis of non-molecular inorganic solids, including perovskite oxides, by utilizing various methods. This primarily focuses on the synthesis, structure determination, and chemical and physical properties characterizations. In past few decades, the field has been expanded to the significant applications of solid-state materials for various systems such as batteries, pseudocapacitors, water electrolyzers, and fuel cells. Therefore, solid-state materials are prepared in various forms such as ceramics, fibers, films, foams, powders, nanoparticles and single crystals. This study is focused on the synthesis, characterization, and application of perovskite oxide ceramics.

In this chapter, the main methods used to synthesize and characterize perovskite oxides are summarized in general. Specifically, the experimental techniques, processing and fabrication methods, and several characterization techniques employed for several studies, are briefly discussed. More details and specific methods and experimental conditions of all chapters are thoroughly discussed. However, additional experiments and methods such as density functional theory (DFT) calculations are separately discussed in chapters as required.

2.2 MATERIAL SYNTHESIS

2.2.1 SOLID-STATE SYNTHESIS

Majority of the materials studied in this work were synthesized using conventional solid-state methods. It is the oldest and still most widely used method to make inorganic solids, where reactant precursor powders are thoroughly mixed together, perhaps pressed them into pellets or some other shape and then sintered in a furnace for prolonged periods.

The intimate mixing and pelletizing approach ensure a homogeneous mixture of desired reaction mixtures. Binary metal oxides or carbonates were mostly utilized during the synthesis. The disks or rectangular bars were then sintered in alumina boats at suitable temperatures under appropriate reaction conditions. The solid-state reaction conditions involved oxidizing (in the air or flowing oxygen gas) or reducing (1-10% H_2 gas balanced with argon gas) or an inert atmosphere (in argon). The first step is called calcination which involves burning off carbonates at 1000 ℃, followed by regrinding, repalletization, and sintering at temperature range of 1100 to 1400 ℃. The general scheme is given in Figure 2.2.1.

The solid-state reaction proceeds via slow ion diffusion mechanism, which occurs at the interfaces between reactant grains at a high temperature. Thus, these reactions solely rest on ions' diffusion rate towards the grain boundaries. Consequently, the reactions are driven by high temperatures and longer reaction times. Therefore, this process requires several intermediate grindings and palletization. In a nutshell, successful solid-state reaction to synthesize pure materials, require the practical consideration of four main

issues: choice of starting materials, mixing method, container and heat treatment conditions.[79]
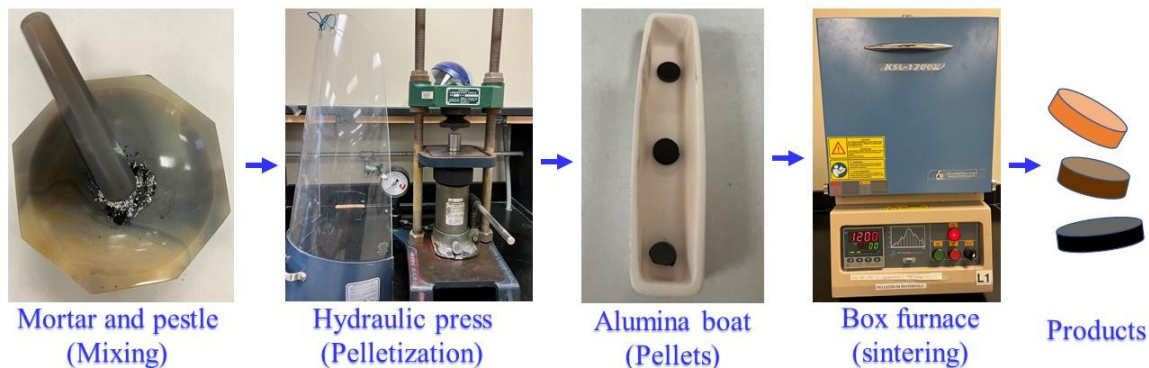
Figure 2.2.1: Schematic representation of steps in solid-state synthesis.

Starting materials

Starting materials should be pure, reactive, and accurately known stoichiometric proportion of precursors. Care should be taken for moisture and CO_2 sensitive reactants, which may be dried at certain temperature and/or stored in a desiccator. Oxy salt reagents such as carbonates and nitrates are ideal for oxide synthesis including perovskite oxide as considered in this study. Additionally, release of gases (CO_2, NH_3, N_2) during the decomposition (calcination step) can aid to mix the solid reactants.

Mixing of reactants

It is necessary to bring particles of reactants into contact during the solid-state reaction. Therefore, precursors powders are intimately mixed and milled. For this purpose, mixing and milling is done manually using a mortar and pestle because they are non-porous, readily cleaned and should not contaminate samples. Another way of mixing is mechanical mixing such as ball milling. This setup has a rotator container with a number of balls, for instance, agate, to mix the reactants. The container is then rotated for at least

3 – 24 hours. Other mechanical mixing methods involve a high-energy milling in planetary ball mills, which are rotated at very high speed. However, such type of mechanical processes have always a possibility of contamination from the milling media. Additionally, a liquid such as water or ethanol is also added to facilitate mixing.

Container

The solid-state reaction mixture is simply heated in a furnace in different atmosphere of gases such as air, argon, hydrogen, and oxygen. But the container should not react during the course of reaction. Frequently-used inert containers for oxides are boats or crucibles of alumina, Pt, Au, SiO_2 glass, graphite (for the synthesis of sulfides, other chalcogenides and Nitrides). Importantly, staining and contamination from products after the reaction should be avoided because temperature limits, reactivity, and cost should be considered while selecting the crucibles or boats made of various materials.

Firing schedule

The heating schedule is carefully designed to cause decomposition of oxy salt reagents (carbonates), avoid melting, and apply temperatures to cause the reagents reaction at reasonable timescale (e.g. 12–24 h). Box and tube furnaces are utilized for reaction in air. But tube furnace is helpful for controlled atmospheres of various gases. There are reported recipes for known materials, whereas new material synthesis may require several trials to get the correct conditions.

Overall, the material synthesis for various property studies in all upcoming chapters were carried out by the solid-state synthesis methods discussed above. This is summarized as follows. Based on the composition of a perovskite oxides, required powders of the precursor compounds such as $CaCO_3$ (Alfa Aesar, 99.95%), $SrCO_3$ (Alfa Aesar, 99.95%),

La$_2$O$_3$ (Alfa Aesar,99.998%), Fe$_2$O$_3$ (Alfa Aesar,99.998%), Mn$_2$O$_3$ (Sigma Aldrich,99.99%), Co$_3$O$_4$ (Alfa Aesar, 99.7%), CoO (Alfa Aesar,99.998%), and MnO (Alfa Aesar,99.998%), were mixed in stoichiometric proportions, and ground together using an agate mortar and pestle, then pressed into a pellet. The pellets were calcined in air or argon at 1000 °C for 24 h as needed for the composition. The samples were then reground and sintered at 1100 to 1400°C for 24 h in the same environment, followed by slow cooling. The heating and cooling rates were 100 °C/h in all cases.

The following table summarizes the solid-state synthesis conditions for all materials discussed in upcoming chapters of this study.

Table 2.1: Solid-state synthesis conditions for the studied materials.[80-87] Note that the heating and cooling rates were 100 °C/h in all cases.

	Materials	Temperature/medium	Total time (h)	Intermediate grindings
1.	BaSrMnMoO$_6$ BaSrFeMoO$_6$	1100 °C, 5% H$_2$/Argon	30	1
	BaSrCoMoO$_6$ BaSrNiMoO$_6$	1200 °C, Argon	96	3
2.	Ca$_2$Fe$_2$O$_5$ Ca$_2$FeMnO$_5$ Sr$_2$Fe$_2$O$_5$ Sr$_2$FeMnO$_5$	1200 °C, Argon	48	1
3.	Ca$_3$GaMn$_2$O$_8$ SrCa$_2$GaMn$_2$O$_8$	1000 °C, Air/1100 °C, Air	12/72	3
4.	Ca$_2$FeMnO$_{6-\delta}$ CaSrFeMnO$_{6-\delta}$ Sr$_2$FeMnO$_{6-\delta}$	1000 °C, Air/1200 °C, Air	24/24	1
5.	LaCa$_2$Fe$_3$O$_8$ LaSr$_2$Fe$_3$O$_8$	1100 °C, Ar/1300 °C/Ar 1300 °C/Ar	48 20	2 1
6.	Ca$_2$Sr$_2$Mn$_2$CoO$_{10-\delta}$ Ca$_2$Sr$_2$Mn$_2$FeO$_{10-\delta}$	1200 °C, Air/1350 °C, Air	48	1
7.	CaSrFe$_{1-x}$Co$_{1-x}$Mn$_{2x}$O$_{6-\delta}$ (x = 0 − 1)	1000 °C, Air/1200 °C, Air	48	1
8.	Sr$_3$Mn$_2$O$_6$ Sr$_3$FeMnO$_6$	1250 °C, Ar	48	1

9.	Ca$_2$FeCoO$_{6-\delta}$ CaSrFeCoO$_{6-\delta}$ Sr$_2$FeCoO$_{6-\delta}$	1000 ℃, Air/1200 ℃, Air	48	1
10.	LaCoO$_3$ La$_3$Co$_3$O$_8$	1150 ℃, Air 350 ℃, 5% H$_2$	48 15	1 -

2.2.2 SOL-GEL SYNTHESIS

Sol-gel is a simple technique to synthesize high-quality nano and microstructures.[88] This method provides several advantages over solid-state method, where grain size is generally in micrometer range. Therefore, sol-gel method controls several aspects such as the texture, surface properties of the materials, and particularly nanometer nanoscale powders. Additionally, the process has features such as easy implementation, low cost, high quality, and production of materials with large surface areas.[89] It is also widely used as a coating method.[90]
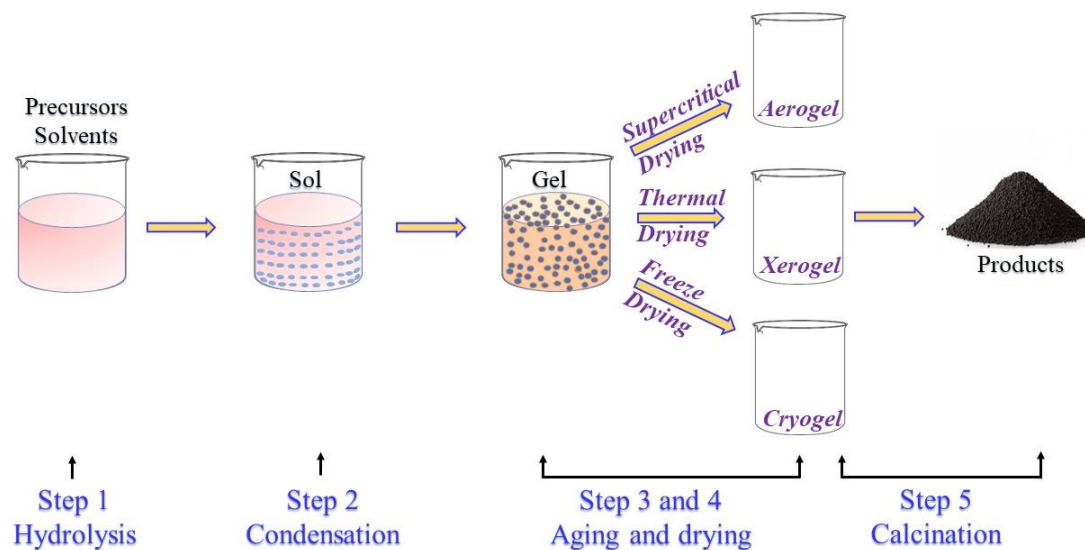
Figure 2.2.2: Schematic representation of steps in sol-gel synthesis.

The Sol-Gel method utilizes a colloidal solution referred as "Sol", which then evolves into a "Gel". Therefore, the sol-gel involves a network that contains both a liquid and a solid phase because of several chemical reactions. It is categorized into two types: aqueous or hydrolytic and non-aqueous or non-hydrolytic. The aqueous Sol-Gel process can be explained in five important steps: hydrolysis, condensation, aging, drying and crystallization as shown in Figure 2.2.2.

2.3 CHARACTERIZATION TECHNIQUES

2.3.1 POWDER DIFFRACTION

The phase identification and characterization are the next steps once a sample is synthesized. A phase refers to a solid with a regular 3-dimensional arrangement of the atoms. X-ray and neutron powder diffraction techniques are considered for the identification of the regular 3D arrangement of the atoms, which includes atomic positions, interatomic distances, and bond angles.[91] Throughout all the studies discussed in several chapters, powder X-ray diffraction (XRD) was used the most. However, powder neutron diffraction (PND) experiments were also used to understand the magnetic structures of some compounds.

2.3.1.1 POWDER X-RAY DIFFRACTION

In a crystal lattice, there are multiple atoms that contribute to the diffraction. Hence, a diffraction peak is observed by the constructive interference of the beams reflected by atoms that correspond to a certain *hkl* set of planes (Figure 2.3.1.1). Therefore, each peak corresponds to a particular *d* spacing (distance between two consecutive planes) in the crystal. Furthermore, constructive interference is observed when the waves are in phase

and a diffraction peak will be possible only if the difference between the travelled distances

is an integer, *n*, of the wavelength, λ. In other words, if AB+BC=*n*λ. Also, note that

AB=BC=*d*sinθ.

Therefore,

$$2dSin\theta = n\lambda \text{ (Bragg's Law)} \tag{2.1}$$

Diffracted beams that do not follow this law (i.e. if path difference is a non-integer)

will interfere destructively.
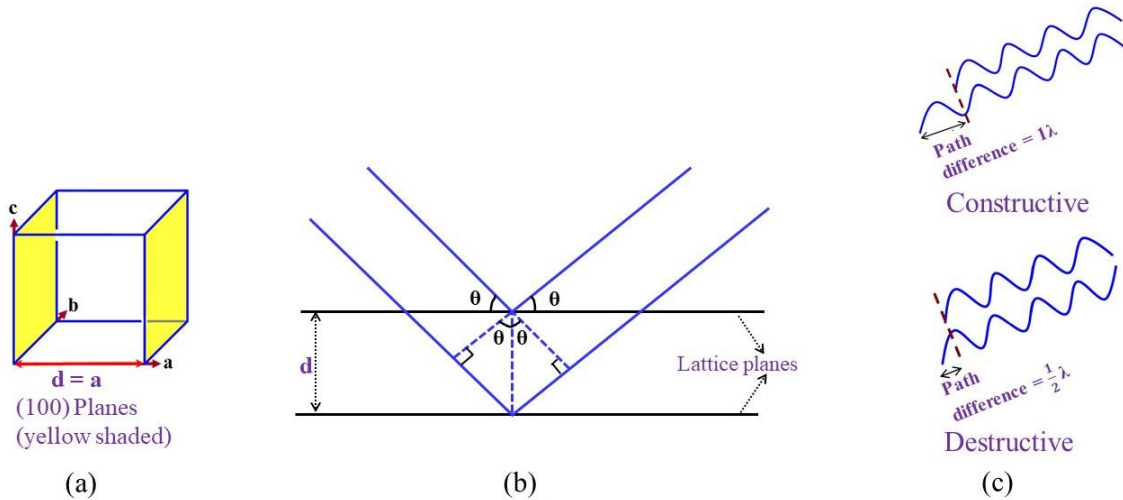
Figure 2.3.1.1: (a) Lattice planes in a unit cell, (b) Scattering of X-rays by lattice planes, and (c) Modes of beam after diffraction.

During the powder XRD data analysis, phase purity is determined by comparison

of the measured pattern with the entries in reference databases using a search-match

algorithm. Then, the powder pattern of a phase in this study is used for Rietveld refinement

using GSAS software[92] with EXPIGUI interface.[93] Other such software include FullProf

and Topaz fitting programs. Finally, these analyses give detailed crystallographic data such

as the site occupancies of atoms and vacancies and interstitial locations within the material.[79]

Powder diffraction is utilized as a fingerprint detection for specific phases present in crystalline solids. It allows for the accurate determination of the unit cell dimensions. The location of diffraction peaks plotted against Bragg's angle (2θ) for both single or polycrystalline materials is dependent on the unit cell parameters. When the cell parameters increase, the entire diffraction pattern shifts towards lower 2θ values though all the diffraction lines may not necessarily move by the same magnitude in non-cubic crystal systems if the expansion is not isotropic. Similarly, the peaks at a high 2θ angle are generally less pronounced because of the dependence on angle.

2.3.1.2 POWDER NEUTRON DIFFRACTION

In some of the projects of this study, powder neutron diffraction (PND) experiments were done at Oak Ridge National Labs to understand the magnetic structures of some of the phases. PND is a powerful technique that requires intense neutron flux, which is generated from a nuclear reactor or a spallation source. Unlike X-ray diffraction, PND uses the diffraction from nuclei of an atom, it allows to study lighter atoms and isotopes with similar atomic numbers. However, scarcity of the facility, low flux of sources, and large sample quantity (3-4 g), are some of the setbacks of this technique.

This technique in this study has been utilized to study the information of the magnetic orders i.e. the relative arrangement of magnetic moments of transition metals in perovskite oxides. In perovskite oxides, magnetic ordering of B-site cations having unpaired d-electrons is possible. Ordering of moment direction for the magnetic behaviors such as paramagnetism, ferromagnetism, antiferromagnetism, are shown in Figure

2.3.1.2.1. Mostly, such moment alignment in cases such as antiferromagnetism and ferromagnetism occur due to double and super exchange mechanisms, respectively.[1] For example, several antiferromagnetic ordering schemes in perovskite oxides are possible such as A-, C-, E-, and G-types (Figure 2.3.1.2.2). Such ordering schemes are obtained by the Rietveld refinement of PND data. The refinement is carried out with at least two different phases- one phase that attributes to crystal lattices, and another phase represent diffraction peaks that arises only from magnetic ions/lattices.
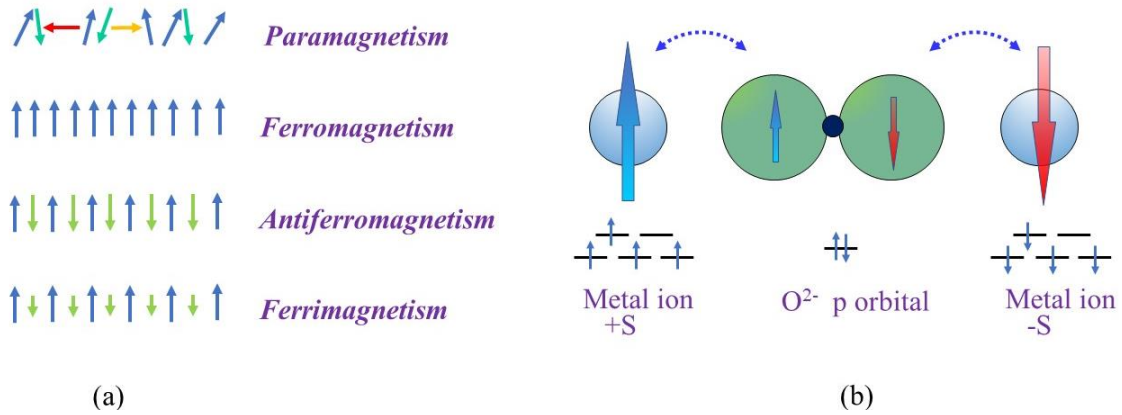
Figure 2.3.1.2.1: Schematic representations of (a) Magnetic phenomena in 1D crystal, and (b) 180° superexchange between two paramagnetic cations (M^{3+}) across the filled p orbitals of oxygen ion (O^{2-}).
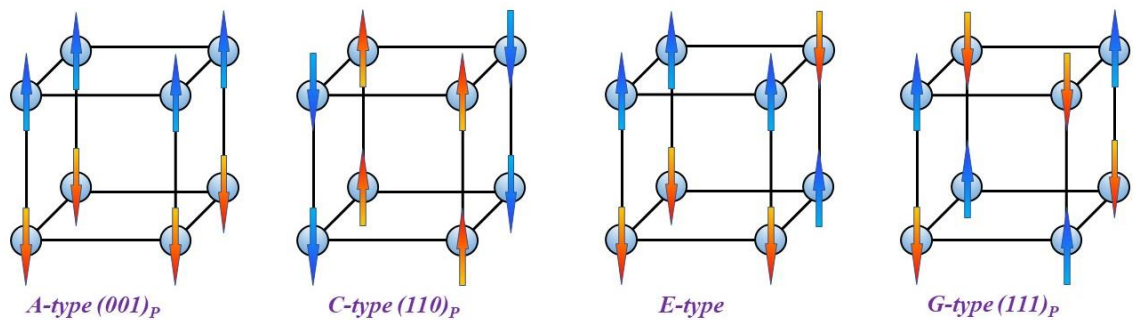
Figure 2.3.1.2. 2: Possible antiferromagnetic spin ordering patterns in an ideal cubic unit cell.

We have studied the magnetism of several materials, as discussed in the future chapters. Neutron diffraction experiments at 10 K were performed on POWGEN diffractometer at Oak Ridge National Laboratory. In addition, magnetization measurements were done on a vibrating sample magnetometer (VSM) to obtain magnetic susceptibility data at the temperature range of $2 - 400K$, and isothermal magnetization data in fields up to 9 T.

2.3.2 ELECTRICAL CONDUCTIVITY MEASUREMENT TECHNIQUES

In this section, conductivity measurement of perovskite oxides is discussed. Electrical conductivity measurement is usually carried out by measuring the electrical resistance of a sample under an applied voltage e.g., 0.01 V. The electrical response changes depending upon the nature of resistance (Figure 2.3.2.1). Generally, the current response plateaus over a time for an electronic conductor. In ionic conductors, on the other hand, the diminished mobility of ions over the time drops the current response. The current theoretically drops to a value that is a function of the magnitude of the electronic conduction in mixed conductors. The measurement is done either using two-probe or four-probe contact technique.
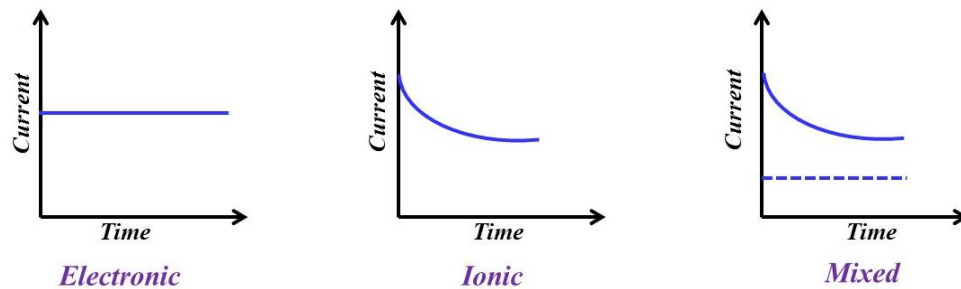
Figure 2.3.2 .1: Variation of current as a function of time in various modes of conduction.

In two-probe technique, the resistivity of a material can be obtained by measuring the resistance and physical dimensions of a bar of material, as shown in Figure 2.3.2.2. The material is cut into the shape of a rectangular bar, which is then painted with gold paste. Gold leads and wires are attached to both ends of the bar. A voltage source applies a voltage (0.01 V) across the bar, causing a current to flow through the bar. the resistance is expressed as:

$$R = \frac{V}{I} \tag{2.2}$$

where, R = resistance, v= applied voltage, and I is current in amperes. Then, resistivity is calculated as:

$$\rho = \frac{Rwh}{l} \tag{2.3}$$

where, ρ, R, w, h, and l are resistivity, width, thickness, and length of the material. Finally, the reciprocal of resistivity provides the conductivity.
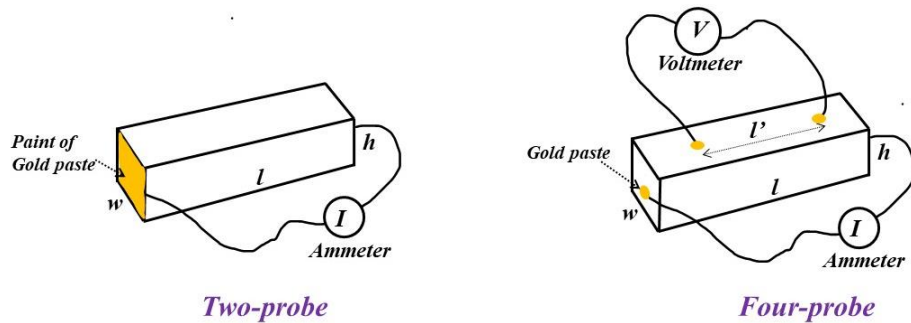
Figure 2.3.2 .2: DC conductivity measurement using two and four-point connections.

In practice, the two-probe method may lead to some errors because of the contribution of current from contacts and wires. Therefore, the four-probe technique gives more accurate measurement. In this technique, four wires are attached to the sample bar as shown in Figure 2.3.2.2. A potential is applied through two wires located on the surface,

causing a current to flow. For a thin enough sample, the current flow can be considered uniform. A separate ammeter measures the amount of current passing through the bar. The four-probe resistivity of the material is calculated as:

$$\rho = \frac{Vwh}{I\,l'} \qquad (2.4)$$

Two-probe direct current (DC) measurements discussed above are not considered to determine ionic conductivity in solids. Instead, AC impedance spectroscopy method is utilized for this purpose.[94] Impedance is the alternating current analog to resistance for direct current.

Several materials of this study were considered for conductivity studies. The variable temperature (25 – 800 °C) electrical conductivity measurements in air were done using a four-probe DC technique on rectangular pellets. Current values were recorded by applying a potential of 0.01 V.

2.3.3 SCANNING ELECTRON MICROSCOPY

Scanning electron microscopy (SEM) provides important information on the micro-structures, particle sizes, and shapes over a broad range of magnifications. SEM also has an additional feature called energy dispersive X-ray detection (EDX). This allows elemental analysis, and the mapping of elemental distributions in a specific solid material. When high-energy electrons impinge on a compound, X-rays are generated. The energies of such X-ray radiations are characteristic of the element producing it. This study has SEM analysis in most chapters.

2.3.4 QUANTIFICATION OF OXYGEN CONTENT VIA IODOMETRIC TITRATION

For the quantification of oxygen non-stoichiometry (δ) per unit formula of perovskite oxides, iodometric titration is used in this study because this has been a powerful tool used in literature.[80, 83, 86, 95]

The principle of iodometric titration is based on the double iodometric titration, that helps to reduce systematic errors.[95] This involves two experiments. In the first experiment, sample is dissolved in an aqueous hydrochloric acid with excess KI, and a reaction occurs. Then, the second experiment involves the reduction of metal to lowest stable oxidation state with the release of I_2. Thus, liberated I_2 is titrated against $Na_2S_2O_3$ solution using starch solution as an indicator. All experiments should be performed under inert atmosphere (argon or nitrogen gas purge and flow) to prevent interference from the atmospheric oxygen. A schematic of iodometric titration is presented in Figure 2.3.4.

Figure 2.3 .4: Schematics showing the steps in iodometric titration.

In the perovskite oxides, iodide reduces B-site ions with variable valency such as B^{3+} and B^{4+} to the lowest stable valence state such as B^{2+}. At the same time, iodide ion is oxidized to form I_2. The amount of I_2 released is then quantified via redox titration with $Na_2S_2O_3$ solution. δ value is then determined based on the amount of I_2 released. Volume

of $Na_2S_2O_3$ solution consumed during the process is recorded. Then, the average valence of B-site and oxygen non-stoichiometry (δ) is determined by the reaction equation and the charge neutrality principle. The average valency of the B-site cation(s) in the sample can be represented by the following titration reaction equations:[96]

$$AB^{X+}O_3 \rightarrow AB^{2+}O_2 + \frac{X-2}{2}I_2 \qquad (2.5)$$

$$I_2 + 2S_2O_3^{2-} \rightarrow 2I^- + S_4O_6^{2-} \qquad (2.6)$$
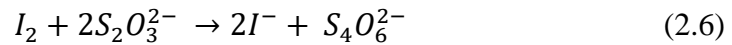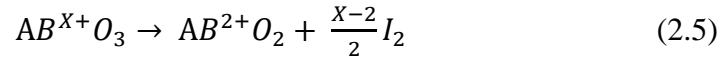
Then, δ value can be calculated as follows:

$$\delta = \frac{(4-Y)\, m - M\, n}{2\, m - 16\, n} \qquad (2.7)$$

where, M = molar mass of the sample, Y = the average valence of the A-site cation (mostly considered stable), m = sample mass, C = concentration of $Na_2S_2O_3$, and $n = C$ x ΔV, where ΔV is the total volume of $Na_2S_2O_3$ solution consumed.

The above literature is summarized to run experiments for iodometric titration for determining oxygen content of several samples, that will be discussed in upcoming chapters. The titrations were performed under an argon atmosphere by dissolving about 50 mg of the sample and excess KI (~2 g) in 100 mL of 1 M HCl. A total of 5 mL of the solution was then pipetted out into a conical flask with 20 mL of water. The solution was titrated against 0.025 M $Na_2S_2O_3$. Near the endpoint of the titration, 0.2 mL of a starch solution was added to act as an indicator. The iodometric titrations were done on three different samples for each compound, and the measurement on each sample was repeated three times to ensure reproducibility.

2.3.5 X-RAY PHOTOELECTRON SPECTROSCOPY (XPS)

The study of oxidation states of transition metal of most of the perovskite oxides is very crucial for this study. This helps to understand the bonding environment of B-site cations. Many properties such as magnetism, electrocatalysis, polaron mechanism in conductivity, etc. require the information of chemical states of metal ions. Therefore, XPS measurement were thoroughly done before and after material's property testing in many cases. They are discussed extensively in several chapters. XPS experiments were performed at room temperature using Al Kα radiation (1486.7 eV).

2.4 MATERIALS PROCESSING AND FABRICATION

In this section, the processing and fabrication of perovskite samples that were utilized for electrochemical application, is briefly discussed. Perovskite oxides have been applied for energy conversion and storage processes. This will be briefly discussed here in general perspectives. However, more detailed fabrication methods and processing will be discussed in future chapters.

Sensor cell fabrication

As a part of this work, perovskite oxides have been studied for gas sensors (chapter 4). For fabrication of a sensor device, either rectangularly shaped or disks of materials can be used. The disk is painted with the gold paste on both sides and dried at 600 ℃ for an hour. Then, using gold leads that are connected with the gold wires, the disk is sandwiched between ceramic pellets using a spring loaded setup. Finally, current responses over time upon exposure to different concentrations of analyte gases such as O_2, CO_2, and CO can be recorded.

Electrochemical measurements and working electrode preparation

Perovskite oxides in this study have been explored for their electrocatalytic performance for electrochemical water splitting to generate clean and green hydrogen gas for fuel. The water splitting process involves two half reactions namely hydrogen evolution reaction (HER) and oxygen evolution reaction (OER). Both reactions are sluggish and bear large overpotential, which is minimized by using perovskite oxide electrocatalysts.

(a)   (b)

(c)
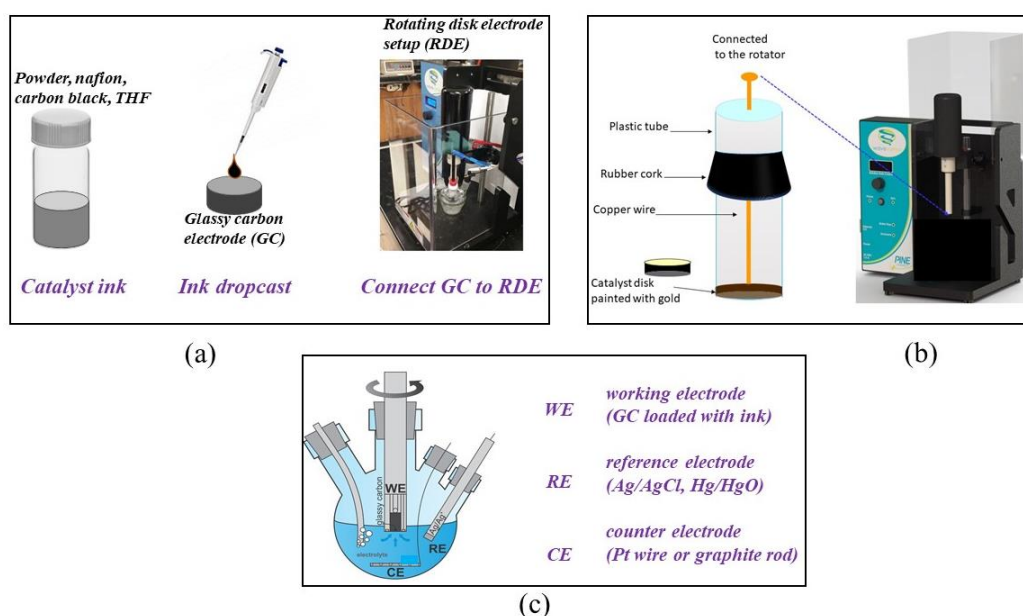
Figure 2.4: (a) Schematics for the preparation of catalyst ink and steps of depositing the catalyst ink film onto the surface of glassy carbon working electrode, (b) the use of disk of catalyst as WE, and (c) Electrochemical cell with electrode types.

The majority of OER and HER studies are concentrated on powder materials to measure the activity.[97] These powdered catalyst materials are first converted into an ink form by dispersing in a suitable solvent (generally ethanol and tetrahydrofuran, THF) to form a homogeneous solution. A binder is added to attach the catalyst on the electrode. Some commercially available binders are Nafion®, Aquivion®, PTFE Fumion®, etc. In most of the literature, Nafion is the most used binder. The Nafion content should be as low

as possible (in micro liters) to minimize the extra diffusion resistance by O_2 and IR drop. Then, additives such as acetylene black or carbon black are also added. This mixture is sonicated at least 15 - 30 minutes to form the homogeneous ink. The catalyst ink is then drop casted onto a glassy carbon electrode surface. A schematic representation of ink preparation, dropcast method for catalyst film, electrochemical cells, rotating disk electrode setup (RDE) for experiments, and disk or pellet OER setup, are shown in Figure 2.4. The experiment is run in a four-neck electrochemical cell that contains an alkaline or acidic electrolyte. The working electrode is attached to the rotator of a rotating disk electrode setup (RDE). For an alkaline electrode, Hg/HgO electrode is used as reference electrode, whereas for an acidic electrolyte, Ag/AgCl is used. Pt wire and graphite rod are used as counter electrode for OER and HER studies, respectively. The working electrode is rotated at 1600 rpm during the experiments to shake off the evolved bubbles of O_2 or H_2 gas. The stability of the electrocatalyst is studied either by running at least 1000 OER/HER cyclic voltammograms (CVs) or by running chronopotentiometry experiments of a two-electrode cell containing catalyst ink for at least 10 hours. In some cases, we have utilized catalyst disk itself as working electrode to prevent the contribution of nafion, carbon black, and other additives used during the preparation of catalyst ink. This not only allows to test the stability of catalysts but also provides information about intrinsic OER/HER activity.

More specifically, the general process discussed above for electrocatalytic experiments, can be summarized as follows. Catalyst ink for HER and OER was prepared by sonicating a mixture of 35 mg perovskite powder, 40 μL Nafion and 7 mL THF for 30 minutes. Then 20 - 40 μL of the ink was drop-casted (10 μL per coating) on the surface of a glassy carbon electrode (with area of 0.196 cm^2) and allowed to air-dry overnight.

Experiments were also done by addition of 7 mg carbon black to the above mixture. For many perovskite oxides discussed in few chapters, the results without or with carbon black were similar.

The glassy carbon electrode loaded with catalyst was used as the working electrode and was rotated using a rotating disk electrode system at 1600 rpm. A commercial Pt electrode and silver/silver chloride electrode were used as counter and reference electrodes, respectively. The OER cyclic voltammetry data were recorded at a scan rate of 10 mV s^{-1} versus Ag/AgCl (3 M KCl), as commonly done for OER experiments.[64, 71, 98, 99] The potential range that was scanned in OER experiments was 0.0 to 0.8 V (vs Ag/AgCl) for basic and 0.0 to 2.1 V (vs Ag/AgCl) for acidic condition. The HER data were obtained using a carbon counter electrode at a scan rate of 10 mV s^{-1} versus Ag/AgCl (4 M KCl), as commonly utilized in HER.[100-102] The potential range that was scanned in HER experiments was -0.5 to -1.6 V (vs Ag/AgCl) for basic and 0.0 to -1.0 V (vs Ag/AgCl) for acidic condition. The ohmic drop (iR) correction was made to all polarization curves by measuring solution resistance via AC impedance, which gave 31 – 50 Ω for 0.1 M HClO$_4$, 50 – 63 Ω for 0.1 M KOH, and 9 – 12 Ω for 1 M KOH. The potential values versus silver/silver chloride ($E_{Ag/AgCl}$) were converted to be expressed against RHE according to the equation

$$E_{RHE} = E_{Ag/AgCl} + 0.059 \text{ pH} + E^o_{Ag/AgCl} \qquad (2.8)$$

where $E^o_{Ag/AgCl}$ = 0.21 V for 3M KCl[98] and 0.197 V for 4 M KCl.[103]

Chronopotentiometry experiments were conducted to test the stability of the catalyst by applying the current of 10 mA and measuring the potential over time.

Pseudocapacitive measurements

For pseudocapacitance studies, the same ink preparation method as above was used for three-electrode cyclic voltammetry (CV) measurements. In the three-electrode cell, the sample ink (40 µL) loaded on GCE was used as a working electrode, Pt as a counter electrode, and Ag/AgCl (in 3M NaCl) as a reference electrode to record CVs by scanning from -1.0 to 0.4 V (vs Ag/AgCl) using rotating disk electrode at 1600 rpm. Pt electrode was cleaned before use by bath sonicating for 15 minutes in 0.5M H_2SO_4.

For the fabrication of a symmetric two-electrode cell for galvanostatic charge/discharge (GCD), 100 µL of the same ink was pipetted in 20 µL increments to drop-cast onto both sides of a 1 cm^2 nickel foam followed by air-drying overnight. Two identical Ni foam electrodes with a total of 1 mg loading of active material were prepared. The two nickel foam electrodes were separated by placing a glass fiber filter paper between them. Gold wires and leads were clipped onto the electrodes to complete the cell circuit for studying GCD in 1 M KOH. The cell was soaked in 1 M KOH for at least an hour before GCD experiment and at least 12 hours before the stability test. The cell was used to record GCD curves at 0.5, 1, 3, 5, and 10 A/g current density. The GCD curves were recorded from 0.0 to 1.4 V vs Ag/AgCl stored in 3M NaCl (ALS Co., Ltd, Japan).

CHAPTER 3

MAGNETIC AND ELECTRICAL PROPERTIES OF BaSrMMoO$_6$ (M = Mn, Fe, Co, Ni)

In this chapter, we study the trends in magnetic and electrical properties of a series of double perovskites, BaSrMMoO$_6$, M = Mn, Fe, Co, Ni, by retaining the 4d element, Mo, and varying the 3d metal, Mn, Fe, Co or Ni. The magnetic properties of these materials have not been studied, with the exception of one report on the Fe-material.[104] The magnetic properties of the Mn, Co and Ni compounds are studied in this work for the first time. In addition, we have employed X-ray photoelectron spectroscopy to gain an in-depth understanding of the valence distribution of cations and the internal redox processes in these materials.

3.1 CRYSTAL STRUCTURE

Rietveld refinements with powder X-ray diffraction were employed to investigate the crystal structures of all compounds. The refinement profiles are shown in Figure 3.1, and the refined structural parameters are listed in Tables 3.1 - 3.4. These materials crystallize in cubic *Fm-3m* space group, consistent with previous reports.[105, 106] As seen in Figure 3.2, these AA′BB′O$_6$ double perovskites possess crystal structures with rock-salt ordering at B-site. The ordered BO$_6$ (B= Mn, Fe, Co, Ni) and B′O$_6$ (B' = Mo) octahedra

are connected through corner-sharing. The B and B′ cations alternate along the three crystallographic directions, such that the BO_6 octahedra only have $B′O_6$ octahedra as nearest neighbors, and vice versa. It is evident that for these materials, the change in the B-site cation does not affect the structure-type, and the crystal symmetry remains cubic in all cases. However, the A/A′-site cations have a major impact on the structural symmetry, as evident from comparison between $BaSrMnMoO_6$ and its analogues, which contain other types of cations on the A/A′-sites. Ca_2MnMoO_6 [107] and Sr_2MnMoO_6 [108] both adopt the monoclinic $P2_1/n$ symmetry. Whereas, $BaSrMnMoO_6$ has cubic *Fm-3m* structure. Similar situation applies to the Fe-compound $BaSrFeMoO_6$ (*Fm-3m*), where its Ca_2 analogue, Ca_2FeMoO_6 is monoclinic *P21/n* [109] and the Sr_2 analogue, Sr_2FeMoO_6 is tetragonal *I4/m*. [108] Likewise, the structure of the Co and Ni compounds are dependent on the A/A′-site cations, where both Sr_2CoMoO_6 and Sr_2NiMoO_6 are reported as tetragonal *I4/m*.[108, 110] Therefore, the presence of 50% Ba on the A/A′-sites helps to stabilize the cubic symmetry in the crystal structure of these double perovskites.[110]

To determine if there was oxygen non-stoichiometry in these compounds, we performed iodometric titrations on all materials. These experiments showed that these compounds do not contain non-stoichiometry, and the oxygen stoichiometry in all materials was almost exactly 6.

The crystallites size and morphology of these materials were examined by scanning electron microscopy (SEM) as shown in Figure 3.3. $BaSrNiMoO_6$ and $BaSrCoMoO_6$ show the largest crystallites, which are ~10 μm or larger, whereas the crystallites become smaller in $BaSrMnMoO_6$ and $BaSrFeMoO_6$. The latter contains the smallest crystallites of about 1 μm.
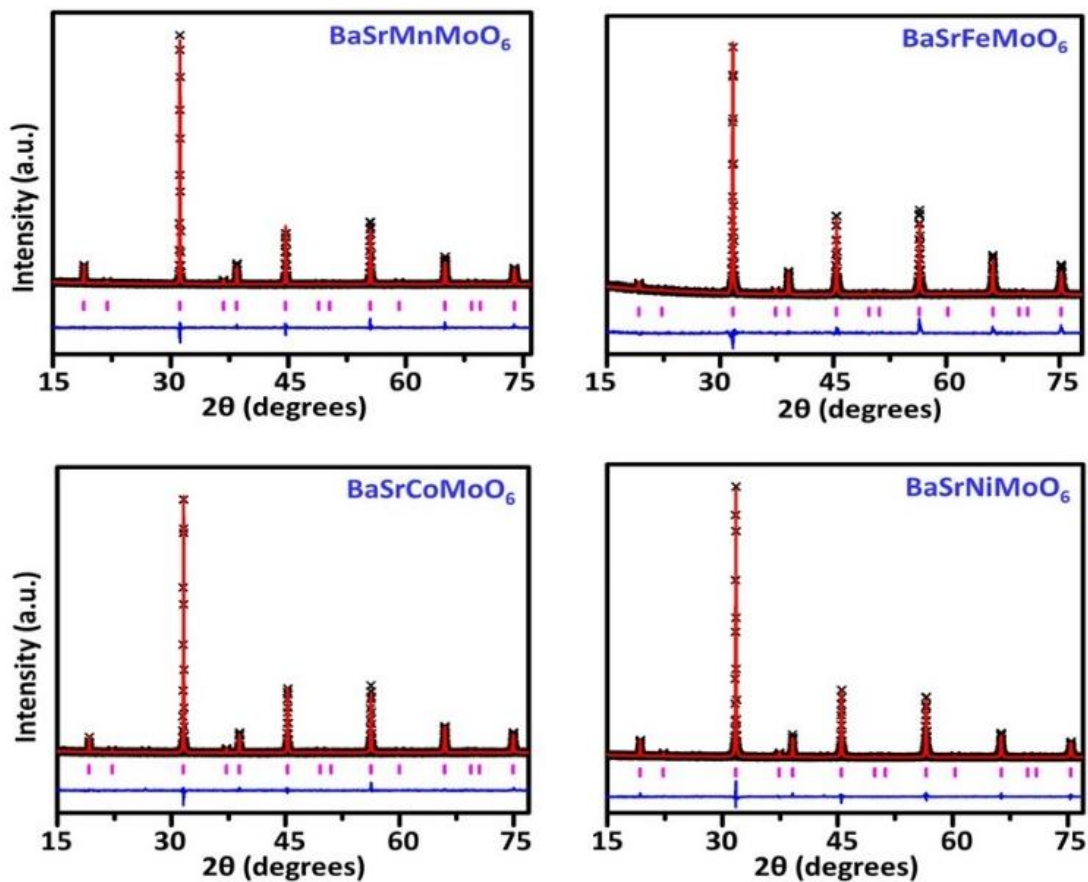
Figure 3.1: Rietveld refinement profiles for PXRD data with *Fm-3m* space group. The black cross symbols, red solid curve, pink vertical tick marks and the lower blue curve correspond to the experimental data, calculated pattern for *Fm-3m* model, the Bragg peak positions and the plot difference, respectively.
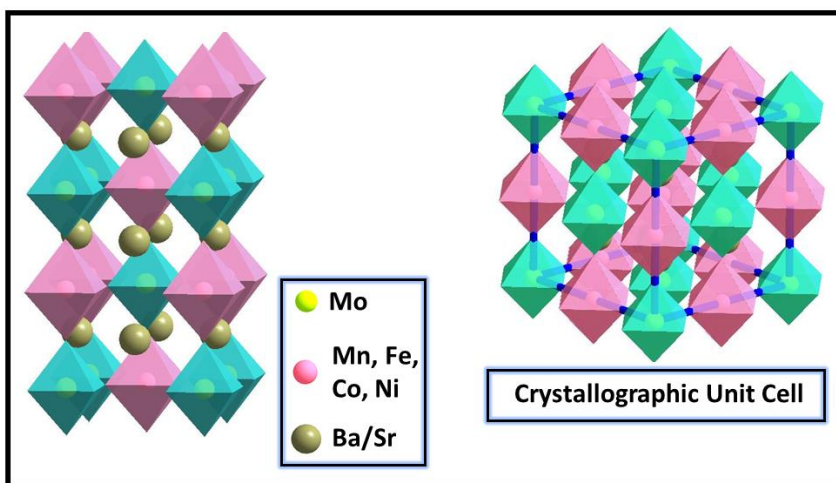
Figure 3.2: Crystal Structures showing the rock-salt-type order and crystallographic unit cell.
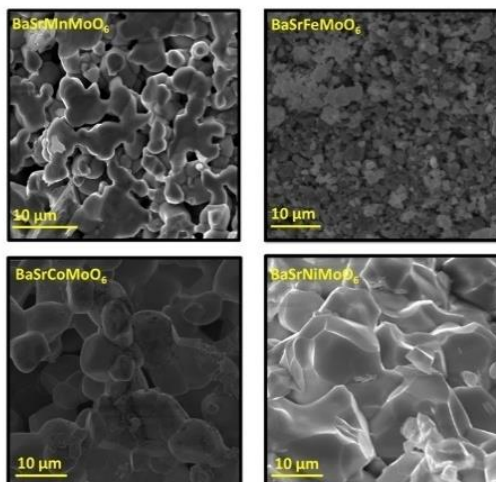
Figure 3.3: Typical SEM micrograph images.

Table 3.1: Refined Structural Parameters of $BaSrMnMoO_6$ Using PXRD[a]

Element	x	y	z	Occupancy	Uiso	Multiplicity
O1	0.2357(5)	0	0	1	0.035(1)	24
Mo1	0	0	0	1	0.0284(7)	4
Mn1	0.5	0.5	0.5	1	0.017(1)	4
Sr1	0.25	0.25	0.25	0.5	0.0271(5)	8
Ba1	0.25	0.25	0.25	0.5	0.0271(5)	8

[a] Space group: *Fm-3m* (#225) a = 8.1073(2) Å, R_p = 0.0421, wR_p = 0.0556, χ^2 = 2.1%.

Table 3.2: Refined Structural Parameters of $BaSrFeMoO_6$ Using PXRD[a]

Element	x	y	z	Occupancy	Uiso	Multiplicity
O1	0.2333(4)	0	0	1	0.041(1)	24
Mo1	0	0	0	1	0.0289(7)	4
Fe1	0.5	0.5	0.5	1	0.027(1)	4
Sr1	0.25	0.25	0.25	0.5	0.0297(4)	8
Ba1	0.25	0.25	0.25	0.5	0.0297(4)	8

[a] Space group: *Fm-3m* (#225) a = 8.1046(2) Å, R_p = 0.0412, wR_p = 0.0583, χ^2 = 3.34%.

Table 3.3: Refined Structural Parameters of $BaSrCoMoO_6$ Using PXRD[a]

Element	x	y	z	Occupancy	Uiso	Multiplicity
O1	0.2396(9)	0	0	1	0.008(2)	24
Mo1	0	0	0	1	0.002(1)	4
Co1	0.5	0.5	0.5	1	0.003(2)	4
Sr1	0.25	0.25	0.25	0.5	0.0032(7)	8
Ba1	0.25	0.25	0.25	0.5	0.0032(7)	8

[a] Space group: *Fm-3m* (#225) a = 8.0049(1) Å, R_p = 0.0548, wR_p = 0.0707, χ^2 = 1.23%.

Table 3.4: Refined Structural Parameters of BaSrNiMoO$_6$ Using PXRD[a]

Element	x	y	z	Occupancy	Uiso	Multiplicity
O1	0.2390(9)	0	0	1	0.024(2)	24
Mo1	0	0	0	1	0.019(1)	4
Ni1	0.5	0.5	0.5	1	0.019(1)	4
Sr1	0.25	0.25	0.25	0.5	0.0222(8)	8
Ba1	0.25	0.25	0.25	0.5	0.0222(8)	8

Space group: *Fm-3m* (#225) a = 7.959(1) Å, R$_p$ = 0.0852, wR$_p$ = 0.1222, χ^2 = 2.29%.

3.2 ELECTRICAL CONDUCTIVITY

The electrical properties were investigated by four-probe technique on rectangular pellets in the temperature range 25 – 800 °C. The resistance values (R) obtained from these measurements were used to calculate the electrical conductivity (σ) using the following equation:

$$\sigma = \frac{L}{RA} \tag{3.1}$$

Here, L is the distance between the voltage leads, and A is the cross-sectional area of the rectangular pellet where the current leads are connected. The above equation is further modified to get the following equation for the calculation of conductivity using four-probe technique:[19, 112]

$$\sigma = \left(\frac{I}{V}\right) \cdot \left(\frac{L}{wh}\right) \tag{3.2}$$

where, I, V, L, w and h are the current, applied potential, the distance between the voltage contacts, width and thickness of the rectangularly shaped sample.

At room temperature, BaSrFeMoO$_6$ shows the highest electrical conductivity, which is several orders of magnitude greater than the conductivities of the other three compounds (Table 3.5). The variable-temperature measurements indicate metallic

behavior for this compound, where a decrease in conductivity is observed as a function of temperature (Figure 3.4), consistent with a previous report. [106] The other three compounds show increase in electrical conductivity as a function of temperature, a property which is typical of semiconductors.[105, 106] A marked increase in conductivity is observed above 200 °C for $BaSrMnMoO_6$, 300 °C for $BaSrCoMoO_6$, and 500 °C for $BaSrNiMoO_6$, as observed in Figure 3.4.
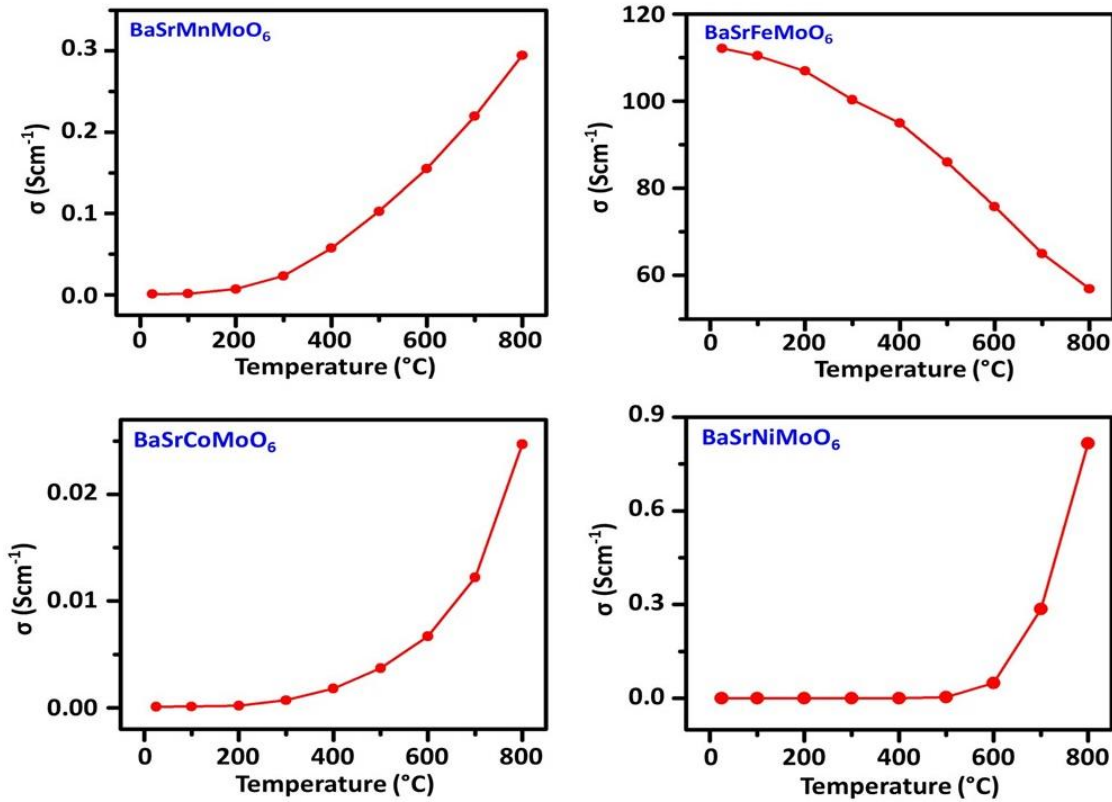
Figure 3.4: Electrical conductivity data from 25 to 800 °C.

Table 3.5: Variable temperature conductivity of Materials Room temperature conductivity of the four compounds

	DC Conductivity at 25 °C (S/cm)
$BaSrMnMoO_6$	9.07×10^{-4}
$BaSrFeMoO_6$	1.12×10^{2}
$BaSrCoMoO_6$	9.05×10^{-5}
$BaSrNiMoO_6$	5.50×10^{-6}

The Arrhenius equation can be used to calculate the activation energies (E_a) for the increase in conductivity as a function of temperature:

$$\sigma = \sigma° \, e^{-E_a/kT} \qquad (3.3)$$

where $\sigma°$ is a pre-exponential factor and a characteristic of a material, and E_a, k, and T are the activation energy, Boltzmann constant, and absolute temperature, respectively. Figure 3.5 shows the Arrhenius plot for all compounds. From this graph, the E_a values for the conductivity increase above 100 °C were calculated to be 0.270 eV, 0.273 eV and 0.558 eV for $BaSrMnMoO_6$, $BaSrCoMoO_6$, and $BaSrNiMoO_6$, respectively.
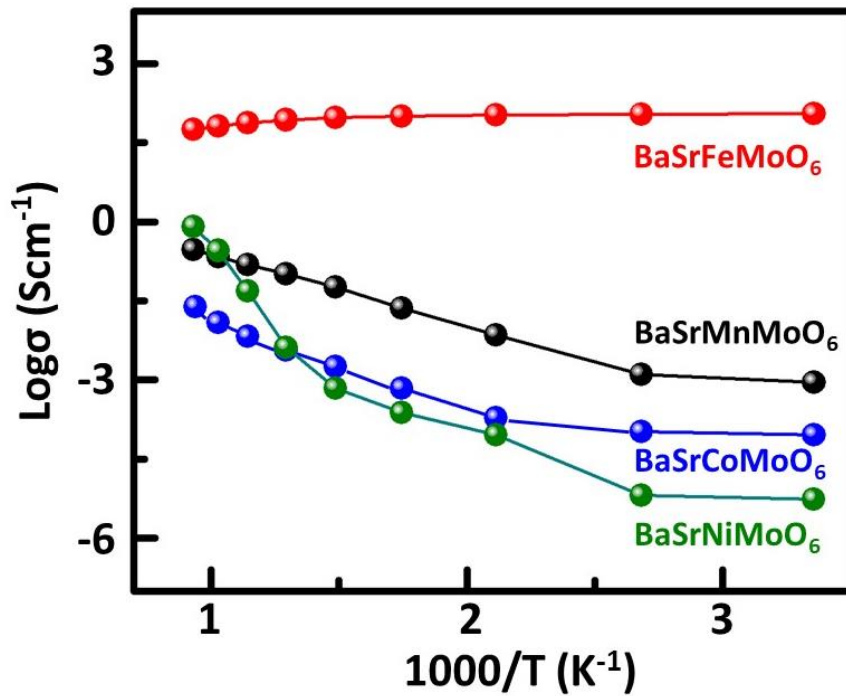
Figure 3.5: Arrhenius plot for the conductivity of all four compounds.

3.3 X-RAY PHOTOELECTRON SPECTROSCOPY

In these materials, the B/B′-site metals Mn, Fe, Co and Mo are capable of adopting different oxidation states. The synthesis conditions and the high temperature required for

the preparation of these compounds can lead to various valence states. Therefore, exploring the oxidation states of B site transition metals is an important part of this work.

In XPS studies, the binding energies associated with 2p states for Mn, Fe and Co, and the 3d states for Mo were examined. The spectra were calibrated based on the carbon 1s line at 284.5 eV. We discuss the XPS analysis of $BaSrFeMoO_6$ first. It should be noted that a previous report on the synthesis of $BaSrFeMoO_6$ uses Fe_2O_3 and MoO_3 as precursors in a mixture of H_2 and Ar.[104] In our experiments, $BaSrFeMoO_6$ could be synthesized using two combinations, Fe_2O_3/MoO_3 or FeO/MoO_3. For iron-containing oxides, the Fe^{3+} $2p_{3/2}$ peak in the XPS spectra consistently appears at 710 – 711 eV with a satellite peak at ~7 – 9 eV higher than the $2P_{3/2}$ peak.[113-117] Whereas, Fe^{2+} $2p_{3/2}$ peak usually appears below 710 eV with a satellite peak at ~4 – 6 eV higher than the $2P_{3/2}$ peak.[113, 116] The XPS spectra of $BaSrFeMoO_6$ show the Fe $2P_{3/2}$ peak at 710.3 eV and a satellite peak at 717.4 eV (Figure 3.6). Therefore, the XPS data indicate the presence of Fe in trivalent state. Regarding molybdenum, the XPS data in Figure 3.7 show that Mo in this compound is in pentavalent state, which was expected given the lack of oxygen non-stoichiometry. As observed in several double perovskites before, the Mo $3d_{5/2}$ peak for hexavalent state usually appears at 232.3 – 232.5 eV.[118-120] The $3d_{5/2}$ peaks for pentavalent molybdenum should appear at ~232 eV or lower. For $BaSrFeMoO_6$, the molybdenum $3d_{5/2}$ peak appears at ~232.1 eV, indicative of Mo^{5+}, as expected (Figure 3.7).

We next discuss the XPS data for $BaSrMnMoO_6$. The analysis of the Mn spectra is not trivial, given the proximity of 2p binding energies for Mn in different oxidation states.[121] The Mn $2p_{3/2}$ peak for divalent manganese in MnO is expected to appear at 640.6 – 641.3 eV.[118, 121] Also, a satellite peak at ~5 – 6 eV higher than the $2p_{3/2}$ peak is sometimes

observed for divalent manganese.[122] $2p_{3/2}$ peak for trivalent manganese in Mn_2O_3 appears at higher binding energies, usually 641.1 – 641.6 eV.[118, 121] For $BaSrMnMoO_6$, the Mn $2p_{3/2}$ peak appears at 641.8 eV (Figure 6), indicating the presence of Mn^{3+}. Regarding molybdenum, given the lack of oxygen non-stoichiometry, the pentavalent sate of Mo, determined from the XPS data in Figure 7, is not surprising. The Mo $3d_{5/2}$ peak for $BaSrMnMoO_6$ appears at ~232.1 eV, indicative of Mo^{5+}.
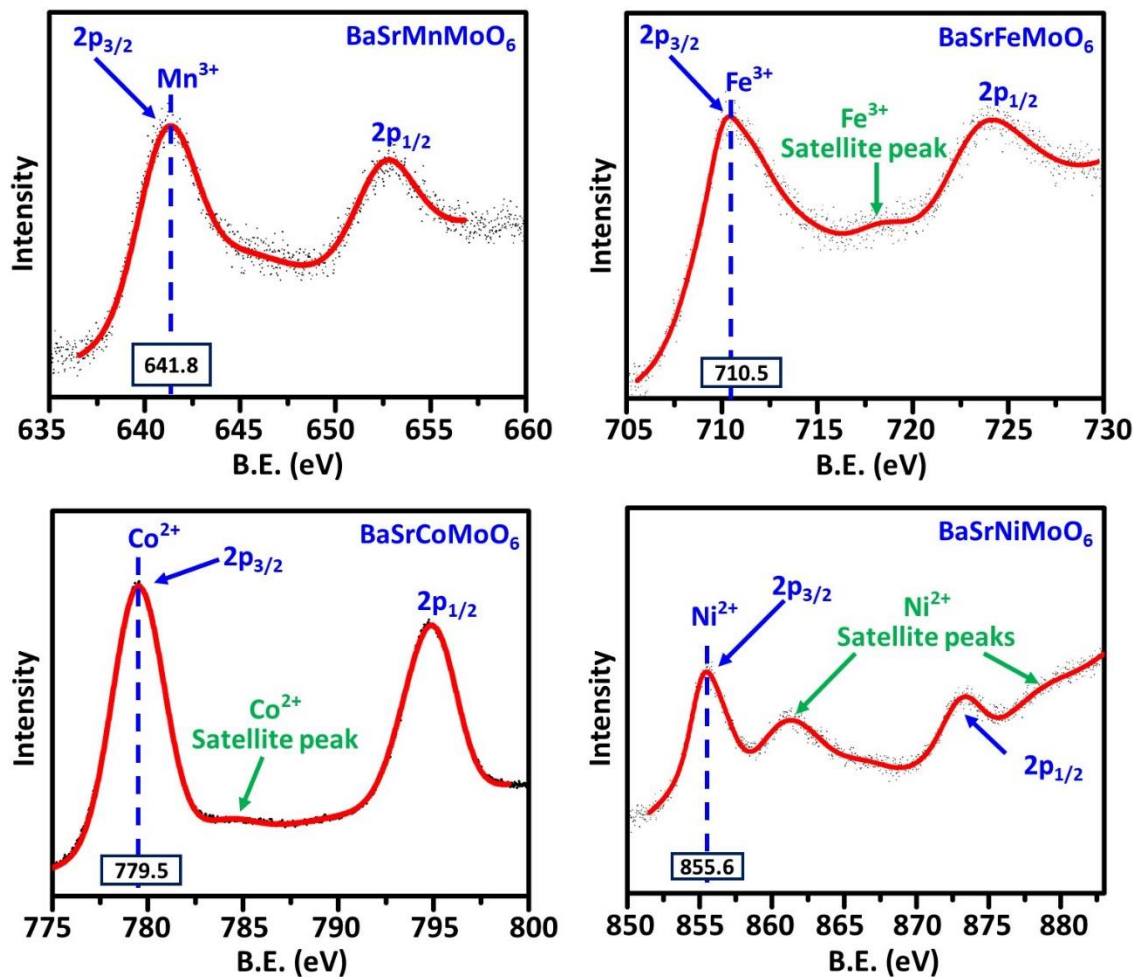
Figure 3.6: XPS spectra of Mn, Fe, Co and Ni in the four compounds.

The situation is different for $BaSrCoMoO_6$. The XPS spectra for this compound show the presence of divalent cobalt. The Co $2P_{3/2}$ peak appears at 779.5 eV (Figure 6)

consistent with Co^{2+}, as observed for other cobalt-containing oxides.[115, 120] More importantly, there is a satellite peak at 784.5 eV. The satellite peak at 5 eV higher than the $2P_{3/2}$ peak is a signature of Co^{2+}.[123] The satellite peak for trivalent cobalt usually appears at much higher binding energy, ~9 eV higher than the $2P_{3/2}$ peak.[124] The XPS data for Mo (Figure 3.7), shows hexavalent state, which is expected considering that this compound does not have any oxygen non-stoichiometry. The XPS spectrum for molybdenum in $BaSrCoMoO_6$ shows the Mo $3d_{5/2}$ peak at 232.3 eV, consistent with Mo^{6+} (Figure 3.7).[118]
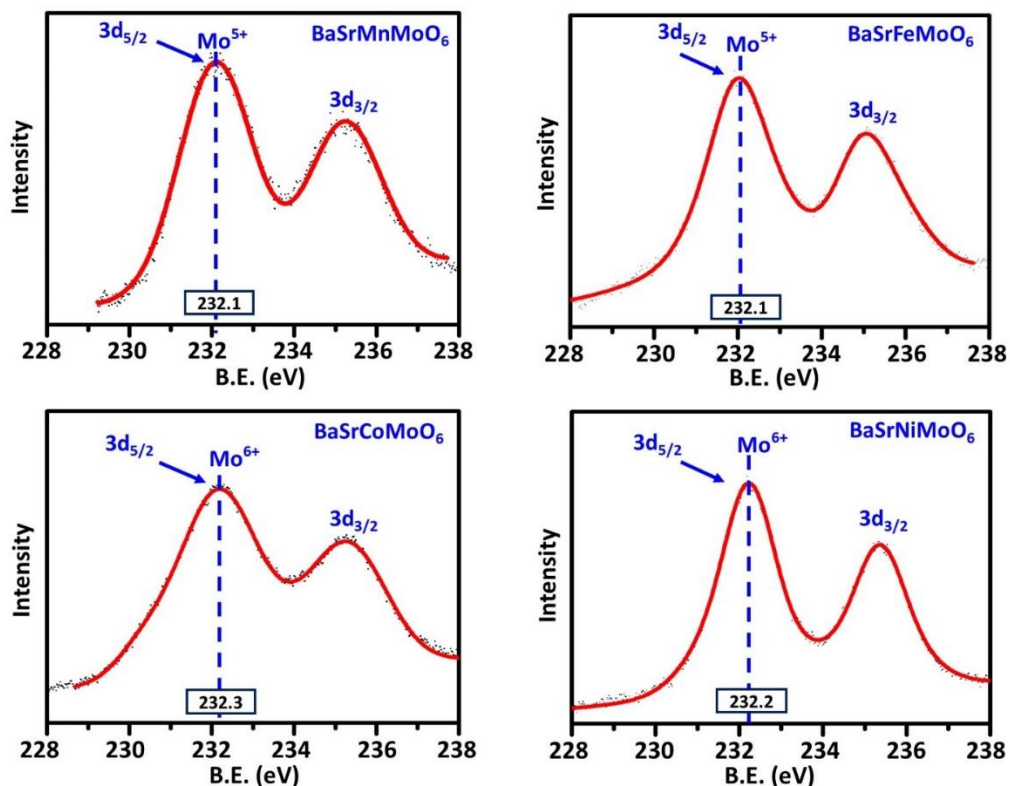
Figure 3 7: XPS spectra of Mo in the four compounds.

The XPS data for $BaSrNiMoO_6$ are also shown in Figures 3.6 and 3.7. Given the high stability of divalent nickel, it is expected that $BaSrNiMoO_6$ contains Ni^{2+} and Mo^{6+}. The XPS spectra show the Ni $2p_{3/2}$ peak at ~855.6 eV with a prominent satellite peak at ~861.6 eV (Figure 6). Also, the Ni^{2+} $2p_{1/2}$ peak appears at ~872.9 eV with a satellite peak

at ~6 eV higher. These binding energies are consistent with those usually observed for Ni^{2+}.[125-128] The Mo $3d_{5/2}$ peak appears at 232.3 eV, consistent with the presence of Mo^{6+} (Figure3.7).[118]

3.4 MAGNETIC PROPERTIES

Magnetic susceptibility studies from 2 K – 400 K, and isothermal magnetization measurements through field-sweep in the range of 0 – 9 T indicate an interesting trend with respect to magnetic order in these compounds. There is one report indicating ferrimagnetic order in the Fe-compound. [104] However, there has been no study on the magnetic properties of the Mn, Co and Ni materials. Here, we show that the latter three compounds undergo transitions into antiferromagnetic state, in sharp contrast to the Fe-material.

The magnetic susceptibility data were obtained by initially cooling the samples to 2 K in the absence of a magnetic field (for zero-field-cooled (ZFC) measurements), and in the presence of a field (for the field-cooled (FC) data). The measurements were done by recording the magnetization in the temperature range of 2 K – 400 K, while applying a magnetic field of 0.1 T. The magnetic susceptibility data, shown in Figure 3.8, indicate that $BaSrFeMoO_6$ undergoes a transition to ferrimagnetic state below ~380 K. For this material, there is an increase in the magnetic susceptibility as the temperature decreases below ~380 K. The increase in susceptibility continues as the temperature is lowered, finally reaching a near-plateau region. The isothermal magnetization data at 5 K confirms the ferrimagnetic order, as evident from the sharp rise and saturation of magnetization at higher field and the absence of any hysteresis or remnant magnetization (Figure 3.9). The isothermal data at

400 K does not reach saturation, indicating that the ferrimagnetic transition occurs below 400 K, consistent with the magnetic susceptibility data.
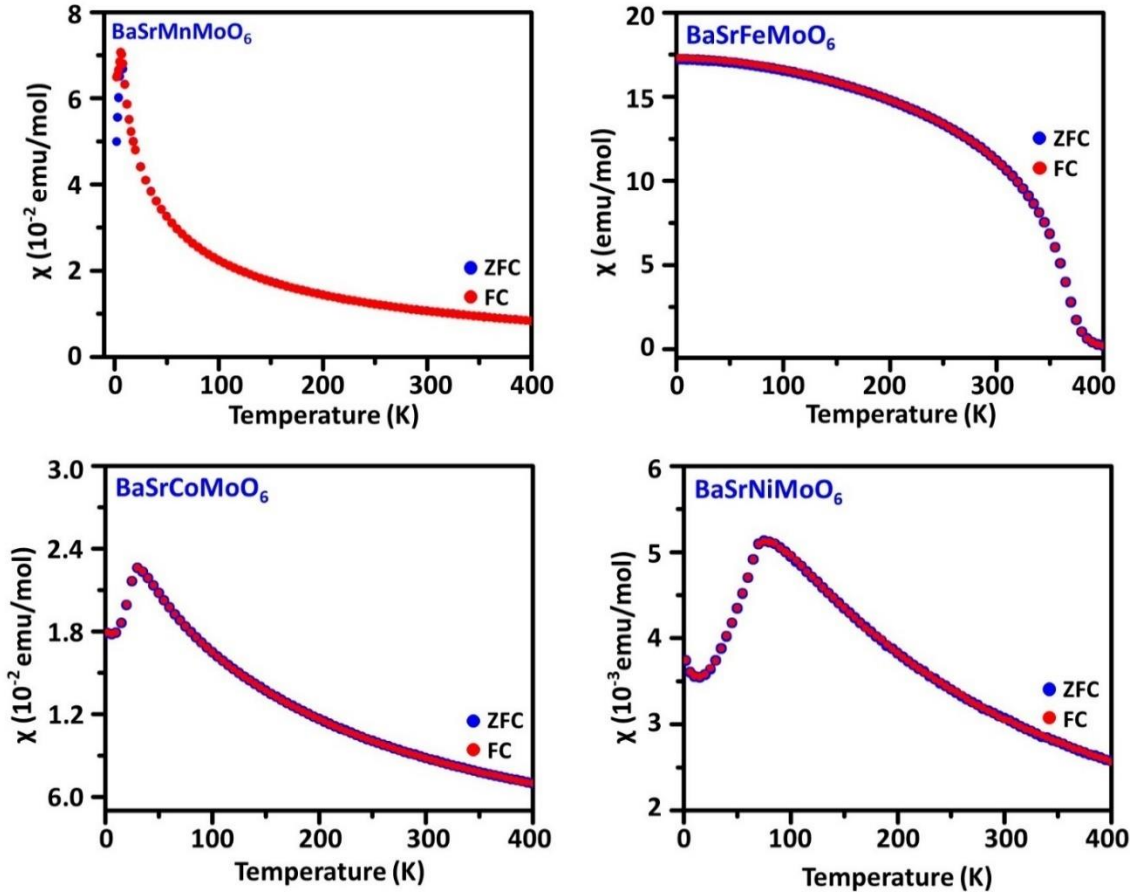
Figure 3.8: Bulk magnetization data for the four compounds.

As noted before, the magnetic properties of the other three compounds are different. As shown in Figure 3.8, the susceptibility data for $BaSrMnMoO_6$ shows a sudden downturn below 6 K, indicating a transition to antiferromagnetic state. $BaSrCoMoO_6$ also shows a similar behavior and an antiferromagnetic transition, but at a higher temperature, 30 K. The transition temperature is even higher for $BaSrNiMoO_6$, which becomes antiferromagnetic below 75 K. The isothermal magnetization data for the Mn, Co and Ni compounds are almost linear, as expected (Figure 3.9).

Table 3.6 lists the experimental Curie constants obtained from fitting with the inverse susceptibility data. These results are compared with theoretical Curie constants, calculated using magnetic moments for Mn^{3+}/Mo^{5+}, Co^{2+}/Mo^{6+}, and Ni^{2+}/Mo^{6+} combinations. The data for $BaSrFeMoO_6$ are not shown in this table, because this material is not paramagnetic in the temperature-range of study, 2-400 K.
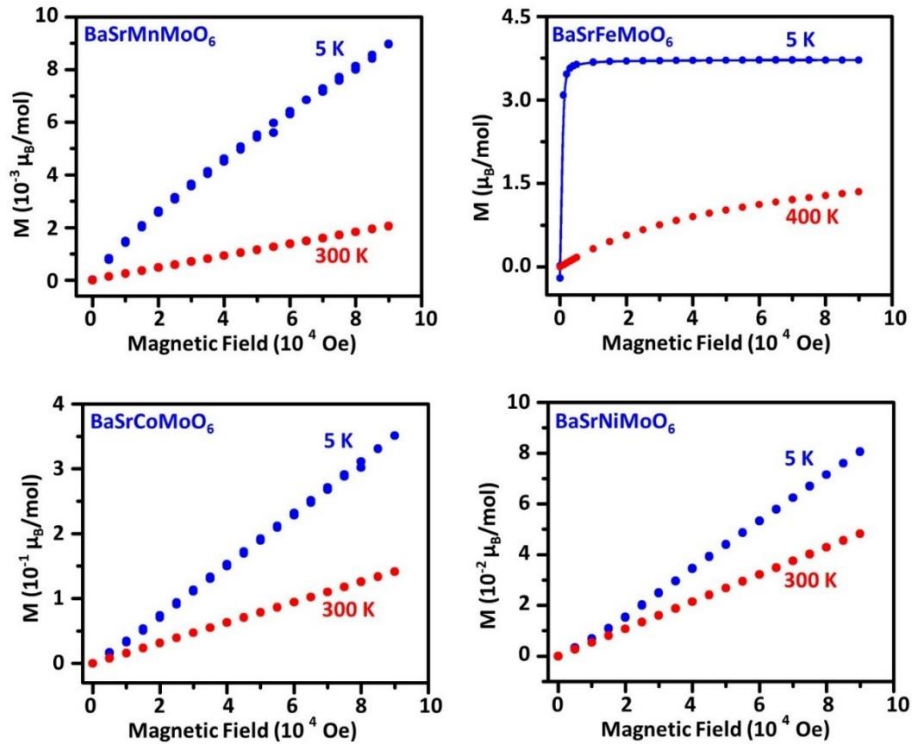
Figure 3.9: Isothermal magnetization versus field at 5 and 300 K for the four compounds.

Table 3.6: Comparison between experimental and theoretical values of Curie constant. $BaSrFeMoO_6$ does not show paramagnetic behavior in the temperature-range of study, 2-400 K.

	C (experimental)	C (theoretical)
$BaSrMnMoO_6$	3.08	3.37 (spin only)
$BaSrNiMoO_6$	1.55	1.0 (spin only)
$BaSrCoMoO_6$	3.44	3.38 (unquenched orbital contribution)*

*For similar cobalt-containing double perovskites, orbital contribution is reported to be unquenched.[129]

Considering that all four compounds have the same type of crystal structure, the above results represent an excellent example of the correlation between magnetic properties and the nature of the B-site cation in isostructural oxide materials. The occurrence of magnetic order in all four compounds, and the strong magnetic coupling in the Fe-compound, which shows a magnetic transition well above room temperature are noteworthy. Furthermore, the systematic change in the Neel temperature among the three antiferromagnetic compounds is interesting.

3.5 CONCLUSIONS

The magnetic and electrical properties of double perovskites, $BaSrMMoO_6$ (M= Mn, Fe, Co, Ni), vary significantly depending on the type of the 3d transition metal. The Fe-containing material is ferrimagnetically ordered, whereas the other three compounds show transitions into antiferromagnetic state. Furthermore, there is a pronounced difference between the electrical properties of these compounds. The Fe-material shows metal-like behavior, while the other three compounds show properties typical of semiconductors, where the electrical conductivity increases as a function of temperature.

CHAPTER 4

EFFECT OF STRUCTURE ON SENSOR PROPERTIES OF OXYGEN-DEFICIENT

PEROVSKITES, $A_2BB'O_5$ (A =Ca, Sr; B=Fe; B'=Fe, Mn) FOR OXYGEN, CARBON

DIOXIDE AND CARBON MONOXIDE SENSING

In this chapter, we have studied the sensor behavior of four different oxygen-deficient perovskites and shown that the formation of brownmillerite structure combined with proper choice of elemental composition can lead to significant improvement in sensing properties. The compounds studied in this work are $Ca_2Fe_2O_5$, $Sr_2Fe_2O_5$, Ca_2FeMnO_5 and Sr_2FeMnO_5, where the A and B-site cations are varied systematically. The systematic change in their structure makes them interesting candidates for investigation of the effect of structure on gas sensing properties. We have shown this correlation and demonstrated the sensor behavior of these materials toward O_2, CO_2 and CO gases.

4.1 SENSOR FABRICATION AND EXPERIMENTAL SETUP

Cylindrical samples with a diameter of 9 – 10 mm and thickness of 2 – 2.5 mm were used for electrochemical sensor fabrication. DC voltage of 0.01 V was applied to record the current response for various amounts of O_2 gas and ppm level concentrations of CO_2 and CO gases. The AC data were obtained in the frequency range of 0.1 Hz to 1 MHz. The pellets were painted with Au-paste on both sides and heated at 700 °C for 2 hours in

argon to remove the organic binder. For each sensor experiment, a fresh pellet was used to ensure the reproducibility of the experiments. A schematic of the experimental setup used for sensor studies is shown in Figure 4.1. The electric circuit for the sensor cell was devised via a spring-loaded contact created by ceramic pellets using Au-leads and Au wire connections. The sensor cells were heated at 700 °C in a tube furnace by supplying the desired concentrations of gases. The gases were mixed precisely using computer-controlled mass flow controllers. A total flow (base gas and sample gas together) of 100 Standard Cubic Centimeters per Minute (sccm) was maintained inside the furnace. Argon was used as base gas to test the O_2 sensing performance. For CO_2 and CO sensor experiments, dry synthetic air was used as base gas. The ppm amounts were controlled by mixing appropriate ratios of the base gas with CO_2 or CO (1% in balance argon).
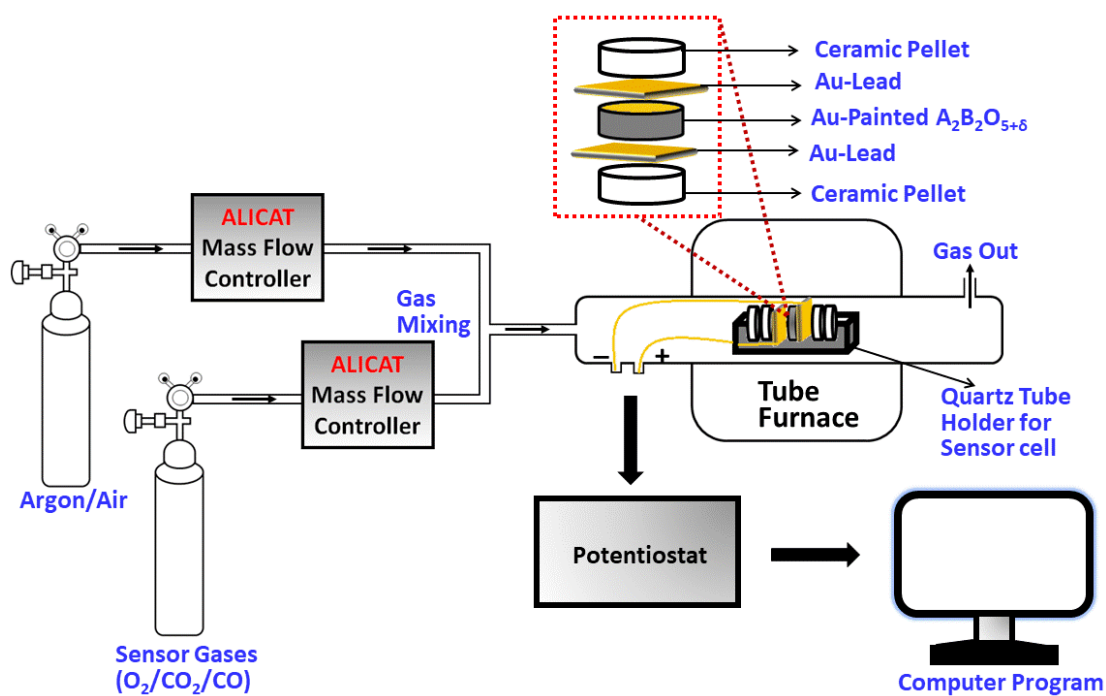
Figure 4.1: A schematic of the experimental setup used for sensor studies.

51

4.2 CRYSTAL STRUCTURE ANALYSIS AND OXYGEN CONTENT

All four compounds are oxygen-deficient perovskites and can be represented by the general formula, $A_2B_2O_5$. The Rietveld refinements with X-ray diffraction data (Figure 4.2) confirm the reported structures of these four compounds.[130-137] It is noted that defects, generated as a result of oxygen-deficiency, can have ordered or disordered distribution in the material structure. One type of ordered arrangement leads to the formation of alternating tetrahedral and octahedral coordination geometry, i.e., brownmillerite-type structure. $Ca_2Fe_2O_5$ has such structure with alternating layers of FeO_6 octahedra and FeO_4 tetrahedra.[137] The tetrahedra form chains that can have either right-handed or left-handed orientation. In this compound, each chain has the same orientation relative to the other chains within the same tetrahedral layer, but opposite to those in neighboring layers, forming an orthorhombic *Pnma* system. On the other hand, $Sr_2Fe_2O_5$ has a similar structure, but the orientation of tetrahedral chains relative to each other is random, leading to an orthorhombic *Imma* system.[136]

The structure of Ca_2FeMnO_5 is similar to that of $Ca_2Fe_2O_5$, with alternating octahedral and tetrahedral geometry and space group *Pnma*. However, there is an additional ordering, where Fe mainly occupies the tetrahedral sites, and Mn the octahedral positions.[134] However, Sr_2FeMnO_5 has a different type of structure. In this material, the defects created due to oxygen deficiency are distributed randomly. Therefore, the average structure retains the perovskite-type framework, but with partial occupancy of oxygen sites. In other words, Sr_2FeMnO_5 has a regular perovskite-type *Pm-3m* structure, but some oxygen positions are vacant.[134]
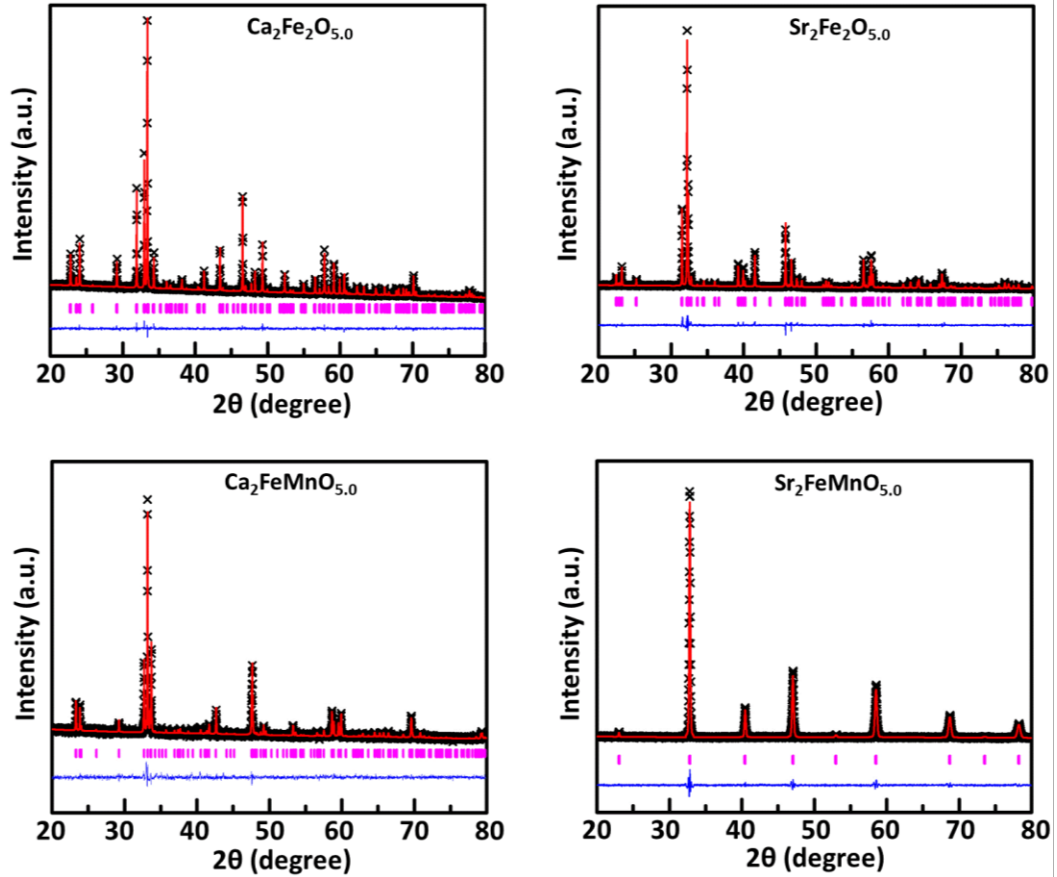
Figure 4.2: Rietveld refinement profiles for $Ca_2Fe_2O_5$, brownmillerite *Pnma*, $Sr_2Fe_2O_5$, brownmillerite *Imma*, Ca_2FeMnO_5, brownmillerite *Pnma*, and Sr_2FeMnO_5, perovskite-type *Pm-3m*.

The oxygen stoichiometry was determined by iodometric titration, indicating 5 oxygen per formula unit for all four materials, which is consistent with the reported oxygen contents of these compounds.[131, 134, 136, 137] Scanning electron microscopy (SEM) images of sintered pellets before and after O_2 sensor studies in Figure 4.3 reveal that $Ca_2Fe_2O_5$ has the largest and most compact crystallites. $Sr_2Fe_2O_5$ has somewhat smaller crystallites and more porosity in its microstructure. The Mn-containing materials have even smaller crystallites, with Ca_2FeMnO_5 showing the smallest crystallite size, and Sr_2FeMnO_5 having the most porosity as observed in Figure 4.3.
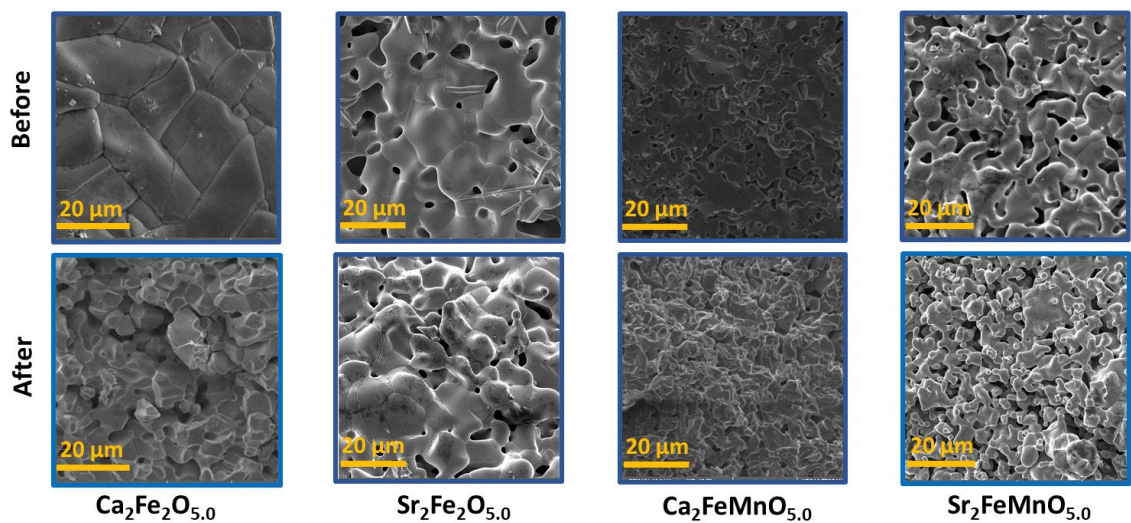
Figure 4.3: Scanning electron microscopy (SEM) images of sintered pellets before and after O_2 sensor studies.

4.3 O_2 SENSOR STUDIES

Oxygen sensors have been predominantly used to monitor air/fuel ratio in combustion engines, petrochemical, steel, oil and gas, power generation, refinery, food and beverage, paper and pulp, and glass industries.[138, 139] These systems operate at high temperatures ranging from 100 to 1000 °C.[138] At such high temperatures, sensing processes in semiconductor-based oxygen sensors occur based on changes in electrical conductivity arising from changes to the defect chemistry by chemisorption of oxygen.[138] For the four compounds studied here, variable temperature electrical conductivity data reveal semiconducting behavior. Furthermore, these materials have oxygen-defects and are synthesized at high temperature, as described in the experimental section. Therefore, these compounds could be ideal for oxygen sensing in systems that operate at high temperature.[135, 140, 141] Sensor output depends logarithmically on the partial pressures of

54

oxygen gas.[138, 142] This allows the investigation of the sensitivity of material toward oxygen gas and calculation of important parameters, such as activation energies, to get insight into the sensing mechanism.[142, 143] Therefore, investigation of sensing behavior in a range of oxygen partial pressure from 1 to 100 % is required.[41, 138, 144, 145] Figure 4.4 shows the response and recovery transients at various concentrations of O_2 (1% - 100%) in argon at 700 °C. The O_2 sensing behavior of each material is described below.
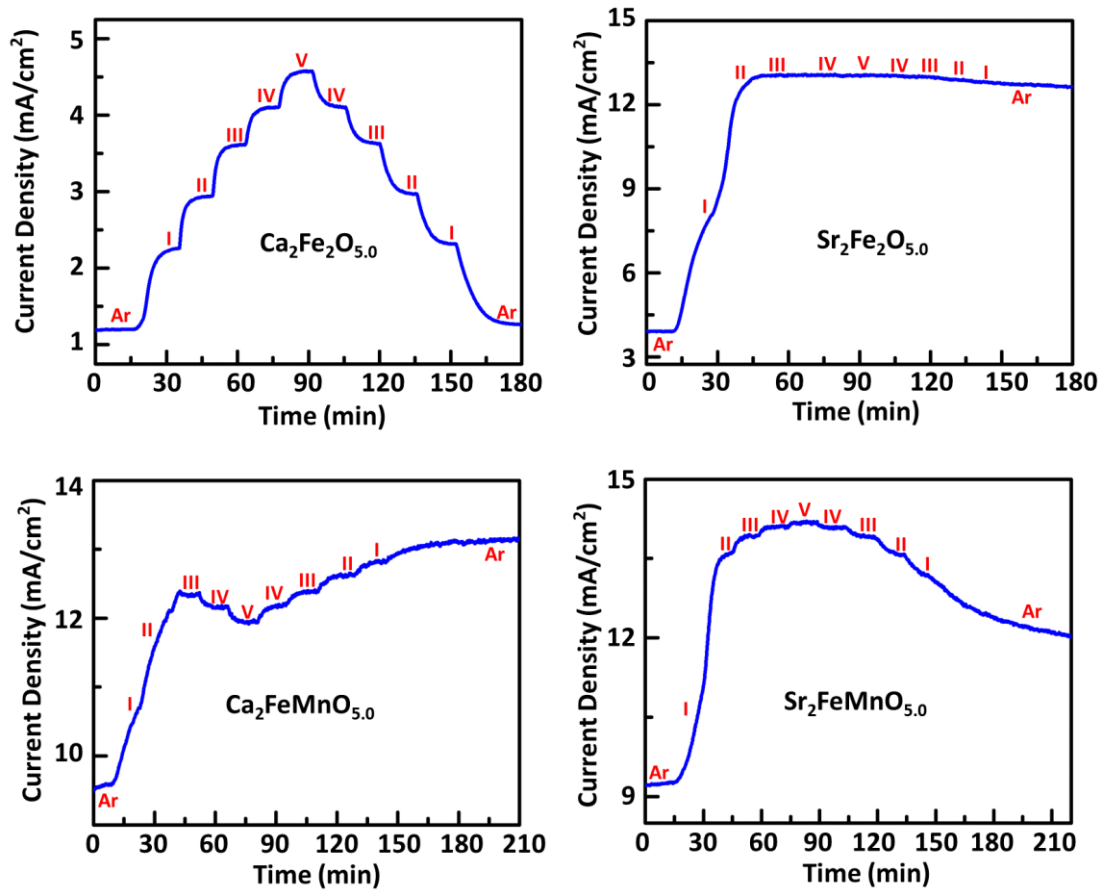
Figure 4.4: The response and recovery transients at various concentrations of O_2 in argon at 700 °C. Steps I, II, III, IV and V indicate 1%, 5%, 21%, 50% and 100% O_2 gas.

$Sr_2Fe_2O_5$: This material does not show a plateau in current density at 1% and 5% oxygen gas but reaches a maximum current at 21% oxygen and does not show a further increase in current. In addition, it does not show recovery upon decreasing the oxygen

concentration. This indicates irreversible oxidation of $Sr_2Fe_2O_5$, as evident from the comparison between powder X-ray diffraction data before and after the sensor experiments in Figure 4.5. The oxidation leads to the formation of an orthorhombic *Cmmm* phase, $Sr_2Fe_2O_{5.5}$, which is one of the known structures for Sr-Fe-O system.[146] This is confirmed by X-ray diffraction data after the sensing experiment (Figure 4.5).
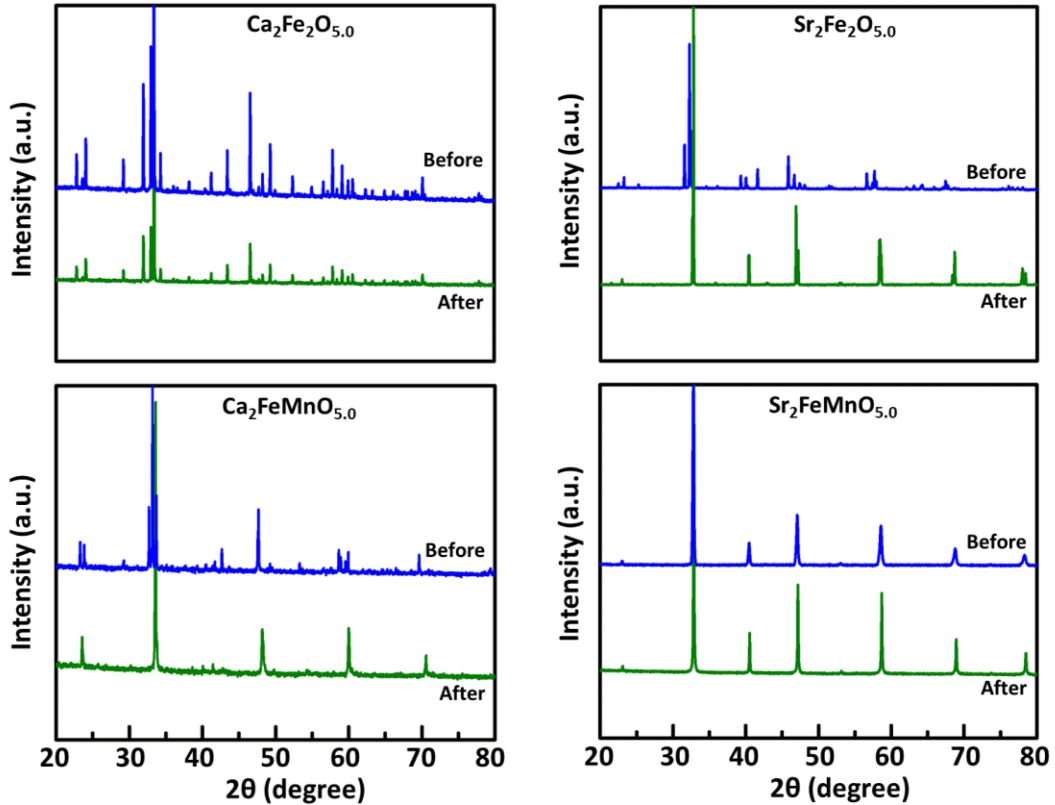
Figure 4.5: Comparison between powder X-ray diffraction data before and after O_2 sensor experiments.

Ca_2FeMnO_5: This material shows a current response that reaches a peak at 21% oxygen, followed by a downturn when the oxygen concentration is raised to 50% and 100%. During recovery, when the oxygen concentration is gradually decreased, the current response shows an upturn. We assign this observation to deterioration of the material structure and formation of a more conducive phase, namely Ca_2FeMnO_6,[147] leading to

higher current response. This interpretation is confirmed by X-ray diffraction data after the sensing experiment (Figure 4.5), which show the conversion of Ca_2FeMnO_5 into Ca_2FeMnO_6.[147]

Sr_2FeMnO_5: This material shows a more reasonable current response and the typical p-type conducting behavior. There is a stepwise increase in current density as the O_2 percentage is increased from 1% to 5%, 21%, 50%, and 100%. Furthermore, a stepwise decrease in current density is observed during recovery, where the O_2 concentration is decreased gradually. However, the recovery for Sr_2FeMnO_5 is not complete, and the current density does not go back to the same level as the start of the experiment. This incomplete recovery is attributed to the formation of the oxidized phase, $Sr_2FeMnO_{5.5}$, [34] demonstrated by X-ray diffraction and iodometric titration after sensor experiment, which confirmed the increase in oxygen content. Nevertheless, X-ray diffraction data (Figure 4.5) before and after the sensor experiment indicate that Sr_2FeMnO_5 retains its crystal structure.

$Ca_2Fe_2O_5$: This material shows the best response and recovery, where a plateau is reached at each O_2 concentration, and there is a stepwise increase in current response as oxygen concentration increases (Figure 4.4). This is followed by a stepwise decrease in current, as the concentration of oxygen decreases. The current response at each O_2 concentration is the same for both sides of the plot. The recovery is nearly perfect, with a current response being the same at the beginning and end of the experiment. The O_2 sensing properties of $Ca_2Fe_2O_5$ are remarkable and comparable to some of the promising sensor materials studied before, such as $Ce_{0.8}Sm_{0.2}O_{1.9}$,[148] $BaFe_{1-x}Ta_xO_{3-\delta}$,[41] and Ni-NiO mixture.[149]

Considering that $Ca_2Fe_2O_5$ shows the best performance, we have also conducted electrochemical impedance spectroscopy studies on this compound, by systematically varying the concentration of oxygen. The Nyquist plot for electrochemical impedance spectroscopy data for $Ca_2Fe_2O_5$ in various O_2 concentrations is shown in Figure 4.6. The impedance data turn from negative to positive at higher frequency region (left inset in Figure 4.6), indicative of inductance effect.[150, 151] The definitive intercept with the real axis at low frequency and the absence of a low-frequency tail indicate the non-blocking nature of the interface between the oxide sample and the electrode, which allows facile flow of electrons. Importantly, the resistance of $Ca_2Fe_2O_5$, estimated from the intercept of data with real axis in Nyquist plot, decreases systematically as the concentration of oxygen gas increases. This trend is the same as that observed in DC data and is the typical p-type semiconductor behavior as a function of oxygen concentration.[150] Additionally, the time-dependent plot of resistivity axis (right inset in Figure 4.6), obtained from the intercept of impedance spectroscopy data with real axis at 100 % O_2, further confirms the consistency of $Ca_2Fe_2O_5$ for O_2 sensor.

By convention, the time required to reach 90% of equilibrium current, denoted t_{90}, is used to evaluate the rate of the sensor response.[144, 150] In particular, the t_{90} value at low O_2 concentration, e.g., 1%, is informative.[144, 152] Among materials studied in this work, the best response time belongs to $Ca_2Fe_2O_5$, ~7 min at 1% O_2, while the other compounds did not reach equilibrium at this oxygen level and response time decreased slightly as the concentration of O_2 gas is increased. The response time of $Ca_2Fe_2O_5$ is better than those reported for some other oxygen-deficient perovskites, including $Ce_{0.8}Sm_{0.2}O_{1.9}$[148] and

BaFe$_{1-x}$Ta$_x$O$_{3-\delta}$.[41] It is also comparable to the response time of TiO$_2$-doped Nb$_2$O$_5$ thin film (~5 min).[153] It is noted that some composites and surface-modified systems (not pure materials) show better response times. Examples are Ga$_2$O$_3$, surface-modified with La$_2$O$_3$ (~2 min),[154] and Pt-incorporated CeO$_2$ (5-11 sec).[155]
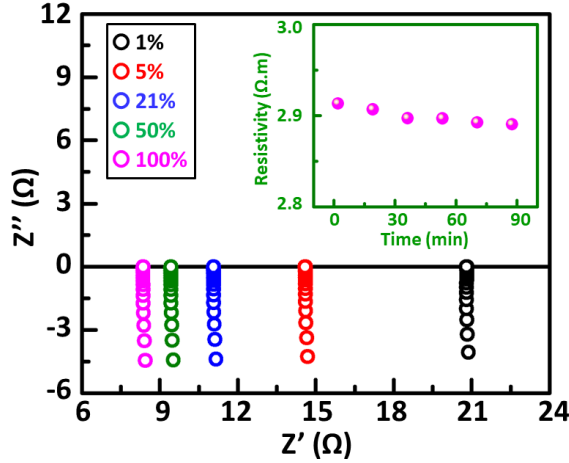
Figure 4.6: Nyquist plot for electrochemical impedance spectroscopy data for Ca$_2$Fe$_2$O$_5$ in various O$_2$ concentrations with inset showing resistance vs time in 100% O$_2$.

4.4 ORIGIN OF DIFFERENCES IN O$_2$ SENSING

Clearly, rapid diffusion of oxygen from the surface into the grains and vice-versa is a basic requirement for sensing oxygen. The role of oxygen-deficiency in this process is therefore significant. The equilibrium reaction between oxygen molecules in a gas phase and the oxygen vacancy ($V_O^{\bullet\bullet}$) in the material can be described as:[156]

$$\frac{1}{2} O_2 + V_O^{\bullet\bullet} + 2e' \leftrightarrow O_O^x \tag{4.1}$$
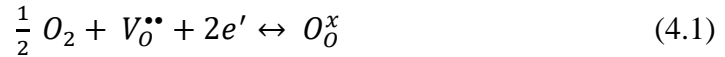
The oxygen vacancies are affected by the partial pressure of oxygen gas. Therefore, the oxygen partial pressure can be related to the electrical conductivity by the following equation:[156]

$$\sigma = A \left(e^{-\frac{E_A}{KT}} \right) P_{O_2}^{1/m} \tag{4.2}$$

where σ is the electrical conductivity, A is the pre-exponential factor, E_A is the activation energy, K is the Boltzmann constant, P_{O_2} is the oxygen partial pressure. The absolute value of *m* is typically between 4 - 6,[152] and depends on the defects involved in the reversible reaction between the oxygen gas and sensor,[156] as well as the range of oxygen partial pressure and temperature.[152] The sign of 1/*m* is determined by the type of conductivity, negative for n-type and positive for p-type semiconducting oxides. The materials studied in this work have p-type properties leading to a positive 1/*m* value. To achieve good sensitivity to variation of oxygen partial pressure, the absolute value of 1/*m* should be large and E_A should be small.[156] The *m* values can be calculated from the slope of *log σ* vs. *logPo2* (Figure 4.7). In this case, σ value was calculated using the equation: σ = L/RA, where, R, L and A are the resistance, thickness, and area of pellet, respectively.[85] Among the materials studied in this work, the *m* value for the best performing materials, $Ca_2Fe_2O_5$ is 6.25. The very large value of *m* for Sr_2FeMnO_5 could be related to the facile oxidation of Mn^{3+} to Mn^{4+}.
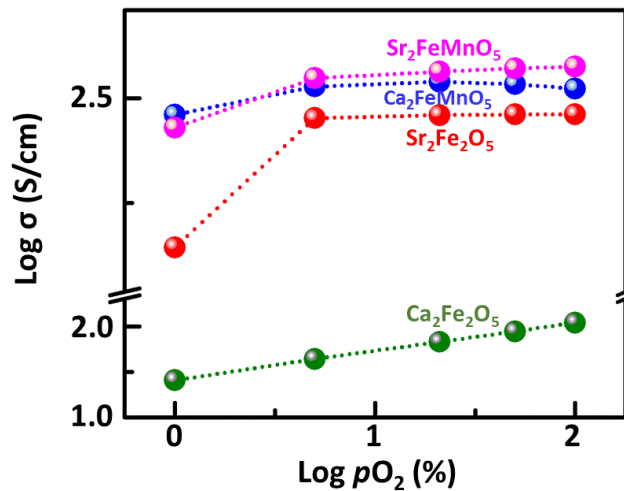
Figure 4.7: Plots of *log σ vs. log pO₂* for different sensors.

There are clearly both compositional and structural factors at play, which affect the sensor response of these materials. For Ca_2FeMnO_5, which has a brownmillerite-type structure, the propensity of Mn to oxidize implies that there will be additional oxygen incorporated into the material lattice as Mn^{3+} ions convert into Mn^{4+}. The brownmillerite structure can accommodate a small amount of interstitial oxygen.[157] However, the tendency of Mn to oxidize will lead to the incorporation of a large amount of excess oxygen into the structure, resulting in irreversible deterioration of the brownmillerite structure and poor sensor properties.

On the other hand, the larger size of Sr^{2+} compared to Ca^{2+} leads to different structure in Sr_2FeMnO_5, where the oxygen sites are only partially occupied. Therefore, the large excess of oxygen that accompanies the $Mn^{3+} \rightarrow Mn^{4+}$ oxidation process can be accommodated, without structural change or decomposition, leading to better sensor response and recovery for Sr_2FeMnO_5 compared to Ca_2FeMnO_5.

The brownmillerite $Ca_2Fe_2O_5$ can accommodate a small amount of excess oxygen in interstitial spaces, as previously observed for some brownmillerite compounds.[157] It is noted that oxidation of iron to tetravalent state is not as facile as that of manganese. Therefore, it is expected that the iron oxidation in $Ca_2Fe_2O_5$ is not as extensive as manganese oxidation in Ca_2FeMnO_5. Thus, $Ca_2Fe_2O_5$ can retain its structure and act as a good sensor.

For $Sr_2Fe_2O_5$, the larger size of Sr leads to more flexibility in the possible structures of Sr-Fe-O system. Indeed, several different structures with various concentrations of oxygen are known for this system. Therefore, $Sr_2Fe_2O_5$ readily accommodates large excess

of oxygen due to the structural transformation into a *Cmmm* structure featuring alternating octahedral and square-pyramidal geometry.[146] However, the oxidized *Cmmm* compound is stable and the excess oxygen incorporated into the material does not leave the structure, leading to poor recovery in sensor experiments for $Sr_2Fe_2O_5$.

Therefore, among these four materials, $Ca_2Fe_2O_5$ shows the best oxygen sensing response due to a combination of structural properties and compositional effects, namely the type of A and B-site cations, and the brownmillerite structure in this material.

4.5 CO_2 AND CO SENSOR STUDIES

Various processes such as enhanced oil recovery[158] and carbon capture and storage, require continuous detection of CO_2 gas.[159] Similarly, pollution control requires monitoring of regulated species such as hydrocarbons, CO and CO_2 at ppm-level.[143] The temperature involved in these processes can be 600 – 1000 °C.[150, 160-162] The development of sensors capable of ppm level detection at such high temperatures is highly desired. Given the high stability of the materials studied in this work, they can be excellent candidates for CO and CO_2 sensing experiments at high temperature. Resistor-type sensors detect analytes based on the adsorption and desorption of gas species on the metal oxide surface in presence of oxygen partial pressure (air).[143] Therefore, experiments with ppm-level concentration of CO or CO_2, and air as base gas were performed.[163] Among the four materials studied in this work, three compounds, $Sr_2Fe_2O_5$, Ca_2FeMnO_5, and Sr_2FeMnO_5, do not show the desired stepwise response and recovery as a function of analyte concentration.

Only one compound, $Ca_2Fe_2O_5$, shows sensing properties toward these gases. Figure 4.8 shows the response and recovery transients of $Ca_2Fe_2O_5$ as a function of

different ppm levels of CO_2 and CO gases at $700\,^\circ$C. As demonstrated in Figure 4.8a, there is a stepwise decrease in current response as the concentration of CO_2 increases. The current recovers nearly perfectly, as the CO_2 concentration is decreased. A similar situation applies to the CO sensing response of $Ca_2Fe_2O_5$ (Figure 4.8b). The graph of saturation-current-density vs. log *ppm* for both CO_2 and CO (Figure 4.9) shows almost the exact same trend. One possible adsorption mechanism for semiconducting metal-oxide sensors in response to oxidizing gases such as CO_2 has been described as having multiple steps that involve the oxygen absorption from air:[162, 164, 165]

$$O_2(gas) \leftrightarrow O_2(absorbed) \tag{4.3}$$

$$O_2(absorbed) + e^- \leftrightarrow O_2^- \tag{4.4}$$

$$O_2^- + e^- \leftrightarrow 2O^- \tag{4.5}$$

$$O^- + e^- \leftrightarrow O^{2-} \tag{4.6}$$
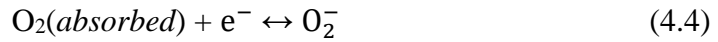
The adsorption of CO_2 has been described based on interactions with electrons on the surface of the material, as well as the oxygen ions: [162]

$$CO_2 + e^- \rightarrow CO_2^-(adsorbed) \tag{4.7}$$

$$CO_2^-(adsorbed) + O^-(adsorbed) + 2e^- \rightarrow CO(g) + 2O^{2-}(adsorbed) \tag{4.8}$$
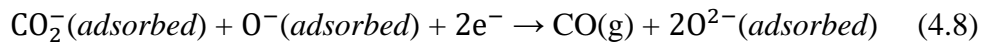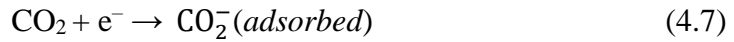
While this mechanism can explain the increase in conductivity of some p-type oxides in response to CO_2,[162] there are some p-type semiconductors that show a different behavior, namely decrease in conductivity upon exposure to CO_2.[166, 167]

The material described in this work, $Ca_2Fe_2O_5$, shows decrease in conductivity as a function of CO_2 concentration. The mechanism of this type of CO_2 adsorption is not clear at this point.[166]
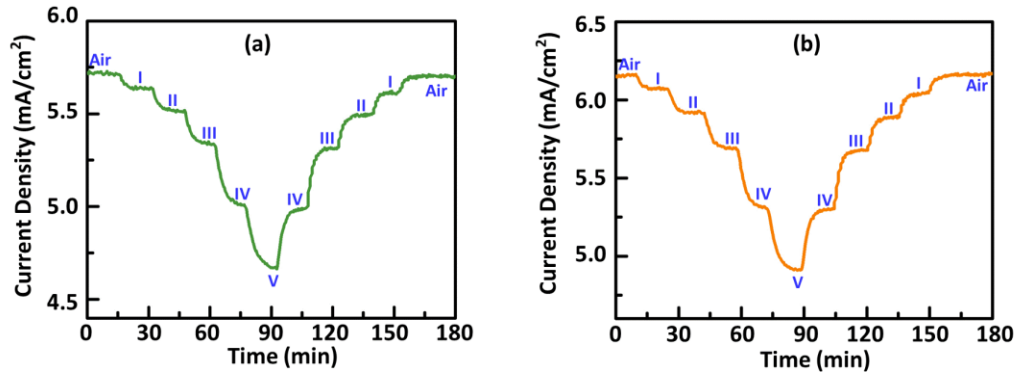
Figure 4.8: The response and recovery transients for $Ca_2Fe_2O_5$ at 700 °C, in various concentrations of (a) CO_2 and (b) CO. Steps I, II, III, IV and V indicate 2000, 4000, 6000, 8000 and 9000 ppm.

Regarding CO adsorption, the generally accepted mechanism for oxide sensors, particularly perovskite oxides, involves the participation of oxygen ions,[168-170] similar to the process described for CO_2. Different processes, involving oxygen species formed in reactions (4) and (5), are shown below. [15],[171]

$$O_{adsorbed}^- + CO \rightarrow CO_2 + e^- \tag{4.9}$$

$$CO_{adsorbed} + O_2^- \rightarrow CO_2 + e^- \tag{4.10}$$
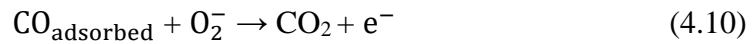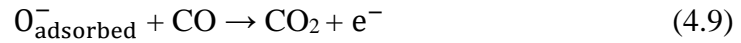
CO also participates in the creation (equation 11) and filling (equation 12) of oxygen vacancies, where O_O^x and $V_O^{\bullet\bullet}$ are the lattice oxygen and vacancy, respectively.

$$CO_{gas} + O_O^x \rightarrow CO_2 + 2e^- + V_O^{\bullet\bullet} \tag{4.11}$$

$$CO + \frac{1}{2}O_2 + V_O^{\bullet\bullet} + 2e^- \rightarrow CO_2 + O_O^x \tag{4.12}$$
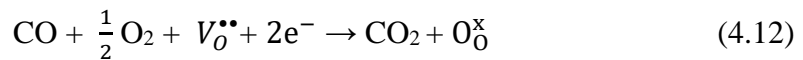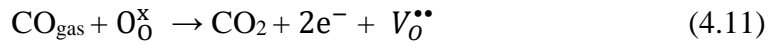
Among four types of interactions between the sensor surface and CO (equations 9-12), only one (equation 12) consumes electrons. Therefore, the change in conductivity is dominated by the generation of electrons, as expected from a reducing gas. As shown in

equation 9 and 10, the reducing gas, CO should be dominating to desorb or remove the chemisorbed oxygen ions and hence change in conductivity.
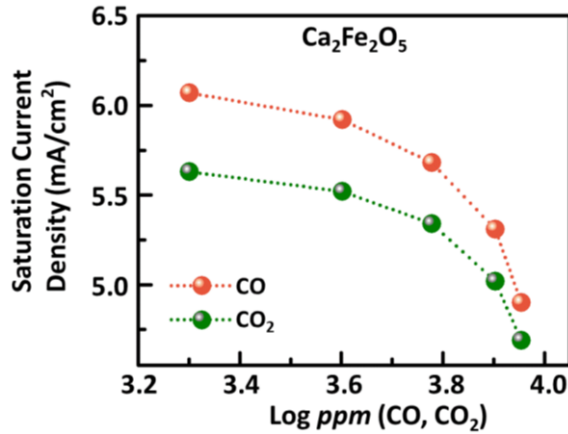
Figure 4.9: Saturation current density vs. log *ppm* for CO_2 (lower spheres) and CO (upper spheres).

The time scale of CO_2 sensing for $Ca_2Fe_2O_5$, $t_{90} \approx 6$ min, is similar to other CO_2 sensing oxides such as $BaCa_{0.33}Nb_{0.34}Fe_{0.33}O_{3-\delta}$ (5 min)[150] and $Ba_2Ca_{0.66}Nb_{0.68}Fe_{0.66}O_{3-\delta}$ (7 min).[172] For CO sensing, $Ca_2Fe_2O_5$ shows $t_{90} \approx 5$ min, which increases as the partial pressure of CO is increased. This time-scale is in the same range as other CO sensing oxides such as $ZnCo_2O_4$ (3 min)[173] and Nb_2O_5 film (2 – 6 min).[174] The observation that $Ca_2Fe_2O_5$ can act as a sensor for either CO_2 or CO is remarkable. Its response and recovery are reminiscent of some of the successful sensors previously reported for CO_2 and CO, such as $BaCa_{0.33}Nb_{0.34}Fe_{0.33}O_{3-\delta}$[150] and $ZnCo_2O_4$.[173]

4.6 CONCLUSIONS

Oxygen-deficient perovskites can act as high-temperature sensors for O_2, CO_2, and CO. The structure and composition of materials play an important role in their sensing properties. Among the four compounds studied in this work, $Ca_2Fe_2O_5$ shows outstanding

sensor activity, with good response and recovery for different percentages of oxygen gas. Furthermore, this material is sensitive to ppm amounts of CO_2 and CO and shows excellent sensing response to these gases. The structural stability, which is a consequence of the specific composition of this material, is an important factor in sensor response and recovery of this compound. The ability of $Ca_2Fe_2O_5$ to demonstrate sensing activity toward all three gases, O_2, CO_2, and CO, is remarkable.

CHAPTER 5

PSEUDOCAPACITIVE ENERGY STORAGE AND ELECTROCATALYTIC

HYDROGEN-EVOLUTION ACTIVITY OF DEFECT-ORDERED PEROVSKITES

$Sr_xCa_{3-x}GaMn_2O_8$ (x = 0 AND 1)

In this chapter, we study the synthesis, crystal structure, electrical conductivity, magnetic properties, electrocatalytic activity, and pseudocapacitive performance of two bilayer brownmillerite compounds, $Ca_3GaMn_2O_8$ and $SrCa_2GaMn_2O_8$, with tetrahedral and octahedral arrangement pattern of TOOTOOT…, and show that these two materials demonstrate a remarkable combination of electrochemical properties that coexist in the same compound.

5.1 CRYSTAL STRUCTURE

The two compounds, $Ca_3GaMn_2O_8$ and $SrCa_2GaMn_2O_8$, belong to a defect-ordered family of oxides. Their crystal structures were determined by Rietveld refinements using powder X-ray diffraction. Figure 5.1 shows the refinement profiles of the two compounds and Tables 5.1 and 5.2 lists the refined structural parameters. These compounds crystallize in the *Pcm2$_1$* space group, consistent with the structure of a similar compound, $Ca_{2.5}Sr_{0.5}GaMn_2O_8$, reported before.[175] Figure 5.2 shows the crystal structure and the distribution of cations, as well as the tetrahedral chain orientation for $Ca_3GaMn_2O_8$ and $SrCa_2GaMn_2O_8$. The structure of these materials is derived from the perovskite structure,

as described in the introduction section. It is noted that regular perovskites (ABO_3) only contain AO_{12} and BO_6 polyhedra. However, the general formula for our compounds is $AA'_2B'B_2O_8$ (or $A_{1/3}A'_{2/3}B'_{1/3}B_{2/3}O_{3-1/3}$), indicating four distinct metal sites with different coordination geometries, namely AO_{12}, $A'O_8$, $B'O_4$, and BO_6 polyhedral units. This is a result of an ordering scheme (Figure 5.2), where oxygen-vacancies only appear in every third layer of a perovskite system, creating tetrahedral $B'O_4$ units that do not exist in a regular perovskite. This also results in the formation of 8-coordinated $A'O_8$ units. There are, therefore, two types of B-sites (Figure 5.2), namely octahedral (B=Mn) and tetrahedral (B'=Ga). There are also two types of A-sites: (a) 12-coordinated A=Ca sites located within bilayer MnO_6 stacks, and (b) 8-coordinated A'= Sr (or Ca for the Ca_3 phase) residing between MnO_6 octahedra and GaO_4 tetrahedra. As observed in Figure 2, the number of A' sites is twice the number of A positions. In $Ca_3GaMn_2O_8$, both A and A' sites are occupied by Ca. However, in $SrCa_2GaMn_2O_8$, the Sr atoms mostly reside in the A-site between neighboring MnO_6 layers, and most of the Ca atoms occupy the A' sites between GaO_4 and MnO_6 layers. The structure of $Ca_3GaMn_2O_8$ was also confirmed by neutron scattering, which showed magnetic peaks as well, and will be discussed further in the magnetic property section. All GaO_4 tetrahedra in these materials have the same orientation, arbitrarily assigned either right-handed or left-handed, throughout the structure, as shown in Figure 5.2c. There is an increase in the unit cell parameters of $SrCa_2GaMn_2O_8$ compared with $Ca_3GaMn_2O_8$ (Tables 5.1 and 5.2), which is expected given the larger ionic radius of Sr^{2+}.

.
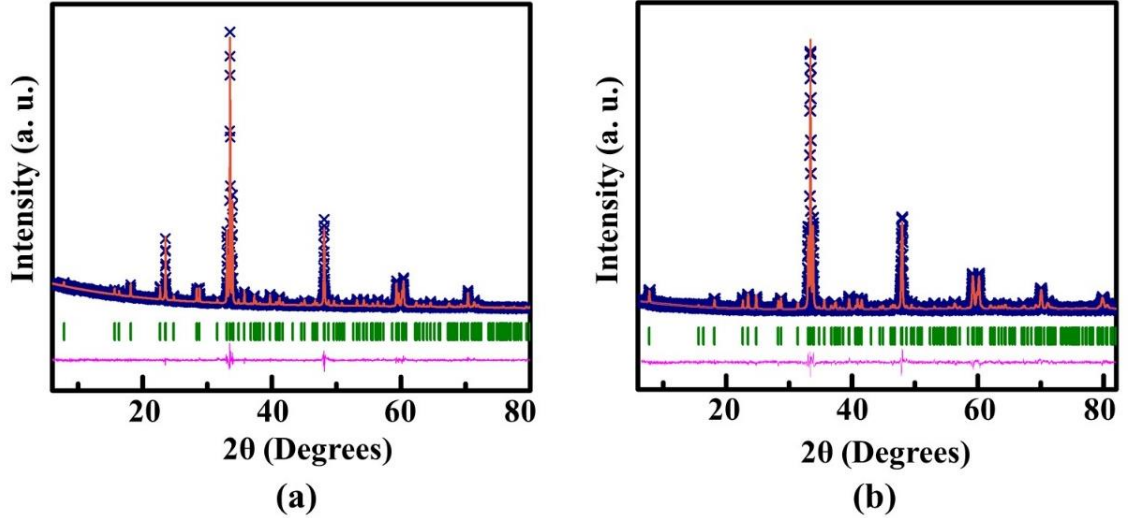
Figure 5.1: Rietveld refinement profiles of (a) $Ca_3GaMn_2O_8$ and (b) $SrCa_2GaMn_2O_8$ for powder X-ray diffraction data with space group *Pcm2₁* (#26). The cross symbols, solid orange line, olive vertical tick marks, and lower magenta line correspond to experimental data, the calculated pattern for the *Pcm2₁* model, Bragg peak positions, and difference plot, respectively.

Table 5.1: Refined structural parameters for $Ca_3GaMn_2O_8$ at room temperature using powder X-ray diffraction data. Space group: *Pcm2₁*, $a = 5.4032(5)$ Å, $b = 11.3013(4)$ Å, $c = 5.2703(5)$ Å, $R_p = 0.03459$, $wR_p = 0.04797$.

Element	x	y	z	Multiplicity	Occupancy	Uiso
Ca1	0.224(1)	0.1881(5)	0.512(3)	4	1.0	0.021(3)
Ca2	0.245(1)	0.5	0.482(3)	2	1.0	0.014(3)
Ga1	0.316(1)	0.0	0.048(2)	2	1.0	0.029(3)
Mn1	0.2576(8)	0.3321(5)	0.0	4	1.0	0.021(2)
O1	0.393(7)	0.0	0.398(6)	2	1.0	0.10(2)
O2	0.298(3)	0.5	-0.013(7)	2	1.0	0.040(9)
O3	0.179(2)	0.139(1)	-0.025(5)	4	1.0	0.053(8)
O4	-0.008(5)	0.344(1)	0.245(8)	4	1.0	0.067(5)
O5	0.464(6)	0.299(1)	0.274(10)	4	1.0	0.047(8)

.

Table 5.2: Refined structural parameters for $SrCa_2GaMn_2O_8$ at room temperature using powder X-ray diffraction data. Space group: $Pcm2_1$, $a = 5.4443(1)$ Å, $b = 11.4387(2)$ Å, $c = 5.31853(9)$ Å, $R_p = 0.0212$, $wR_p = 0.0294$.

Element	x	y	z	Multiplicity	Occupancy	Uiso
Ca1/Sr1	0.2273(7)	0.1858(3)	0.509 (2)	4	0.85(1)/0.15(1)	0.047(2)
Ca2/Sr2	0.2429(6)	0.5	0.499(2)	2	0.40(2)/0.60(2)	0.031(2)
Ga1	0.317(1)	0.0	0.045(2)	2	1.0	0.054(3)
Mn1	0.2549(6)	0.3315(4)	0.0	4	1.0	0.043(2)
O1	0.387(6)	0.0	0.381(6)	2	1.0	0.13(2)
O2	0.294(3)	0.5	0.010(9)	2	1.0	0.068(8)
O3	0.175(2)	0.142(1)	-0.043(4)	4	1.0	0.048(6)
O4	0.004(5)	0.339(1)	0.257(8)	4	1.0	0.034(3)
O5	0.491(4)	0.3058(8)	0.256(8)	4	1.0	0.055(4)

Table 5.3: Selected bond distances and angles for $Ca_3GaMn_2O_8$ and $SrCa_2GaMn_2O_8$.

$Ca_3GaMn_2O_8$					
Mn–O (Å)		Ga–O (Å)		Mn–O–Mn (degrees)	
Mn–O2	1.910(6)	Ga–O1	1.86(4)	Mn1–O2–Mn1	166.84(2)
Mn–O3	2.23(2)	Ga–O1	1.77(5)	Mn1–O4–Mn1	171.40(2)
Mn–O4	1.93(4)	Ga–O3	1.78(2)	Mn1–O5–Mn1	153.53(2)
Mn–O4	1.91(4)	Ga–O3	1.78(2)	Ga1–O1–Ga1	130.70(2)
Mn–O5	1.86(3)				
Mn–O5	1.95(3)				

$SrCa_2GaMn_2O_8$					
Mn–O (Å)		Ga–O (Å)		Mn–O–Mn (degrees)	
Mn–O2	1.940(5)	Ga-O1	1.83(3)	Mn1–O2–Mn1	167.2(11)
Mn–O3	2.22(7)	Ga-O1	1.83(3)	Mn1–O4–Mn1	174.1(12)
Mn–O4	1.93(3)	Ga-O3	1.86(2)	Mn1–O5–Mn1	161.9(7)
Mn–O4	1.92(3)	Ga-O3	1.86(2)	Ga1–O1–Ga1	131.0(2)
Mn–O5	1.90(3)				
Mn–O5	1.92(3)				

.

The microstructure is also affected by the type of A-site cations. As shown in scanning electron microscopy (SEM) images in Figure 5.3, there is an increase in the size of crystallites for $SrCa_2GaMn_2O_8$ as compared with $Ca_3GaMn_2O_8$. The oxygen stoichiometry in these materials was also determined using iodometric titration, giving 8 oxygens per formula unit for both compounds, which matches the formulas of $Ca_3GaMn_2O_8$ and $SrCa_2GaMn_2O_8$.

(a)   (b)   (c)
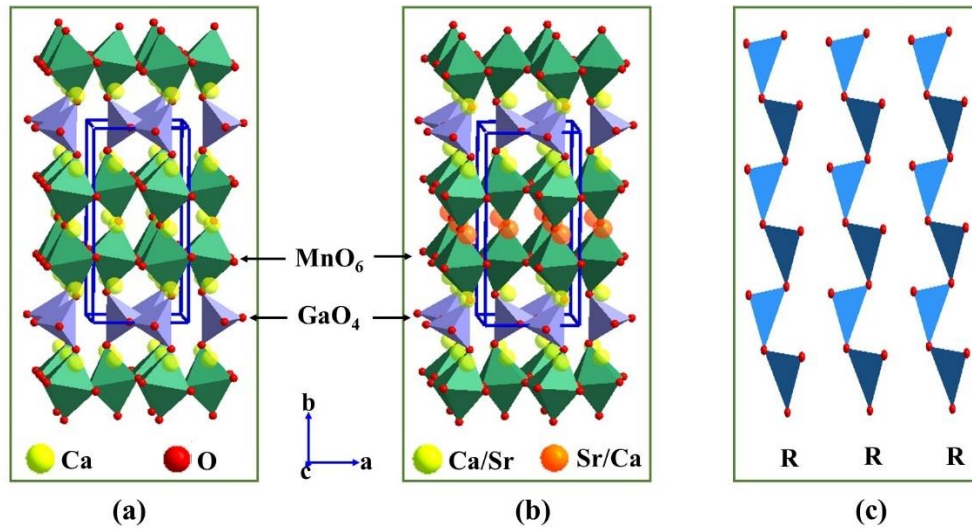
Figure 5 2: Crystal structures of (a) $Ca_3GaMn_2O_8$ and (b) $SrCa_2GaMn_2O_8$. Image (c) shows the relative orientation of tetrahedral chains in these compounds, viewed through the *b* axis.

(a)   **(b)**
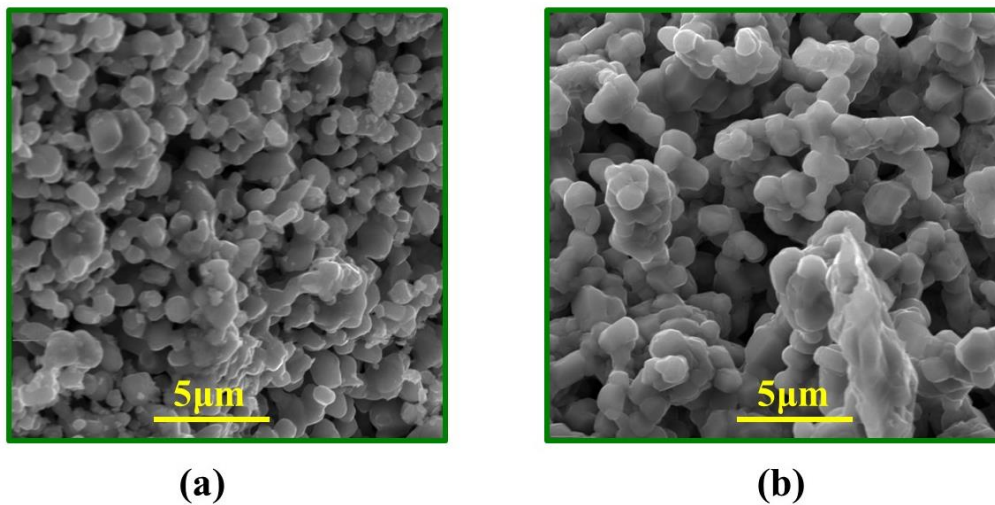
Figure 5.3: Scanning electron microscopy (SEM) images for sintered pellets of (a) $Ca_3GaMn_2O_8$ and (b) $SrCa_2GaMn_2O_8$.

.

5.2 ELECTRICAL CHARGE TRANSPORT

Variable temperature electrical conductivity was studied for both $Ca_3GaMn_2O_8$ and $SrCa_2GaMn_2O_8$ from 25 °C to 800 °C (298 K -1073 K). The current response from DC measurement is used to obtain the resistance using Ohm's law, which is then converted into conductivity (σ) using equation 1.[85]

$$\sigma = \left(\frac{I}{V}\right) \cdot \left(\frac{L}{wh}\right)$$ (5.1)

where, I, V, L, w, and h are the current, applied potential, the distance between the voltage contacts in four-probe setup, width, and thickness of the rectangularly shaped sample, respectively. Figure 5.4a shows the variable-temperature conductivity data. $Ca_3GaMn_2O_8$ shows higher conductivity than $SrCa_2GaMn_2O_8$ in the whole temperature range. The electrical conductivity of both materials increases as a function of temperature, a behavior typical of semiconducting materials. The temperature-dependent increase in conductivity can be due to the increase in mobility of charge carriers as a function of temperature, described by equation 2.[176]

$$\sigma = n\,e\,\mu$$ (5.2)

where σ is conductivity, n is the concentration of electrons/holes, e is the charge of the electron, and μ is the mobility of charge carriers. The activation energy (E_a) for the temperature-dependent increase in the conductivity of these materials can be calculated using the Arrhenius equation:[85]

$$\log \sigma T = \log A - \left(\frac{E_a}{2.303k T}\right)$$ (5.3)

where A, k, and T represent the pre-exponential factor, Boltzmann constant, and temperature, respectively. Figure 5.4b shows the plot of log (σT) versus 1000/T. The
.

activation energy is obtained using the slope from the linear fit to the data above 200 °C

(473 K). The E_a values are equivalent to the slope multiplied by k value (8.62×10^{-5} eV.

K^{-1}), 2.303, and 1000. The observed linear fit suggests that the conduction process obeys

the Arrhenius law given by equation 3. The E_a values are consistent with the conductivity

trend. $Ca_3GaMn_2O_8$, which shows higher conductivity, has lower activation energy.

Whereas $SrCa_2GaMn_2O_8$ with lower conductivity shows higher activation energy.
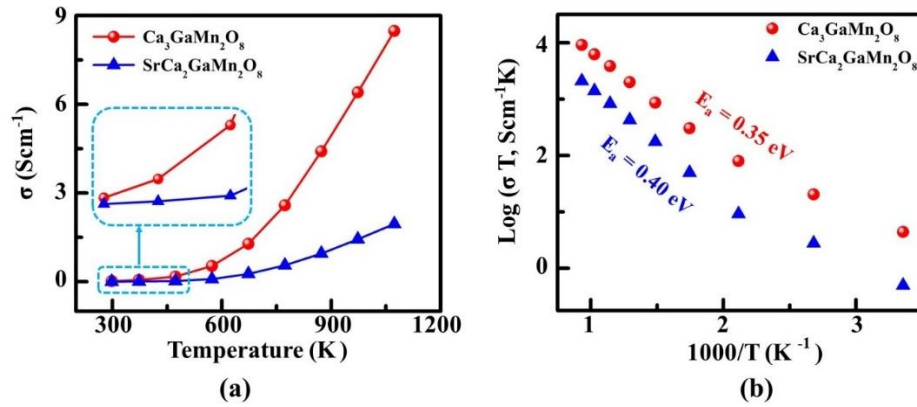
Figure 5.4: (a) Variable-temperature electrical conductivity, and (b) Arrhenius plots for the conductivity data of $Ca_3GaMn_2O_8$ and $SrCa_2GaMn_2O_8$.

The difference between the electrical charge transport of the two materials is due

to the structural differences. In oxides, electronic conduction takes place through M^{m+}–O–

M^{n+} pathway,[177] where M represents a transition metal with variable oxidation states.[176] In

the two materials studied in this work, the presence of manganese atoms is repsosible for

the conduction. It has been shown that the bond lengths and angles play an important role

in conductivity. Shorter M–O bonds and more linear M–O–M angles lead to enhanced

conductivity.[26] It appears that in this case, the effect of shorter bond length is dominant.

While the bond angles in $SrCa_2GaMn_2O_8$ are closer to linear (Table 5.3), the Mn–O bond

distances in $Ca_3GaMn_2O_8$ are slightly shorter. Furthermore, as observed from the SEM

.

images in Figure 5.3, the grains in the sintered pellet of $Ca_3GaMn_2O_8$ are packed more closely, which can contribute to the enhanced conductivity.

5.3 MAGNETIC PROPERTIES

Zero-field cooled and field cooled magnetization data of $Ca_3GaMn_2O_8$ and $SrCa_2GaMn_2O_8$ are shown in Figure 5.5. The magnetization data reveal magnetic transitions below 120 K and 150 K, for $Ca_3GaMn_2O_8$ and $SrCa_2GaMn_2O_8$, respectively. The low values of magnetic susceptibility in the entire temperature range (2 K - 400 K), indicate that there is little uncompensated moment in both materials. This is further confirmed by isothermal magnetization data shown in Figure 5.5. These data reveal low magnetization values even at a magnetic field of 9 T at 2 K, where magnetization values reach a maximum of 0.19 µB and 0.10 µB per mole for $Ca_3GaMn_2O_8$ and $SrCa_2GaMn_2O_8$, respectively. These low magnetizations, along with the transition observed in magnetic susceptibility indicate that the magnetic state of these materials at low temperature is antiferromagnetic, which is also reported for a similar compound $Ca_{2.5}Sr_{0.5}GaMn_2O_8$.[175] The antiferromagnetic order in our materials was further confirmed by neutron scattering at 10 K for $Ca_3GaMn_2O_8$. The magnetic structure was analyzed using GSAS software and EXPEGUI interface.[93, 178] Figure 5.6a shows the Rietveld refinement profile with both magnetic and atomic phases.

The magnetic peaks in the neutron scattering pattern could be defined by the same unit cell as that of the chemical structure. The magnetic structure consists of a three-dimensional G-type antiferromagnetic arrangement, where the Mn moments are aligned antiparallel to all nearest neighbors along the b-axis (Figure 5.6b). The moment of Mn was

.

refined to 3.31(4) µB. This value is lower than the average theoretical moment expected

for a 1:1 ratio of Mn^{3+} (d^4) and Mn^{4+} (d^3) cations in $Ca_3GaMn_2O_8$, which is 4.39 µB.

However, low moments have been observed for Mn in other Ga-containing oxides such as

$Ca_2GaMnO_{5.045}$ (3.6 µB), $SrCaMnGaO_{5+\delta}$ (3.3 µB), and $Sr_2GaMnO_{5.0}$ (3.2 µB).[175, 179-181]
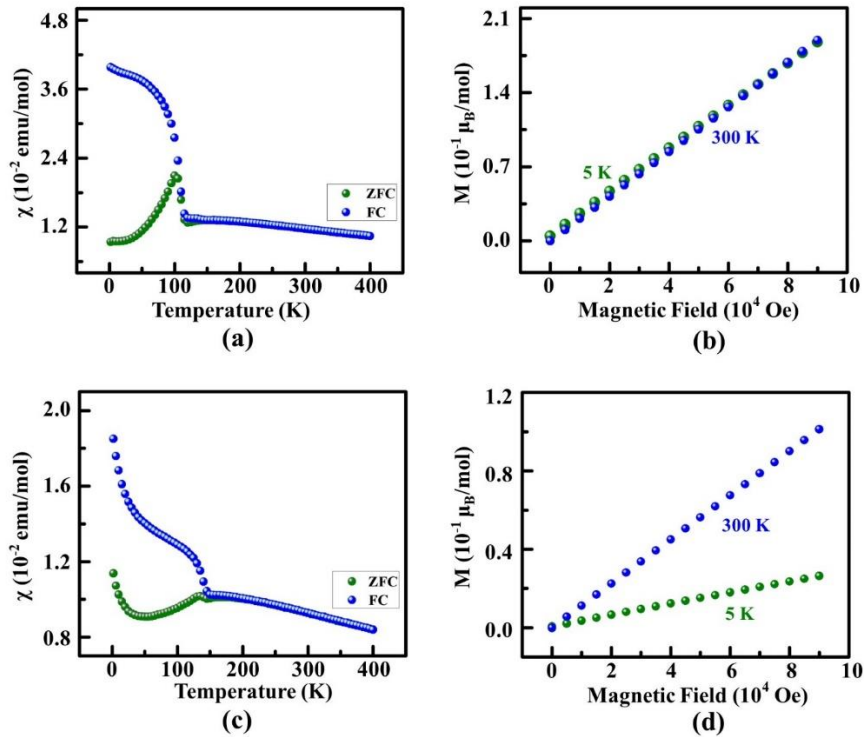
Figure 5.5: (a) and (b) show magnetic susceptibility and isothermal magnetization data, respectively, for $Ca_3GaMn_2O_8$. Parts (c) and (d) show the data for $SrCa_2GaMn_2O_8$.
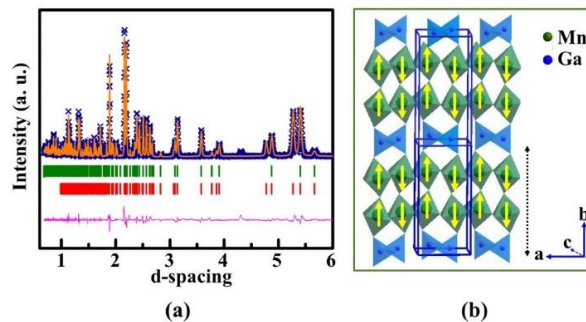
Figure 5.6: (a) Neutron refinement profile for magnetic (red vertical tick marks) and chemical structure (green vertical tick marks) of $Ca_3GaMn_2O_8$. Small additional peaks at d ≈ 4.3 Å could be due to $CaMnO_{3-\delta}$[175] or MnO[182] that have been reported for similar materials. These small peaks appear when the synthesis is scaled up to gram level (~4 g) for neutron experiments. (b) G-type antiferromagnetic structure of $Ca_3GaMn_2O_8$ with moments along *b* direction.

.

5.4 ELECTROCATALYTIC ACTIVITY FOR HYDROGEN-EVOLUTION REACTION

To our knowledge, the electrocatalytic activity for water splitting has not been studied for this structural family. Therefore, through this work, we introduce another class of materials that can be utilized for water splitting. We investigated the electrocatalytic activity of $Ca_3GaMn_2O_8$ and $SrCa_2GaMn_2O_8$ for hydrogen evolution reaction (HER) and oxygen-evolution reaction (OER) of water splitting process. These compounds showed some degree of OER activity (Figure 5.7c), but their performance was not high enough to be competitive with existing catalysts. However, remarkably, both materials exhibited very high HER activity, as demonstrated in Figure 5.7.

For HER studies, the onset potential and overpotential at the current density of 10 mA/cm^2 are used to describe the performance of electrocatalysts.[70, 183] Lower values of onset potential and overpotential are indicative of better HER catalysts. The HER studies are often done in either acidic or basic conditions. The basic media (0.1 M or 1 M KOH) did not lead to high activity, but acidic condition (0.5 M H_2SO_4) was found to result in an excellent HER activity for the materials studied here. Figure 5.7 shows the polarization curves of the two compounds as well as that of the reference electrocatalyst, Pt/C. Clearly, the platinum catalyst shows very good activity, but the high cost of precious metals, such as platinum, is a major problem. There is a substantial ongoing effort toward the discovery of economical HER catalysts.[70, 183] Both materials studied in this work show significant HER activity, with an onset potential of ~ -0.27 V for $Ca_3GaMn_2O_8$ and ~ -0.21 V for $SrCa_2GaMn_2O_8$, beyond which the cathodic current increases rapidly. The overpotential (η_{10}) needed to drive a current density of 10 mA/cm^2 is η_{10} ~ -367 mV for $Ca_3GaMn_2O_8$

.

and $\eta_{10}\sim$ -315 mV for SrCa$_2$GaMn$_2$O$_8$. The latter is only ~215 mV higher than that of Pt/C.

This is a remarkable performance.
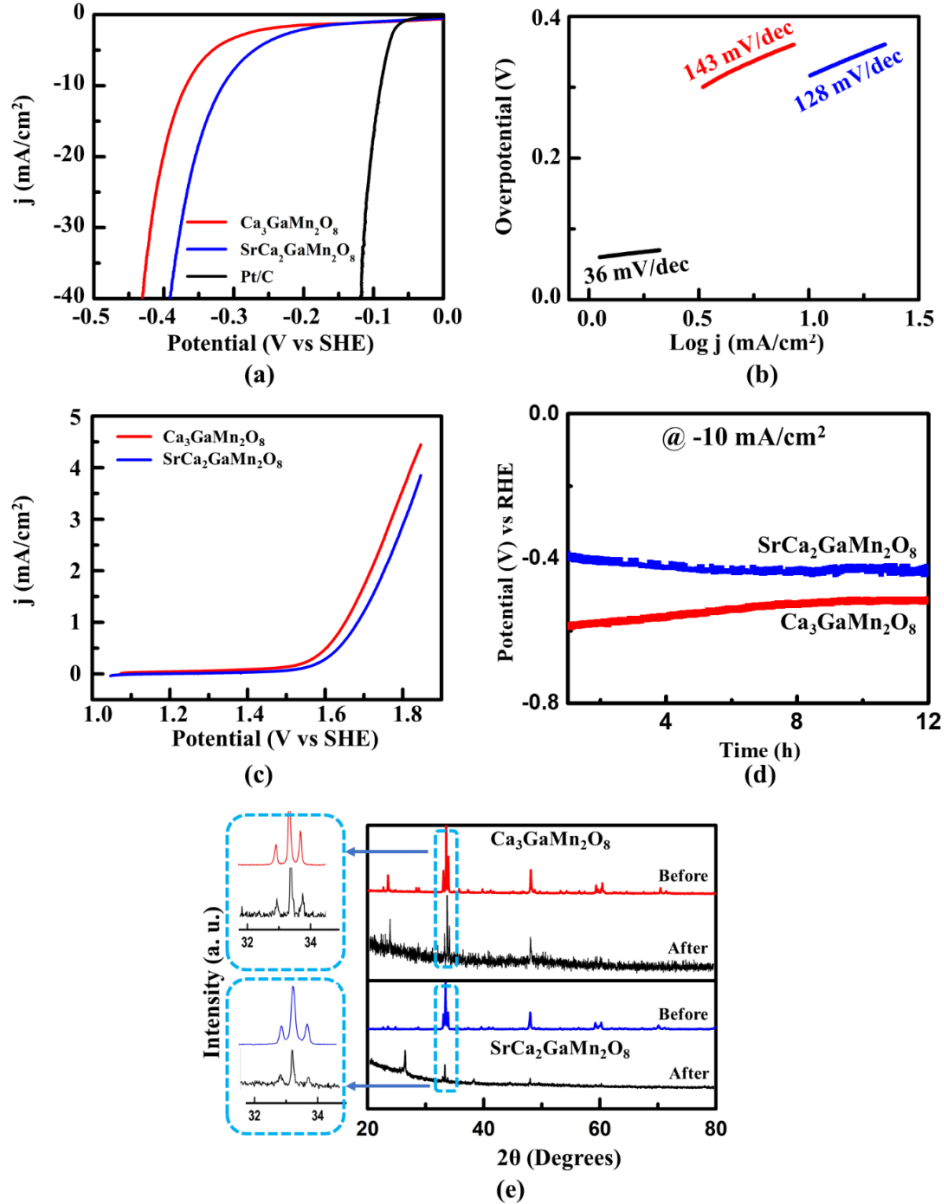
Figure 5.7: (a) HER activity in 0.5M H$_2$SO$_4$. (b) Tafel slopes for HER activity of Ca$_3$GaMn$_2$O$_8$ (red), SrCa$_2$GaMn$_2$O$_8$ (blue), and Pt/C (black). (c) OER activity in 0.1M KOH. (d) Chronopotentiometry response in 0.5M H$_2$SO$_4$ to test the stability during HER. (e) X-ray diffraction data before and after the chronopotentiometry.

The kinetics of HER can be investigated using the Tafel equation,[184]

.

$$\eta = a + b \log j \qquad\qquad (5.4)$$

where η and j are overpotential and current density, respectively. The slope of η versus log j plot (Tafel slope) is used to show the relative reaction rates for different catalysts. As shown in Figure 7, the Tafel slopes for $Ca_3GaMn_2O_8$, $SrCa_2GaMn_2O_8$, are 143 mV/dec, and 128 mV/dec, respectively. Chronopotentiometry experiments in 0.5M H_2SO_4 were conducted to test the stability under HER conditions. As shown in Figure 5.7d, these measurements indicated excellent stability. In addition, X-ray diffraction data (Figure 5.7e), in particular the largest diagnostic peaks close to 33-34° (enlarged in the inset), before and after chronopotentiometry showed the retention of the materials structures, further confirming the stability of these compounds. Furthermore, the double layer capacitance, C_{dl}, which is often taken as representative of electrochemically active surface area,[185] was calculated as 127 μF and 649 μF for $Ca_3GaMn_2O_8$ and $SrCa_2GaMn_2O_8$, respectively, matching the trend of HER activity (Figures 5.8).

It is noted that some oxide electrocatalysts show higher activity than our materials.[70, 183] For example, some nano-materials or composites based on metal oxides, such as WO_3 nanosheets ($\eta_{10} \sim$ -38 mV)[186], MoO_{3-y} nanofilms ($\eta_{10} \sim$ -201 mV)[187], and WO_3 nanoplates ($\eta_{10} \sim$ -117 mV)[188], perform better than our compounds in 0.5M H_2SO_4. However, these systems need additional fabrication steps, such as composite formation or nanofabrication. Regarding bulk oxide electrocatalysts, the recently reported $CaSrFeMnO_{6-\delta}$ shows HER catalytic activity with $\eta_{10} \sim$ -310 mV.[189] Nevertheless, the materials studied in this work are still among high performing HER catalysts and show better activity than the extensively studied catalysts MoS_2,[190] gold,[191] and bulk WO_3[192] in

.

acidic condition. In addition, while nanofabricated oxide catalysts for acidic HER, such as those described above, have been reported, perovskite-based oxides, especially in bulk form, that are capable of acidic HER catalysis are uncommon.[189]
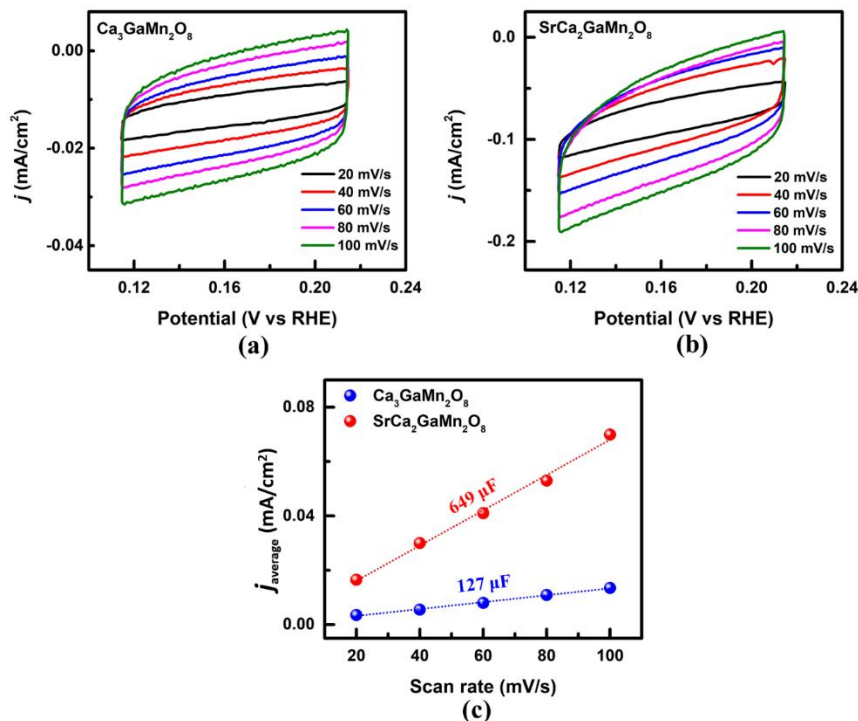
Figure 5.8: (a) and (b) Cyclic voltammetry data in non-faradic region for the two compounds. (c) Plot of $j_{average}$ versus scan rate (v). Here, $j_{average}$ is the average of j_{anodic} and $j_{cathodic}$ absolute values at the middle potential of the CV at each scan rate. The C_{dl} value is often taken as a measure of electrochemically active surface area (ECSA),[185] and is obtained from the slope of $j_{average}$ versus v graph according to the equation $C_{dl} = j_{average}/v$. [189, 193]

5.5 PSEUDOCAPACITIVE CHARGE STORAGE

Another remarkable feature of the materials studied in this work is their pseudocapacitive properties. Supercapacitors have been extensively investigated due to their significant advantages in power density and cycling stability. However, they suffer from low energy density, and their charge storage capacity is limited. Unlike traditional electric double-layer capacitors that rely on non-Faradaic electrostatic charge storage, pseudocapacitors operate

.

based on Faradaic processes, and therefore show greater charge storage capacity.[194] However, since the Faradaic charge transfers in pseudocapacitors occur on or near the surface, they are not limited by bulk diffusion, leading to cyclic voltammetry (CV) and galvanostatic charge-discharge (GCD) behavior similar to traditional capacitors. In theory, pseudocapacitors can possess both high power density of capacitors and high energy density of batteries.[44] Intercalation-based pseudocapacitors involve Faradaic electron transfer that occurs upon intercalation and de-intercalation of ions.[44] The intercalation of oxygen anion was first observed in 1975 in perovskite oxide, $Nd_{1-x}Sr_xCoO_3$, in an alkaline solution.[45] Further utilization of this phenomenon for pseudocapacitive energy storage was shown several decades later in 2014.[44] Since then, some other pseudocapacitive materials based on oxygen anion intercalation have been studied. Examples of the materials that have been investigated are $La_{1-x}Sr_xMnO_3$,[3, 44, 46] $La_{1-x}Ca_xMnO_3$,[47] $SrCo_{0.9}Nb_{0.1}O_3$,[48] and $LaNi_{1-x}Fe_xO_{3-\delta}$.[49] The compounds studied before have been primarily perovskite-based oxides, ABO_3, where the A or B sites were occupied by two cations that were distributed randomly. Here, we show that vacancy-ordered systems, such as bilayer structures can also exhibit oxygen-based pseudocapacitive properties.

Figure 5.9 shows the CVs of $Ca_3GaMn_2O_8$ and $SrCa_2GaMn_2O_8$ in the three-electrode setup at varying scan rates of 5, 20, 40, 60, and 80mV/s in the voltage range of 0.4 to -1.0 V vs Ag/AgCl. The quasi rectangular CV shapes indicate pseudocapacitive behavior, and Mn^{2+}/Mn^{3+} and Mn^{3+}/Mn^{4+} redox peaks are indicative of the Faradaic processes. [3, 44, 46-49, 195] At a scan rate of 5 mV/s, a pair of oxidation and reduction peaks are observed for both compounds during the anodic and cathodic scans, respectively. These redox peaks become more discernible at faster scan rates as shown in the representative
.

scan rate of 20 mV/s in Figure 5.9 (a, b). At 5 mV/s, a less intense oxidation peak appears

in $Ca_3GaMn_2O_8$ at –0.10 V vs Ag/AgCl (3M NaCl) along with another sharp peak at –0.61

V vs Ag/AgCl (3M NaCl), which are indicative of $Mn^{3+\leftrightarrow 4+}$ and $Mn^{2+\leftrightarrow 3+}$ surface redox

reactions, respectively. Similarly, two reduction peaks for this material are observed at –

0.35 V and –0.66 V vs Ag/AgCl (3M NaCl) that correspond to the reverse reactions during

the cathodic scans. Similarly, for $SrCa_2GaMn_2O_8$, two pairs of oxidation and reduction

peaks indicate similar $Mn^{3+\leftrightarrow 4+}$ and $Mn^{2+\leftrightarrow 3+}$ redox events.

Figure 5.9: Cyclic voltammetry (CV) curves at 20 mV/s showing the pseudocapacitive properties of (a) $Ca_3GaMn_2O_8$ and (b) $SrCa_2GaMn_2O_8$. The inset shows the CVs at different scan rates, 5, 20, 40, 60, and 80 mV/s in black, red, blue, green, and magenta, respectively. Parts (c) and (d) show the CV curves at 100 mV/s in different electrolytes (KNO_3 and KOH) for $Ca_3GaMn_2O_8$ (c) and $SrCa_2GaMn_2O_8$ (d), respectively.

.

81

At a scan rate of 5 mV/s, a pair of oxidation and reduction peaks are observed for both compounds during the anodic and cathodic scans, respectively. These redox peaks become more discernible at faster scan rates as shown in the representative scan rate of 20 mV/s in Figure 5.9 (a, b). At 5 mV/s, a less intense oxidation peak appears in $Ca_3GaMn_2O_8$ at –0.10 V vs Ag/AgCl (3M NaCl) along with another sharp peak at –0.61 V vs Ag/AgCl (3M NaCl), which are indicative of $Mn^{3+\leftrightarrow 4+}$ and $Mn^{2+\leftrightarrow 3+}$ surface redox reactions, respectively. Similarly, two reduction peaks for this material are observed at –0.35 V and –0.66 V vs Ag/AgCl (3M NaCl) that correspond to the reverse reactions during the cathodic scans. Similarly, for $SrCa_2GaMn_2O_8$, two pairs of oxidation and reduction peaks indicate similar $Mn^{3+\leftrightarrow 4+}$ and $Mn^{2+\leftrightarrow 3+}$ redox events.

As stated before, the peaks are indicative of pseudocapacitive properties, as observed in other pseudocapacitors.[3, 44, 46, 47] Examples are the $Mn^{3+/4+}$ and $Mn^{2+/3+}$ oxidation peaks at –0.1 V and –0.3 V vs Hg/HgO for $La_{1-x}Sr_xMnO_{3-\delta}$ (x= 0 – 1) at 10 mV/s (1M KOH),[3] ~ –0.1 V and ~ –0.4 V vs saturated calomel electrode for $La_xSr_{1-x}Cu_{0.1}Mn_{0.9}O_{3-\delta}$ at 10 mV/s (1M KOH),[196] above 0.2 V and ~ –0.1 V vs Hg/HgO for $LaMnO_{2.91}$ at 40 mV/s (1M KOH), [44] and 0.07 V and –0.25 V vs Hg/HgO for $CaMnO_3$ and its Ruddlesden–Popper counterparts at 5 mV/s (1M KOH).[197]

To confirm that these redox processes are dependent on oxygen intercalation facilitated by hydroxide ion, we conducted additional experiments in 1M KNO_3 in the same voltage window (Figure 5.9c and d), which did not show the redox peaks for any of the two compounds. This indicates that the observed process is dependent on the hydroxide intercalation.[44] As described for other oxygen-based pseudocapacitors,[44, 195] during these surface reactions[46] the intercalated oxygen anion comes from OH^- ion,[195] which loses a

.

proton to another OH⁻ ion from the electrolyte to produces water,[44] and leaves behind the oxygen ion that is intercalated into the electrode.

At higher scan rates, there is a small shift of the anodic and cathodic peaks to higher and lower potentials, respectively. This shift is commonly observed in pseudocapacitors and is assigned to the internal resistance of the electrode,[198, 199] or an indication that the charge transfer kinetics is the limiting step in this process.[200] The peak current increases as a function of increasing the scan rate, which suggests rapid electronic and ionic transport rates.[195, 200] Additionally, while the area changes, the shape of the CV curve remains the same, which indicates enhanced mass transport and electron conduction.[195, 199, 200]

The galvanostatic charge-discharge (GCD) behavior of these defect-ordered materials was examined in the potential range of 0.0 to 1.4 V vs Ag/AgCl through the construction of symmetric two-electrode cells, as described in the experimental section. Figure 5.10a shows the charge/discharge cycles for both materials at the current density of 1 A/g. Also, the GCD curves at various current densities for the best performing material, $Ca_3GaMn_2O_8$, are shown in Figure 9b. The inverted V shape of charge/discharge curves is signature behavior of pseudocapacitors and indicates excellent pseudocapacitive properties for these compounds.[46, 47] It is noted that GCD data in batteries, where the processes are controlled by bulk diffusion, do not show the inverted V curves.

The GCD curve can be used to obtain specific capacitance of an electrode at different discharge currents, using equation 4.[194, 201, 202]

$$C_s = \frac{4I\,\Delta t}{m\,\Delta V} \quad \text{or} \quad C_s = \frac{4I}{m\,dV/dt} \tag{5.5}$$

.

where, I is the constant current used for GCD, and dv/dt is the slope of the discharge curve, with ΔV being the voltage window and Δt the discharge time. Also, *m* is the total mass of the active material in both electrodes.[194, 202] Equation 4 may be simplified further by replacing the I/*m* part with current density, *i*, such that mass is not shown in the equation. The multiplier 4 is used to normalize for masses and capacitance of both electrodes and adjust for one electrode. [194, 201, 202] Some researchers use equation 4 without the multiplier 4 [195, 199, 200, 203] and take *m* as the mass of the active material in each electrode,[195] although sometimes the meaning of *m* is not explicitly stated.[199, 200] In some reports, dv/dt was calculated using two data points on the discharge curve, V_{max} and $1/2V_{max}$,[202, 203] to get $dV/dt = (V_{max} - 1/2V_{max})/(t_2-t_1)$,[202, 203] where t_2 and t_1 were the discharge times corresponding to V_{max} and $1/2V_{max}$, respectively.[202, 203] Equation 4 has also been used to obtain volumetric capacitance, using volume instead of mass.[204]

The C_s values obtained from the GCD curves of our symmetric cells at a current density of 0.5 A/g are 39.2 F/g and 4.5 F/g for $Ca_3GaMn_2O_8$ and $SrCa_2GaMn_2O_8$, respectively. In comparison, a symmetric cell reported using the perovskite $La_{1-x}Sr_xMnO_3$, resulted in the specific capacitance of ~7.75 F/g at 0.5 A/g.[46] Similarly, a symmetric cell based on $La_{1-x}Ca_xMnO_3$ shows the specific capacitance of ~13 F/g at 0.5 A/g,[47] which quickly deteriorates to about 2 F/g.

The energy density of the cell (Wh/Kg) is calculated using the following equation:[205, 206]

$$E = \frac{C_s V^2}{2 \times 3.6} \qquad (5.6)$$

Here, C_s is the specific capacitance and V is the cell voltage window in the GCD curve. The multiplier, $\frac{1}{3.6}$, is needed to obtain the energy density in units of Wh/Kg when the C_s

.

unit is F/g. It is noted that $1F = 1\frac{s\,A}{V}$ and $1W = 1V \times 1A$. If the unit of C_s is F/Kg, then the multiplier should also be different, $\frac{1}{3600}$.[201] The latter multiplier has also been used for calculating areal energy density in units of Wh/cm^2 (using areal capacitance)[207, 208] and volumetric energy density (using volumetric capacitance) in units of Wh/cm^3.[209] In some cases, researchers have chosen not to show any multipliers, and write the formula as $E = \frac{C_s\,V^2}{2}$.[44, 210, 211] We assume that they have applied the multipliers separately to obtain the right units.

The power density of the cell (unit: W/Kg) is obtained by dividing the energy density by discharge time, Δt:[205, 206]

$$P = \frac{E \times 3600}{\Delta t} \qquad (5.7)$$

The constant, 3600, is used to obtain the power density in W/Kg when the unit of Δt in seconds, s.[205, 206] The same multiplier is used for calculating areal power density (in W/cm^2)[207, 208] and volumetric power density (in W/cm^3).[209] In some cases Δt is expressed in hours (h) with no multiplier.[210, 211]

Symmetric cells based on $Ca_3GaMn_2O_8$ and $SrCa_2GaMn_2O_8$ can deliver respective energy densities of 10.69 Wh/Kg and 1.23 Wh/Kg at a power density of 1400 Wkg^{-1}, based on the current density of 0.5A/g. Our best material, $Ca_3GaMn_2O_8$, shows superior energy density and power density compared with many other systems, including a symmetric pseudocapacitor based on $La_{1-x}Sr_xMnO_3$, which has an energy density of ~1.55 Whkg^{-1} with power density less than 1000 Wkg^{-1}, at the current density of 0.5 A/g.[46] Similarly, the symmetric cell reported for $La_{1-x}Ca_xMnO_3$, shows energy density of ~2.6 Whkg^{-1} and power density of ~800 Wkg^{-1} at 0.5 A/g.[47]

.
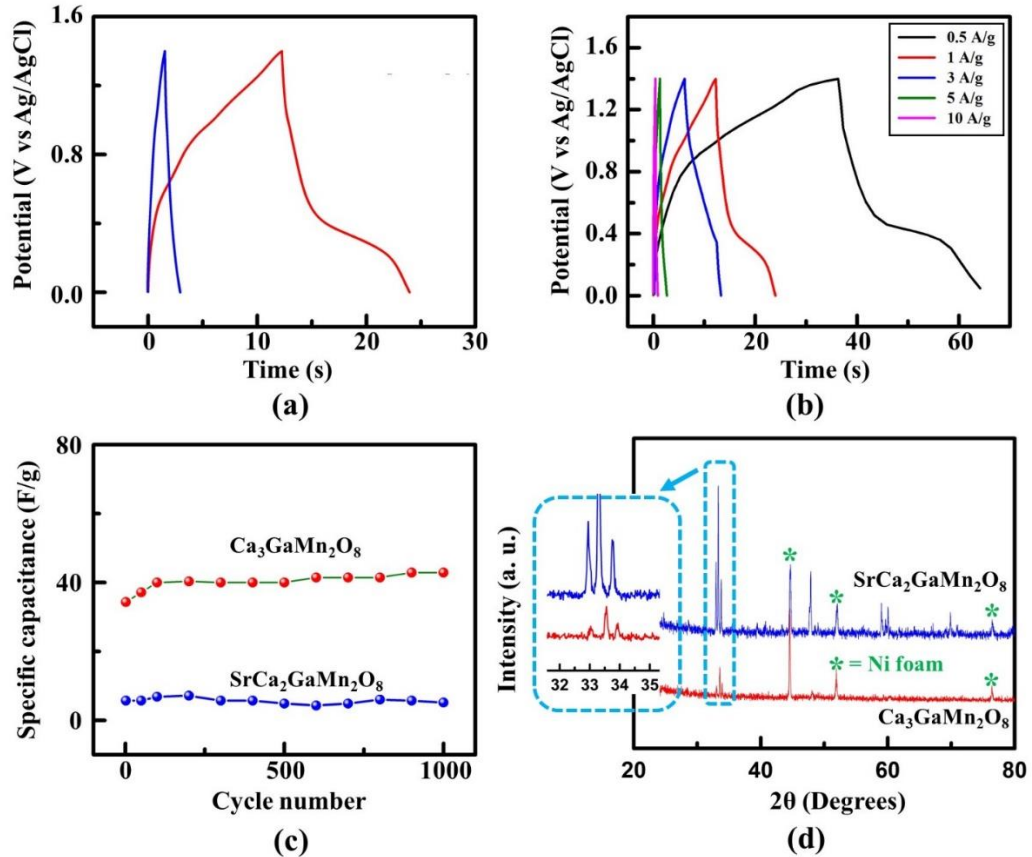
Figure 5.10: (a) Galvanostatic charge-discharge (GCD) profiles for Ca$_3$GaMn$_2$O$_8$ (red) and SrCa$_2$GaMn$_2$O$_8$ (blue) at current density of 1 A/g. (b) GDC profiles at various current densities for the best performing material, Ca$_3$GaMn$_2$O$_8$. (c) Stability tests up to 1000 cycles. (d) X-ray diffraction data after 1000 GCD cycles.
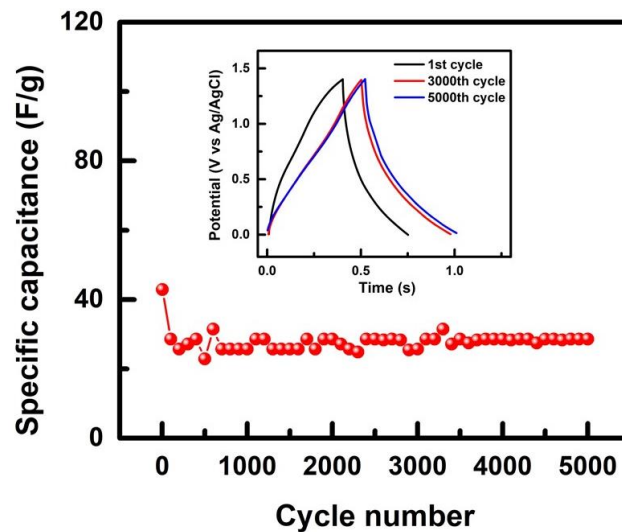
Figure 5.11: Specific capacitance obtained from 5000 GCD cycles for Ca$_3$GaMn$_2$O$_8$ at 10 A/g, indicating high stability. The inset shows the 1st, 3000th, and 5000th GCD cycles.

.

Long cycle life is another crucial criterion of a pseudocapacitor for practical applications. Therefore, an endurance test was conducted using GCD cycles at 1 A/g (Figure 5.10c) for 1000 cycles. Both materials show remarkable retention of specific capacitance after 1000 cycles. The retention of pseudocapacitive properties can be attributed to the high degree of stability of these compounds. Figure 5.10d shows the X-ray diffraction data of both compounds after 1000 GCD cycles. In particular, the largest peaks close to 33-34° (enlarged in the inset) are often used as diagnostic peaks for this class of materials. As evident from this figure, both materials retain their structural integrity without the collapse of the material framework or any phase transformation, which leads to a stable pseudocapacitive response. Further stability tests were done for our best pseudocapacitor, $Ca_3GaMn_2O_8$, by repeating 5000 GCD cycles at 10 A/g, as shown in Figure 5.11, indicating its remarkable stability. The crystallite morphology is also retained after GCD cycles, as shown by SEM images in Figure 5.12.

Thus, the high energy and power density, combined with outstanding stability, make these defect-ordered materials excellent pseudocapacitors.
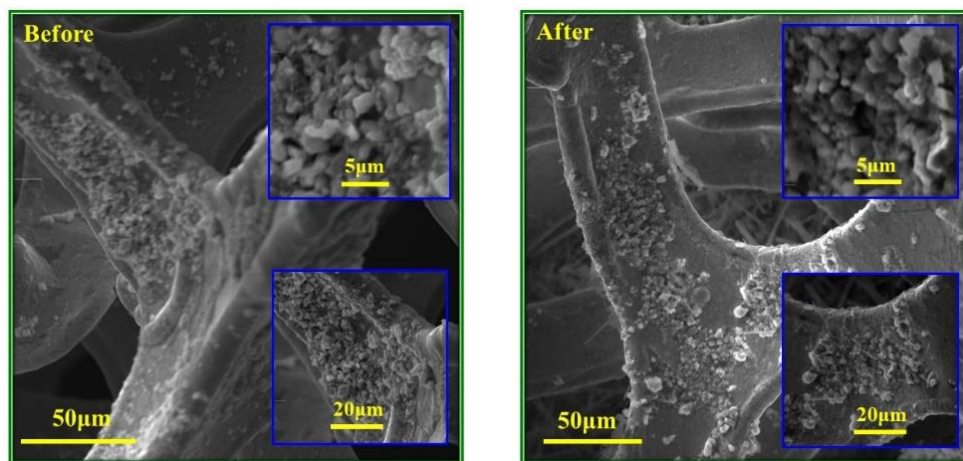
Figure 5.12: Scanning electron microscopy (SEM) images of $Ca_3GaMn_2O_8$ particles on nickel foam before and after 5000 GCD cycles.

.

5.6 CONCLUSIONS

This study highlights the great potential of ordered bilayer systems, an underexplored class of oxides, for electrochemical applications. The simultaneous occurrence of an array of remarkable properties in the same compound is noteworthy. The two materials, $Ca_3GaMn_2O_8$ and $SrCa_2GaMn_2O_8$, are semiconductors in the entire temperature range of $25 - 800$ °C, show long-range G-type antiferromagnetic order, and are also capable of catalyzing hydrogen-evolution reaction (HER) of water splitting. They also show excellent pseudocapacitive energy storage with outstanding stability up to 1000 cycles of charge-discharge. The observation of all these properties in this class of materials warrants further studies with the aim of developing active materials for cost-effective and efficient electrochemical applications.

.

CHAPTER 6

OXIDE ELECTROCATALYSTS BASED ON EARTH-ABUNDANT METALS FOR

BOTH HYDROGEN- AND OXYGEN-EVOLUTION REACTIONS

In this chapter, we demonstrate that the oxygen-deficient perovskite series, $Ca_2FeMnO_{6-\delta}$, $CaSrFeMnO_{6-\delta}$ and $Sr_2FeMnO_{6-\delta}$ are outstanding electrocatalysts for water-splitting and show unique bifunctional properties. We also show the correlations between crystal structure and electrocatalytic activity for both hydrogen- and oxygen-evolution reaction. Furthermore, we demonstrate the relationship between structural properties and electrical charge-transport, which in turn affects the electrocatalytic properties of these materials.

6.1 CONTROLLED ELCTROCHEMICAL EXPERIMENTAL CONDITIONS

In this chapter, all the experimental conditions are similar as discussed in chapter 2. However, few additional experimental methods were used during electrocatalytic studies. This involved control experiments to understand the effect of role of carbon black during the OER and HER studies. Furthermore, gas chromatography was done to show the evidence of evolved O_2 gas during the process. Experiments using several counter electrodes such as Pt wire, graphite rod, and carbon rod were also checked. Running the experiments under either OER or HER conditions using only carbon ink led to negligible

activity, as shown in Figure 6.1. Control experiments were also done with carbon counter electrode to eliminate the possibility of dissolution of platinum counter electrode and its contribution to HER.[212] The results from both platinum and carbon counter electrodes were similar (Figure 6.2).
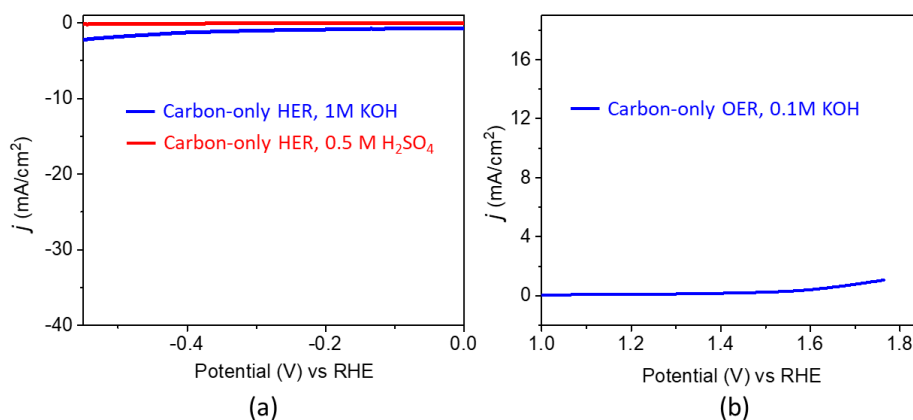
Figure 6.1: The HER (a) and OER (b) data from control experiments using only carbon black on the working electrode, indicating little contribution from carbon to electrocatalytic activity.

For OER, gas chromatography experiments were also done to confirm the formation of oxygen. Before starting the electrolysis, the electrolyte was purged with nitrogen for 60 minutes. The electrolyte was then stirred during electrolysis. Prior to applying any potential, chromatograms were obtained to show that the cell has been purged and contained no ambient oxygen. A constant potential of 0.62 V vs Ag/AgCl was then applied and data were collected at 30, 45, and 60 minutes of the OER. Oxygen gas was detected by online automatic injection (1 mL sample) using a thermal conductivity detector. The carrier gas for the column was nitrogen. The gas was injected every 15 minutes.

90
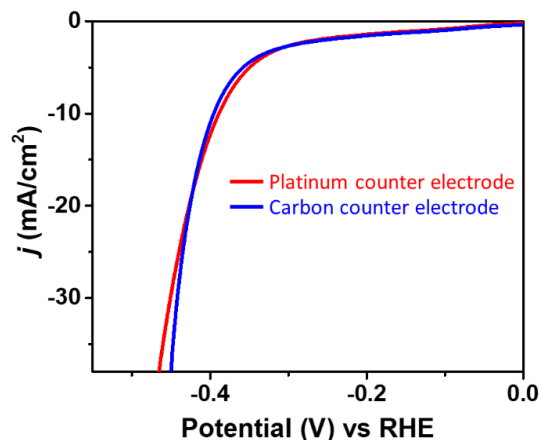
Figure 6.2: HER data for CaSrFeMnO$_{6-\delta}$ in 1 M KOH using carbon or platinum counter electrodes.

6.2 CRYSTAL STRUCTURE

In oxygen-deficient perovskites, ABO$_{3-\delta}$ or A$_2$B$_2$O$_{6-\delta}$, the cations on the B-site often have octahedral, square-pyramidal or tetrahedral coordination geometry,[10, 12] while the larger A-cations reside in spaces between the above polyhedra. In this class of materials, the vacancies, created due to oxygen-deficiency, can have either random or ordered distribution. The variation in the arrangement of oxygen-vacancies is a primarily factor that leads to different structures and various coordination geometries for B-site cations. The oxygen-deficient perovskites studied in this work, Sr$_2$FeMnO$_{6-\delta}$, CaSrFeMnO$_{6-\delta}$ and Ca$_2$FeMnO$_{6-\delta}$, show variation in crystal structure (Figure 6.3) due to the change in the ionic radius of the A-site cation, leading to different arrangements of oxygen-vacancies. It is noted that all three materials are synthesized under identical conditions. Therefore, the structural changes between them are a function of the A-site cation. Our Rietveld refinements (Figure 6.3) confirm the previously reported crystal structures.[130, 213] In Ca$_2$FeMnO$_{6-\delta}$, the oxygen-vacancies are distributed in an ordered arrangement and only appear in alternating layers, leading to an orthorhombic *Pnma* structure. The structure consists primarily of alternating FeO$_4$ tetrahedra and MnO$_6$

91

octahedra (Figure 6.3).[130] The FeO_4 tetrahedra form chains that are sandwiched between MnO_6 octahedral layers. The degree of oxygen-deficiency is determined by iodometric titration, which indicates $\delta \approx 1$ for this compound.

Conversely, in $CaSrFeMnO_{6-\delta}$ and $Sr_2FeMnO_{6-\delta}$, the oxygen-vacancies are disordered,[130, 213] and the average structure resembles that of a regular perovskite (Figure 6.3), but with partial occupancy on oxygen sites. The space group is cubic *Pm-3m* and there is no ordering in the structure, as confirmed by Rietveld refinements (Figure 6.3). Ca and Sr are on the same crystallographic site (0,0,0), and Fe and Mn also share the same position (½,½,½). The degree of oxygen-deficiency is different in these two compounds, $\delta = 0.57$ for $CaSrFeMnO_{6-\delta}$ and $\delta = 0.22$ for $Sr_2FeMnO_{6-\delta}$, as determined by iodometric titrations. Furthermore, the Fe(Mn)–O bond distances are shorter in $CaSrFeMnO_{6-\delta}$, 1.9062(1) Å, compared with those of $Sr_2FeMnO_{6-\delta}$, 1.92526(7) Å.

These results are consistent with previous neutron scattering studies, which have shown the perovskite-type average structure for $CaSrFeMnO_{6-\delta}$ and $Sr_2FeMnO_{6-\delta}$,[130] but with partial occupancy on oxygen sites, indicating long-range disordered arrangement of vacancies. However, neutron pair distribution function analyses[214, 215] have shown that at the local level there are domains where the vacancies are ordered in these long-range disordered systems. For $Ca_2FeMnO_{6-\delta}$, neutron scattering studies[130, 132] have indicated long-range vacancy order, evident from conversion of the octahedral geometry into tetrahedral in alternating layers (i.e., the vacancies only appear in alternating layers).
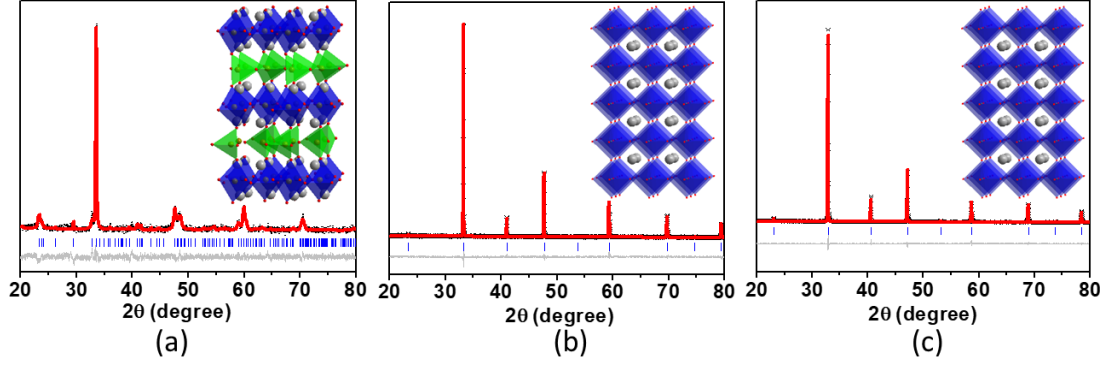
Figure 6.3: Rietveld refinement profiles for powder X-ray diffraction data of (a) $Ca_2FeMnO_{6-\delta}$, *Pnma*, $a = 5.3350(8)$ Å, $b = 14.957(4)$ Å, $c = 5.460(2)$ Å (b) $CaSrFeMnO_{6-\delta}$, *Pm-3m*, $a = 3.8124(2)$ Å and (c) $Sr_2FeMnO_{6-\delta}$, *Pm-3m*, $a = 3.8505(4)$ Å. In the insets, $(Fe/Mn)O_6$ octahedra are shown in blue, FeO_4 tetrahedra are in green, and Ca/Sr atoms are represented by gray spheres.

The microstructure of the three materials is also different, as demonstrated by scanning electron microscopy micrographs of the sintered pellets (Figure 6.4). $Ca_2FeMnO_{6-\delta}$ shows the largest grains among the three compounds. In addition, significant degree of porosity is observed in this material. The grain size for $CaSrFeMnO_{6-\delta}$ and $Sr_2FeMnO_{6-\delta}$ is similar, but the latter shows somewhat higher degree of porosity.

A measure of the relative porosity can also be found using saturation method,[216] In this method, a solid sintered pellet was weighed before (W_{dry}) and after being submerged (W_{sat}) in boiling water for 2 hours in order to determine the amount of fluid that filled the pores of each sample. The percent mass of fluid in pores provides a measure of the porosities of different samples relative to each other:

$$\% \text{ mass of water in pores} = \frac{W_{sat} - W_{dry}}{W_{dry}} \times 100 \tag{6.1}$$

The percent mass of fluid in pores is 8.7%, 6.3%, and 7.8% for $Ca_2FeMnO_{6-\delta}$, $CaSrFeMnO_{6-\delta}$, and $Sr_2FeMnO_{6-\delta}$, respectively. This trend in porosity is the same as that observed from SEM. We assign the change in porosity to the variation in sinterability,

where an intermediate degree of Ca incorporation leads to optimum sinterability. The change in sinterability as a function of change in the A-site cation in perovskite-based oxides has been observed previously.[217]

The structural dissimilarities between the three materials, in particular the changes in distribution of oxygen-vacancies and the ensuing structural order/disorder, give rise to significant differences in electrical charge-transport, as well as electrocatalytic properties. As will be discussed in detail in next sections, the vacancy-ordered compound, $Ca_2FeMnO_{6-\delta}$, has the least electrocatalytic activity, whereas the disordered compounds, $Sr_2FeMnO_{6-\delta}$ and $CaSrFeMnO_{6-\delta}$, are significantly more active, with latter material showing the most activity. It is also noted that among the two disordered structures that have good electrocatalytic activity, the degree of oxygen deficiency, δ, for the most active material, $CaSrFeMnO_{6-\delta}$ ($\delta = 0.57$), is greater than that of $Sr_2FeMnO_{6-\delta}$ ($\delta = 0.22$). This effect, *i.e.*, the impact of oxygen vacancies on electrocatalytic activity, has been demonstrated for other oxides before.[218-220]

The cooperative effect due to the presence of both Ca and Sr in $CaSrFeMnO_{6-\delta}$ should also be noted. The synergetic effect between Ca/Sr on the A-site and Fe/Mn on the B-site can lead to the enhanced electrocatalytic activity, similar to the cooperative coupling effect observed previously in some perovskites.[221] Furthermore, the compositional and structural changes lead to significant variation in electrical conductivity, which in turn affect the electrocatalytic activity. In fact, the trend in electrical conductivity matches nicely with the trend in electrocatalytic activity, as will be discussed later in connection with structural properties.
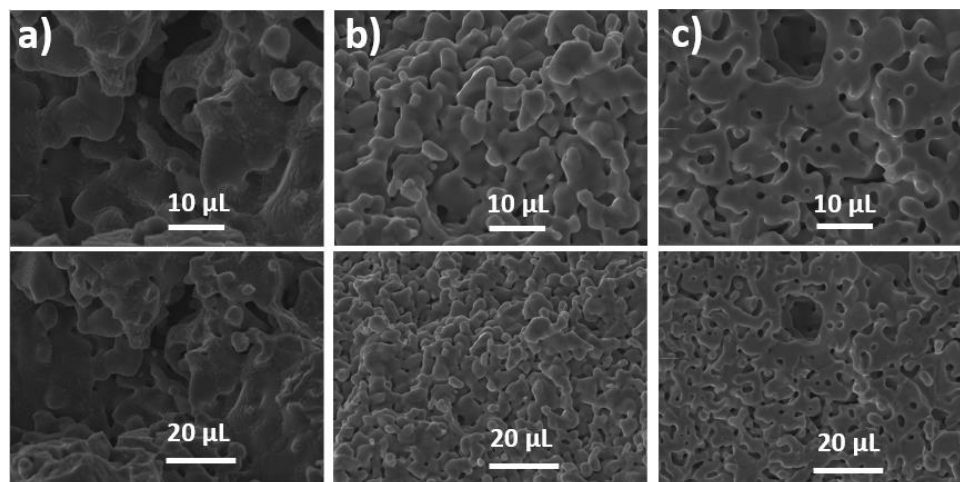
Figure 6.4: Scanning electron microscopy images of (a) $Ca_2FeMnO_{6-\delta}$ (b) $CaSrFeMnO_{6-\delta}$ and (c) $Sr_2FeMnO_{6-\delta}$. Note that $Ca_2FeMnO_{6-\delta}$ has the largest grains and highest porosity. The grain size for $CaSrFeMnO_{6-\delta}$ and $Sr_2FeMnO_{6-\delta}$ is similar, but the latter has somewhat higher porosity.

6.3 HYDROGEN-EVOLUTION ACTIVITY

Researchers have studied HER in either acidic or basic media depending on the catalyst. As described before, most of the catalysts utilized for HER are non-oxide materials. In acidic condition, materials such as sulphides[222, 223], carbides[224], nitrides[224], and metals[225] have been used. Similarly, in basic medium, catalysts such as sulphides[226], phosphides[227], carbides[224] and nitrides[224] have been utilized. Very few oxides have shown HER activity in either acidic[228] or alkaline[229] environment. Recently, a perovskite oxide has been studied for HER in 1 M KOH.[183] The electrocatalytic activity of perovskite oxides for HER in acidic environment is even less common. One study that briefly studied a perovskite oxide, reproted very low HER acitivty in acidic medium.[230] In general, it is uncommon to find bulk oxide materials that exhibit HER activity both in acidic and basic media. In fact, no perovskite oxide with such property has been reported to date. However, the materials studied in this work show HER activity in both conditions, as described below.

Given that HER experiments are frequently done in 0.5 M H_2SO_4 or 1 M KOH,[101, 224, 229, 231, 232] the same conditions were used in the study of the HER activities of $Ca_2FeMnO_{6-\delta}$, $CaSrFeMnO_{6-\delta}$, and $Sr_2FeMnO_{6-\delta}$. Figure 6.5 shows the polarization curves of the three materials, as well as that of the reference Pt/C catalyst (20 wt. % Pt). The onset potential, where the HER process commences, and the overpotential at 10 mA/cm^2 are frequently used as indications of catalysts performance.[233, 234] The reference Pt/C catalyst shows onset potential of almost zero, as expected.[77, 183, 224] The HER activities of our materials show the following order: $Ca_2FeMnO_{6-\delta}$ < $Sr_2FeMnO_{6-\delta}$ < $CaSrFeMnO_{6-\delta}$. Among the three compounds, $CaSrFeMnO_5$ shows the best (lowest) onset potential and overpotential in both acidic and basic conditions. It also shows the best mass activity, 43.5 A/g in acidic condition and 13.5 A/g in basic condition at –0.3 V. Whereas, the mass activities for the other two compounds are in the range of 3.0 A/g to 5.5 A/g at –0.3 V.

The onset potential values for $CaSrFeMnO_{6-\delta}$ are –0.10 V vs RHE in acidic condition, and –0.14 V vs RHE in basic condition. Its overpotential values at 10 mA/cm^2 are –0.31 V and –0.39 V vs RHE in acidic and basic conditions, respectively. While there are some oxides, such as $Pr_{0.5}BSCF$[183] and $PrBaCo_2O_{5+\delta}$[69], that show better HER performance in basic condition, the remarkable feature of $CaSrFeMnO_{6-\delta}$ is its ability to catalyze HER in both acidic and alkaline conditions. Furthermore, its HER activity in acidic condition, is superior to those of gold[191], boron nitride/GC[191], WO_3[192], and the widely studied MoS_2[190] in acidic condition. It is also superior to the activity of MoS_2 in alkaline medium.[235]

The better performance in acidic condition can be attributed to relatively higher energy requirement for the proton generation in alkaline solution.[236] Enhanced HER activity in acidic condition compared with basic environment has been observed for another catalyst before.[231] Nevertheless, it is important to note that oxide HER catalysts capable of functioning in both acidic and basic conditions are uncommon.

The kinetics of the HER reaction was also investigated. Tafel slope is generally utilized to study the HER kinetics, which is evaluated using Tafel equation $\eta = a + b \log j$,[229] where η is overpotential, and j is current density. The slope of the plot of η versus log j is indicative of the reaction rate (Figures 6.5c and 6.5d). The smaller the slope, the faster the reaction. The Tafel slope of the reference Pt/C catalyst is also shown, matching those reported before in acidic and basic conditions.[224]
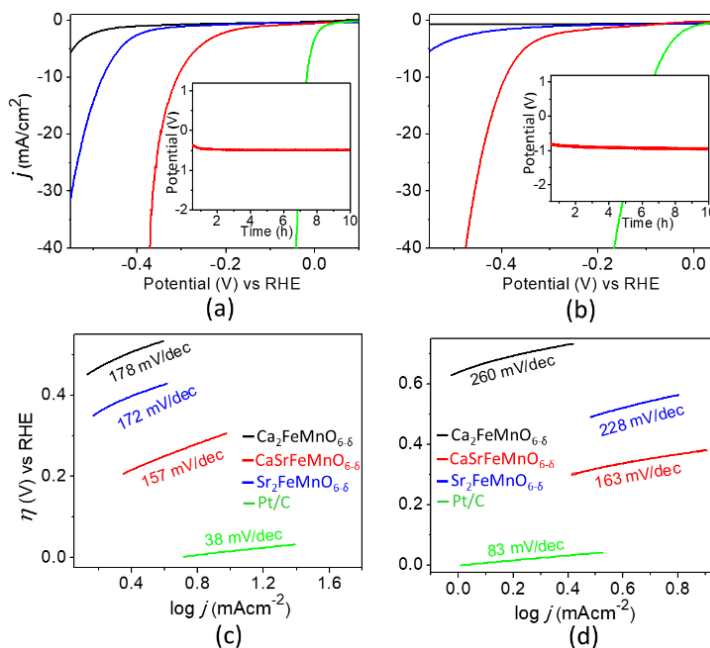
Figure 6.5: (a) and (b) show HER polarization curves in acidic and basic conditions, respectively. Pt/C data are shown in green, $Ca_2FeMnO_{6-\delta}$ in black, $CaSrFeMnO_{6-\delta}$ in red, and $Sr_2FeMnO_{6-\delta}$ in blue. Inset presents chronopotentiometry data, showing the stability of the best catalyst, $CaSrFeMnO_{6-\delta}$, as a function of time. (c) and (d) show Tafel slopes

97

for HER in acidic and basic media, respectively. $CaSrFeMnO_{6-\delta}$ is the best catalyst in the series, with lowest Tafel slope and overpotential.

The reaction kinetics follow the same trend as catalytic performance, with $CaSrFeMnO_{6-\delta}$ exhibiting the best kinetics and smallest Tafel slope, 157 mV/dec in acidic condition, and 163 mV/dec in basic condition. The relatively large Tafel slopes can be indicative of the mixed HER mechanism. It is known that the HER mechanism involves an initial binding between the catalyst and hydrogen atom (either from H_2O or H_3O^+) depending on the condition, i.e., basic or acidic. This is the Volmer reaction, which is then followed by either Heyrovsky or Tafel reaction. Either of these reactions can be the rate-determining step, resulting in a different Tafel slope, which is expected to have respective values of 120 mV/dec, 40 mV/dec and 30 mV/dec if the rate-determining reaction is Volmer, Heyrovsky or Tafel.[237] However, the Tafel slope can have a different value if more than one of the three steps are the rate-determining reactions. For example, the Mo_2C film shows Tafel slope of 166 mV/dec, which is qualitatively attributed to having two or three rate-determining steps.[237] Similarly large Tafel slopes have also been reported for MoS_2/graphene,[238] surface-functionalized MoS_2 nanosheets,[239] P-doped NiMoO4,[240] and Co/NBC,[241] indicating the mixed mechanism.

The electrochemically active surface area (ECSA) is often evaluated through determination of double layer capacitance, C_{dl}, in the non-faradaic region.[242] Given the direct proportionality between the two,[185] the C_{dl} value is often taken as a measure of ECSA.[185] The magnitude of C_{dl} is obtained from the slope of Δj, which is the average of j_{anodic} and $j_{cathodic}$ absolute values at middle potential of the CV, versus scan rate, v,

according to the equation $C_{dl} = \Delta j/v$. As shown in Figure 6.6, the most active catalyst, $CaSrFeMnO_{6-\delta}$, also has the largest C_{dl} in both acidic and basic media.
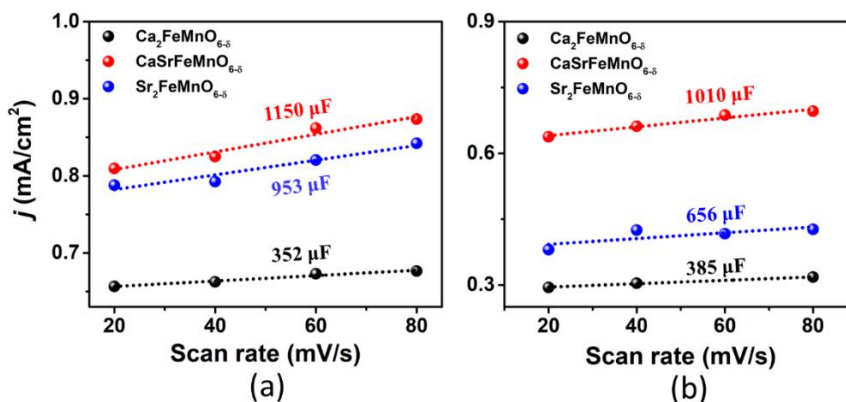
Figure 6.6: Double layer capacitance obtained from the slope of $J_{average}$ plotted against scan rate for (a) 1 M KOH, and (b) 0.5 M H_2SO_4.

6.4 OXYGEN-EVOLUTION ACTIVITY

Remarkably, in addition to HER activity, all of our three materials show catalytic activity for OER (Figure 6.7). Given that most reports on OER electrocatalysis are in 0.1 M KOH, the same conditions were used for our materials to allow direct comparison to other reported catalysts. However, experiments in the same conditions as those of HER, namely 1 M KOH and 0.5 M H_2SO_4 were also performed. The OER tests in acidic condition (0.5 M H_2SO_4) led to very high overpotentials, while OER experiments in 1 M KOH resulted in reasonable activity, but still less than the activity in 0.1 M KOH. The results for 0.1 M KOH are described here to allow comparison to previously reported catalysts. The most structurally ordered compound, $Ca_2FeMnO_{6-\delta}$, shows the lowest OER activity, while the best performance is observed for $CaSrFeMnO_{6-\delta}$. This is the same trend observed in the HER activity of these materials. In OER experiments the onset potential in cyclic voltammetry, where the reaction commences, as well as the overpotential, η, beyond the ideal 1.23 V, are important parameters that are commonly used to evaluate the activity of

catalysts. The overpotential is usually evaluated at 10 mA/cm^2, which has been adopted as a convention for comparing different catalysts.[243] The three compounds show onset potentials of ~1.45 V to 1.50 V in 0.1 M KOH. The overpotential at 10 mA/cm^2 varies significantly, from $\eta \approx 0.56$ V for Ca$_2$FeMnO$_{6-\delta}$, to $\eta \approx 0.37$ V for CaSrFeMnO$_{6-\delta}$, and $\eta \approx 0.42$ V for Sr$_2$FeMnO$_{6-\delta}$ (Figure 6.7).
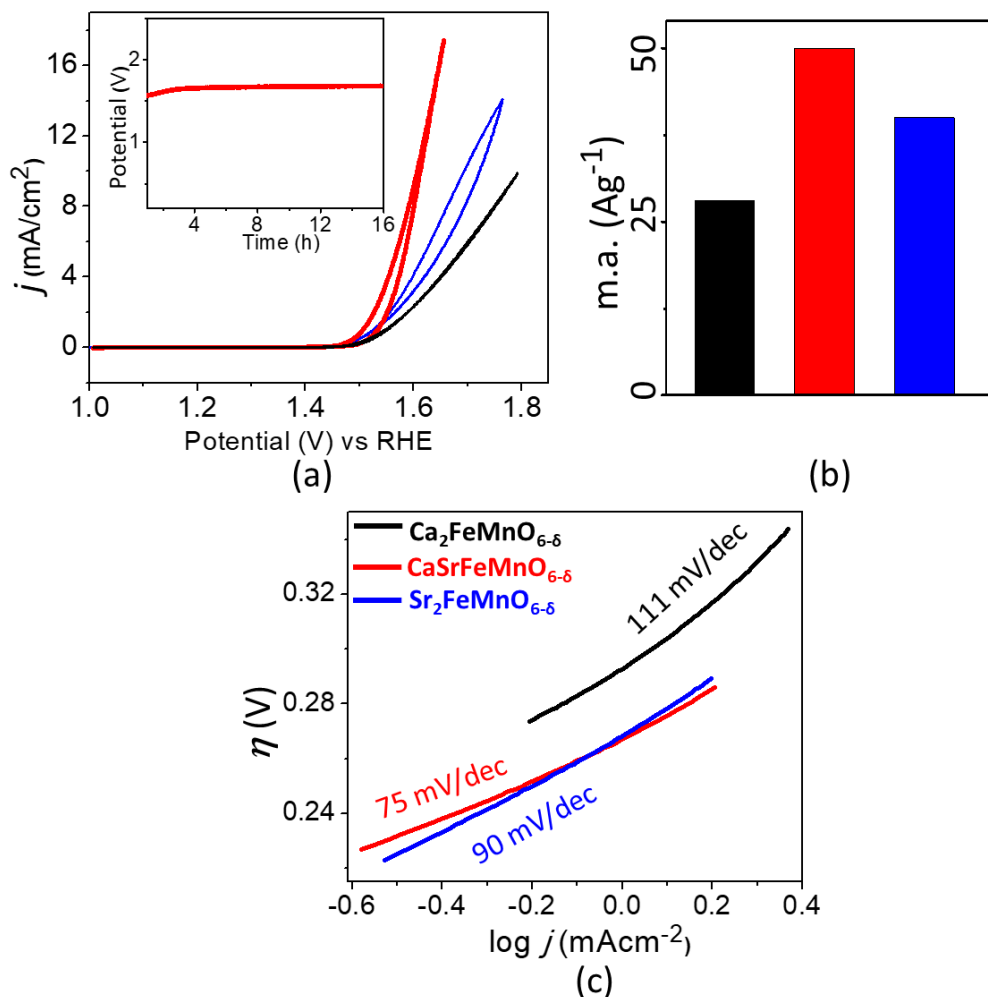
Figure 6.7: (a) OER polarization curves in 0.1 M KOH. Inset presents chronopotentiometry data, showing the stability of the best catalyst, CaSrFeMnO$_{6-\delta}$, as a function of time. (b) Mass activities at 1.7 V in 0.1 M KOH. (c) Tafel slopes indicating the OER kinetics. Data for Ca$_2$FeMnO$_{6-\delta}$ are shown in black, CaSrFeMnO$_{6-\delta}$ in red, and Sr$_2$FeMnO$_{6-\delta}$ in blue. CaSrFeMnO$_{6-\delta}$ is the best catalyst in the series, with lowest Tafel slope and overpotential.

The mass activity (A/g) was also calculated using the catalyst loading mass (0.1 mg cm^{-2}) and the measured current density J (mA cm^{-2}). Figure 6.7b compares the OER mass activities of these materials at 1.70 V vs RHE. CaSrFeMnO$_{6-\delta}$ shows significantly greater mass activity (~50 A/g) than Sr$_2$FeMnO$_{6-\delta}$ (~40 A/g) and Ca$_2$FeMnO$_{6-\delta}$ (~28 A/g). The mass activity of CaSrFeMnO$_{6-\delta}$ and Sr$_2$FeMnO$_{6-\delta}$ are higher than that of a previously reported Mn-based oxygen-deficient perovskite, Ca$_2$Mn$_2$O$_5$, 30.1 A/g at 1.7 V.[218]

The kinetics of OER was also investigated for all three materials. Similar to HER, Tafel slope is frequently utilized to study the OER kinetics based on the Tafel equation η = a + b log j [185, 244] where η is the overpotential, and j is the current density. The kinetics, represented by the Tafel plot, η vs. log j, is affected by electron and mass transport.[245, 246] Thus, Tafel plot can provide information about electronic transport in electrocatalysts.[246] Smaller slope of Tafel plot indicates faster reaction and better kinetics of OER. The Tafel slopes for Ca$_2$FeMnO$_{6-\delta}$, CaSrFeMnO$_{6-\delta}$ and Sr$_2$FeMnO$_{6-\delta}$ are 111 mV/dec, 75 mV/dec and 90 mV/dec, respectively, as shown in Figure 6.7c. The smaller Tafel slop of CaSrFeMnO$_{6-\delta}$ is indicative of faster OER kinetics and is consistent with its high electrocatalytic activity.

The comparison of electrocatalytic activity of the materials described in this work with those reported for precious metal catalysts, IrO$_2$ and RuO$_2$, indicates the remarkable OER performance of these new electrocatalysts. The catalyst CaSrFeMnO$_{6-\delta}$, described in this work, shows superior OER activity to IrO$_2$ (Figure 6.8), which has overpotential of η ≈ 0.45 V.[247] It is also superior to RuO$_2$, which has overpotential of η ≈ 0.42 V.[248] In addition, it is better than some of the oxide catalysts reported before, such as SrNb$_{0.1}$Co$_{0.7}$Fe$_{0.2}$O$_{3-\delta}$[66] and Pr$_{0.5}$Ba$_{0.3}$Ca$_{0.2}$CoO$_{3-\delta}$.[64]
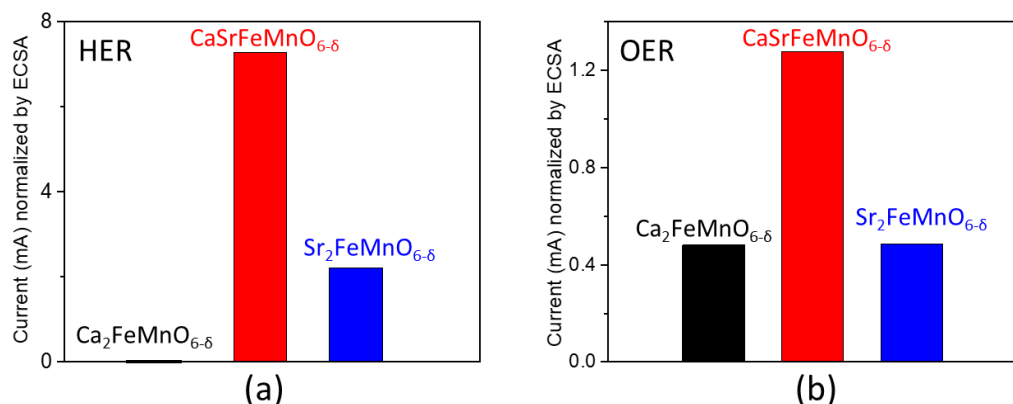
Figure 6.8: The current response normalized by ECSA for (a) HER in 0.5 M H_2SO_4 at -0.5 V, and (b) OER in 0.1 M KOH at 1.6 V.

Furthermore, the kinetics of OER is significantly enhanced by $CaSrFeMnO_{6-\delta}$, as evident from the Tafel slope, 75 mV/dec, compared with that reported for IrO_2, 83 mV/dec.[247] These observations are remarkable, as oxide materials based on earth-abundant metals, which show such high electrocatalytic activity and enhanced kinetics are uncommon.
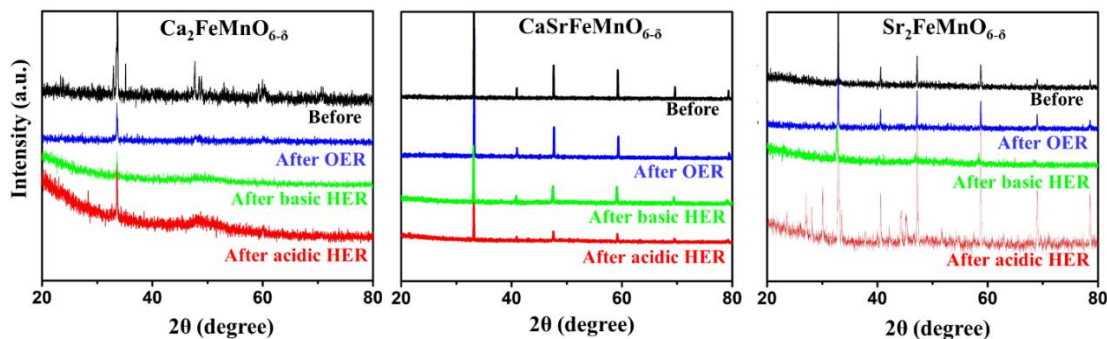
Figure 6.9: X-ray diffraction data before and after 100 cycles of electrocatalytic OER and HER.

To examine the stability of catalysts under OER and HER conditions, X-ray diffraction experiments were done before and after 100 cycles of electrocatalytic OER. Similar tests were done before and after 100 cycles of HER. These experiments show that the least electrocatalytically active material, $Ca_2FeMnO_{6-\delta}$, also has the least stability, and disintegrates under OER or HER conditions. The compound with better electrocatalytic

performance, $Sr_2FeMnO_{6-\delta}$, shows better stability than $Ca_2FeMnO_{6-\delta}$, but still decomposes under some electrocatalytic conditions. However, the best electrocatalyst, $CaSrFeMnO_{6-\delta}$, also shows the best stability, retaining its structural integrity in all experimental conditions in this work, as shown in Figure 6.9. Under these OER and HER conditions, the vacancy-ordered structure of $Ca_2FeMnO_{6-\delta}$ can not be retained, whereas the disordered structure of $Sr_2FeMnO_{6-\delta}$ and $CaSrFeMnO_{6-\delta}$ are more stable. Among $Sr_2FeMnO_{6-\delta}$ and $CaSrFeMnO_{6-\delta}$, the latter has better stability due to the synergetic effect of Ca/Sr. As mentioned before, bond distances in $CaSrFeMnO_{6-\delta}$ are shorter than those in $Sr_2FeMnO_{6-\delta}$, indicating the formation of stronger bonds in $CaSrFeMnO_{6-\delta}$, which may contribute to its stability. Similarly, the evolution of gas is also verified by gas chromatography as shown in Figure 6.10.
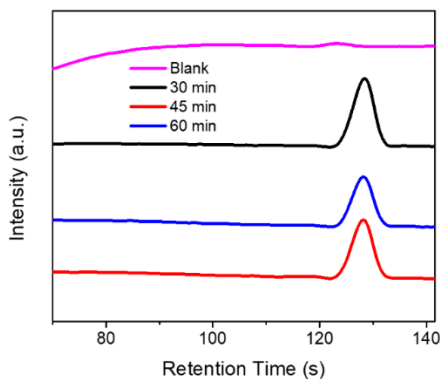
Figure 6.10: Gas chromatography data showing the oxygen peak for the OER experiment using $CaSrFeMnO_{6-\delta}$.

Considering that HER and OER are processes that involve the transfer of electrons, we speculated that the observed trend in electrocatalytic properties of $Ca_2FeMnO_{6-\delta}$, $CaSrFeMnO_{6-\delta}$ and $Sr_2FeMnO_{6-\delta}$ could be related to the electrical charge-transport properties. Therefore, we conducted a thorough investigation of the electrical charge-transport, as described below.

6.5 ELECTRICAL CONDUCTIVITY

The semiconducting charge-transport properties in some oxygen-deficient perovskites have been demonstrated before.[21, 249, 250] In materials where electronic conductivity is dominant, the semicircles in AC conductivity data can sometimes disappear, and only a straight line is observed.[251, 252] In these situations, the intercept of the line on the x-axis gives the total resistance,[251] and is expected to match the resistance from the DC measurements. This property was observed for the materials studied in this work. The resistance values (R) obtained from AC and DC measurements were used to calculate the conductivity (σ) using the equation[253] $\sigma = L/RA$, where L and A represent the voltage-probe spacing in 4-probe set-up and cross-sectional area of the rectangular sample, respectively. The electrical conductivity of $CaSrFeMnO_{6-\delta}$ (4.31×10^{-1} Scm^{-1} at 25 °C and 122×10^2 Scm^{-1} at 800 °C) was found to be 1-2 orders of magnitude greater than those of $Sr_2FeMnO_{6-\delta}$ (2.07×10^{-2} Scm^{-1} at 25 °C and 5.40 Scm^{-1} at 800 °C) and $Ca_2FeMnO_{6-\delta}$, (2.59×10^{-3} Scm^{-1} at 25 °C and 3.68 Scm^{-1} at 800 °C), as shown in Figure 6.11. The applied potential in these measurements was 10 mV. It should be recognized that electrical conductivity is potential-dependent, and its absolute value can vary depending on the potential. Nevertheless, the important observation here is the systematic trend in electrical conductivity of the three materials, $Ca_2FeMnO_{6-\delta}$, $CaSrFeMnO_{6-\delta}$ and $Sr_2FeMnO_{6-\delta}$.

This remarkable difference can arise from structural differences. In perovskite-based oxides, transition metals with variable oxidation states, such as Fe and Mn, are responsible for electronic conductivity. Electron hopping takes place through the M–O–M bond system,[254, 255] where M represents the transition metal. The electronic conductivity depends on various factors such as the M–O–M bond angle,[25, 256] which appears to be a

dominant structural parameter.[27] As the M–O–M bond angle becomes larger and gets closer to 180°, the M 3d and O 2p orbitals become more axially aligned, leading to better overlap and enhanced conductivity.[257] Given the corner-sharing connectivity of both tetrahedra and octahedra in $Ca_2FeMnO_{6-\delta}$, the bond angles in this compound are highly distorted, and can be as small as ~130°, which can impede the orbital overlap, and electrical conductivity. The bond angles in $Sr_2FeMnO_{6-\delta}$ and $CaSrFeMnO_{6-\delta}$ are much larger, 180°. Therefore, better orbital overlap is expected. However, the (FeMn)–O bond distances in $CaSrFeMnO_{6-\delta}$, 1.9062(1) Å, are shorter than those in $Sr_2FeMnO_{6-\delta}$, 1.92526(7) Å, which can enhance the overlap of M 3d and O 2p orbitals,[25, 256] leading to greater conductivity. The effect of bond distance has been previously observed for other perovskite oxides.[25, 256] Furthermore, the concentration of defects in $CaSrFeMnO_{6-\delta}$, $\delta = 0.57$, is greater than that of $Sr_2FeMnO_{6-\delta}$, $\delta = 0.22$. This can be another reason for the higher conductivity of $CaSrFeMnO_{6-\delta}$. A similar effect, namely variation of the defect-concentration, was recently reported for another series of perovskite-based oxides.[12]

The temperature-dependent conductivity of these materials was also studied in a wide temperature-range, from 25 – 800 °C (Figure 6.11a). These data can be used to calculate the activation energy using Arrhenius equation for thermally activated conductivity,[176, 258, 259]

$$\sigma T = \sigma^o e^{\frac{-E_a}{KT}} \quad\quad\quad (6.2)$$

where σ^o is a preexponential factor and a characteristic of the material. E_a, K, and T are the activation energy for the electrical conductivity, Boltzmann constant, and absolute temperature, respectively.

Table 6.1: A comparison of properties of the three compounds.

	$Ca_2FeMnO_{6-\delta}$	$CaSrFeMnO_{6-\delta}$	$Sr_2FeMnO_{6-\delta}$
Porosity	Highest	Lowest	Intermediate
HER Overpotential	Highest	Lowest	Intermediate
OER Overpotential	Highest	Lowest	Intermediate
Electrical Conductivity	Highest	Lowest	Intermediate
ECSA	Lowest	Highest	Intermediate
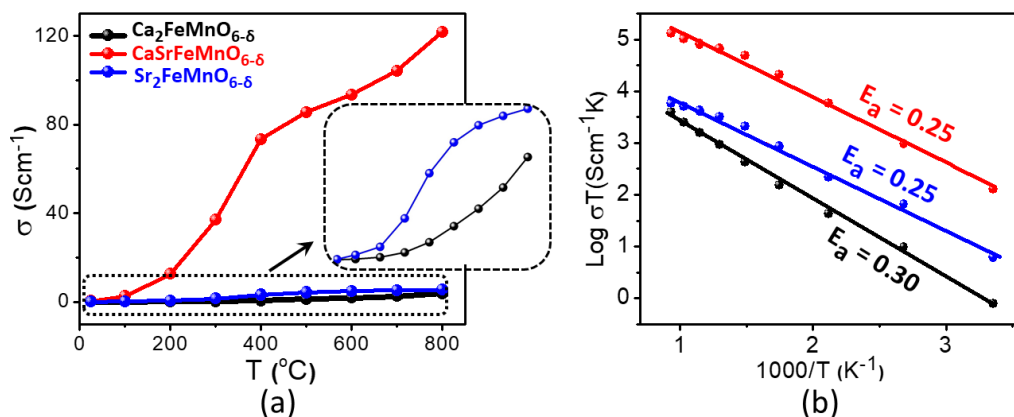
Figure 6.11: (a) Temperature-dependent electrical conductivity of $Ca_2FeMnO_{6-\delta}$ (black), $CaSrFeMnO_{6-\delta}$ (red) and $Sr_2MnO_{6-\delta}$ (blue). (b) Arrhenius plots and activation energies. In this series, $CaSrFeMnO_{6-\delta}$ shows the highest conductivity in the entire range of 25 – 800 °C.

The activation energy (E_a) can be calculated from the slope of the line of best fit in the log σT vs. 1000/T plot, as shown in Figure 6.11b. All compounds show an increase in conductivity as a function of temperature, indicative of their semiconducting nature. As temperature rises, there is an increase in the mobility of charge-carriers, which leads to the increase in conductivity. The relation between conductivity and the mobility of charge-carriers for temperature-activated conductivity in semiconductors can be represented as[260]

$\sigma = $ neμ, where σ, n, e, and μ are the conductivity, concentration of charge-carriers, charge of the electron, and mobility of the charge-carriers, respectively. As shown in Figure 6.11a, the superior conductivity of $CaSrFeMnO_{6-\delta}$ persists in the entire temperature-range. The trend in electrical charge transport, shown in Figure 6.11, is the same as the trend in HER and OER activity. As discussed above, charge-transport is in turn controlled by compositional and structural characteristics of materials. Table 6.1 shows a comparison of properties of the three compounds.

The effect of electrical conductivity on electrocatalytic activity is demonstrated by other researchers as well.[261-265] For example, the effect of conductive substrates on the OER activity of an oxyhydroxide has been shown,[264] where the formation of conductive gold oxide on the surface of gold substrate is proposed to result in better OER activity compared with platinum substrate that does not form a conductive oxide.[264] However, gold and platinum are not commonly used as substrates in electrocatalytic OER or HER. Another study on the essential role of electrical conductivity in electrocatalysis demonstrates that the improvement of charge-transport upon nanostructuring of an insulating material results in a significant enhancement of OER activity.[265] This is because nanostructuring enables tunneling mechanism, resulting in an improved charge-transport, leading to enhanced OER.[265]

6.6 CONCLUSION

The extraordinary combination of properties observed in above materials, namely their ability to act as bifunctional electrocatalysts for both OER and HER, and the capability to catalyze HER in both acidic and basic media, is unprecedented. The structure-

property relationships demonstrated by these materials is notable, where the disparity in structural properties leads to significant variations in electrical charge-transport and electrocatalytic activity. The structural properties are the underlying basis for the catalytic properties of the best catalyst in the series, $CaSrFeMnO_{6-\delta}$, which not only catalyzes both HER and OER, but also shows superior catalytic performance to the state-of-the-art precious-metal catalysts.

CHAPTER 7

BIFUNCTIONAL WATER-SPLITTING ELECTROCATALYSIS ACHIEVED BY

DEFECT-ORDER IN $LAA_2FE_3O_8$ (A = Ca, Sr)

In this chapter, we demonstrate the realization of electrocatalytic properties for hydrogen and oxygen evolution reactions in perovskite oxides through creation of structural order in materials with formulae $LaSr_2Fe_3O_8$ (disordered) and $LaCa_2Fe_3O_8$ (ordered). These compounds are derived from the oxygen-deficient perovskite $ABO_{3-\delta}$, where $\delta = 1/3$. Therefore, the general formula can be represented as $La_{1/3}A_{2/3}FeO_{3-1/3}$ or $LaA_2Fe_3O_8$ (A=Ca, Sr).

7.1 DFT CALCULATIONS

We employ ab initio calculations performed within the density functional theory (DFT) at the level of the spin polarized generalized gradient approximation (SGGA) and the Perdew-Burke-Ernzerhof (PBE)[266] level of approximation augmented by including Hubbard-U corrections[267] based on Dudarev's approach[268] as implemented in the Vienna Ab-initio Simulation Package (VASP)[269-271]. The projected augmented wave (PAW) potential[270, 271] is used to describe the core electron.

The Hubbard-U parameter is applied as a many-body correction to overcome the underestimation of electronic correlation due to the approximate nature of the exchange-

correlation functionals in the traditional single particle Kohn-Sham DFT. It partially corrects the electronic self-interaction error inherent in DFT and leads to better gap estimations. The U parameters are obtained by fitting our results so as to reproduce the experimental band gaps and, if available, additional experimental spectral properties[267, 272]. We have used this formalism successfully in the treatment of a wide range of materials recently[273, 274]. The Hubbard parameters are used only for the d-orbitals of the transition metal (TM) atoms. This is set to $U=U_{d,TM}=5.5$ eV.[275] We also tested other U values, 4.0 eV,[276] 4.5 eV,[277] 5.0 eV,[278] and 7.5 eV, all resulting in similar band structures. It is worth noting that the standard DFT theory fails when applied to multi-metal oxide perovskites by giving incorrect total energies and band gap values. This is because these materials exhibit strong electronic correlations. The use of DFT/GGA+U, however, has been shown to work very well for ternary alloys of the type ABO_3 by producing correct total energies and band gap values.[279]

We considered $LaSr_2Fe_3O_8$ and $LaCa_2Fe_3O_8$ systems simulated by supercells consisting of 84 atoms for both systems, periodically repeated along x, y and z-directions. For $LaCa_2Fe_3O_8$, which has an ordered structure, the atomic positions were taken from Table S2 and the unit cell was expanded into a supercell with 84 atoms. On the other hand, the supercell for $LaSr_2Fe_3O_8$ was obtained by extending the $LaFeO_3$ unit cell. The $LaFeO_3$ skeleton was expanded by $3\times3\times2$ to initially create a 90 atom cell. We then used a computer generated random substitution algorithm for creating 6 oxygen vacancies and random substitutional placings of 12 Sr atoms on the expanded unit cell to create a disordered 84 atom supercell. Several of these structures were fully optimized without any symmetry constraints and the structure with the lowest energy was chosen for the band structure and

DOS calculations. The plane wave cutoff was 500 eV. A Monkhorst- Pack 2×3×3 k-point mesh was used in all our calculations. All structures were subjected to full symmetry unconstrained geometric relaxation of all atom positions and cell parameters. We note that the relaxation of the cell volume is extremely critical for an accurate estimation of the ground state.

7.3 CRYSTAL STRUCTURE

Following our recent work on oxide electrocatalysts,[81, 86, 193, 280-282] we now demonstrate the realization of these properties in perovskite oxides through creation of structural order in materials with formulae $LaSr_2Fe_3O_8$ (disordered) and $LaCa_2Fe_3O_8$ (ordered). These compounds are derived from the oxygen-deficient perovskite $ABO_{3-\delta}$, where $\delta = 1/3$. Therefore, the general formula can be represented as $La_{1/3}A_{2/3}FeO_{3-1/3}$ or $LaA_2Fe_3O_8$ (A=Ca,Sr). In the disordered compound, $LaSr_2Fe_3O_8$, the distribution of oxygen-vacancies is random and the average structure resembles that of a typical perovskite (Figure 7.1a), but with partial occupancy on oxygen sites (Table 7.1). On the other hand, $LaCa_2Fe_3O_8$ has a structure where the oxygen-vacancies are distributed in an ordered fashion. Indeed, the level of oxygen-deficiency found in these compounds, i.e., $\delta = 1/3$, has the potential to create an ordered arrangement if the oxygen-vacancies only appear in every third layer of the perovskite structure, converting the octahedral coordination into tetrahedral (Figure 7.1b). Such arrangement also results in two different coordination numbers for the A-sites, CN = 8 and CN = 12. We postulated that this type of ordering may be achieved through incorporation of a smaller A-site cation, Ca^{2+}, which can comfortably reside in the 8-coordinated site, leaving the 12-coordnated site to La^{3+}.

Note that the stoichiometric ratio of CN = 12 to CN = 8 sites is 1:2, hence the composition $LaCa_2Fe_3O_8$, which can accommodate the targeted ordering scheme. Figure 7.2 and Table 7.1 and 7.3 show the Rietveld refinement results, consistent with an earlier structural report.[283] Iodometric titrations were also used to confirm the oxygen stoichiometry.
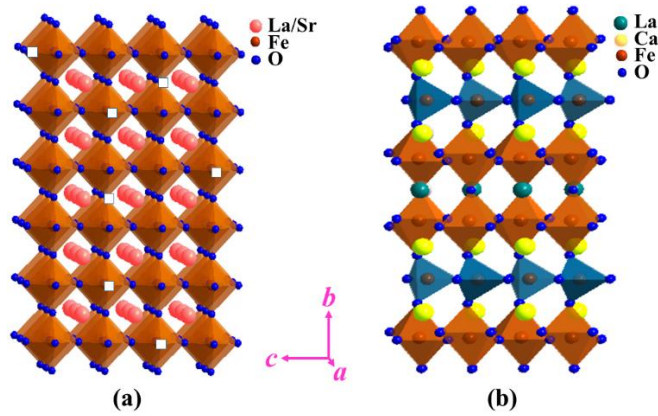
Figure 7.1: (a) Perovskite structure with random vacancy distribution for $LaSr_2Fe_3O_8$. White squares are a schematic representation of the random distribution of oxygen-vacancies. (b) Ordered structure of $LaCa_2Fe_3O_8$, with vacancies only appearing in every third layer, hence creating FeO_4 tetrahedral coordination in every third layer.
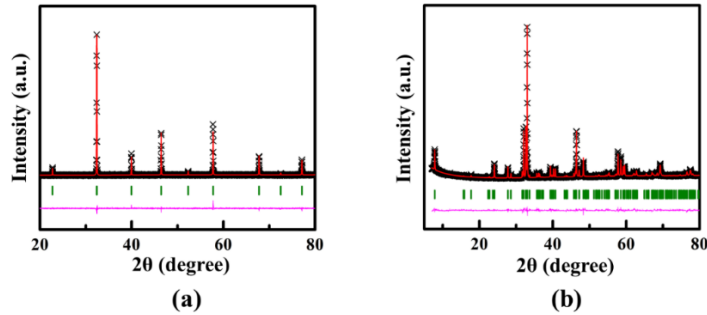
Figure 7.2: Rietveld refinement profiles for powder X-ray diffraction data of (a) $LaSr_2Fe_3O_8$ and (b) $LaCa_2Fe_3O_8$.

Table 7.1: Refined structural parameters of $LaSr_2Fe_3O_8$ at room temperature by using powder X-ray diffraction data[a]

Element	x	y	z	Occupancy	Uiso	Multiplicity
La1	0.5	0.5	0.5	0.333	0.0034(9)	1
Sr1	0.5	0.5	0.5	0.666	0.0034(9)	1
Fe1	0	0	0	1	0.003(1)	1
O1	0.5	0	0	0.89	0.021(3)	3

[a] Space group: *Pm-3m*, a = 3.9087(2) Å, R_p = 0.0593, wR_p = 0.0799, and χ^2 = 1.201%.

Table 7.2: Refined structural parameters of $LaCa_2Fe_3O_8$ at room temperature by using powder X-ray diffraction data[a]

Element	x	y	z	Occupancy	Uiso	Multiplicity
La1	0.0	0.259(1)	0.809(2)	0.685(5)	0.012(2)	2
Ca1	0.0	0.259(1)	0.809(2)	0.365(5)	0.012(2)	2
La2	0.3170(4)	0.272(2)	0.786(4)	0.155(5)	0.054(4)	4
Ca2	0.3170(4)	0.272(2)	0.786(4)	0.845(5)	0.054(4)	4
Fe1	0.1731(4)	0.238(2)	0.331(3)	1.0	0.026(3)	4
Fe2	0.5	0.190(2)	0.25	1.0	0.015(4)	2
O1	0.2045(15)	-0.031(5)	0.122(5)	1.0	0.017(4)	4
O2	0.1617(17)	0.545(5)	0.045(6)	1.0	0.017(4)	4
O3	0.5	0.099(6)	0.950(6)	1.0	0.017(4)	2
O4	0.0	0.185(5)	0.309(9)	1.0	0.017(4)	2
O5	0.3649(20)	0.324(3)	0.349(5)	1.0	0.017(4)	4

[a]Space group: $Pmc2_1$, a = 11.2834(2) Å, b = 5.58409(8) Å, c = 5.48297(8) Å, R_p = 0.0228, wR_p = 0.0504, and χ^2 = 2.01%.

7.3 ACTIVITY TOWARD HYDROGEN AND OXYGEN EVOLUTION REACTIONS

The transformation of the crystal structure from disordered to ordered results in remarkable changes to electrocatalytic properties. There is a significant enhancement of the HER activity from $LaSr_2Fe_3O_8$ (disordered) to $LaCa_2Fe_3O_8$ (ordered), as shown in Figure 7.3. The latter compound shows overpotential of η_{10} = 0.4 V in 1 M KOH. This is close to the values reported for some other oxygen-deficient perovskites, such as $Ba_{0.5}Sr_{0.5}Co_{0.8}Fe_{0.2}O_{3-\delta}$[284] and $Ba_{0.95}Co_{0.4}Fe_{0.4}Zr_{0.1}Y_{0.1}O_{3-\delta}$.[284] It is also significant that $LaCa_2Fe_3O_8$ is able to catalyze the HER in bulk form, without any need for composite formation or nanofabrication. Even more significant is the structure-property relationship, where the electrocatalytic activity is enhanced as a function of structural transformation from disorder to order. We note that this catalyst also shows better HER activity than the non-defect oxide $LaFeO_3$, as shown in Figure 7.4. $LaCa_2Fe_3O_8$ is also very stable, as demonstrated by chronopotentiometry data presented in the inset of Figure 7.3a. The Tafel slope, i.e., the slope of η versus log j, based on the Tafel equation, η = a + b log j, is

commonly used to evaluate the HER kinetics.[184, 285] Smaller Tafel slopes indicate faster reactions. The Tafel plots in Figure 7.3b show that the reaction kinetics are also enhanced as a function of structural order, with $LaCa_2Fe_3O_8$ showing a smaller Tafel slope.
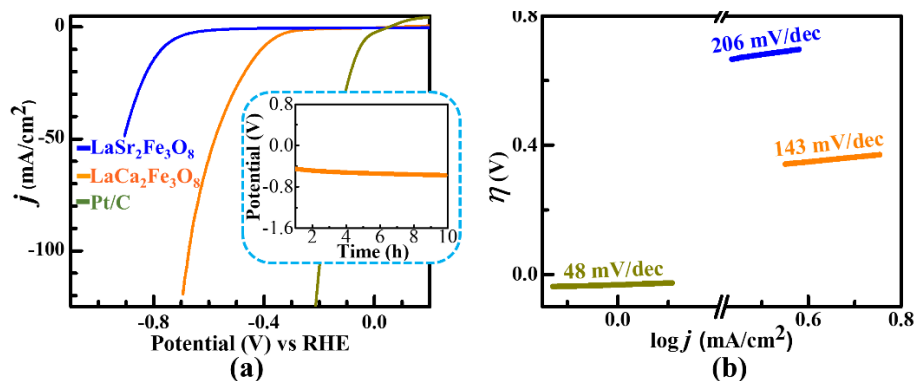
Figure 7.3: (a) Polarization curves showing the HER activity in 1 M KOH. The inset shows the chronopotentiometry data for $LaCa_2Fe_3O_8$. (b) Tafel plots and Tafel slopes.
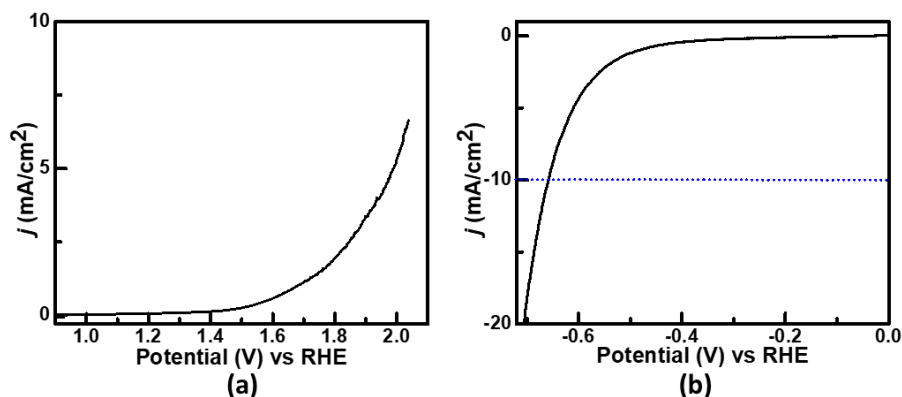
Figure 7.4: (a) OER and (b) HER polarization curves of $LaFeO_3$, indicating low activity of this material.

Remarkably, these catalysts also show electrocatalytic activity for the other half-reaction of water-splitting, namely OER (Figure 7.5). The structure-property relationships are on full display, where the transition from disorder to order leads to a significant enhancement in OER activity from $LaSr_2Fe_3O_8$ (disordered) to $LaCa_2Fe_3O_8$ (ordered). The latter material shows an outstanding activity for OER, on par with the state-of-the-art precious metal electrocatalyst, RuO_2. It shows an overpotential of $\eta_{10} = 0.36$ V in 1M KOH,

114

on par with that of RuO_2 (Figure 7.5a).[286-288] It is also highly stable, as shown by chronopotentiometry experiments presented in the inset of Figure 7.5a. In addition, X-ray diffraction and X-ray photoelectron spectroscopy before and after electrocatalytic reaction (Figures 7.6 and 7.7) indicate the structural stability of this catalyst. The kinetics of the OER was evaluated using the Tafel plot,[289, 290] indicating the enhancement of kinetics, where $LaCa_2Fe_3O_8$ shows a smaller Tafel slope, consistent with faster charge transport during OER.[193, 245]
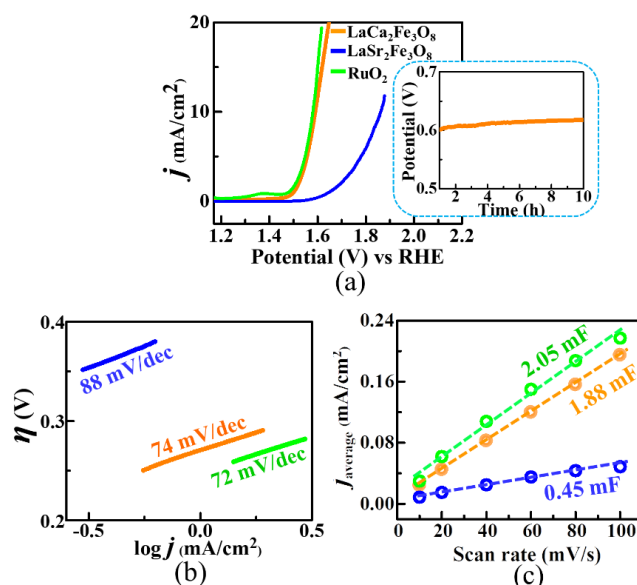
Figure 7.5: (a) Polarization curves showing the OER activities in 1M KOH. Inset shows chronopotentiometry for $LaCa_2Fe_3O_8$. (b) Tafel plots. (c) Double layer capacitance values, C_{dl}, obtained from CVs in non-Faradaic region.

The electrochemically active surface areas (ECSA) were also evaluated by examining the electrochemical double-layer capacitance (C_{dl}) in the non-faradaic region of the voltammograms (Figure 7.8).[70, 291] In this region, the electrode reactions are considered negligible and the current originates from electrical double layer charge and discharge.[291] ECSA and C_{dl} are related to each other by ECSA = C_{dl} / C_s,[193, 292] where C_s is the specific capacitance. Given this direct relationship, the C_{dl} is typically considered to be

115

representative of the magnitude of ECSA.[185, 193] The value of C_{dl} is calculated from the equation[293, 294] $C_{dl} = \Delta j / v$, where Δj is the absolute value of the difference between the anodic (j_{anodic}) and cathodic ($j_{cathodic}$) current densities from the flat regions of the CV in the non-faradic region and v is the scan rate. The C_{dl} value is equivalent to half of the slope of Δj versus v plot.[185, 294] Alternatively, some reports have used $j_{average}$ versus v, where $j_{average}$ is the average of the absolute values of j_{anodic} and $j_{cathodic}$. In that case, C_{dl} is simply equal to the slope of the $j_{average}$ versus v plot.[295, 296] Figure 7.5c shows the C_{dl} values obtained using $j_{average}$ at middle potential[184] of the non-Faradaic CVs. The C_{dl} value for $LaCa_2Fe_3O_8$ is similar to that of RuO_2, and significantly larger than that of $LaSr_2Fe_3O_8$, consistent with high electrocatalytic activity of $LaCa_2Fe_3O_8$.
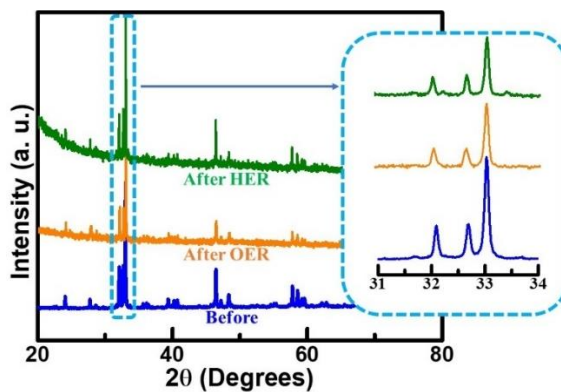
Figure 7.6: X-ray diffraction data before and after 1000 cycles of OER and HER in 1M KOH for $LaCa_2Fe_3O_8$.
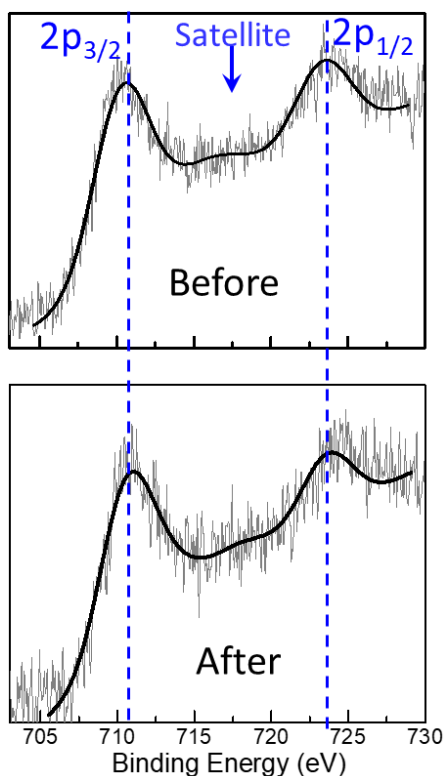
Figure 7.7: X-ray photoelectron spectroscopy data for $LaCa_2Fe_3O_8$, indicating similar binding energies for Fe before and after 1000 cycles of OER.
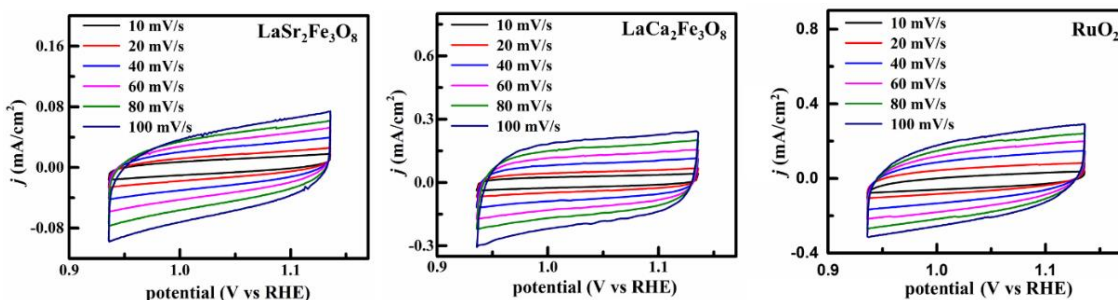
Figure 7.8: Cyclic voltammograms in non-Faradaic region of OER data to obtain double layer capacitance, C_{dl}, in 1M KOH.

The novel and intriguing nature of the observed trends in electrocatalytic activity as a function of structural order prompted us to employ density-functional-theory (DFT) to examine the changes in electronic structure due to the ordering (Figure 7.9). The electronic band structure for $LaSr_2Fe_3O_8$ indicates the crossing of a few spin-up bands through the Fermi level, implying a half-metallic character. On the other hand, the band structure for

LaCa$_2$Fe$_3$O$_8$ shows a semiconducting behavior with a small band gap and no bands crossing the Fermi level.
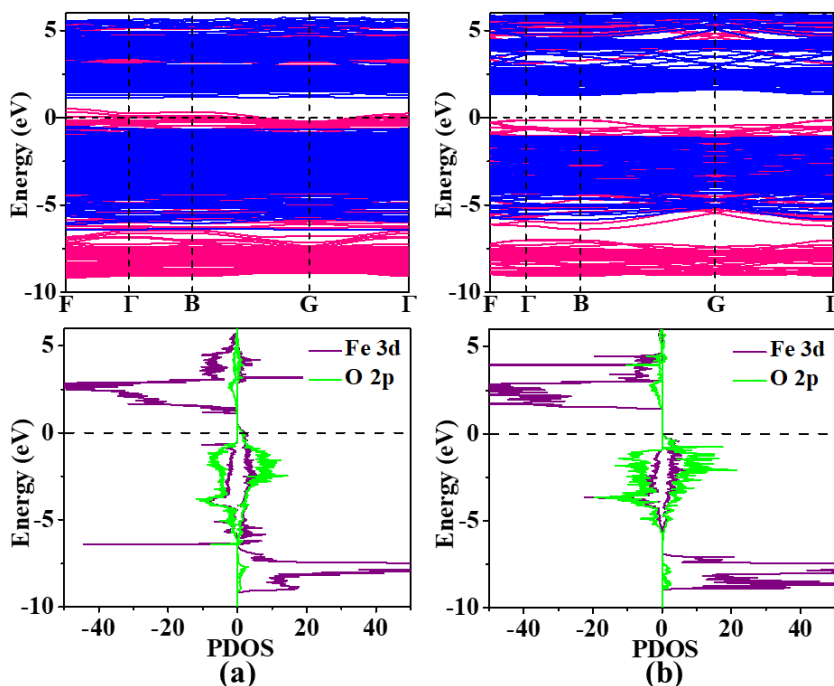
Figure 7.9: DFT calculated band structure and PDOS for (a) LaSr$_2$Fe$_3$O$_8$ and (b) LaCa$_2$Fe$_3$O$_8$. The energy of the Fermi-level is set to zero. In band structures, red and blue lines denote contributions from spin-up and spin-down electrons, respectively.

Several OER descriptors, such as proximity of the transition metal d and oxygen p band centers[297] and hybridization between them, [297, 298] have been proposed. The degree of hybridization between Fe d and O p bands is indicated by the overlap area of the DOS of these bands,[298] normalized based on all participating orbitals in the supercell. For LaSr$_2$Fe$_3$O$_8$, the Fe d and O p overlap areas are 0.666 (spin up) and 0.288 (spin down). The corresponding values for LaCa$_2$Fe$_3$O$_8$ are 0.562 (spin up) and 0.295 (spin down). Some researchers have focused on the proximity of the d-band center to the Fermi level and have correlated this parameter with enhanced electrocatalytic activity due to enhanced bonding with adsorbates.[299, 300] The DOS shows that the average d-band center (for both spin up and

down) is -5.285 eV for $LaSr_2Fe_3O_8$ and -5.191 eV for $LaCa_2Fe_3O_8$. These differences are a result of the structural differences between the two systems. The coordination number of metal atoms and the directions of the bonds will be different between the disordered and ordered systems. Similar effects on catalytic activity have been previously observed in other contexts, such as CO oxidation.[301] Furthermore, it is evident from the partial density of states (PDOS) in Figure 7.9 that unlike O p-bands that are similar in both disordered $LaSr_2Fe_3O_8$ and ordered $LaCa_2Fe_3O_8$, there is a difference in the localization of Fe d-bands, which are more localized in $LaCa_2Fe_3O_8$.

7.4 CONCLUSIONS

In summary, this work demonstrates the rational design of a highly active electrocatalyst for water-splitting by creation of structural order. The transition from disorder to order leads to the transformation of the electrocatalytic properties, where the activity of the ordered system rivals that of the state-of-the-art precious metal electrocatalysts. We expect this structure-property principle to be applicable to a wide range of oxide materials given that structural order also affects the electronic structure. Currently, we are exploring several other series of oxygen-deficient perovskites to show the relationship between structural order and electrocatalytic activity.

CHAPTER 8

ELECTROCATALYTIC ACTIVITY AND STRUCTURAL TRANSFORMATION OF

$Ca_2Sr_2Mn_2MO_{10-\delta}$ (M = Fe, Co)

In this chapter, we discuss the enhancement of electrocatalytic activity for both OER and HER through replacing iron in the Ruddlesden-Popper oxide $Ca_2Sr_2Mn_2FeO_{10-\delta}$ by cobalt to form $Ca_2Sr_2Mn_2CoO_{10-\delta}$, which has a 1-dimensional structure, consisting of infinite chains of face-sharing octahedra and trigonal prisms. While the magnetic properties of the latter material have been studied,[302] the electrocatalytic properties for water-splitting and the major impact of compositional and structural transformation on electrocatalytic activity of these materials have not been investigated.

8.1 CRYSTAL STRUCTURE

$Ca_2Sr_2Mn_2FeO_{10-\delta}$, forms the so-called Ruddlesden-Popper type structure with tetragonal $I4/mmm$ space group, resembling $Ca_4Mn_2FeO_{10-\delta}$ and $Sr_4Mn_2FeO_{10-\delta}$.[303] Figure 8.1 shows the Rietveld refinement profile and crystal structure of $Ca_2Sr_2Mn_2FeO_{10-\delta}$, based on the same model as $Sr_4Mn_2FeO_{10-\delta}$.[303] The refined structural parameters are listed in Table 8.1. Its structure comprises corner-sharing units of $(Fe/Mn)O_6$ octahedra that form triple-layered stacks. The alkaline-earth metals Ca/Sr reside in spaces within and between the octahedral stacks. Considering the occurrence of oxygen-deficiencies in this compound, as indicated by iodometric titration and consistent with the presence of trivalent

---

The work described in this chapter was published in Ionics, 2021, 28, 397 - 406.

iron, some of the oxygen sites in the structure should be only partially occupied. Previous studies on similar materials using neutron diffraction[303] have indicated that vacancies appear on oxygen sites located within the stacks, namely O1 and O4 site in Figure 8.1b.
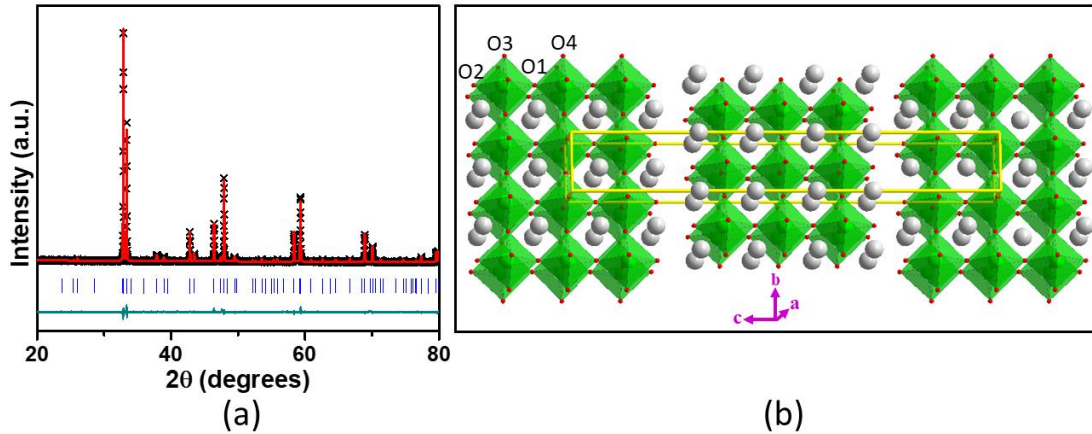
Figure 8.1: (a) Rietveld refinement profile for powder X-ray diffraction data of $Ca_2Sr_2Mn_2FeO_{10-\delta}$. Black crosses, red line, vertical tick marks and lower green line represent experimental data, the model, peak positions, and difference plot, respectively. **(b)** Crystal structure of $Ca_2Sr_2Mn_2FeO_{10-\delta}$, showing $(Fe/Mn)O_6$ octahedral units in green. Grey spheres represent Ca/Sr. Yellow lines show the unit cell.

Table 8.1: Refined structural parameters for $Ca_2Sr_2Mn_2FeO_{10-\delta}$ using powder X-ray diffraction data. Space group *I4/mmm,* a = 3.79541(2) Å, b = 3.79541(2) Å, c = 27.3699(2) Å, V = 394.267(7) Å^3, Rp=0.0231, wRp= 0.0304, χ^2 = 1.865.

Elements	x	y	z	Multiplicity	Occupancy	Uiso
Ca1/Sr1	0	0	0.5711(1)	4	0.5/0.5	0.012(1)
Ca2/Sr2	0	0	0.7026(1)	4	0.5/0.5	0.029(2)
Mn1/Fe1	0	0	0	2	0.6667/0.3333	0.023(4)
Mn2/Fe2	0	0	0.1420(2)	4	0.6667/0.3333	0.020(1)
O1	0	0	0.0696(7)	4	0.8750	0.035(1)
O2	0	0	0.2112(4)	4	1	0.035(1)
O3	0	0.5	0.6399(4)	8	1	0.035(1)
O4	0	0.5	0.5	4	0.8750	0.035(1)

$Ca_2Sr_2Mn_2CoO_{10-\delta}$ forms a completely different structure, featuring 1-dimensioanl chains, consistent with a previous report.[302] Figure 8.2 shows the Rietveld refinement profile and crystal structure of $Ca_2Sr_2Mn_2CoO_{10-\delta}$, matching a previously reported model.[304] The refined structural parameters are listed in Table 8.2. The trigonal structure

of $Ca_2Sr_2Mn_2CoO_{10-\delta}$ with space group $P321$ consists of chains of face-sharing polyhedra running along the c-axis.[302] The chains comprise an ordered arrangement of CoO_6–MnO_6–MnO_6–CoO_6, where two MnO_6 units alternate with a single unit of CoO_6. The MnO_6 polyhedra form distorted trigonal prismatic and octahedral geometry, while the CoO_6 units form two types of trigonal prisms, one highly distorted and another close to the ideal geometry. The polyhedra in each chain are connected through face-sharing. The spaces between the one-dimensional chains are occupied by Ca and Sr.
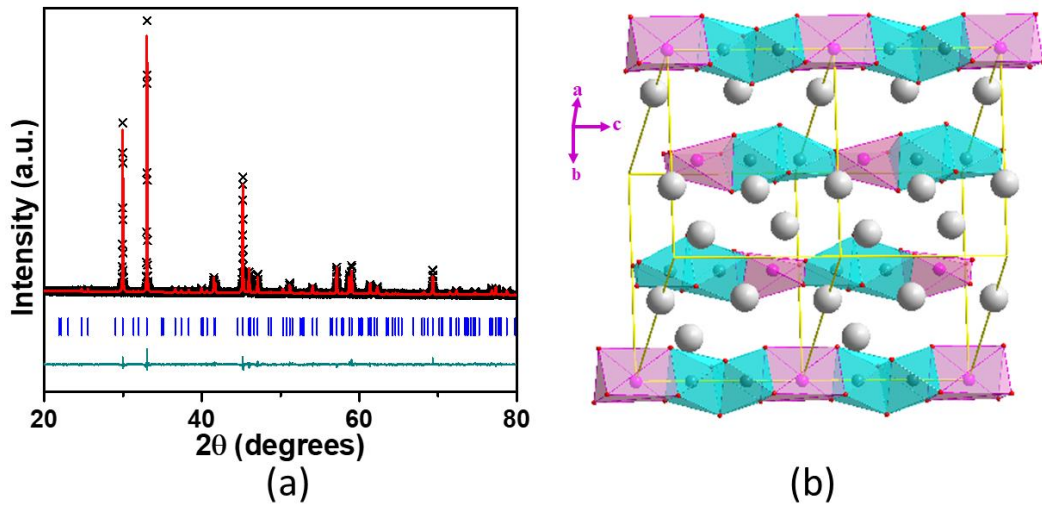
Figure 8.2: **(a)** Rietveld refinement profile for powder X-ray diffraction data of $Ca_2Sr_2Mn_2CoO_{10-\delta}$. Black crosses, red line, vertical tick marks and lower green line represent experimental data, the model, peak positions, and difference plot, respectively. **(b)** Crystal structure of $Ca_2Sr_2Mn_2CoO_{10-\delta}$, showing the polyhedra for Mn (turquoise) and Co (purple). Grey spheres represent Ca/Sr. Some of the polyhedral chains and Ca/Sr atoms are omitted for clarity. Yellow lines show the unit cell.

Table 8.2: Refined structural parameters for $Ca_2Sr_2Mn_2CoO_{10-\delta}$ using powder X-ray diffraction data. Space group $P321$, a = 9.3838(4)Å, b = 9.3838(4))Å, c = 7.7138(3)Å, V = 588.25(7)Å^3, Rp=0.0227, wRp= 0.0306, χ^2 = 2.806

Elements	x	y	z	Multiplicity	Occupancy	Uiso
Ca1/Sr1	0.020(1)	0.682(1)	0.253(2)	3	0.5/0.5	0.019(3)
Ca2/Sr2	0.341(2)	0	0.5	3	0.5/0.5	0.030(5)
Ca3/Sr3	0.3267(3)	0	0	6	0.5/0.5	0.026(5)
Mn1	0	0	0.176(3)	2	1	0.037(2)

Mn2	0.3333	0.6666	0.097(2)	2	1	0.037(2)
Mn3	0.3333	0.6666	0.356(3)	2	1	0.037(2)
Co1	0	0	0.5	2	1	0.028(3)
Co2	0.3333	0.6666	0.749(3)	1	1	0.028(3)
O1	0.499(6)	0.664(8)	0.213(5)	6	1	0.048(3)
O2	0.666(6)	0.201(4)	0.468(7)	6	1	0.048(3)
O3	0.833(8)	0	0	3	1	0.048(3)
O4	0.666(6)	0.173(6)	0.039(7)	6	1	0.048(3)
O5	0.001(6)	0.158(6)	0.273(8)	6	1	0.048(3)

Iodometric titrations show the oxygen stoichiometry of ~9 for $Ca_2Sr_2Mn_2CoO_{10-\delta}$, which implies $\delta = 1$, consistent with a previous report.[302] For $Ca_2Sr_2Mn_2FeO_{10-\delta}$, the oxygen stoichiometry was found to be ~9.5, which is nicely consistent with the replacement of Co^{2+} by Fe^{3+}. This is also consistent with the X-ray photoelectron spectroscopy data, shown in Figure 8.3.

The micro-structures of the two materials are studied by high resolution scanning electron microscopy (SEM). Figure 8.4 shows the SEM images of sintered pellets of $Ca_2Sr_2Mn_2CoO_{10-\delta}$ and $Ca_2Sr_2Mn_2FeO_{10-\delta}$. The micrographs indicate smaller crystallites for $Ca_2Sr_2Mn_2FeO_{10-\delta}$. In addition, there appears to be a denser packing of crystallites in $Ca_2Sr_2Mn_2FeO_{9.5}$.

Overall, it is remarkable that the variation of transition metal from iron to cobalt transforms the structure from two-dimensional stacks in $Ca_2Sr_2Mn_2FeO_{10-\delta}$ to one-dimensional chains in $Ca_2Sr_2Mn_2CoO_{10-\delta}$. Importantly, this change has significant impact on electrocatalytic properties, as discussed below.
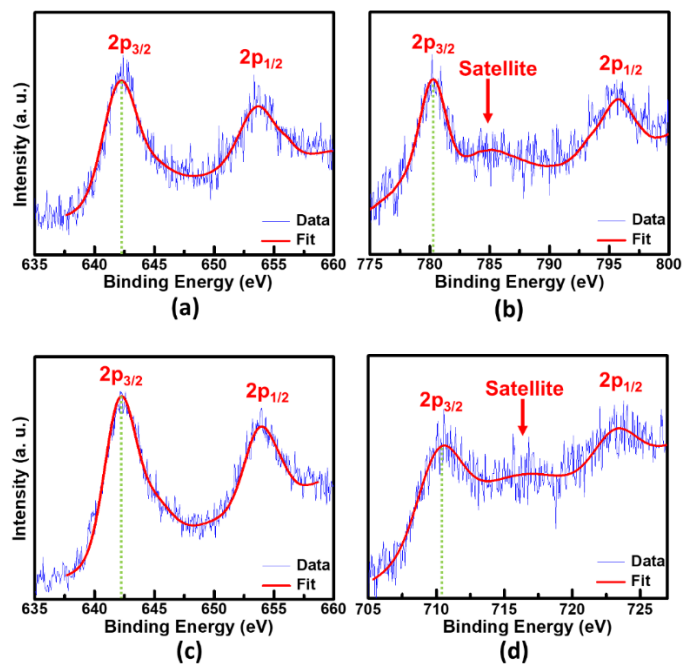
Figure 8.3: XPS spectra, consistent with iodometric titration results. (a) Mn spectrum for $Ca_2Sr_2Mn_2CoO_{10-\delta}$, indicating tetravalent manganese.[121, 305] (b) Co spectrum for $Ca_2Sr_2Mn_2CoO_{10-\delta}$. The pronounced satellite at ~785 eV signifies divalent cobalt.[85, 123] (c) Mn spectrum for $Ca_2Sr_2Mn_2FeO_{10-\delta}$, indicating tetravalent manganese.[121, 305] (d) Fe spectrum for $Ca_2Sr_2Mn_2FeO_{10-\delta}$. The binding energy of $2p_{3/2}$ peak and the satellite around ~717 eV indicate trivalent iron.[85, 121]
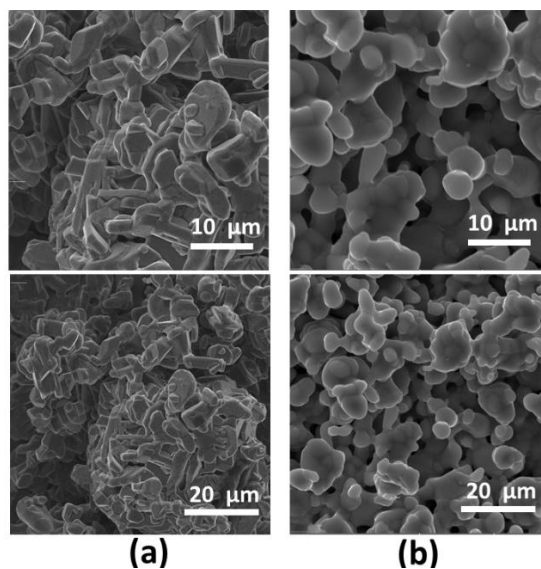
Figure 8.4: Scanning electron microscopy images of (a) $Ca_2Sr_2Mn_2FeO_{10-\delta}$ and (b) $Ca_2Sr_2Mn_2CoO_{10-\delta}$.

8.2 ELECTROCATALYTIC ACTIVITY FOR HER

Figure 5a shows the HER polarization curves of $Ca_2Sr_2Mn_2FeO_{10-\delta}$ and $Ca_2Sr_2Mn_2CoO_{10-\delta}$. Since electrocatalytic HER is commonly done in 1M KOH,[224, 306-308] the same condition was used here to provide direct comparison to other catalysts. The electrocatalytic activity toward HER during heterogeneous catalysis is frequently gauged by the onset potential and the overpotential at 10 mA/cm^2.[234, 309] The onset potential, where the HER begins (indicated by a rise in current) is almost 0.0 V versus RHE for the benchmark Pt/C (20 wt. % Pt) catalyst.[77, 183]

The onset potential values for $Ca_2Sr_2Mn_2FeO_{10-\delta}$ and $Ca_2Sr_2Mn_2CoO_{10-\delta}$ are ~ – 0.44 V and –0.34 V, respectively. These compounds show respective overpotential (η_{10}) values of –0.66 V and –0.45 V at –10 mA/cm^2 (Figure 5a). HER experiments were also attempted in acidic condition, 0.5 M H_2SO_4, giving overpotential of $\eta_{10} \approx 0.48$ V for $Ca_2Sr_2Mn_2CoO_{10-\delta}$, while the current response for $Ca_2Sr_2Mn_2FeO_{10-\delta}$ in this condition does not even reach 10 mA/cm^2. While oxide catalysts with better performance have been reported,[69, 81] the electrocatalytic activity of $Ca_2Sr_2Mn_2CoO_{10-\delta}$ is better than some of the previously reported catalysts with Ruddlesden-Popper type structure, as shown in Table 3. This catalyst is also very stable, as shown by chronopotentiometry data in the inset of Figure 5a.

Utilizing the Tafel equation, $\eta = a + b \log j$ (where η is overpotential and j is current density), the slope of the plot of η versus $\log j$, namely Tafel slope,[86, 292, 310] is determined to evaluate the kinetics of HER (Figure 8.5b). Faster HER process is marked by smaller value of the Tafel slope. As shown in Figure 8.5b, Tafel slopes for

$Ca_2Sr_2Mn_2FeO_{10-\delta}$ and $Ca_2Sr_2Mn_2CoO_{10-\delta}$ are determined to be 186 mV/dec and 154 mV/dec, respectively. A smaller Tafel slope for the latter compound indicates faster electron transfer processes, consistent with its enhanced HER activity.
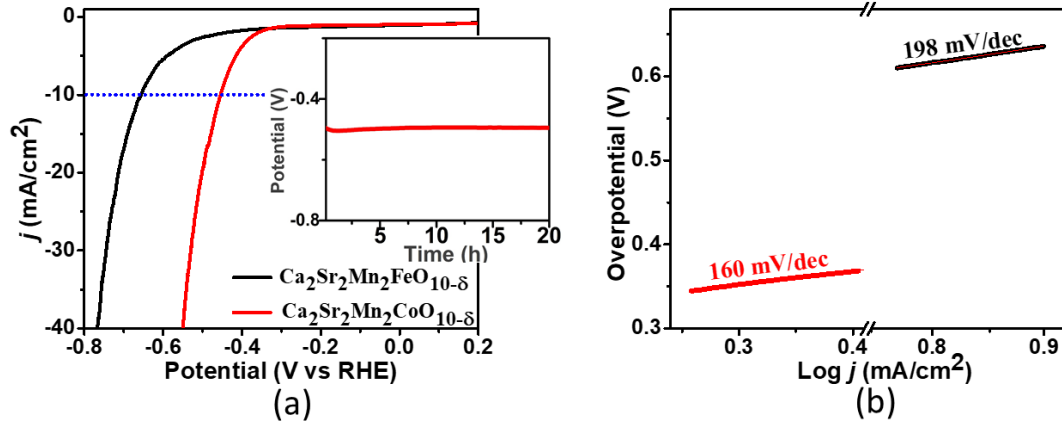
Figure 8.5: (a) HER polarization curves in 1 M KOH. The inset shows chronopotentimetry data, indicating the stability of $Ca_2Sr_2Mn_2CoO_{10-\delta}$. (b) Tafel plots and Tafel slopes for $Ca_2Sr_2Mn_2FeO_{10-\delta}$ (black) and $Ca_2Sr_2Mn_2CoO_{10-\delta}$ (red).

Table 8.3: Comparison of OER/HER overpotentials for some Ruddlesden-Popper oxides.

	OER η_{10} (mV)	HER η_{10} (mV)	Reference
$Ca_2Sr_2Mn_2CoO_{10-\delta}$	400 (0.1 M KOH)	-450 (1 M KOH)	This work
$Ca_2Sr_2Mn_2FeO_{10-\delta}$	510 (0.1 M KOH)	-660 (1 M KOH)	This work
$LaSr_3Fe_3O_{10-\delta}$	522 (0.1 M KOH)	-	[311]
$LaSr_3Co_2FeO_{10-\delta}$	475 (0.1 M KOH)	-	[311]
$LaSr_3Co_{1.5}Fe_{1.5}O_{10-\delta}$	388 (0.1 M KOH)	-	[312]
$SrLaCoO_{4-\delta}$	510 (0.1 M KOH)	-541 (1 M KOH)	[282]
$Sr_2LaCoMnO_7$	538 (0.1 M KOH)	-612 (0.5 M H_2SO_4)	[58]
$La_{0.5}Sr_{1.5}Ni_{0.7}Fe_{0.3}O_{4.04}$	360 (0.1 M KOH)	-	[313]
$Sr_3(Co_{0.8}Fe_{0.1}Nb_{0.1})_2O_{7-\delta}$	334 (0.1 M KOH)	-	[314]
$La_{1.9}Ca_{0.1}NiO_4$	>450 (0.1 M KOH)	-	[315]
Sr_2RuO_4	-	-61 (1 M KOH)	[316]

8.3 ELECTROCATALYTIC ACTIVITY FOR OER

The electrocatalytic activity of these materials toward OER was also investigated. Figure 8.6a shows the OER polarization curves for $Ca_2Sr_2Mn_2FeO_{10-\delta}$ and $Ca_2Sr_2Mn_2CoO_{10-\delta}$ in 0.1M KOH electrolyte, a condition that is commonly utilized for electrocatalytic OER.[281, 317, 318] The onset potentials, marked by an increase in current, are 1.50 V and 1.40 V for $Ca_2Sr_2Mn_2FeO_{10-\delta}$ and $Ca_2Sr_2Mn_2CoO_{10-\delta}$, respectively. The onset potential of the latter compound is better than that reported for the well-known perovskite oxide electrocatalyst, $Ba_{0.5}Sr_{0.5}Co_{0.8}Fe_{0.2}O_{6-\delta}$ (BSCF), (~1.5 V). [319, 320]

The overpotential (η_{10}), beyond the ideal 1.23 V, at 10 mAcm^{-2} is another parameter to evaluate the OER performance.[321, 322] The overpotential (η_{10}) values, obtained from η_{10} = E_{RHE} − 1.23 V, are 0.51 V and 0.40 V for $Ca_2Sr_2Mn_2FeO_{10-\delta}$ and $Ca_2Sr_2Mn_2CoO_{10-\delta}$, respectively (Figure 8.6a). For comparison, the η_{10} of the latter material is better than that of BSCF (~0.50 V) [183, 290] and several other oxides with Ruddlesden-Popper structure, as shown in Table 8.3.

The OER kinetics is again evaluated using the Tafel equation $\eta = a + b \log j$,[193, 310] where η is the overpotential and j is the current density. This provides information on electron and mass transport of an electrocatalyst during the OER.[246] The Tafel plot, η vs $\log j$,[81, 292] is shown in Figure 8.6b, indicating Tafel slopes of 128 mV/dec and 86 mV/dec for $Ca_2Sr_2Mn_2FeO_{10-\delta}$, and $Ca_2Sr_2Mn_2CoO_{10-\delta}$, respectively. This is consistent with the enhanced OER activity of the latter material. In addition, this catalyst is very stable under OER conditions, as shown by the chronopotentiometry data in the inset of Figure 8.6a.

The electrochemically active surface area (ECSA) was also evaluated. The ECSA is commonly assessed through determination of the double layer capacitance (C_{dl}),[212, 323] given the proportional relationship between ECSA and C_{dl}.[185] The C_{dl} is obtained from cyclic voltammograms collected in the non-Faradaic region (Figures 8.6c and 8.6d) based on the equation $C_{dl} = j_{average}/\nu$,[296] where $j_{average}$ is the average of the absolute values of j_{anodic} and $j_{cathodic}$ at middle potential of the CV and ν is the scan rate. Therefore, the C_{dl} value is calculated from the slope of a linear fit to $j_{average}$ versus ν.[296] As shown in Figure 8.6e, $Ca_2Sr_2Mn_2CoO_{10-\delta}$ shows a significantly larger C_{dl} value (385 μF) as compared to $Ca_2Sr_2Mn_2FeO_{10-\delta}$ (140 μF), consistent with the improved electrocatalytic activity of the former material.

From the above discussion on electrocatalytic activity toward HER and OER, it is evident that oxygen-vacancies and structural changes play an important role in electrocatalytic properties. As mentioned before, the δ values of ~0.5 and ~1 are confirmed from iodometric titration for $Ca_2Sr_2Mn_2FeO_{10-\delta}$ and $Ca_2Sr_2Mn_2CoO_{10-\delta}$, respectively. This is accompanied by a structural transformation from 3D in $Ca_2Sr_2Mn_2FeO_{10-\delta}$ to 1D in $Ca_2Sr_2Mn_2CoO_{10-\delta}$. The structure-property relationships have been observed in some perovskite-based oxides before.[193, 281, 324, 325] For examples, the transformation of the crystal structure between $Sr_2Mn_2O_6$ and $CaSrMn_2O_6$ resulted in an improved OER activity for $CaSrMn_2O_6$.[324] Another study revealed the systematic trends in OER activity as a function of structure and the degree of oxygen-deficiency between $SrMnO_{2.5}$, $SrMnO_{2.6}$ and $SrMnO_3$.[281] The transformation of crystal structure between the two compounds studied in this work, $Ca_2Sr_2Mn_2FeO_{10-\delta}$ and $Ca_2Sr_2Mn_2CoO_{10-\delta}$, has a clear impact on the electrocatalytic activity. In addition, the presence of Co^{2+}, a d^7 ion, as opposed to Fe^{3+}, a d^5

ion, can have an important effect on electrocatalytic properties.
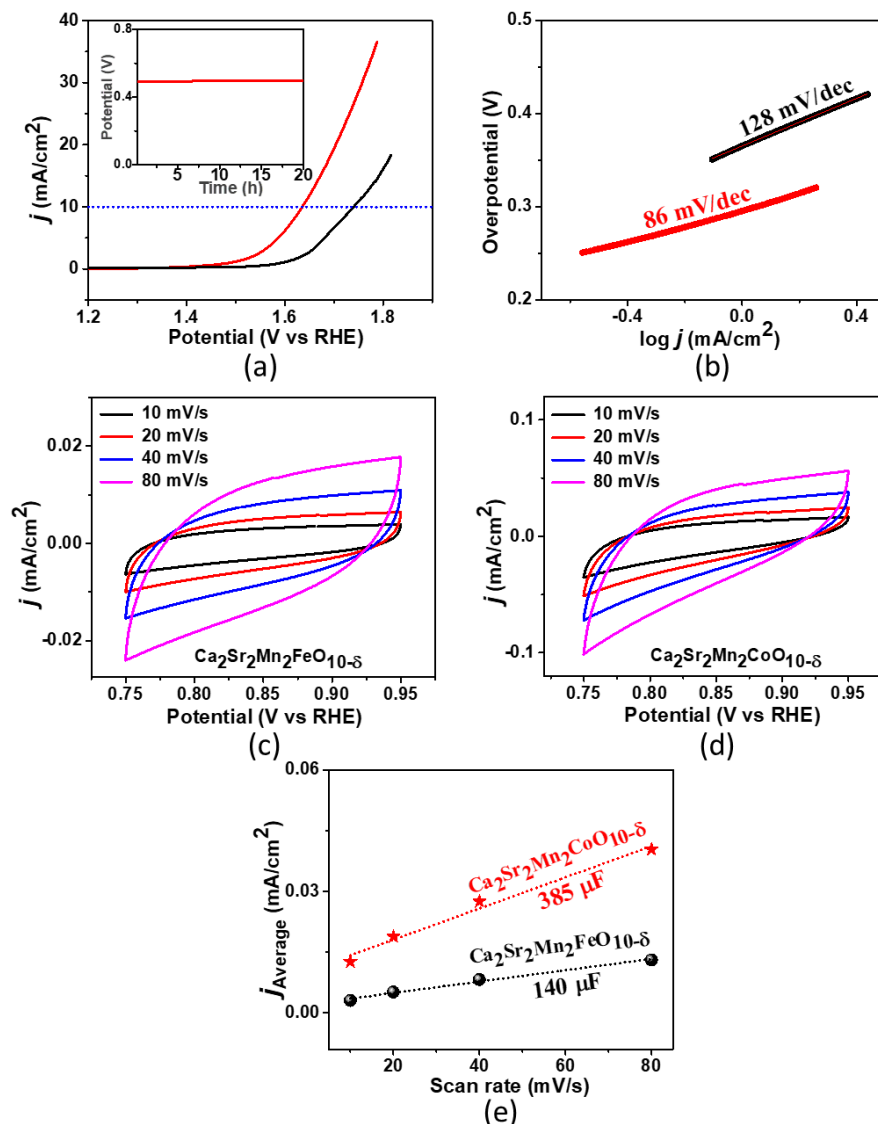
Figure 8.6: (a) OER polarization curves in 0.1 M KOH, for $Ca_2Sr_2Mn_2FeO_{10-\delta}$ (black) and $Ca_2Sr_2Mn_2CoO_{10-\delta}$ (red). The inset shows chronopotentiometry data, indicating the stability of $Ca_2Sr_2Mn_2CoO_{10-\delta}$. (b) Tafel plots. (c-d) Cyclic voltammetry data in non-Faradaic region. (e) Plot of $j_{average}$ versus scan rate, indicating the double layer capacitance (C_{dl}) as slope.

It is noted that in the well-known BSCF oxide,[74] the electrocatalytic activity is primarily explained in terms of the electronic configuration of cobalt, rather than iron. Therefore, a combination of factors, namely the type of transition metal, the oxygen

stoichiometry, and the transformation of the crystal structure all lead to the enhanced properties of $Ca_2Sr_2Mn_2CoO_{10-\delta}$.

8.4 CONCLUSIONS

Changes in composition, oxygen stoichiometry, and crystal structure can all have an impact on functional properties, in particular electrocatalytic activity for water-splitting. These changes result in a significant improvement of electrocatalytic performance of $Ca_2Sr_2Mn_2CoO_{10-\delta}$ over $Ca_2Sr_2Mn_2FeO_{10-\delta}$. The latter compound exhibits superior activity toward both half-reactions of water splitting, HER and OER, as indicated by enhanced overpotential and reaction kinetics. In addition, this catalyst shows greater electrochemically active surface area and high stability in HER and OER conditions, further indicating the important impact of structural changes on functional properties.

CHAPTER 9

A SUSTAINABLE OXIDE ELECTROCATALYST FOR HYDROGEN AND

OXYGEN-EVOLUTION REACTIONS

In this chapter, we discuss an outstanding perovskite oxide of the formula, $CaSrFe_{0.75}Co_{0.75}Mn_{0.5}O_{6-\delta}$ (CSFCM), which is capable of catalyzing both half reactions of water splitting in bulk form without the need for composite preparation, nanofabrication or any other type of processing. In particular, it shows a remarkably low overpotential for OER and retains its performance even after 1000 cycles. Using density-functional-theory (DFT) calculations, we find that the experimentally observed OER activity correlates with the number of free e_g carriers, which could be used as a descriptor, in addition to the e_g orbital occupancy, to further tailor the performance of oxide perovskite electrocatalysts.

9.1 X-RAY ABSORPTION NEAR-EDGE STRUCTURE (XANES) AND FITTING METHODS

XANES spectra were collected at beamline 9-BM of the Advanced Photon Source at Argonne National Laboratory. $CaSrFe_{1-x}Co_{1-x}Mn_{2x}O_{6-\delta}$ powders with $x = 0.2, 0.25, 0.3$ were studied at the Co, Fe, and Mn K-edges. The energy of the X-rays was selected with a Si (111) double crystal monochromator, and the X-ray beam was focused to a spot of approximately 500 μm in diameter using a Rh coated toroidal mirror. Higher energy harmonics were rejected using a Rh coated flat mirror. XANES spectra from multiple

reference materials were also collected, including powders of CoO, LaCoO$_3$, FeO, Fe$_2$O$_3$, SrFeO$_3$, MnO, Mn$_2$O$_3$, and MnO$_2$. The absorption was determined by measurement of the X-ray transmission through the powder, which was either spread in a thin uniform layer onto tape, of which multiples were stacked, or pressed into a pellet after dilution with polyethylene glycol powder. Details of the XANES data analysis and fitting methods are provided in the Supporting Information.

Each XANES spectrum was normalized by first fitting a line to the relatively featureless x-ray absorption that precedes the onset of the pre-edge and white-line features of the K-edges. This line was subtracted from the spectrum, and the spectrum was then divided by a constant that is taken as the difference at E_0 between the pre-edge line and a first or second order polynomial fit to a subrange of the post-edge region beyond the white line. The position of E_0 is taken as the energy position at which the maximum of the first derivative of the absorption spectrum occurs.

The energy at which the onset of the X-ray absorption edge occurs increases with increasing oxidation state. Thus, XANES can provide detailed information about oxidation states. This is typically achieved by comparison of E_0 to those of reference spectra of known oxidation state.

As has been done elsewhere for other mixed cobalt oxides,[326] the Co K-edge E_0 values of CaSrFe$_{1-x}$Co$_{1-x}$Mn$_{2x}$O$_{6-\delta}$ powders, were compared to those of the CoO and LaCoO$_3$ powders to determine the oxidation state of the cobalt ions. The E_0 positions were taken as the root of the second derivative of the Co K-edge XANES. For CaSrFe$_{1-x}$Co$_{1-x}$Mn$_{2x}$O$_{6-\delta}$, a line was fit to a 2.25 eV energy range of the second derivative that included

the root. The zero crossing of the line was taken as the E_0 value and the standard deviation of the data from the line was taken as the error in the E_0 value. The oxidation states of the $CaSrFe_{1-x}Co_{1-x}Mn_{2x}O_{6-\delta}$ powders were then determined by using the E_0 values determined from XANES to linearly interpolate between known oxidation states of the references, with CoO containing Co^{2+} and $LaCoO_3$ containing Co^{3+}. Error in the oxidation state is directly derived from the error in E_0 by linear interpolation as well.

At the Fe K-edge, the centroid (C) of the XANES pre-edge has been shown to correlate strongly with oxidation state.[327] Thus, the pre-edge centroids of the Fe K-edge XANES spectra were used to determine the oxidation states of the $CaSrFe_{1-x}Co_{1-x}Mn_{2x}O_{6-\delta}$ powders by comparison with those of reference compounds. The pre-edge centroids were determined by fitting the pre-edge with a series of pseudo-Voigt functions. The Gaussian to Lorentzian weighting fraction was fixed to 0.5, consistent with other works.[327, 328]All other fit parameters were allowed to vary. At the same time the pseudo-Voigt functions were fit to the spectra, a line and a Lorentzian function were fit to the rising edge of the white line to account for the background on which the pre-edge sits. Additional pseudo-Voigt peaks are sometimes added to account for shoulder features on the white line. However, these are not included in the calculation of the centroid. Wilke et al.[327] reported that three and five pseudo-Voigt peaks are required to fit the pre-edges of FeO and Fe_2O_3, respectively. Here, we use pseudo-Voigt functions of variable width, which results in fewer peaks being needed to fit the pre-edge intensities of these compounds. For FeO, two peaks of variable width are required as shown in Figure 9.2a. Both peaks are used to calculate the centroid. For Fe_2O_3, three peaks of variable width are required as shown in Figure 9.2b.

Following the same procedure as Wilke et al.,[327] only the two lowest energy peaks are used to calculate the centroid, the third broad peak being omitted because it accounts for intersite Fe transitions. Two peaks are used to fit the pre-edge of $SrFeO_3$, shown in Figure 9.2c, and an additional peak is used to fit a higher energy shoulder feature. Similarly, for $CaSrFe_{1-x}Co_{1-x}Mn_{2x}O_{6-\delta}$, two peaks are used to fit the pre-edge, while two additional peaks are used to account for shoulder intensity on the white line as shown in Figure 9.2d-f. A line was fit to the oxidation states of the reference samples as a function of centroid. The equation for the line obtained from the fit was used to determine the oxidation states of the $CaSrFe_{1-x}Co_{1-x}Mn_{2x}O_{6-\delta}$ powders from their pre-edge centroids (C). Uncertainties in the values of C were determined from the errors in the pseudo-Voigt fitting parameters. Uncertainties in the oxidation states of the $CaSrFe_{1-x}Co_{1-x}Mn_{2x}O_{6-\delta}$ powders were derived from the errors in C as well as the error in the linear fit to the reference-spectra oxidation states as a function of centroid. The Fe oxidation states are plotted as a function of C in Figure 9.3d.

In examining a series of molecular complexes having different iron valence and spin-state, Westre et al.,[328] showed both variables impact the Fe pre-edge features. By comparing the pre-edge line shapes of $CaSrFe_{1-x}Co_{1-x}Mn_{2x}O_{6-\delta}$ with those of the molecular complexes, we can begin to gauge the spin state of Fe in $CaSrFe_{1-x}Co_{1-x}Mn_{2x}O_{6-\delta}$. The two pseudo-Voigt peaks that fit the pre-edge of $CaSrFe_{0.75}Co_{0.75}Mn_{0.50}O_{6-\delta}$ have an intensity ratio, defined as the area of the first peak divided by the sum of the peak areas, equal to 0.42 and a separation of 1.61 eV. Of the molecular complexes examined by Westre et al.,[328] these are most similar to the high spin Fe^{3+} compounds in octahedral coordination, which

have intensity ratios and peak separations of around 0.6 and 1.5, respectively. This is a strong indication that iron in $CaSrFe_{1-x}Co_{1-x}Mn_{2x}O_{6-\delta}$ has a high-spin state. Furthermore, the second derivative of the absorption over the pre-edge energy range, seen in the inset to Figure 9.2e, has a similar line shape to that of a five-coordinate square pyramidal high-spin Fe^{3+} complex, further supporting the presence of high-spin iron and consistent with the oxygen deficiency in $CaSrFe_{1-x}Co_{1-x}Mn_{2x}O_{6-\delta}$.

For the Manganese K-edge, Dau et al.[329] have shown the average edge energy (E_A), as determined from the integral method, provides a more linear relationship with oxidation state than the E_0 value. Thus, we apply the integral method here. In this method, an average edge energy is determined by integration of the X-ray energy taken as a function of the absorption over the rising edge of the white line and is given by the expression $E_A = \frac{1}{\mu_2 - \mu_1} \int_{\mu_1}^{\mu_2} E(\mu)d\mu$, where μ is the absorption. Following the same method as Dau et al.,[329] we choose μ_1 to be just above the maximum pre-edge intensity and select a value of 0.12. A value of 1.12 was selected for μ_2 such that $\mu_2 - \mu_1 = 1$. A line was fit to the oxidation states of the reference samples as a function of E_A. The equation for the line determined from the fit was used to determine the oxidation states of $CaSrFe_{1-x}Co_{1-x}Mn_{2x}O_{6-\delta}$ powders from their average edge energies. Uncertainties in the values of E_A represent the range of E_A values found for the same dataset with different normalization parameters when they were reasonably adjusted. The uncertainties in the oxidation states are calculated from the error in E_A as well as the uncertainty in the linear fit to the reference spectra.

9.2 DENSITY-FUNCTIONAL-THEORY CALCULATIONS AND METHODS

DFT calculations, as implemented in the VASP package,[330] were used to investigate the electronic structure of $CaSrFe_{0.8}Co_{0.8}Mn_{0.4}O_6$, $CaSrFe_{0.75}Co_{0.75}Mn_{0.5}O_6$, and $CaSrFe_{0.6}Co_{0.6}Mn_{0.8}O_6$. To simulate the random distribution of the transition metal ions within small supercells for DFT calculations, we used special quasirandom structures (SQS) as implemented in the Alloy Theoretic Automated Toolkit (ATAT).[331, 332] We adopted SQS supercells having paramagnetic order[333] with 100 atoms for $CaSrFe_{0.75}Co_{0.75}Mn_{0.5}O_6$ and $CaSrFe_{0.8}Co_{0.8}Mn_{0.4}O_6$, and 80 atoms for $CaSrFe_{0.6}Co_{0.6}Mn_{0.8}O_6$ (see Supplementary Information). PDOS of the compounds were calculated to analyze their electronic structure and orbital occupation. The effect of oxygen deficiency on the distribution and occupancy of the e_g states in these compounds is simulated by introducing one oxygen vacancy within the supercells used above. The orbital hybridization between e_g states of transition metal and $2p$ states of oxygen is calculated through integration of their shared area in the PDOS.

We now discuss the DFT methods. DFT calculations as implemented in the VASP package,[330] were used to investigate these materials. To simulate the random distribution of the transition metal ions within small supercells for DFT calculations, we used special quasirandom structures (SQS) as implemented in the Alloy Theoretic Automated Toolkit (ATAT).[331, 332] The SQS method uses a Monte Carlo algorithm to generate and find structures where the correlation of the nearby atomic sites matches, as closely as possible, that of a truly disordered alloy. We adopted SQS supercells (Figure 9.11) having paramagnetic order[333] with 100 atoms in $CaSrFe_{0.75}Co_{0.75}Mn_{0.5}O_6$ and

$CaSrFe_{0.8}Co_{0.8}Mn_{0.4}O_6$, and 80 atoms in $CaSrFe_{0.6}Co_{0.6}Mn_{0.8}O_6$, which do not include oxygen vacancies. These SQS structures were based on the DFT-optimized unit-cell of $CaCoO_3$ having an $a^\square b^\square c^\square$ tilt pattern using the Glazer's notation.[334] Subsequently, we optimized the SQS cells using DFT calculations, implemented in the VASP package.[330] The energy cutoff for the plane waves was set at 500 eV, the threshold for energy convergence for the self-consistent loop was to $1eV - 5$ eV, and the convergence for forces was set to 0.01 eV $Å^{-1}$. We used projector augmented-wave (PAW)[271] potentials and the generalized gradient approximation (GGA) within the Perdew-Burke-Ernzerhof (PBE)[266] parameterization to describe the electron-ion and the electronic exchange-correlation interactions, respectively. We added an on-site repulsion term to the localized $3d$ electrons in Co, Fe and Mn using an effective Hubbard-U parameter of 3.32 eV, 5.30 eV and 3.90 eV, respectively.[335] These U values were obtained from Wang et al.'s work,[336] which can accurately reproduce phase stabilities of metal oxides. The optimized orthogonal supercell lattice parameters for $CaSrFe_{0.8}Co_{0.8}Mn_{0.4}O_6$, $CaSrFe_{0.75}Co_{0.75}Mn_{0.5}O_6$, $CaSrFe_{0.6}Co_{0.6}Mn_{0.8}O_6$, were 5.26Å×7.46Å×26.40Å, 5.26Å×7.46Å×21.12Å and 5.32Å×7.54Å×26.67Å, respectively. The Brillouin zone was sampled by a $8 \times 8 \times 1$ k-points mesh obtained using the Monkhorst-Pack scheme.[337] Projected density of states (PDOS) of these phases are calculated to analyze the electronic structure of these compounds and their orbital occupations. These supercells are rotated to ensure that the orientation of the t_{2g} and e_g orbitals are along the Cartesian axes. The free carriers belonging to e_g states at room temperature (298 K) are calculated using the equation $\int g(E) * f(E,T)dE$, where $g(E)$ is the density of e_g states and $f(E,T)$ is the Fermi-Dirac

distribution at room temperature. The effect of oxygen deficiency on the distribution and occupancy of the e_g states in these compounds is simulated by introducing one oxygen vacancy within the supercells used above. The orbital hybridization between e_g states of transition metal and $2p$ states of oxygen is the calculated through integration of their shared area in the PDOS. This results in a vacancy concentration of 1.7%, 2.0% and 1.7% in $CaSrFe_{0.6}Co_{0.6}Mn_{0.8}O_6$, $CaSrFe_{0.75}Co_{0.75}Mn_{0.5}O_6$, and $CaSrFe_{0.8}Co_{0.8}Mn_{0.4}O_6$, respectively.

9.3 CRYSTAL STRUCTURE

Initially, a series of oxygen-deficient perovskites with formula $CaSrFe_{1-x}Co_{1-x}Mn_{2x}O_{6-\delta}$ (x = 0 − 1) were synthesized, as shown in Figure 9.1. The best electrocatalytic performance was observed in the composition $CaSrFe_{0.75}Co_{0.75}Mn_{0.5}O_{6-\delta}$ (CSFCM). The structural framework of this material is similar to that of a perovskite (Figure 9.1), but with partial occupancy on oxygen sites, as shown in Table 9.1. The oxygen-vacancies have a disordered distribution in the crystal lattice, which forms a cubic *Pm*-3*m* structure, as demonstrated by Rietveld refinement with X-ray diffraction data in Figure 9.1a. It is noted that the formation of the cubic structure is a function of the Mn stoichiometry. As shown in Figure 9.1b, the structure of materials in the series $CaSrFe_{1-x}Co_{1-x}Mn_{2x}O_{6-\delta}$ changes as the Mn concentration (represented by 2x) is increased systematically. The materials with 2x = 0 – 0.2 form structures where the oxygen vacancies are ordered, leading to the so-called brownmillerite type structure (Figure 9.1b), in which the transition metals have alternating octahedral and tetrahedral coordination.[12] The 2x = 0.3 phase is an intermediate where the transformation of brownmillerite to cubic perovskite

structure begins. The compound with 2x = 0.4 shows cubic structure with relatively wide diffraction peaks, which indicate that transformation to the cubic structure is incomplete. Finally, the compounds with 2x = 0.5 – 1.0 show cubic perovskite structure. We examined the electrocatalytic activity of the entire series, and among them, the compound with 2x = 0.5 showed the highest activity. Its superior performance compared with the adjacent compositions is shown in Figure 9.9. Therefore, this material, along with two adjacent compositions with 2x = 0.4 and 2x = 0.6, were studied in greater detail to develop the structure-property relationships. Scanning electron microscopy data (Figure 9.2) show similar grain sizes for the three compounds. Oxygen vacancies have been found to influence the catalytic activity of perovskite-based catalysts.[218, 338, 339] Therefore, iodometric titrations were carried out to determine the degree of oxygen-deficiency in $CaSrFe_{0.75}Co_{0.75}Mn_{0.5}O_{6-\delta}$. These titrations showed $\delta \approx 0.56$, for this compound, which indicates a significant degree of oxygen-deficiency. Clearly the presence of these oxygen-vacancies has an impact on the valence states of transition metals, which were studied by X-ray absorption spectroscopy, as described in the next section.
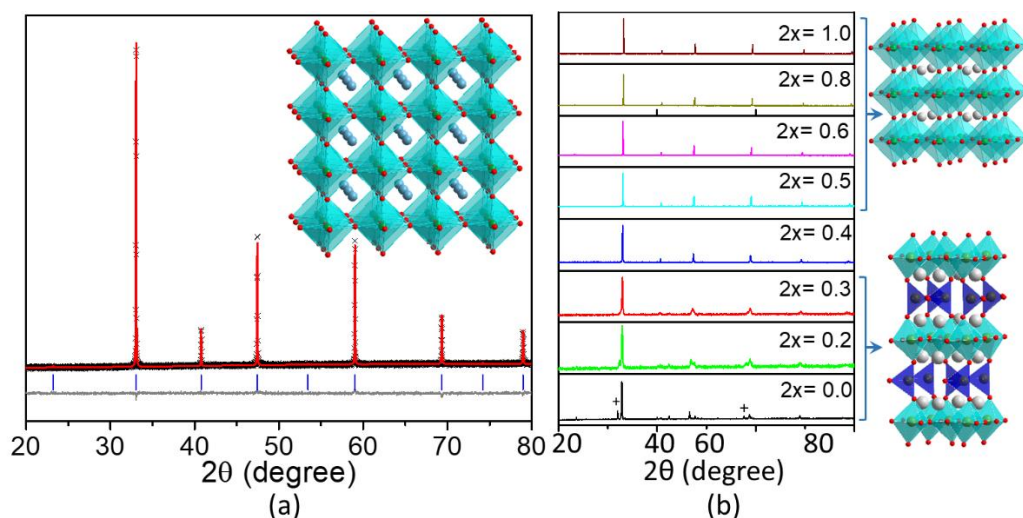
Figure 9.1: (a) Rietveld refinement profile and crystal structure of CSFCM. (b) Change in the X-ray diffraction data for $CaSrFe_{1-x}Co_{1-x}Mn_{2x}O_{6-\delta}$ as a function of Mn-concentration, from brownmillerite structure ($2x = 0 - 0.3$) to perovskite structure ($2x = 0.5 - 1.0$). Crosses show two of the distinct brownmillerite peaks.
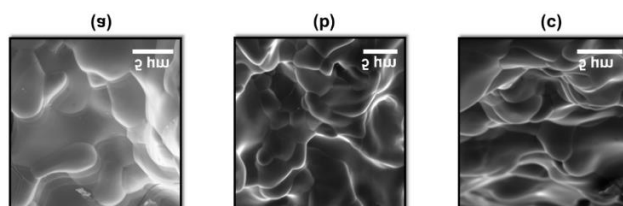
Figure 9.2: Scanning electron microscopy data for (a) $CaSrFe_{0.8}Co_{0.8}Mn_{0.4}O_{6-\delta}$, (b) $CaSrFe_{0.75}Co_{0.75}Mn_{0.5}O_{6-\delta}$, and (c) $CaSrFe_{0.7}Co_{0.7}Mn_{0.6}O_{6-\delta}$.

Table 9.1: Atomic positions of $CaSrFe_{0.75}Co_{0.75}Mn_{0.5}O_{6-\delta}$, *Pm-3m*, $a = 3.8312(1)$ Å.

	x	y	z	U_{iso}	multiplicity	occupancy
Ca/Sr	0.5	0.5	0.5	0.0138(8)	1	0.50/0.50
Fe/Co/Mn	0.0	0.0	0.0	0.031(1)	1	0.375/0.375/0.250
O	0.5	0.0	0.0	0.048(1)	3	0.91

9.4 X-RAY ABSORPTION NEAR-EDGE STRUCTURE

X-ray absorption near-edge structure (XANES), shown in Figure 9.3, was used for detailed analysis of the oxidation states of transition metals in $CaSrFe_{0.75}Co_{0.75}Mn_{0.5}O_{6-\delta}$ (CSFCM), as well as two adjacent compositions, containing 0.4 and 0.6 Mn per formula unit, i.e., $CaSrFe_{0.8}Co_{0.8}Mn_{0.4}O_{6-\delta}$ and $CaSrFe_{0.7}Co_{0.7}Mn_{0.6}O_{6-\delta}$. In addition, XANES

spectra were obtained on multiple reference materials, including powders of CoO, LaCoO$_3$, FeO, Fe$_2$O$_3$, SrFeO$_3$, MnO, Mn$_2$O$_3$, and MnO$_2$.

Table 9.2: Transition metal oxidation states for CaSrFe$_{1-x}$Co$_{1-x}$Mn$_{2x}$O$_{6-\delta}$ from XANES.

x	Mn oxidation state	% Mn^{3+}	% Mn^{4+}
0.20	3.895(73)	10.5	89.5
0.25	3.898(70)	10.2	89.8
0.30	3.916(70)	8.4	91.6
x	Fe oxidation state	% Fe^{3+}	% Fe^{4+}
0.20	3.724(50)	27.6	72.4
0.25	3.830(62)	17.0	83.0
0.30	3.952(97)	4.8	95.2
x	Co oxidation state	% Co^{2+}	% Co^{3+}
0.20	2.700(82)	30.0	70.0
0.25	2.736(25)	26.4	73.6
0.30	2.76(14)	24	76

XANES experiments show that the Mn oxidation state is very similar in all three compounds, CaSrFe$_{0.8}$Co$_{0.8}$Mn$_{0.4}$O$_{6-\delta}$, CaSrFe$_{0.75}$Co$_{0.75}$Mn$_{0.5}$O$_{6-\delta}$, and CaSrFe$_{0.7}$Co$_{0.7}$Mn$_{0.6}$O$_{6-\delta}$. As shown in Table 9.2, most of the manganese in these materials is in tetravalent state, with a smaller percentage of trivalent manganese. For iron, all three compounds contain a combination of trivalent and tetravalent states (Figure 9.4). However, there is a systematic increase in the iron oxidation state among these materials. A similar increase also appears to be present for the oxidation state of cobalt, although the variation is on the order of the measurement error. For all three compositions, the cobalt oxidation state is a combination of divalent and trivalent, as shown in Table 9.2.
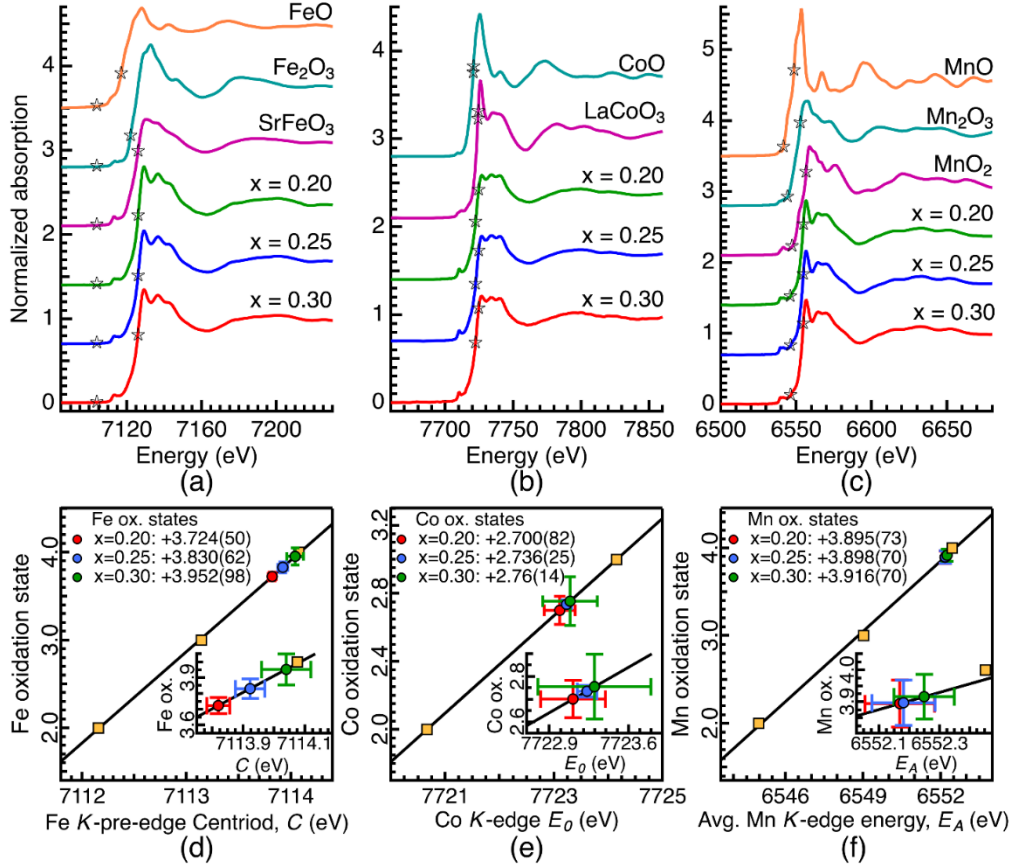
Figure 9.3: The spectra of (a) Fe, (b) Co, and (c) Mn for $CaSrFe_{1-x}Co_{1-x}Mn_{2x}O_{6-\delta}$ and reference compounds. The edges used for determination of oxidation states are marked by asterisks. (d), (e) and (f) show the oxidation states of Fe, Co and Mn, respectively, in $CaSrFe_{1-x}Co_{1-x}Mn_{2x}O_{6-\delta}$ (x = 0.20, 0.25, 0.30) as well as in reference compounds FeO, Fe_2O_3, $SrFeO_3$, CoO, $LaCoO_3$, MnO, Mn_2O_3, and MnO_2. The straight line shows the fit.
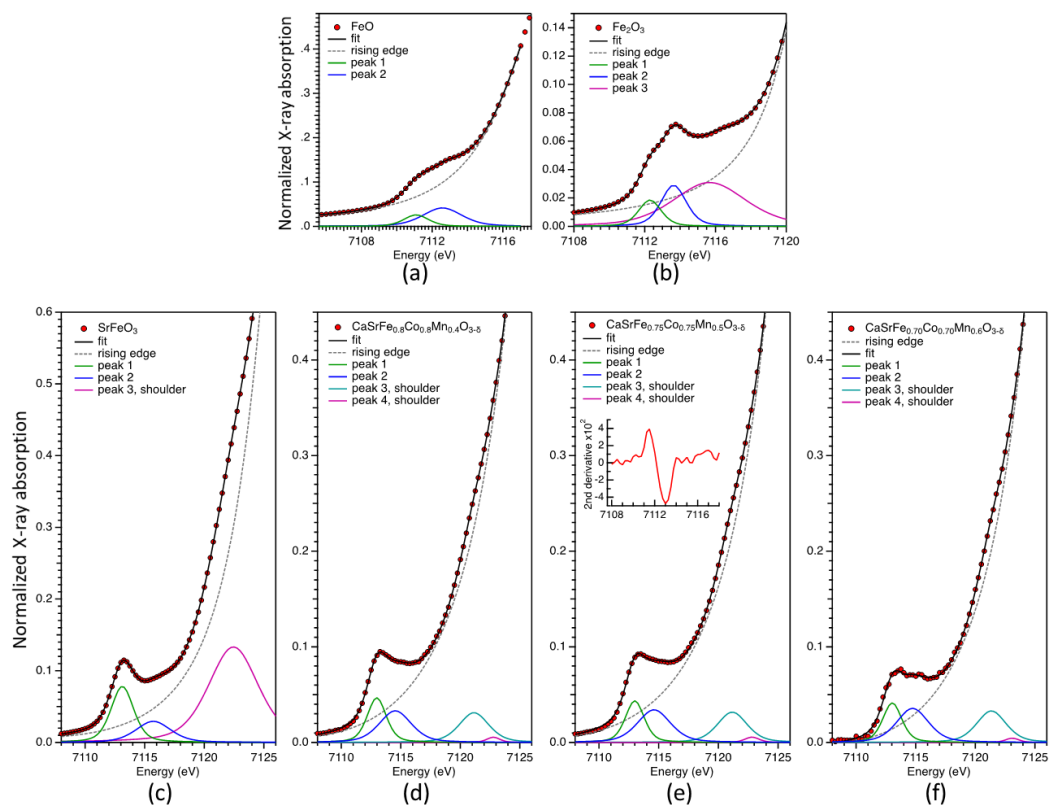
Figure 9.4: The Fe *K*-edge XANES pre-edge (a) FeO, (b) Fe_2O_3, (c) $SrFeO_3$, (d) $CaSrFe_{0.80}Co_{0.80}Mn_{0.40}O_{6-\delta}$, (e) $CaSrFe_{0.75}Co_{0.75}Mn_{0.50}O_{6-\delta}$, and (f) $CaSrFe_{0.70}Co_{0.70}Mn_{0.60}O_{6-\delta}$, and fits thereof using pseudo-Voigt peaks and a rising edge composed of a Lorentzian and a line. The inset in (e) shows a representative example of the 2nd derivative of the XANES pre-edge.

9.5 HYDROGEN AND OXYGEN EVOLUTION ACTIVITY

Since HER catalysts are commonly investigated in either alkaline, i.e., 1M KOH,[56, 101, 224] or acidic media, e.g., 0.1M $HClO_4$,[56, 224, 340] we examined CSFCM under both conditions. Although oxygen-deficient perovskites show good OER performance, very few compounds from this class of materials show catalytic activity for HER. The few examples that have been reported are HER-active in alkaline environment.[70, 183] Even less common are perovskite-type oxides based on non-precious metals that show HER activity in acidic

media. A brief report on La-based perovskites shows very low HER activity in acidic conditions.[230]

Remarkably, CSFCM shows comparable HER activity in both acidic and basic conditions (Figure 9.5), a rare property for a perovskite-type oxide. The onset potential where the electrocatalytic activity commences and the polarization curve begins to depart from a flat line is one of the parameters used for comparing the activity of HER catalysts. Also, by convention, the overpotential required to achieve the current density of 10 mA/cm^2 (η_{10}) is taken as an indication of the performance of an electrocatalyst.[233, 234] CSFCM shows overpotentials of 0.35 V and 0.31 V in acidic and basic conditions, as shown in Figure 9.5. We note that CSFCM acts as a catalyst in bulk form with no additional processing. Also, as presented in Figure 9.5, it shows high stability over 12 hours.
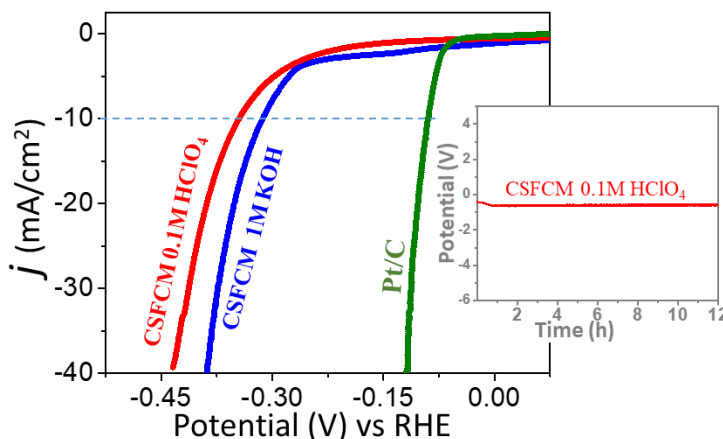
Figure 9.5: HER polarization curves for CSFCM in acidic and basic conditions. The inset shows the stability over 12 hours in 0.1 M HClO$_4$.

The OER activity was also studied for CSFCM along with that of the precious metal catalyst RuO$_2$. Carbon black is generally added to the electrode composition during OER

measurements to enhance the conductivity within the electrode and improve the utilization of the catalyst.[341-343] However, recent studies have shown that the role of carbon is more complex than originally thought.[344, 345] For example, it has been shown that during the preparation of $Ba_{0.5}Sr_{0.5}Co_{0.8}Fe_{0.2}O_{3-\delta}$/carbon electrode, cobalt does not retain its valency and gets reduced.[346] Therefore, OER experiments without carbon black are adopted by some researchers to avoid the interference from carbon.[257] We performed OER experiments for the new compound, CSFCM, both without and with carbon black. Both methods gave similar results, indicating that the catalytic performance of this compound is not dependent on carbon black. The experiments without carbon are more desirable, as they demonstrate the intrinsic catalytic performance of the catalyst, without any contribution form carbon. Therefore, we used this method for further studies, where the catalyst was dropcasted on the surface of a glassy carbon electrode without the addition of carbon black powder. The OER experiments are commonly done in 0.1 M KOH. We used the same condition to be able to directly compare our results to those reported for other catalysts. However, other conditions (1 M KOH and 0.1 M $HClO_4$) were also tested as shown in Figure 9.10. The best results were those of 0.1 M KOH, which is the typical OER condition.[64, 71, 99, 219, 326]
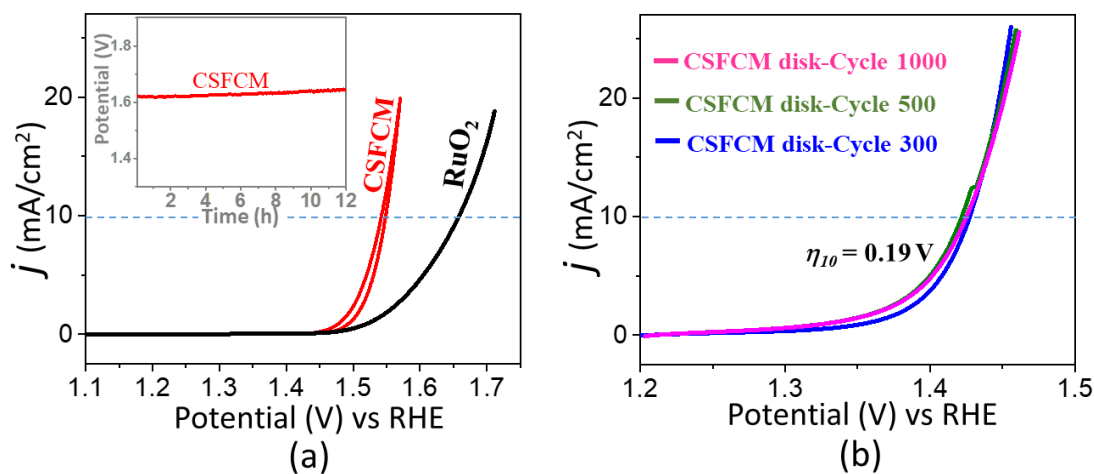
Figure 9.6: (a) OER polarization curves in 0.1 M KOH for CSFCM and RuO_2 dropcasted on a glassy carbon electrode. The inset shows stability over 12 hours. (b) OER polarization curves for pure disk of CSFCM without glassy carbon electrode or any additives. Note the low overpotential, $\eta_{10} = 0.19$ V, and excellent performance over 1000 cycles.

In addition, given the fundamental nature of this study, methods of investigation of the OER activity that can further examine the intrinsic catalytic properties by eliminating all other contributions, are highly desired. One of the electrode components that is nearly always used in OER studies is glassy carbon electrode, on which the catalyst is drop-casted. The glassy carbon electrode provides high electrical conductivity, while the catalyst film facilitates the OER. Recently some researchers have examined pure disks of catalytic materials to eliminate all electrode components, even the glassy carbon electrode.[347, 348] Given that the magnitude of OER potential is greater than that of HER, we speculated that the conductivity of the catalyst might be enough to be used alone without being loaded on a glassy carbon electrode. Therefore, in addition to the conventional glassy carbon method, we also conducted OER experiments using pure disks of the catalyst.

Again, the onset potential and the overpotential beyond the ideal potential of 1.23 V (at 10 mA/cm^2) were evaluated. In 0.1 M KOH, the conventional drop-cast experiments

for CSFCM give onset potential of 1.45 V and overpotential of $\eta_{10} \approx 0.31$ V (Figure 9.6a). The inset of Figure 9.6a shows the stability of this catalyst even after 12 hours. The pure disks of CSFCM show onset potential of 1.30 V and overpotential of $\eta_{10} \approx 0.19$ V (Figure 9.6b). In pure disk experiments, the whole surface of the disk contributes to the OER, leading to the enhanced overpotential. As shown in Figure 9.6b, the CSFCM disk shows excellent performance even up to 1000 cycles.

In addition, CSFCM retains its structural integrity during the electrocatalysis process as evident form X-ray diffraction (Figure 9.7) and X-ray photoelectron spectroscopy data (Figure 9.8). The remarkable performance of CSFCM becomes more evident when its activity is compared to that of the traditional precious metal catalyst RuO_2, which shows overpotential of $\eta_{10} \approx 0.42$ V.[248] Its activity is also superior to that of the highly regarded perovskite oxide BSCF, with overpotential of $\eta_{10} \approx 0.4 - 0.5$ V.[71, 99, 349] While in recent years there have been reports of some catalysts with comparable OER overpotentials to CSFCM, they often utilize precious metals, either in the catalyst composition or as substrate.[350, 351] Such high OER activity in a non-precious-metal oxide is uncommon.

The kinetics of OER is commonly examined based on the Tafel equation $\eta = a + b$ $\log j$. [64, 71, 99, 326] The slope of the Tafel plot, η vs. $\log j$, is indicative of the reaction rate. Smaller slope indicates smaller overpotential required to deliver the same current density increment, which implies faster electron-transfer and enhanced reaction kinetics.[56] To obtain the Tafel slope, we first collected steady state chronoamperometry data (Figure

9.11) at different potentials starting from the OER onset potential. The steady state output currents from these measurements were then iR-corrected and plotted against the applied potentials. The overpotentials from these iR-corrected steady state data were then used to obtain the Tafel plots and Tafel slopes (Figure 9.11). As seen here, the Tafel slope for CSFCM is 71 mV/dec, as compared to ~71–94 mV/dc reported for the well-known BSCF catalyst.[71, 99, 349] This is consistent with the high OER activity of CSFCM and indicates the facile charge transport and enhanced kinetics.[245]
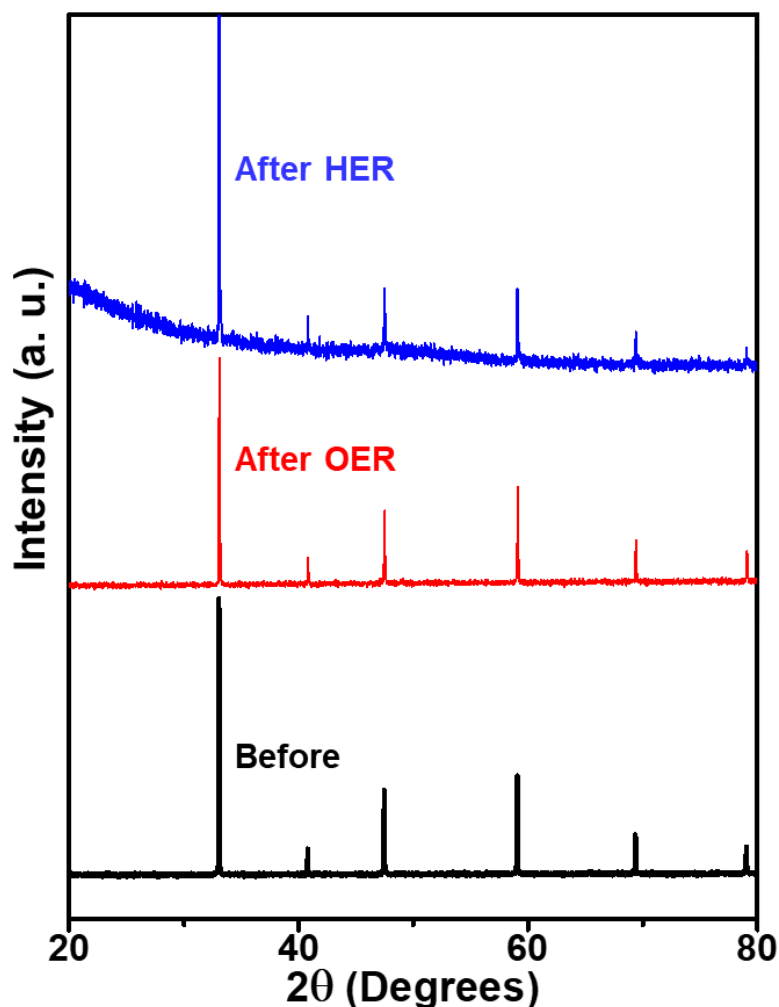
Figure 9.7: X-ray diffraction data for CSFCM before and after OER (0.1 M KOH) and HER (0.1 M HClO$_4$).
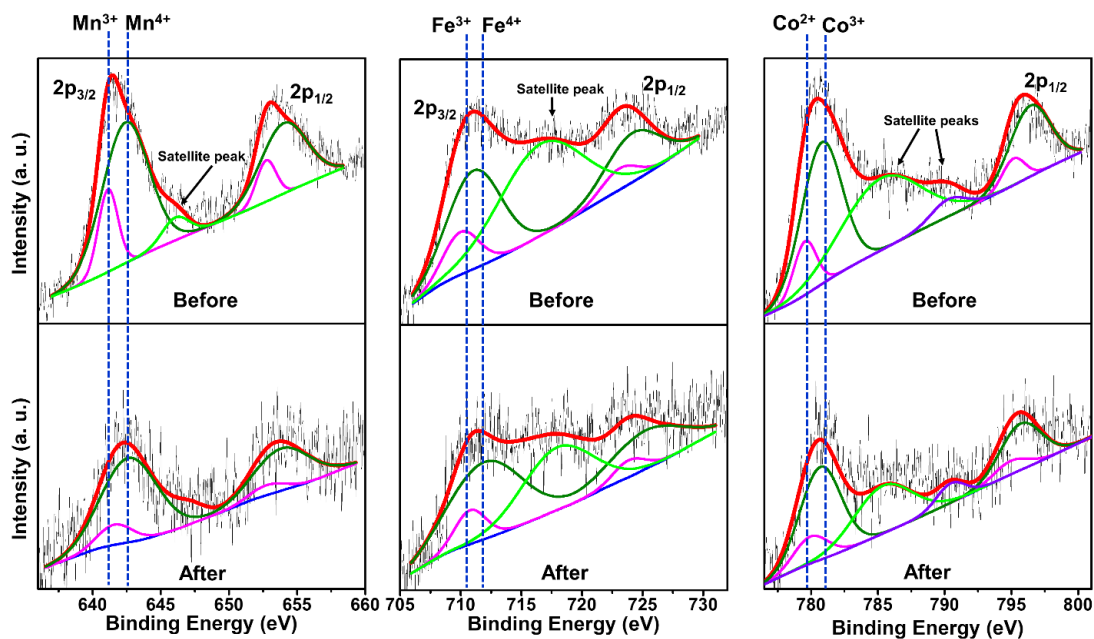
Figure 9.8: X-ray photoelectron spectroscopy data for CSFCM indicating nearly the same binding energies before and after 1000 cycles of OER.
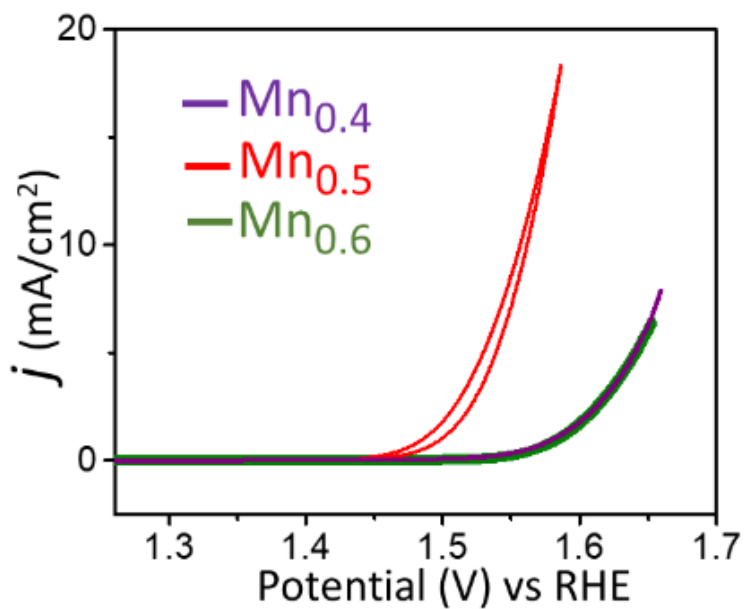
Figure 9.9: Representative example of the effect of Mn-concentration. The OER activities of $CaSrFe_{0.8}Co_{0.8}Mn_{0.4}O_{6-\delta}$, $CaSrFe_{0.75}Co_{0.75}Mn_{0.5}O_{6-\delta}$ and $CaSrFe_{0.7}Co_{0.7}Mn_{0.6}O_{6-\delta}$ are compared.

149
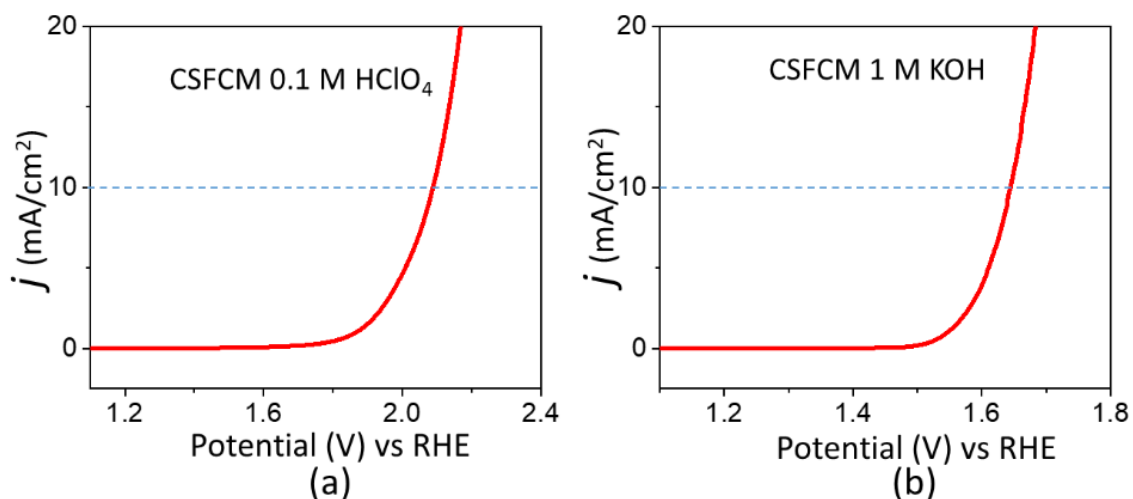
Figure 9.10: OER polarization curves for CSFCM in (a) 0.1 M HClO₄ and (b) 1 M KOH.

We also examined the electrochemically active surface area (ECSA) of CSFCM, as compared to RuO$_2$. This is often done using the electrochemical double layer capacitance (C$_{dl}$) of the catalysts using cyclic voltammetry in non-faradic region,[352] where electrode reactions are negligible and the electrical double layer charge and discharge is the main source of the current.[352, 353] The ECSA value is related to C$_{dl}$ through the relationship ECSA=C$_{dl}$/C$_s$, where C$_s$ is specific capacitance.[244, 352, 354] Irrespective of the C$_s$ value, given the proportionality between the double layer capacitance, C$_{dl}$, and the electrochemically active surface area,[355-358] it is common to take C$_{dl}$ as a representative of the magnitude of ECSA.[356-358] The C$_{dl}$ value is obtained using the equation C$_{dl}$ = Δj/v,[356-358] where Δj is the absolute value of the difference between j$_{anodic}$ and j$_{catodic}$ in cyclic voltammetry data and v is the scan rate.[356-358] Usually, Δj is plotted against v, and the value of C$_{dl}$ is determined as half of the slope of this plot.[356-358]
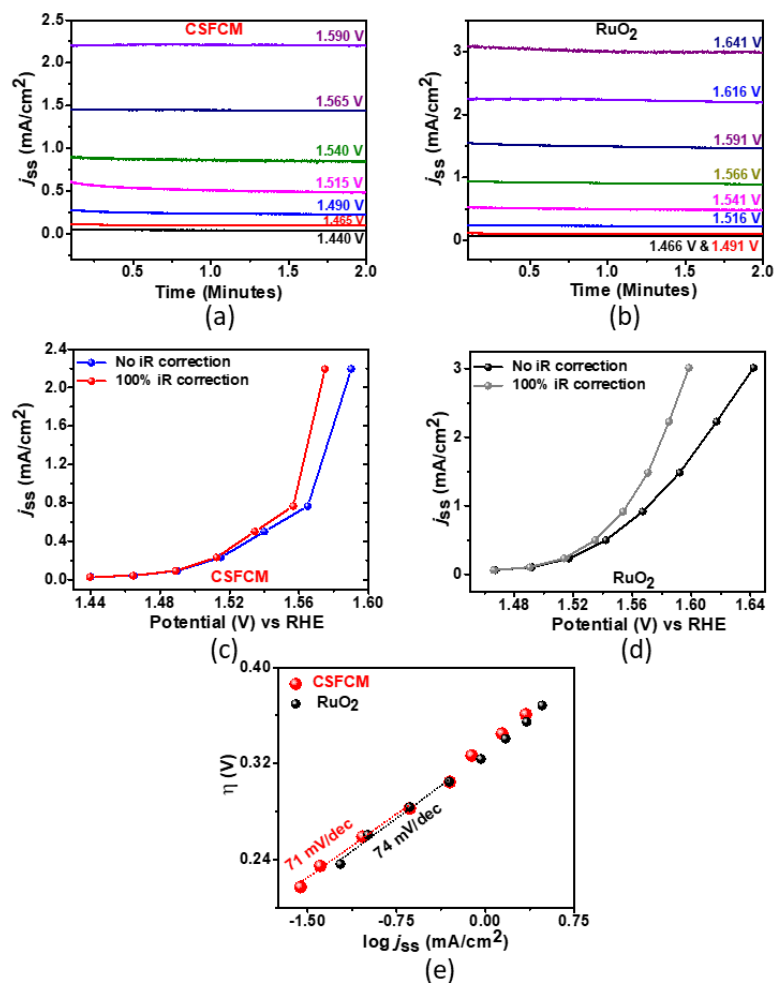
Figure 9.11: (a) and (b) show the steady state chronoamperometry data at different potentials starting from the OER onset. In (c) and (d) the currents (j_{ss}) obtained at different potentials from a and b, are plotted with and without iR correction. Part (e) shows the Tafel plot, where the iR corrected overpotential (beyond 1.23 V) is plotted against log j_{ss}. The Tafel slopes are 74 and 71 mV/dec for RuO_2 and CSFCM, respectively.

Alternatively, some researchers have used the plot of $j_{average}$ versus v, where $j_{average}$ is the average of the absolute values of j_{anodic} and $j_{catodic}$,[355, 359] and the slope is equivalent to C_{dl} without the need to divide by 2.[355] Figure 9.12 shows the plot of Δj at the middle potential,[357] 0.977 V, against the corresponding scan rates. The value of C_{dl} is determined by dividing the slope of this plot by 2.[356-358] As shown in Figure 9.12, the C_{dl} for CSFCM is considerably larger than that of RuO_2, which is consistent with the high OER activity of

CSFCM. Further analyses can also provide information about specific capacitance, as shown in Figure 9.13.
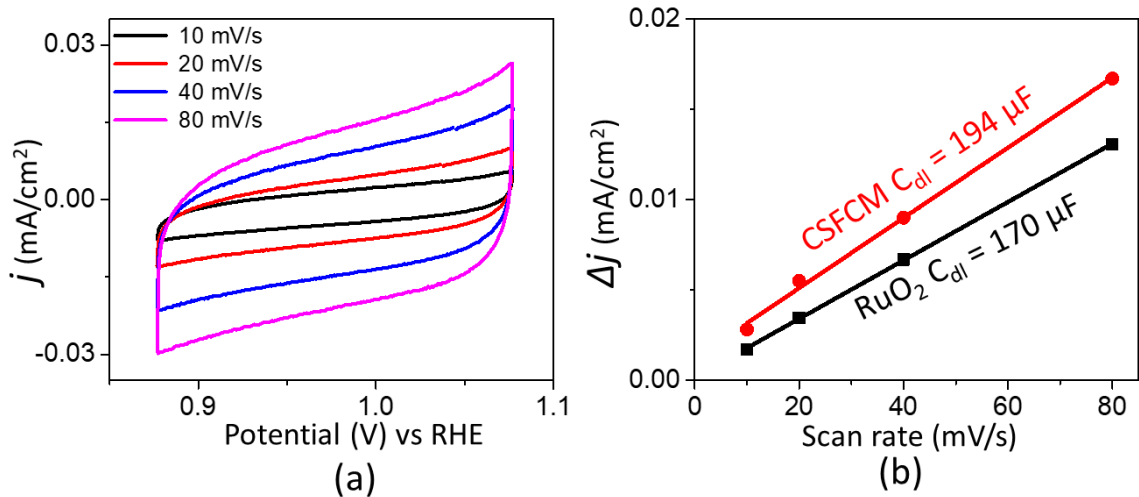
Figure 9.12: (a) Cyclic voltammetry data in non-Faradic region with different scan rates for CSFCM. (b) The plot of Δj versus scan rate. The value of double layer capacitance, C_{dl}, is equivalent to half of the slope of this plot.
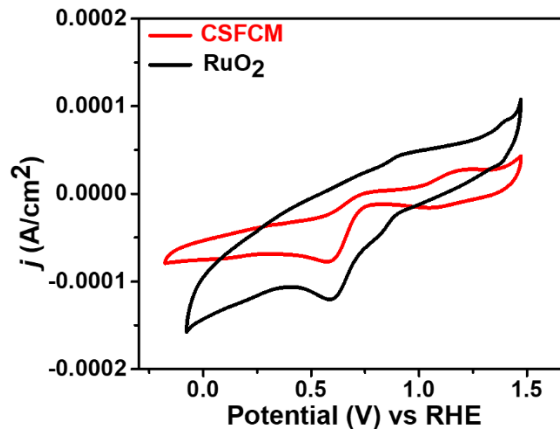
Figure 9.13: From above CVs, the Cs can be obtained using $C_s = \frac{1}{2mv|\Delta V|}\int i(V)dV$,[3] where m, v, ΔV and $i(V)$ are mass, scan-rate, voltage range, and current response at potential V, respectively.[3] Some researchers have normalize C_s by electrode area,[360] which can then be used in ECSA=C_{dl}/C_s.
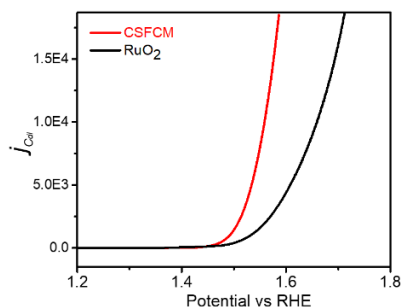
Figure 9.14: The C_{dl}-normalized polarization curve for OER in 0.1 M KOH.
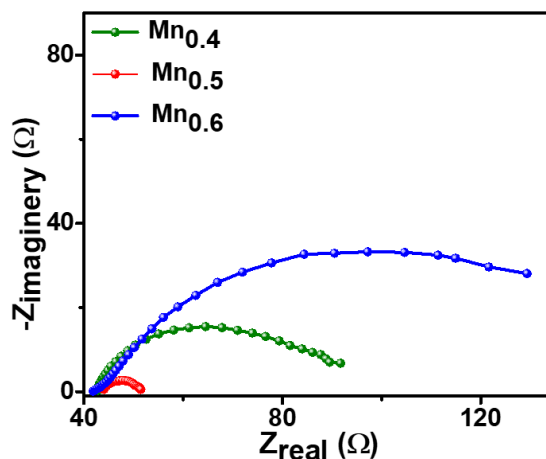
Figure 9.15: Charge transfer resistance under OER condition at 1.55 V vs RHE.

9.5 ELECTRONIC STRUCTURE

The electronic structure of perovskites, such as the filling of e_g states of the transition metals, have been suggested to explain their catalytic activity. Initially, the high OER activity of BSCF led to the proposal that e_g filling of near unity is optimum for obtaining the best OER performance.[326] Other researchers have since used this descriptor to explain the performance of various electrocatalysts for OER.[71, 361] The importance of e_g orbitals is that they form σ-bonding with oxygen-containing intermediates during the electrocatalytic process, unlike t_{2g} orbitals that form π-bonds. Therefore, the electron transfer between catalyst and reaction intermediates is more directly promoted by e_g orbitals.[326] Perovskite-related oxides with e_g electron occupation close to 1,[70, 313, 326, 361, 362]

have been reported to show high catalytic activity. This has been explained in terms of a moderate binding strength between the catalyst surface and reaction intermediates, optimizing both adsorption and desorption. It has been proposed that the catalyst-adsorbate interaction is relatively weak when e_g orbital occupation is larger than 1. Conversely, if e_g orbital occupation is less than 1, the strong bonding between the catalyst and the adsorbate can poison the catalyst by hindering the desorption process and reducing the number of available binding sites. A correlation between activity and e_g orbital filling has been suggested for some HER catalysts as well.[57, 363] However, in many cases, the assignment of e_g orbital occupancy has been done by electron count and based on the assumption of a certain spin state.[57, 71, 326, 361, 363]
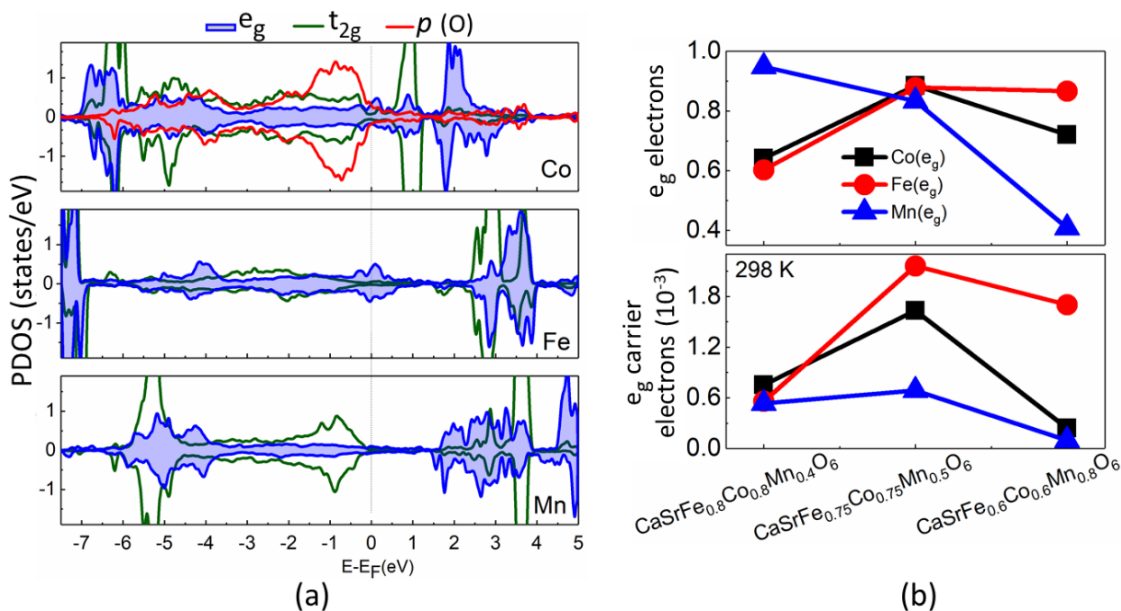
Figure 9.16: (a) Spin-polarized projected density of states (PDOS) of e_g and t_{2g} state of Co, Fe and Mn, as well as oxygen $2p$ state for $CaSrFe_{0.75}Co_{0.75}Mn_{0.5}O_6$. (b) Top panel shows the average occupancy of e_g states of Co, Fe, Mn, and the bottom panel shows free e_g carriers at room temperature (298 K) in $CaSrFe_{0.75}Co_{0.75}Mn_{0.5}O_6$, $CaSrFe_{0.8}Co_{0.8}Mn_{0.4}O_6$, and $CaSrFe_{0.6}Co_{0.6}Mn_{0.8}O_6$.

We used DFT calculations to investigate the electronic structure and identify descriptors that lead to the enhanced electrocatalytic activity of $CaSrFe_{0.75}Co_{0.75}Mn_{0.5}O_{6-\delta}$ (CSFCM). We also calculated the electronic structure of two other compositions with lower and higher Fe/Co contents, namely $CaSrFe_{0.6}Co_{0.6}Mn_{0.8}O_{6-\delta}$ and $CaSrFe_{0.8}Co_{0.8}Mn_{0.4}O_{6-\delta}$, to highlight the unique features of CSFCM. Initially, oxygen-vacancy-free models were examined and then vacancies were introduced into the structure. In both cases, the same trends for t_{2g} and e_g states were observed among the three materials. Figure 9.16 shows the projected density of states (PDOS) of t_{2g} and e_g states for the transition metals hybridized with the p states of oxygen. The $3d$ states of Fe and Co dominate the Fermi energy (E_F) with the empty e_g states of Mn being at relatively higher energies. Therefore, it is reasonable to assume that, in these $CaSrFe_xCo_xMn_{2-x}O_{6-\delta}$ catalysts, the Co and Fe sites determine the catalytic properties, as they can bind most easily with the adsorbates.
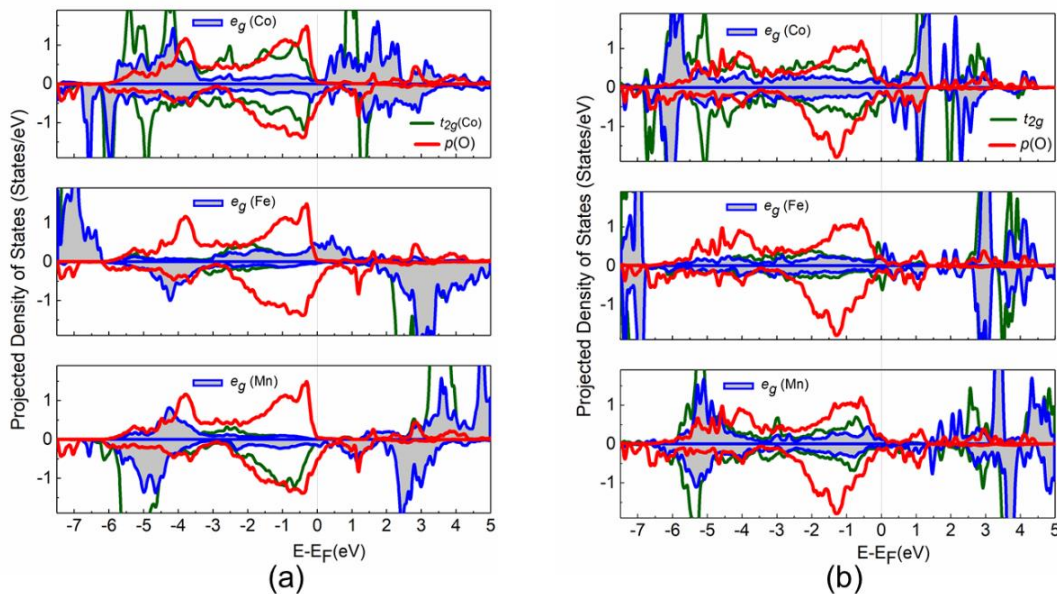
Figure 9.17: Spin-polarized projected density of states of e_g and t_{2g} orbitals of Co, Fe and Mn, as well as O $2p$ are shown for **(a)** $CaSrFe_{0.6}Co_{0.6}Mn_{0.8}O_6$ and **(b)** $CaSrFe_{0.8}Co_{0.8}Mn_{0.4}O_6$.

A quantitative analysis of the PDOS shows that $CaSrFe_{0.75}Co_{0.75}Mn_{0.5}O_6$, exhibits the highest density of e_g states (4.43×10^{-2} states/eV) around E_F as shown in Table 9.3. We also find a strong hybridization between e_g states of Co (1.37 e), Fe (1.41 e) and Mn (1.92 e) with oxygen $2p$ states in $CaSrFe_{0.75}Co_{0.75}Mn_{0.5}O_6$, which would suggest efficient charge transfer within the $CaSrFe_{0.75}Co_{0.75}Mn_{0.5}O_6$ structure. Stronger hybridization between the transition metal d states and oxygen p states is likely to facilitate efficient charge transfer between the transition metal and reaction intermediates during HER and OER.[298] The average hybridization of the three transition metals with O $2p$ is 1.57 e for $CaSrFe_{0.75}Co_{0.75}Mn_{0.5}O_6$, which is greater than that of $CaSrFe_{0.6}Co_{0.6}Mn_{0.8}O_6$ (1.25 e) and $CaSrFe_{0.8}Co_{0.8}Mn_{0.4}O_6$ (1.34 e). The PDOS of $CaSrFe_{0.6}Co_{0.6}Mn_{0.8}O_6$ and $CaSrFe_{0.8}Co_{0.8}Mn_{0.4}O_6$ are shown in Figure 9.17. Their e_g states around the Fermi energy are mainly comprised of Fe and Co contributions, similar to $CaSrFe_{0.75}Co_{0.75}Mn_{0.5}O_6$. However, the density of e_g states around the Fermi energy is reduced in these two compositions compared with $CaSrFe_{0.75}Co_{0.75}Mn_{0.5}O_6$, as shown in Table 9.3. Moreover, the average e_g states hybridization between different transition metals and oxygen $2p$ states in these two compounds is relatively small. Therefore, the catalyst-adsorbate charge transfer in $CaSrFe_{0.6}Co_{0.6}Mn_{0.8}O_6$ and $CaSrFe_{0.8}Co_{0.8}Mn_{0.4}O_6$ is expected to be weaker than that of $CaSrFe_{0.75}Co_{0.75}Mn_{0.5}O_6$, resulting in reduced catalytic activity.
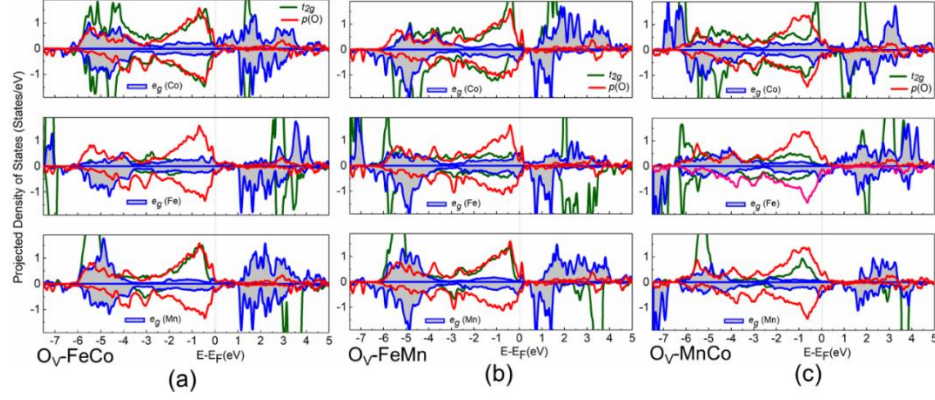
Figure 9.18: Spin-polarized projected density of states of e_g and t_{2g} orbitals of Co, Fe and Mn, as well as O $2p$ in $CaSrFe_{0.75}Co_{0.75}Mn_{0.5}O_{6-\delta}$ with one oxygen vacancy located in (a) Fe-Co bridge (O_v-FeCo), (b) Fe-Mn bridge (O_v-FeMn), and (c) Mn-Co bridge (O_v-MnCo).
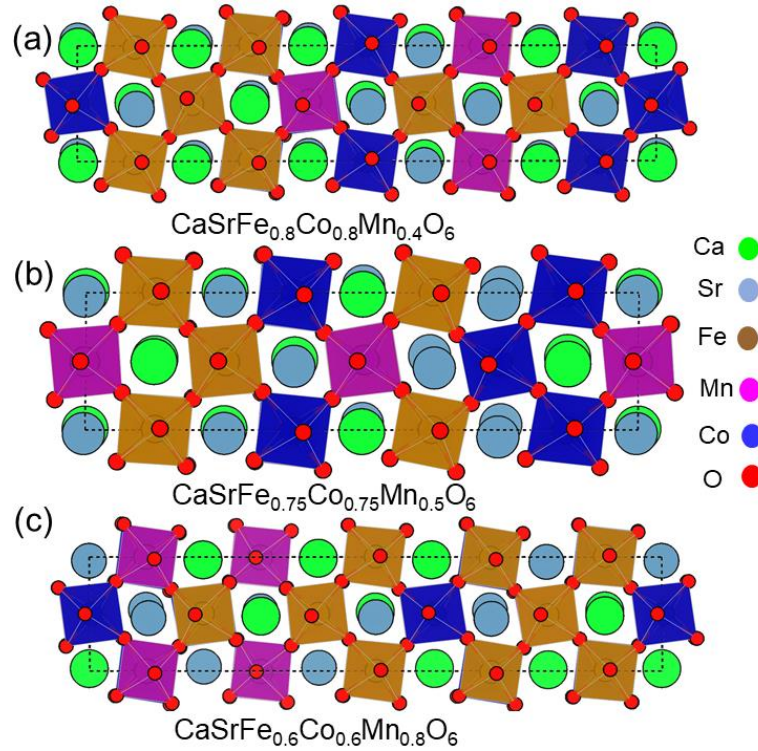
Figure 9.19: Atomic models of special quasirandom structures used to simulate (a) $CaSrFe_{0.8}Co_{0.8}Mn_{0.4}O_6$, (b) $CaSrFe_{0.75}Co_{0.75}Mn_{0.5}O_6$, and (c) $CaSrFe_{0.6}Co_{0.6}Mn_{0.8}O_6$.

We have calculated the e_g orbital occupation in $CaSrFe_{0.75}Co_{0.75}Mn_{0.5}O_6$, as well as

$CaSrFe_{0.6}Co_{0.6}Mn_{0.8}O_6$ and $CaSrFe_{0.8}Co_{0.8}Mn_{0.4}O_6$, from the PDOS, shown in Figure 9.16

and Table 9.4. The results show that e_g orbital occupancy of the three transition metals in

CaSrFe$_{0.75}$Co$_{0.75}$Mn$_{0.5}$O$_6$, is similar, with an average value of ~0.87e. The average e_g occupancy of the three transition metals decreases to 0.73e in CaSrFe$_{0.8}$Co$_{0.8}$Mn$_{0.4}$O$_6$ and 0.69e in CaSrFe$_{0.6}$Co$_{0.6}$Mn$_{0.8}$O$_6$. The relation between the e$_g$ orbital occupancy and electrocatalytic activity has been previously studied for some other perovskite-type oxides, such as (Ln$_{0.5}$Ba$_{0.5}$)CoO$_{3-\delta}$[361] and Nd$_{1-x}$Ba$_x$MnO$_{3-\delta}$.[70] A similar effect has also been investigated for oxides such IrO$_2$, where Cu coping has been used to tune the electron occupation between t$_{2g}$ and e$_g$ states, resulting in the enhancement of electrocatalytic properties.[364]

Table 9.3: The average e_g density of states around Fermi level (E$_F$ - 0.026, E$_F$ + 0.026). Here at room temperature (298K), kT = 0.026 eV is used as a reference.

e_g intensity (States/eV)	CaSrFe$_{0.6}$Co$_{0.6}$Mn$_{0.8}$O$_6$ (1×10^{-2})	CaSrFe$_{0.75}$Co$_{0.75}$Mn$_{0.5}$O$_6$ (1×10^{-2})	CaSrFe$_{0.8}$Co$_{0.8}$Mn$_{0.4}$O$_6$ (1×10^{-2})
Co	2.86	4.44	2.43
Fe	3.95	6.58	1.62
Mn	0.94	2.28	2.33
Average	2.58	4.43	2.13

Table 9.4: The e_g orbital occupations (es) assuming no vacancy, as well as situations with oxygen vacancy in Fe-Mn bridge (Ov-FeMn), Fe-Co bridge (Ov-FeCo) and Mn-Co (Ov-MnCo) bridge.

CaSrFe$_{0.6}$Co$_{0.6}$Mn$_{0.8}$O$_6$	e_g (Fe)	e_g (Mn)	e_g (Co)	e_g (average)
No vacancy	0.86	0.41	0.80	0.69
Ov-FeMn	0.86	0.42	0.82	
Ov-FeCo	0.86	0.41	0.74	0.70
Ov-MnCo	0.88	0.50	0.88	
CaSrFe$_{0.75}$Co$_{0.75}$Mn$_{0.5}$O$_6$				
No vacancy	0.88	0.83	0.89	0.87
Ov-FeMn	0.42	0.77	0.84	
Ov-FeCo	0.88	0.82	0.74	0.72
Ov-MnCo	0.77	0.42	0.84	
CaSrFe$_{0.8}$Co$_{0.8}$Mn$_{0.4}$O$_6$				
No vacancy	0.60	0.95	0.64	0.73

Ov-FeMn	0.84	0.79	0.45	
Ov-FeCo	0.64	0.60	0.42	0.64
Ov-MnCo	0.60	0.83	0.61	

In addition to the e_g-occupancy, we find that the free e_g carriers can also be used as a descriptor for electrocatalytic activity in this class of compounds. An analysis of free e_g carriers at room temperature (Figure 9.16b) shows that the best catalyst, $CaSrFe_{0.75}Co_{0.75}Mn_{0.5}O_6$, has the largest free carriers among the three compounds. This indicates a more facile charge transfer between the catalyst and the reaction intermediates, which can enhance the catalytic activity.

It is noted that there is oxygen deficiency in all experimental samples, with the oxygen site occupancy being close to 0.90 for all materials. Therefore, we incorporated oxygen vacancies in DFT models (Figure 9.18) and analyzed the electronic structure of these compounds. The results show the same trend of e_g orbital distribution and occupation (Table 9.4) for the three compounds. The density of e_g states around E_F in $CaSrFe_{0.75}Co_{0.75}Mn_{0.5}O_{6-\delta}$ is again the largest among all compounds, and its average e_g orbital occupancy is higher than $CaSrFe_{0.6}Co_{0.6}Mn_{0.8}O_{6-\delta}$ and $CaSrFe_{0.8}Co_{0.8}Mn_{0.4}O_{6-\delta}$.

Overall, DFT calculations show that the enhanced electrocatalytic activity of $CaSrFe_{0.75}Co_{0.75}Mn_{0.5}O_{6-\delta}$ can be attributed to: (a) greater density of e_g states around the Fermi energy, (b) optimum electron occupancy of e_g states, resulting in moderate binding between catalyst and reaction intermediates, (c) enhanced hybridization between transition metals and oxygen $2p$ states, and (d) the number of free e_g carriers, which in concert with

optimum e_g-occupancy and hybridization, can facilitate efficient charge-transfer and enhance the electrocatalytic activity.

We note that electronic structure of these materials is a function of crystal structure and the ratio of transition metals, Fe/Co/Mn. While the optimum e_g filling correlates with high electrocatalytic activity, the underlying factors that lead to a certain type of e_g filling are indeed related to the structure and composition.

9.6 CONCLUSIONS

Controlled manipulation of the composition and structure can be a powerful tool in designing inexpensive electrocatalysts for water splitting based on transition metal oxides. Systematic control of the composition can result in structural transformations, which in turn affect the catalytic activity. We have shown that it is possible to find an optimum oxide system, with perovskite-type structure, which exhibits remarkable electrocatalytic properties for water splitting. The new catalyst, CSFCM, shows intrinsic catalytic activity in bulk form without the need for additional processing or microfabrication. This catalyst is highly stable and can be used for hundreds of cycles of catalysis. It features optimum e_g occupancy and free e_g carriers, which correlate with its high electrocatalytic activity.

CHAPTER 10

Sr$_3$Mn$_2$O$_6$ AND Sr$_3$FeMnO$_6$ FOR OXYGEN AND HYDROGEN EVOLUTION

ELECTROCATALYSIS

In this chapter, the bifunctional electrocatalytic activity in oxygen-deficient RP oxides, Sr$_3$Mn$_2$O$_6$ and Sr$_3$FeMnO$_6$ is demonstrated. Structural studies on similar systems, Sr$_3$Mn$_2$O$_{7-\delta}$[365] and Sr$_3$FeMnO$_{7-\delta}$,[366] have been reported, where the degree of oxygen deficiency is lower ($\delta = 0 - 0.5$). In this work, the careful control of synthesis conditions using inert atmosphere has resulted in a greater degree of oxygen-deficiency, to form Sr$_3$Mn$_2$O$_6$ and Sr$_3$FeMnO$_6$, similar to the previously reported materials Sr$_3$Co$_2$O$_6$[367] and Sr$_3$Fe$_2$O$_6$.[368] In addition, the significant enhancement of electrocatalytic activity toward both OER and HER for Sr$_3$FeMnO$_6$ as compared to Sr$_3$Mn$_2$O$_6$, has been observed The observation of bifunctional electrocatalytic properties for Sr$_3$FeMnO$_6$ is remarkable.

10.1 STRUCTURAL CHARACTERIZATION

Since both materials were synthesized under argon atmosphere using oxides of trivalent manganese and iron, the ideal formulas should be Sr$_3$Mn$_2$O$_6$ and Sr$_3$FeMnO$_6$, to maintain the charge neutrality. Iodometric titrations were used to reliably determine the oxygen content. These experiments indicate oxygen stoichiometries of Sr$_3$Mn$_2$O$_{6.04(2)}$ and Sr$_3$FeMnO$_{5.96(2)}$. Rietveld refinements using powder X-ray diffraction data show that the two materials are isostructural and have a tetragonal structure with space group *I4/mmm*,

similar to that reported for several analogous oxygen-deficient Ruddlesden-Popper systems, such as $Sr_3Co_2O_6$,[367] $Sr_3Fe_2O_6$,[368] and $La_{1.9}Ca_{1.1}Cu_2O_6$.[369]
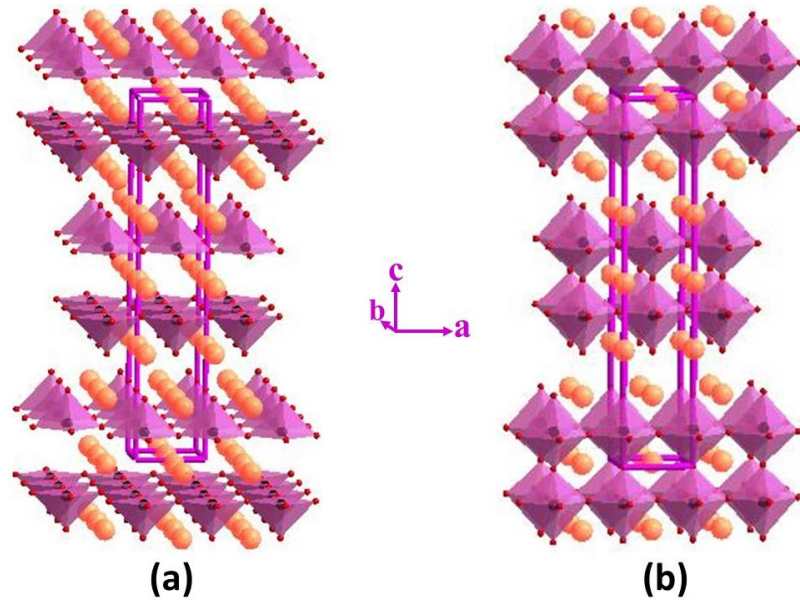
Figure 10.1: (a) Crystal structure of $Sr_3Mn_2O_6$ and Sr_3FeMnO_6. The (Fe/Mn)O_5 square-pyramids are shown in purple and Sr atoms are in orange. (b) Typical Ruddlesden-Popper structure is shown for comparison.

Table 10.1: Refined structural parameters for $Sr_3Mn_2O_6$ using powder X-ray diffraction data. Space group: *I4/mmm,* a = 3.84393(8) Å, b = 3.84393(8) Å, c = 20.2105(5) Å, Rp=0.0558, wRp= 0.0785, χ^2 = 2.589.

Elements	x	y	z	Uiso	Occupancy	Multiplicity
Sr1	0.0	0.0	0.5	0.021(2)	1	2
Sr2	0.0	0.0	0.3153(2)	0.036(2)	1	4
Mn1	0.0	0.0	0.0996(3)	0.013(2)	1	4
O1	0.0	0.5	0.1011(7)	0.035(3)	1	8
O2	0.0	0.0	0.1884(9)	0.035(3)	1	4
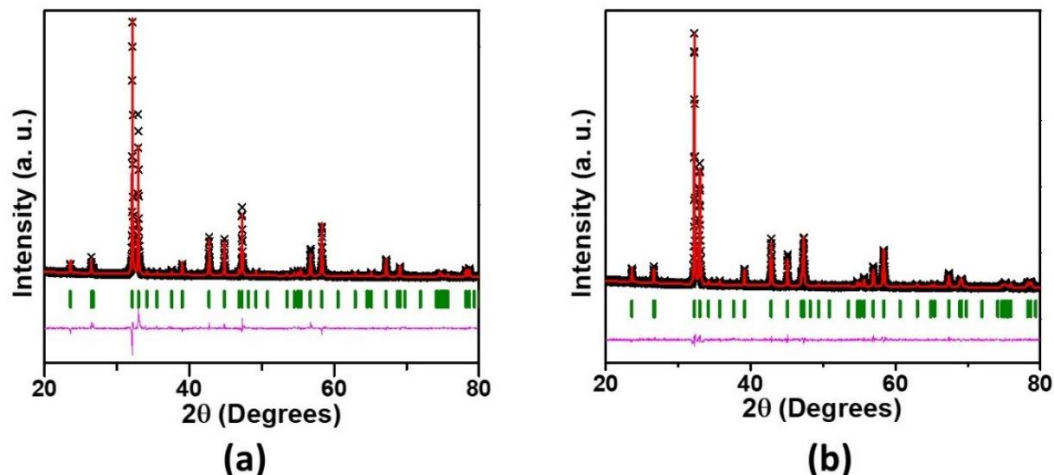
Figure 10.2: Rietveld refinement profile for powder X-ray diffraction data of **(a)** $Sr_3Mn_2O_6$ and **(b)** Sr_3FeMnO_6. Black crosses, red line, vertical green tick marks and lower magenta line represent experimental data, the model, peak positions, and difference plot, respectively.

Table 10.2: Refined structural parameters for Sr_3FeMnO_6 using powder X-ray diffraction data. Space group: *I4/mmm,* a = 3.8446(4) Å, b = 3.8446(4) Å, c = 20.123(2) Å, Rp=0.0399, wRp= 0.0512, χ^2 = 1.596.

Elements	x	y	z	Uiso	Occupancy	Multiplicity
Sr1	0.0	0.0	0.5	0.036(2)	1	2
Sr2	0.0	0.0	0.3177(2)	0.027(2)	1	4
Fe1	0.0	0.0	0.1005(2)	0.015(2)	0.5	4
Mn1	0.0	0.0	0.1005(2)	0.015(2)	0.5	4
O1	0.0	0.5	0.0910(8)	0.087(9)	1	8
O2	0.0	0.0	0.193(1)	0.087(9)	1	4

Figure 10.2 shows the Rietveld refinement profiles for both compounds, and Tables 10.1 and 10.2 list the refined structural parameters. Compared to a typical Ruddlesden-Popper structure (Figure 10.1b) that has the general formula $A_3B_2O_7$, these two materials feature an oxygen-deficiency (Figure 10.1a), leading to the formula $A_3B_2O_6$. A typical Ruddlesden-Popper structure with *I4/mmm* space group has oxygen atoms on three crystallographic sites, 0,½,z, 0,0,z, and 0,0,0. In oxygen-deficient systems, the latter site is commonly vacant or partially occupied.[367-370] As a consequence of this, the coordination

geometry around Fe and Mn changes from octahedral to square-pyramidal. This leads to 2-dimensional layers of corner-sharing $(Fe/Mn)O_5$ square-pyramids, which alternate in orientation and are separated by Sr atoms (orange spheres in Figure 10.1a). Scanning electron microscopy (SEM) was used to investigate the microstructure of both materials. As observed in Figure 10.3, the SEM micrographs show that grain sizes are larger for Sr_3FeMnO_6 as compared with those of $Sr_3Mn_2O_6$.
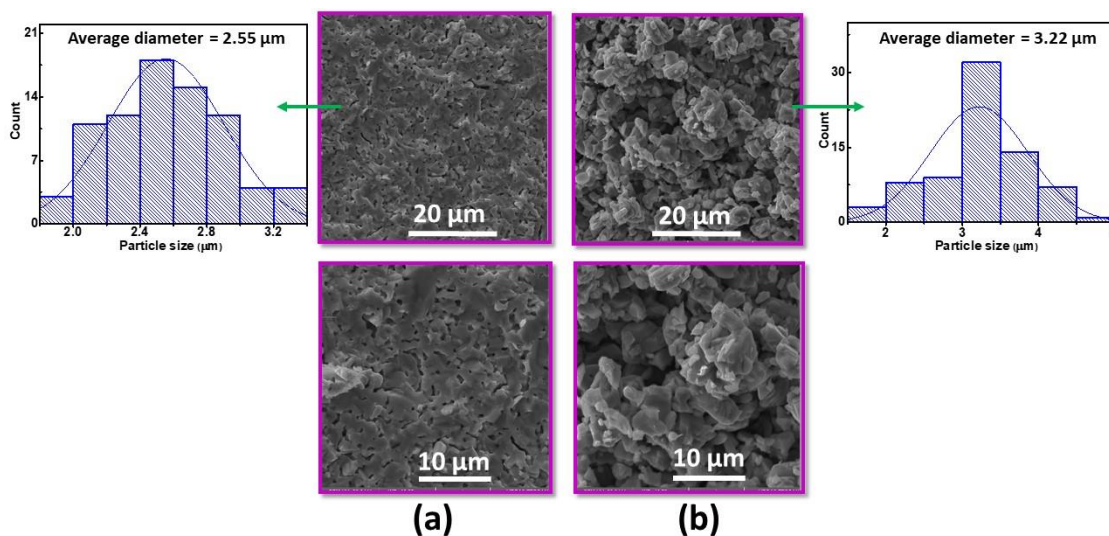
Figure 10.3: Scanning electron microscopy images for **(a)** $Sr_3Mn_2O_6$ and **(b)** Sr_3FeMnO_6.

10.2 ELECTROCATALYTIC ACTIVITY FOR HYDROGEN-EVOLUTION REACTION

The electrocatalytic activity for hydrogen-evolution reaction (HER) was studied for both compounds in 1M KOH, as commonly utilized for HER.[371, 372] The onset potential and the overpotential at 10 mA/cm^2 are the two most important parameters for evaluation of the electrocatalytic activity for HER during heterogeneous catalysis.[234, 309, 373] The onset potential corresponds to the start of the Faradaic process, where a rise of current begins.

An onset potential of almost 0.0 V versus RHE is observed for the benchmark Pt/C (20 wt. % Pt) catalyst.[77, 183] The HER polarization curves of $Sr_3Mn_2O_6$ and Sr_3FeMnO_6 are shown in Figure 10.4a, where the respective onset potential values of ~ –0.38 V and –0.30 V are observed. Similarly, the corresponding overpotential (η_{10}) values are –0.59 V and –0.45 V at –10 mA/cm^2 (Figure 10.4a) for both catalysts. The best performing catalyst, Sr_3FeMnO_6, is also very stable, as shown by the chronopotentiometry data in the inset of Figure 10.4a. While there are some oxide, such as $PrBaCo_2O_{5+\delta}$ (η_{10} = –0.356 V),[69] and $CaSrFeMnO_{6-\delta}$ (η_{10} = –0.39 V)[81] which show better catalytic performance, the overpotential values of the catalysts in this work are better than those of some other oxide catalysts in alkaline electrolyte, such as the perovskite oxide $Ba(Fe_{0.7}Ta_{0.3})O_{3-\delta}$ (η_{10} = ~ –0.70 V).[374]

The evaluation of the reaction kinetics is done using Tafel slopes. The Tafel equation, η = a + b log j (where η is overpotential and j is current density), is utilized to determine the Tafel slope from the linear fit to the plot of η versus log j (Figure 10.4b), where the data from the curved region of the polarization curve are considered.[86, 292, 310] We note that the cathodic and anodic scans in polarization curves of these materials almost overlap. Nevertheless, the average of both scans are commonly used for evaluation of the electrocatalytic activity.[74, 350, 375-377] Faster electron transfer during the HER process is indicated by a smaller value of the Tafel slope. As shown in Figure 10.4b, Tafel slopes for $Sr_3Mn_2O_6$ and Sr_3FeMnO_6 are determined to be 240 mV/dec and 215 mV/dec, respectively. These are in the same range as the values reported for some other HER catalysts, such as $MgCr_2O_4$ (217.51 mV/dec)[378] and CuO (243 mV/dec).[379] The smaller Tafel slope for Sr_3FeMnO_6 compared to that of Sr_3FeMnO_6 indicates faster reaction kinetics and is consistent with the higher electrocatalytic activity of the former material.
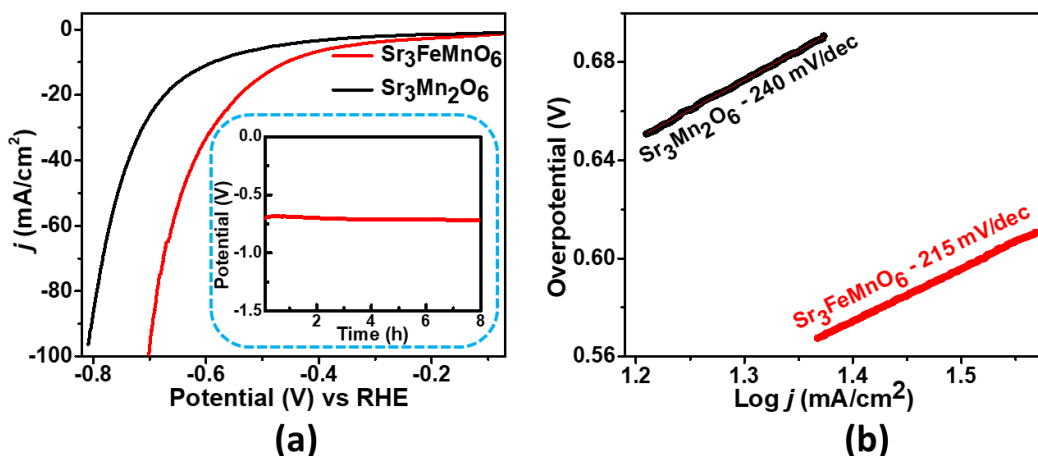
Figure 10.4: (a) HER polarization curves in 1 M KOH. The inset shows chronopotentiometry data for Sr_3FeMnO_6. (b) The Tafel plot showing Tafel slopes for both compounds.

10.3 ELECTROCATALYTIC ACTIVITY FOR OXYGEN-EVOLUTION REACTION

The electrocatalytic activity for oxygen-evolution reaction (OER) was studied for both compounds in 0.1M KOH, as commonly used for OER.[317, 318, 380] Figure 10.5a shows the polarization curves from cyclic voltammetry for both materials. Similar to the HER, the onset potential, overpotential at 10 mA cm^{-2}, and Tafel slope were evaluated. The corresponding onset potentials for Sr_3FeMnO_6 and $Sr_3Mn_2O_6$ are 1.51 V and 1.63 V, respectively. The onset potential of Sr_3FeMnO_6 is close to that of the well-known OER catalyst $Ba_{0.5}Sr_{0.5}Co_{0.8}Fe_{0.2}O_{6-\delta}$ (BSCF), ~1.5 V.[319, 320] The OER overpotential (η_{10}) is evaluated as the potential, beyond the ideal 1.23 V, which is needed to deliver the current density of 10 mAcm^{-2}.[212,381] Sr_3FeMnO_6 has an overpotential of $\eta_{10} = 0.59$ V vs RHE, while the data from $Sr_3Mn_2O_6$ does not even reach the current density of 10 mA cm^{-2} (Figure 10.5a). The overpotential of Sr_3FeMnO_6 is not as low as some other electrocatalysts, such as RuO_2 (η_{10}=0.42 V)[382] and BSCF (η_{10}=0.51 V).[290] However, it is

166

comparable to those of several other oxide catalysts, such as $CoFe_2O_4$ ($\eta_{10}=0.59$ V), Co_3O_4 ($\eta_{10}=0.60$ V),[383] and $Ca_2FeMnO_{6-\delta}$ ($\eta_{10}=0.56$ V).[81]
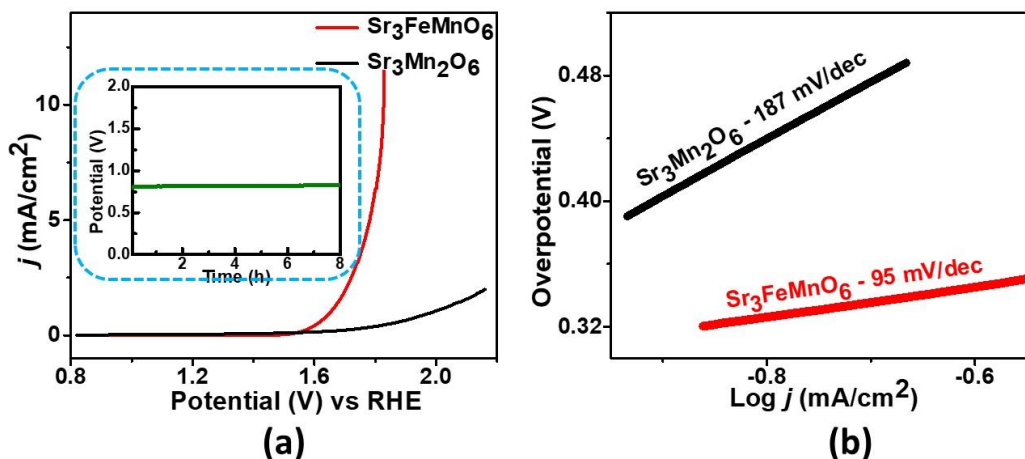
Figure 10.5: (a) OER polarization curves in 0.1 M KOH. The inset shows chronopotentiometry data for Sr_3FeMnO_6. (b) The Tafel plot showing Tafel slopes for both compounds.

The Tafel slopes for OER were obtained from the linear fit of the plot of η versus log j[86, 292, 310] to evaluate the reaction kinetics, which is related to the electron and mass transport.[245, 246] The Tafel slope values of 187 mV/dec and 95 mV/dec (Figure 10.5b) were determined for $Sr_3Mn_2O_6$ and Sr_3FeMnO_6, respectively. This is consistent with the enhanced OER activity of the latter material. Moreover, Sr_3FeMnO_6 is very stable under OER conditions, as shown by the chronopotentiometry data in the inset of Figure 10.5a.

We have also calculated electrochemically active surface area (ECSA) for these two materials. The ECSA is estimated from double-layer capacitance, C_{dl}, in the non-Faradic region.[352] In this region, the current is considered to originate mainly from the electrical double layer charge and discharge, which does not have an electron transfer contribution.[352, 353] The ESCA is calculated from the relation ECSA = C_{dl}/C_s,[244, 352] where C_s is specific capacitance.[244, 352] Therefore, ECSA is directly proportional to C_{dl}. Hence, it

is common practice to use the value of C_{dl} as an indication of the magnitude of ECSA.[185, 294, 384] The C_{dl} value can be obtained from the equation $C_{dl} = j_{average}/v$,[355, 359] where $j_{average}$ is the average of the absolute values of anodic and cathodic current densities in non-Faradic region. The slope of the plot of $j_{average}$ versus v gives the C_{dl} value.

Figures 10.6a and b show the CVs in non-Faradic region, measured at the different scan rates of 10, 20, 40, and 80 mV/s, from which double-layer capacitance (C_{dl}) is obtained. Figure 10.6c shows comparative plots of $j_{average}$ versus v, which indicate the C_{dl} values of 494 µF for Sr_3FeMnO_6 and 194 µF for $Sr_3Mn_2O_6$. This is consistent with the greater electrocatalytic activity of the former material, which also showed lower values of overpotential and Tafel kinetics compared to the latter compound.
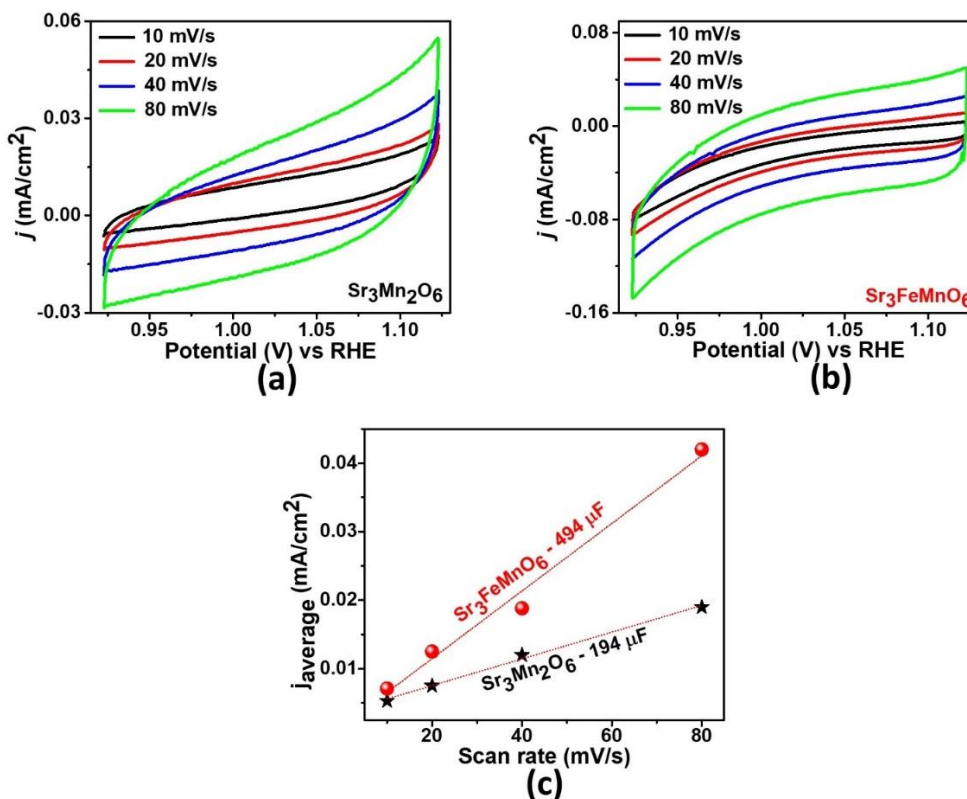
Figure 10.6: (a) and (b) Cyclic voltammetry data in the non-Faradaic region in 1 M KOH. (c) Plot of $j_{average}$ versus scan rate. The double-layer capacitance (C_{dl}) is obtained as the slope of the line of best fit.
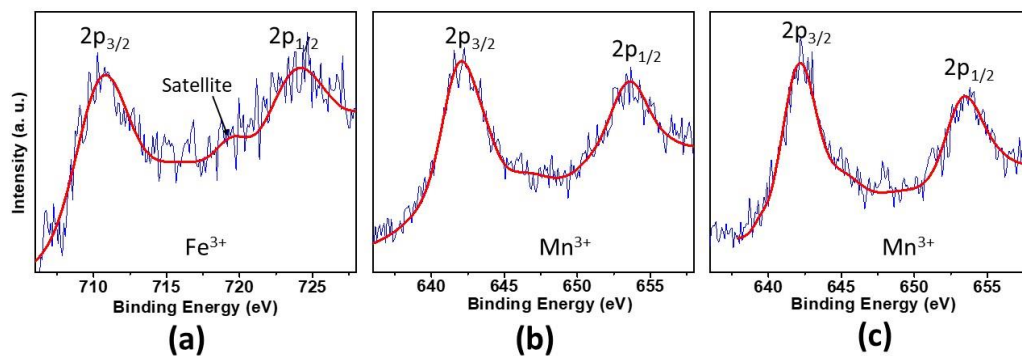
Figure 10.7: (a) and (b) XPS data for Sr_3FeMnO_6, and (c) $Sr_3Mn_2O_6$. In both compounds, binding energies of Fe and Mn indicate trivalent states, that are in line with previous reports.[114, 121]
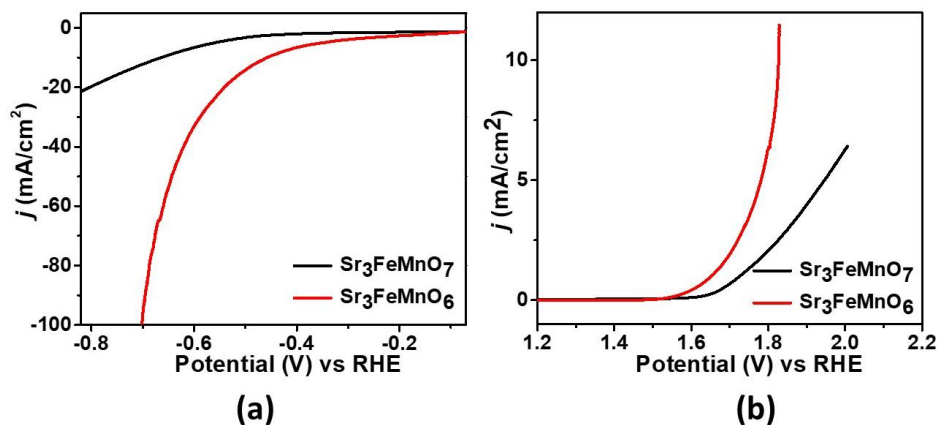
Figure 10.8: (a) HER and (b) OER activity comparison of $Sr_3FeMnO6$ with its parent compound Sr_3FeMnO_7.

The enhanced electrocatalytic properties of Sr_3FeMnO_6 compared with $Sr_3Mn_2O_6$ can be attributed to the electronegativity effect, given the significantly greater electronegativity of Fe relative to Mn. It has been shown previously that the increase in electronegativity results in the lowering of the energy of d orbitals.[385] The lowering of the metal d-band in oxides can result in an improvement of the overlap between metal d and oxygen p bands, leading to enhanced covalency and hybridization,[386, 387] which serve to boost the electrocatalytic activity.[386, 387] Additionally, the XPS data show (Figure 10.7) the trivalent oxidation states of Fe and Mn on both compounds. This creates oxygen vacancies

169

to balance charge on the formula as opposed to the parent phase $A_3B_2O_7$ with tetravalent B-site metals. In fact, the OER and HER activities of the oxygen deficient Sr_3FeMnO_6 compound is better than its parent compound Sr_3FeMnO_7, as shown in Figure 10.8. The remarkable enhancement of the catalytic properties of Sr_3FeMnO_6 is consistent with these electrocatalytic descriptors and indicate the important role of electronegativity in directing functional properties such as electrocatalysis.

10.4 CONCLUSIONS

The 2-dimensional oxides $Sr_3Mn_2O_6$ and Sr_3FeMnO_6 have been synthesized and their structural and electrocatalytic properties have been investigated. Their structures consist of square-pyramidal $(Fe/Mn)O_5$ units that form 2D layers, separated by strontium ions. There is a persistent enhancement of electrocatalytic properties for Sr_3FeMnO_6 as compared to $Sr_3Mn_2O_6$. The former shows enhanced activity toward both OER and HER, exhibiting improved overpotential, Tafel kinetics and electrochemically active surface area. The significantly enhanced electrocatalytic performance is attributed to the effect of electronegativity, given the considerably higher electronegativity of Fe compared with Mn, which can lead to the lowering of the *d*-band energy, resulting in better overlap with oxygen *p* bands.

CHAPETR 11

SYSTEMATIC ENHANCEMENT OF ELECTROCATALYTIC ACTIVITY AS A

FUNCTION OF STRUCTURAL ORDER IN PEROVSKITE OXIDES

In this chapter, a remarkable finding, where the electrocatalytic activity for both

HER and OER is systematically enhanced as a function of vacancy-order, is demonstrated.

In particular, the ordering of vacancies leads to a catalyst which is by far superior to

precious metal catalysts, such as RuO_2. Furthermore, the remarkably high intrinsic activity

of this catalyst enables it to catalyze the HER and OER in bulk form, without the need for

elaborate nanofabrication or composite formation.

11.1 CRYSTAL STRUCTURE

All three materials are synthesized under the same conditions, as described in

chapter 2 (Table 2.1). Iodometric titrations show that the degree of oxygen-deficiency is δ

= 0.5 for $Sr_2FeCoO_{6-\delta}$, δ = 0.8 for $CaSrFeCoO_{6-\delta}$, and δ = 1.0 for $Ca_2FeCoO_{6-\delta}$. Rietveld

refinements (Figure 11.1a and Table 11.1-3) using X-ray diffraction data confirm that the

structure of $Sr_2FeCoO_{6-\delta}$ resembles that of a typical perovskite with octahedral

coordination around transition metals (Figure 11.2a).[12] The vacant oxygen sites are

distributed randomly, as required by the cubic perovskite structure, which contains one

crystallographic position for the A-site, one for the B-site metal, and one for oxygen.

The work described in this chapter is under review in a Journal.
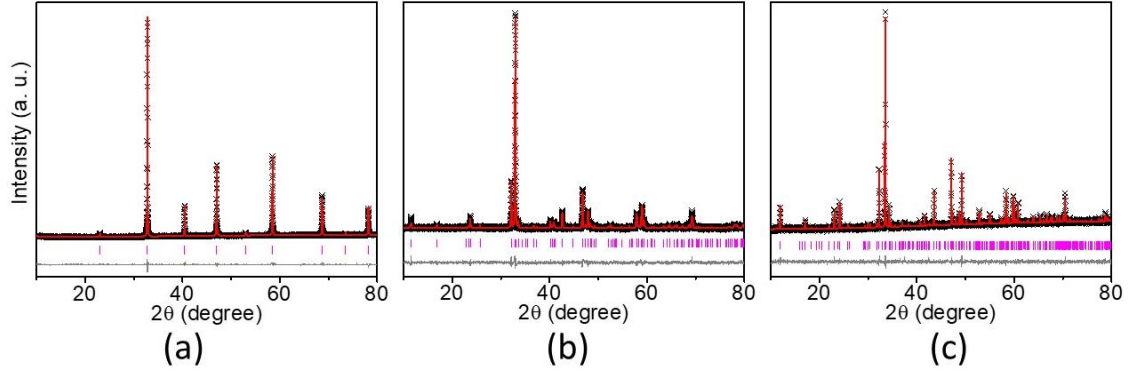
Figure 11.1: The Rietveld refinement profiles using powder X-ray diffraction data for (a) $Sr_2FeCoO_{6-\delta}$ (*Pm-3m*), (b) $CaSrFeCoO_{6-\delta}$ (*Ibm2*), and $Ca_2FeCoO_{6-\delta}$ (*Pbcm*). Black crosses, red line, pink vertical tick marks and lower gray line represent experimental data, the model, peak positions, and the difference plot, respectively.

Table 11.1: Refined structural parameters of $Sr_2FeCoO_{6-\delta}$ using powder X-ray diffraction data. Space group: *Pm-3m;* a = 3.8653(1) Å; R_p = 0.0148, wR_p = 0.0202, χ^2 = 1.05%.

Element	x	y	z	Occupancy	Uiso	Multiplicity
Sr1	0.5	0.5	0.5	1	0.0165(3)	1
Fe1/Co1	0.0000	0.0000	0.0000	0.5/0.5	0.0182(4)	1
O3	0.5	0.0000	0.0000	0.8333	0.0278(7)	3

Table 11.2: Refined structural parameters of $CaSrFeCoO_{6-\delta}$ using powder X-ray diffraction data. Space group: *Ibm2*; a = 5.5576(2) Å, b = 15.1647(5) Å, c = 5.4141(2) Å; R_p = 0.0163, wR_p = 0.0217, χ^2 = 1.77%.

Element	x	y	z	Occupancy	Uiso	Multiplicity
Ca1/Sr1	0.5105(5)	0.1118(2)	-0.003(6)	0.5/0.5	0.021(1)	8
Fe1/Co1	0.0000	0.0000	0.0000	0.5/0.5	0.031(2)	4
Fe2/Co2	0.0769(9)	0.25000	-0.010(8)	0.5/0.5	0.027(2)	4
O1	0.253(11)	0.0010(7)	0.265(8)	1	0.037(3)	8
O2	-0.075(2)	0.1556(6)	-0.005(12)	1	0.037(3)	8
O3	0.363(3)	0.25000	0.851(10)	1	0.037(3)	4

Table 11.3: Refined structural parameters of $Ca_2FeCoO_{6-\delta}$ using powder X-ray diffraction data. Space group: *Pbcm*; a = 5.3686(1) Å, b = 11.1063(2) Å, c = 14.8080(2) Å; R_p = 0.0166, wR_p = 0.0213, χ^2 = 1.31%.

Element	x	y	z	Occupancy	Uiso	Multiplicity
Ca1	-0.005(2)	0.758(2)	0.390(1)	1	0.023(6)	8
Ca2	-0.490(3)	0.515(3)	0.607(2)	1	0.058(2)	8
Fe1/Co1	0.439(4)	0.717(2)	0.25	0.5/0.5	0.041(2)	4

Fe2/Co2	-0.048(3)	0.535(4)	0.25	0.5/0.5	0.030(8)	4
Fe3/Co3	-0.506(3)	0.75	0.5	0.5/0.5	0.033(8)	4
Fe4/Co4	0.000	0.000	0.000	0.5/0.5	0.037(8)	4
O1	0.105(11)	0.661(5)	0.25	1	0.035	4
O2	0.607(10)	0.556(4)	0.25	1	0.035	4
O3	-0.260(11)	0.633(6)	0.490(2)	1	0.035	8
O4	-0.742(12)	0.626(6)	0.490(2)	1	0.035	8
O5	0.029(7)	0.472(6)	0.361(4)	1	0.035	8
O6	0.517(7)	0.784(6)	0.360(4)	1	0.035	8
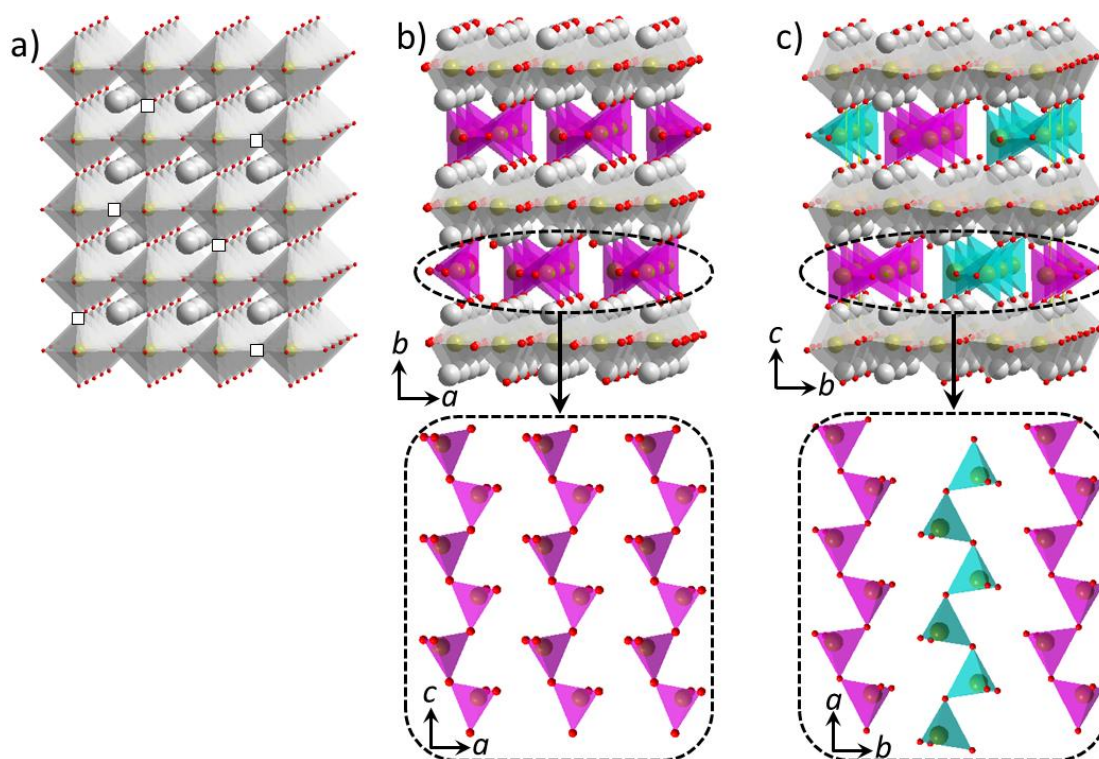
Figure 11.2: (a) Structure of $Sr_2FeCoO_{6-\delta}$, containing a random distribution of oxygen-vacancies, represented by white squares. (b) and (c) show $CaSrFeCoO_{6-\delta}$ and $Ca_2FeCoO_{6-\delta}$, respectively, where oxygen-vacancies only appear in every other layer. Dotted panels show the top view of the orientation of tetrahedral chains that form due to oxygen-vacancies.

However, the decrease in the average ionic radius of the A-site, by incorporation of calcium, leads to an ordered structure in $CaSrFeCoO_{6-\delta}$. The structure and Rietveld refinement profile are shown in Figures 11.2b and 11.1b, respectively.[12] In this structure,

the oxygen-vacancies are present in every other layer, lowering the coordination number of the B-site metals from 6 to 4. This leads to the formation of $(Fe/Co)O_4$ tetrahedral units in every other layer (purple polyhedra in Figures 11.2b). The remaining layers (grey polyhedra in Figures 11.2b) do not have oxygen vacancies and retain the typical octahedral coordination of a perovskite structure. The connectivity of all polyhedra is through corner-sharing. The tetrahedral $(Fe/Co)O_4$ units are connected to form chains that are sandwiched between the octahedral layers. All tetrahedral chains have the same orientation, as observed in Figures 11.2b.

An even higher degree of order can be attained when the average ionic radius of the A-site is decreased further to form $Ca_2FeCoO_{6-\delta}$.[12] In this material, the oxygen-vacancies are ordered, and occur only in every other layer, forming 4-coordinated tetrahedral units similar to the above structure. However, there is an additional degree of order, where the tetrahedral chains that form due to the oxygen vacancies, have alternating orientations (Figures 11.2c), forming an R-L-R-L-… arrangement (R = right handed; L = left handed).

11.2 HYDROGEN AND OXYGEN EVOLUTION ACTIVITIES

There is a methodical increase in the ordering of oxygen-vacancies from $Sr_2FeCoO_{6-\delta}$ (disordered) to $CaSrFeCoO_{6-\delta}$ (ordered) and $Ca_2FeCoO_{6-\delta}$ (highly ordered). These changes correlate directly with electrocatalytic properties. The HER overpotential at 10 mA/cm^2 (η_{10})[247, 293, 388] for the disordered material $Sr_2FeCoO_{6-\delta}$ is 490 mV in 1 M KOH, which is lowered to $\eta_{10} = 390$ mV for the vacancy-ordered material $CaSrFeCoO_{6-\delta}$. Further lowering of the overpotential is observed for the highly ordered material $Ca_2FeCoO_{6-\delta}$, η_{10} = 250 mV (Figure 11.3a). The latter material shows better electrocatalytic activity than

some reported perovskite oxides such as $Ba_{0.5}Sr_{0.5}Co_{0.8}Fe_{0.2}O_{3-\delta}$ ($\eta_{10} = 430$ mV),[284] $La_{0.96}Ce_{0.04}CoO_{3-\delta}$ ($\eta_{10} = 305$ mV),[389] $NdBaMn_2O_{6-\delta}$ ($\eta_{10} = 290$ mV),[70] $CaSrFeMnO_{6-\delta}$, (390 mV),[81] and $SrNb_{0.1}Co_{0.7}Fe_{0.2}O_{3-\delta}$ nanorods (262 mV).[77] There is also a methodical enhancement of the HER kinetics as a function of the structural order, as evident from the slopes of Tafel plots, η vs log j (Figure 11.3b).[184, 185] The decrease in Tafel slope correlates with the increase in structural order, indicating faster charge-transfer and enhanced kinetics for the ordered materials.[245, 246] Furthermore, the enhanced charge-transfer is evident from the systematic decrease in the charge-transfer resistance in impedance spectroscopy data in the HER region,[70] which matches the trend in structural order, as shown in Figure 11.3c. The best catalyst, $Ca_2FeCoO_{6-\delta}$, maintains its high activity for at least 2000 cycles, as demonstrated in Figure 11.3d.

The correlation between the electrocatalytic activity and vacancy-order is also observed for the OER electrocatalysis, as evident from the overpotential values (η_{10}) beyond the thermodynamic potential of 1.23 V at 10 mA/cm^2. The disordered material, $Sr_2FeCoO_{6-\delta}$, shows an overpotential of $\eta_{10} = 280$ mV in 1 M KOH, which is lowered to $\eta_{10} = 270$ mV for the vacancy-ordered material $CaSrFeCoO_{6-\delta}$, and $\eta_{10} = 250$ mV for the highly ordered $Ca_2FeCoO_{6-\delta}$. This is a remarkably low overpotential for a single-phase bulk oxide, based on non-noble metals. It is by far superior to that of the noble metal catalyst RuO_2,[286-288] as shown in Figure 11.4a. The vast majority of the previously reported oxide electrocatalysts show an OER overpotential of $\eta_{10} > 300$ mV, such as $La_{0.6}Sr_{0.4}Co_{0.8}Fe_{0.1}Mn_{0.1}O_3$ (343 mV),[390] $PrBaCo_2O_{5.75}$ (360 mV),[391] $PrBa_{0.25}Sr_{0.75}Co_2O_{5.95}$ (420 mV),[392] and $Pr_{0.5}Ba_{0.5}Co_{0.8}W_{0.2}O_{3-\delta}$ (325 mV).[393]
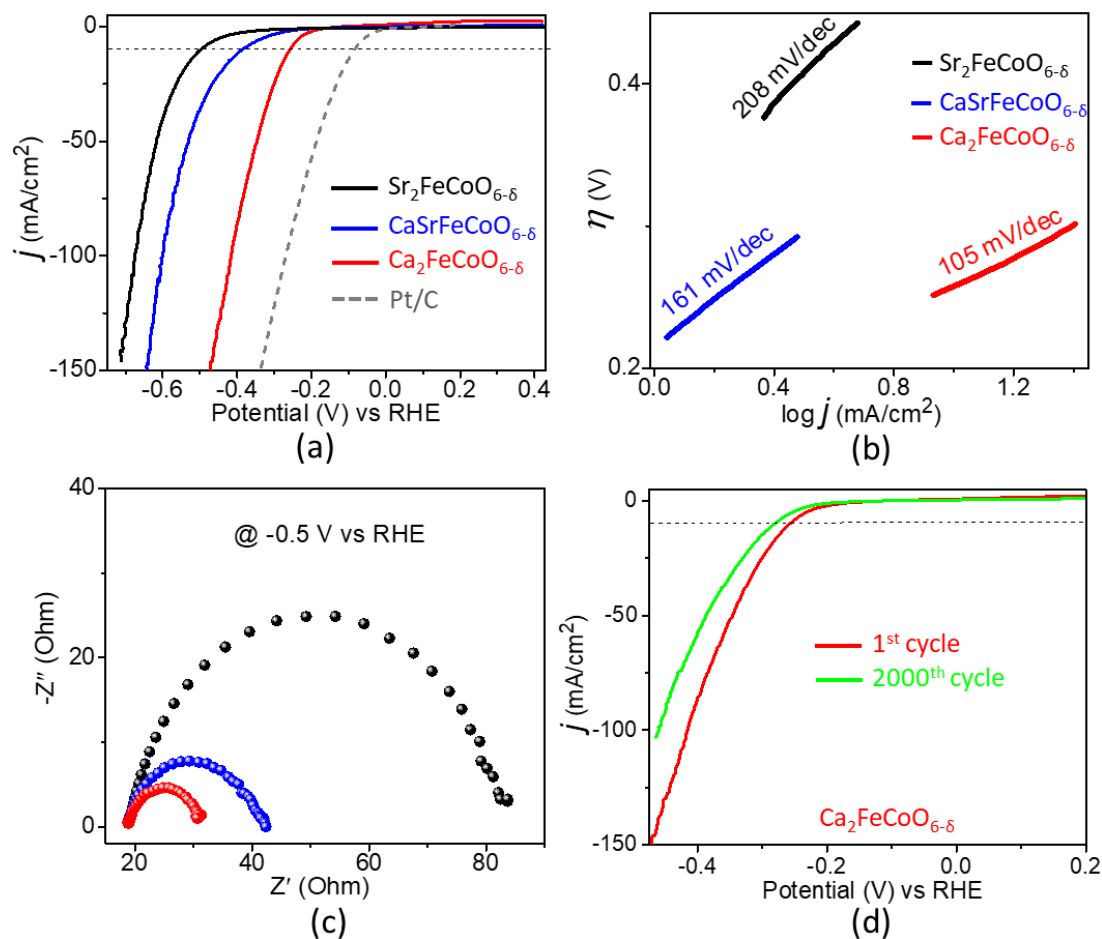
Figure 11.3: (a) HER polarization curves in 1M KOH. (b) Tafel plots and slopes. (c) Impedance spectroscopy data indicating the charge transfer resistance in the HER region. (d) Polarization curve for $Ca_2FeCoO_{6-\delta}$ after 2000 cycles.

In addition, the vacancy-ordered $Ca_2FeCoO_{6-\delta}$ has a unique property, which is its ability to act as a highly active electrocatalyst without the need for nanofabrication, composite formation, or any additional processing. It does not even need the addition of carbon black, which is routinely added to catalysts for OER/HER, indicating its superior intrinsic activity. The few existing oxide catalysts that show such high level of OER activity, often require elaborate nanofabrication processes or multicomponent composite formation. For example, an OER overpotential of $\eta_{10} = 297$ mV has been observed for Co_3O_4/Co-Fe oxide double-shelled nanoboxes, obtained using a multi-step process

involving metal-organic frameworks.[394] Also an overpotential of $\eta_{10} = 240$ mV is reported for 3D hybrid porous $CoFe_2O_4/C$ nanorod arrays supported on nickel foam, obtained from a metal-organic framework.[395] Another example is the reduced necklace-like multishelled hollow structure of a spinel transition-metal oxide, obtained using sacrificial templates of carbonaceous microspheres, which leads to an overpotential of $\eta_{10} = 240$ mV.[396] Catalysts with ultrahigh activity that can be used in bulk form, without intricate nanofabrication or multicomponent composite formation are rare.
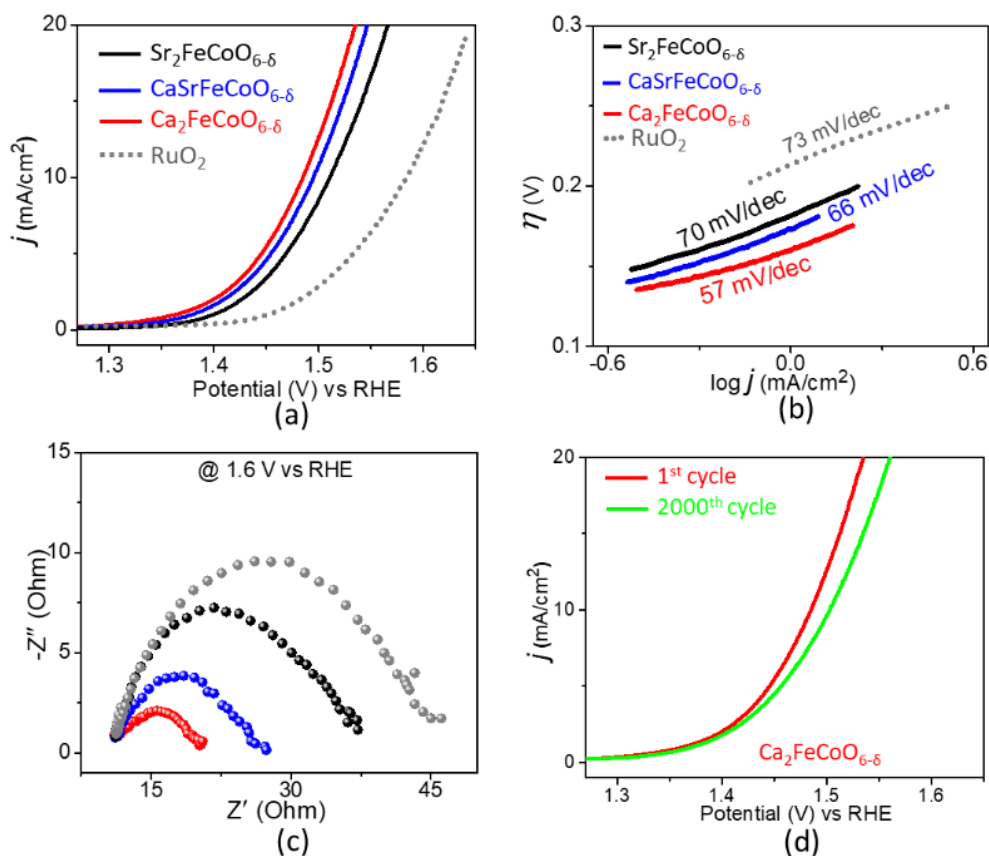
Figure 11.4: (a) OER polarization curves in 1M KOH. (b) Tafel plots and slopes. (c) Impedance spectroscopy data indicating the charge transfer resistance in the OER region. (d) Polarization curve for $Ca_2FeCoO_{6-\delta}$ after 2000 cycles.

The trend in the OER kinetics, evident from the Tafel slopes (Figure 11.4b), and the charge-transfer resistance, from impedance spectroscopy (Figure 11.4c), match the

trend of the electrocatalytic activity. Importantly, the best catalyst, $Ca_2FeCoO_{6-\delta}$, is highly stable and retains its high catalytic activity for at least 2000 cycles, as shown in Figure 11.4d. In addition, the structural integrity and transition metal oxidation states are maintained, as demonstrated by X-ray diffraction and X-ray photoelectron spectroscopy (XPS) experiments before and after 2000 cycles (Figures 11.5).
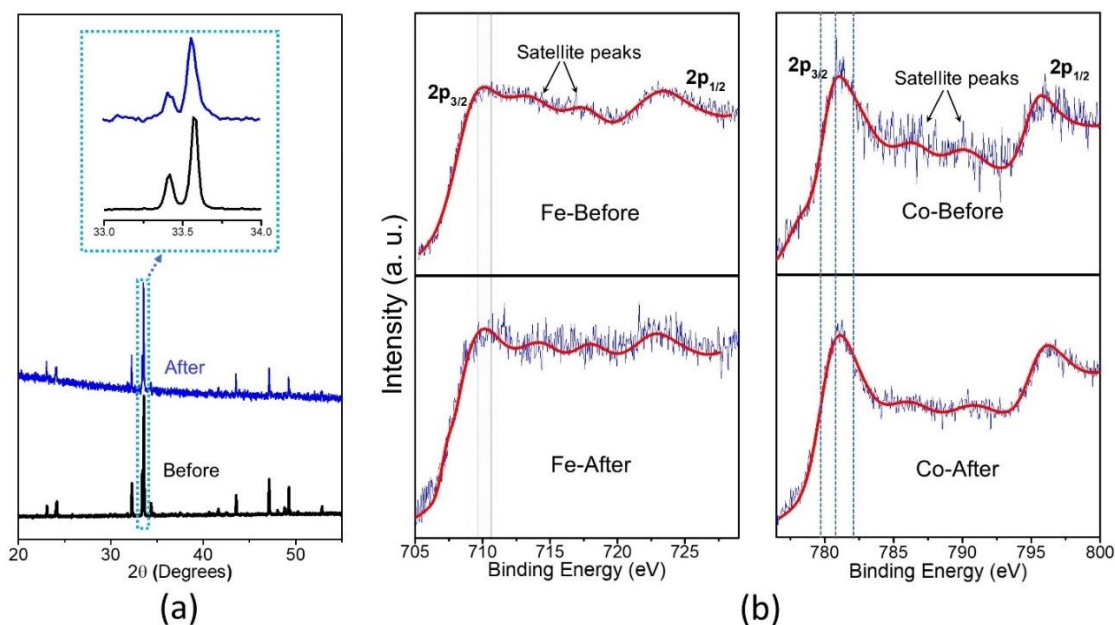
Figure 11.5: (a) X-ray diffraction, and (b) XPS data, before and after 2000 cycles of OER for $Ca_2FeCoO_{6-\delta}$.

11.3 DENSITY FUNCTIONAL THEORY CALCULATIONS

The density functional theory (DFT)[397, 398] framework, implemented in the Vienna Ab-initio Simulation Package (VASP, version 5.4)[399] was used for computational calculations. The Projector Augmented Wave (PAW)[400] was utilized for the electron-ion interactions, and the generalized gradient approximation (GGA)[401] in the scheme of Perdew Burke Ernzerhof (PBE)[402] was used for treatment of electron exchange-correlation interactions. The spin polarized behavior was also taken into consideration. The

Congregate-Gradient algorithm,[403] implemented in VASP, was used for structural relaxation. The energy cutoff for the plane wave basis was set at 400 eV, and the criteria for convergences of energy and force in relaxation processes were set to be 10^{-5} eV and 10^{-4} eV/Å, respectively. Primitive cells, 1×1×1 for *pbcm* and 2×2×2 for *Pm-3m* symmetry, were chosen. The respective Brillouin zones (BZ) were sampled by $11 \times 7 \times 5$ and $9 \times 9 \times 9$ k-point meshes, created based on the Monkhorst-Pack scheme.[404] The LDA+U Approach (A Simple Hubbard Correction for Correlated Ground States) was adopted[405] with tested Hubbard (U) values for Fe (5.3 eV) and Co (5.8 eV), respectively. A Gaussian smearing method was used to determine the partial occupancies of electrons on orbitals during the relaxation process and the tetrahedron method with Blöchl corrections was used for electronic density-of-states calculations. The electronic band structures were calculated at the DFT-PBE level.

To explore the effect of structural order in more depth, we conducted density functional theory (DFT) calculations on the disordered material $Sr_2FeCoO_{6-\delta}$, as well as the highly ordered compound $Ca_2FeCoO_{6-\delta}$ (Figure 11.6). These calculations indicate that the structural order leads to a methodical shift of centers of the transition-metal *d*-bands and oxygen *p*-band toward the Fermi level. For the disordered system $Sr_2FeCoO_{6-\delta}$, the centers of the bands are at -4.885 eV (Fe *d*), -4.446 eV (Co *d*), and -2.417 eV (O *p*). On the other hand, DFT calculations for the ordered material $Ca_2FeCoO_{6-\delta}$ show a shift toward the Fermi level, leading to band center energies of -4.403 eV (Fe *d*), -3.713 eV (Co *d*), and -2.215 eV (O *p*). It has been previously proposed that the shift in the center of the *d*-band toward the Fermi level can result in enhanced interactions with the OER intermediates,[299, 300] leading

to an improvement in the electrocatalytic activity. A further outcome of the structural order, indicated by DFT calculations, is a greater proximity of the centers of the transition-metal d-bands to the oxygen p-band for $Ca_2FeCoO_{6-\delta}$ as compared to $Sr_2FeCoO_{6-\delta}$. Some researchers have suggested that this proximity leads to enhanced covalency and a greater degree of p-character of the transition metal d bands, resulting in better charge-transfer between the catalyst and the oxygen-containing intermediates.[297] Therefore, in transition from a disordered system to an ordered structure, the combined effect of the shift of the band centers toward the Fermi level and the enhanced proximity of the centers of the metal d and oxygen p bands can contribute to the remarkable enhancement of the electrocatalytic activity.
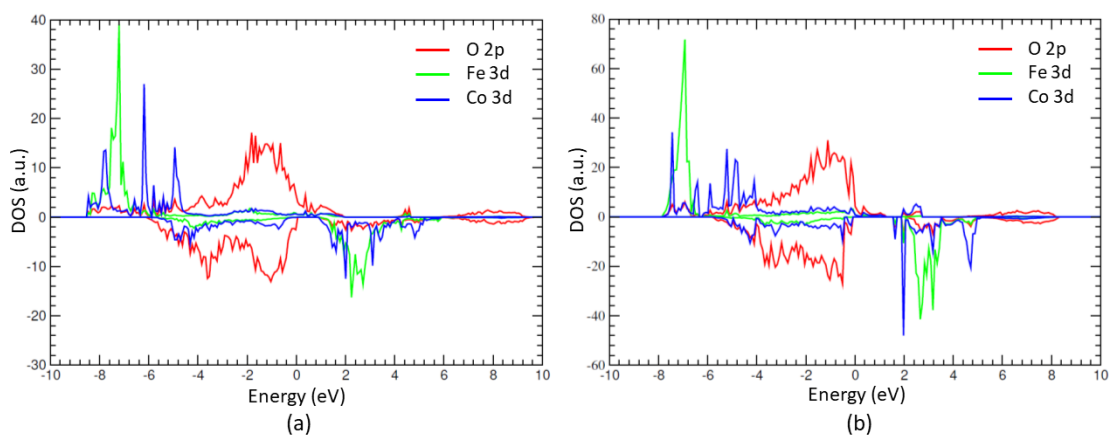
Figure 11.6: Density of States (DOS) from DFT calculations on (a) disordered $Sr_2FeCoO_{6-\delta}$, and (b) ordered $Ca_2FeCoO_{6-\delta}$.

To further demonstrate the impact of structural order, we conducted additional DFT calculations for $Ca_2FeCoO_{6-\delta}$ using a hypothetical disordered model. The hypothetical structure was similar to that of $Sr_2FeCoO_{6-\delta}$, but contained calcium instead of strontium. The simulations indicated that a hypothetical disordered structure for $Ca_2FeCoO_{6-\delta}$ would

have lower band center energies, -5.2023 eV (Fe *d*) and -4.3388 eV (Co *d*), compared to those of the real, ordered structure of $Ca_2FeCoO_{6-\delta}$. These findings indicate that a disordered structure, whether containing Sr or Ca, consistently has lower band energies than the ordered structure. These calculations underline the crucial impact of structural order in modifying the electronic structure and the subsequent enhancement of the electrocatalytic performance.

11.4 CONCLUSIONS

In summary, we have shown a remarkably high electrocatalytic performance, achieved through a novel approach, i.e., the systematic increase in the degree of ordering of oxygen-vacancies. This approach leads to a remarkably low overpotential for an oxide catalyst, which can be used in bulk form, without the need for elaborate nanofabrication, multi-component composite formation, or any additional processing. We propose that the modification of the ordering schemes of oxygen-vacancies can be used as a tool for the design of highly active oxide electrocatalysts for water electrolysis.

CHAPTER 12

ENHANCED PERFORMANCE OF AN OXIDE ELECTROCATALYST,

BaSrCoMoO$_6$, FOR BOTH HYDROGEN AND OXYGEN EVOLUTION REACTIONS

This chapter presents a remarkable bifunctional electrocatalyst BaSrCoMoO$_6$ for both OER and HER in an alkaline medium, which outperforms the catalytic activity of the perovskite-oxide-based benchmark catalyst Ba$_{0.5}$Sr$_{0.5}$Co$_{0.8}$Fe$_{0.2}$O$_{3-\delta}$ (BSCF).[74]

12.1 CRYSTAL STRUCTURE

Both BaSrCoMoO$_6$ and BSCF belong to the perovskite family, represented by the general formula ABO$_3$ (A = Ba/Sr, B = Co/Mo or Co/Fe). Both oxides have cubic structures, but with different space groups, *Fm-3m*[23-25] for BaSrCoMoO$_6$ and *Pm-3m*[17] for BSCF. As we have previously described,[85] the structure of BaSrCoMoO$_6$, consists of six-coordinated Co^{2+} and Mo^{6+} ions, which are ordered in the material lattice (Figure 12.1). On the other hand, BSCF does not have such ordering pattern and both Fe and Co share the same crystallographic site.[17] Figures 12.2-12.3 and Tables 12.1-12.2 provide further information about structural analyses of these materials.
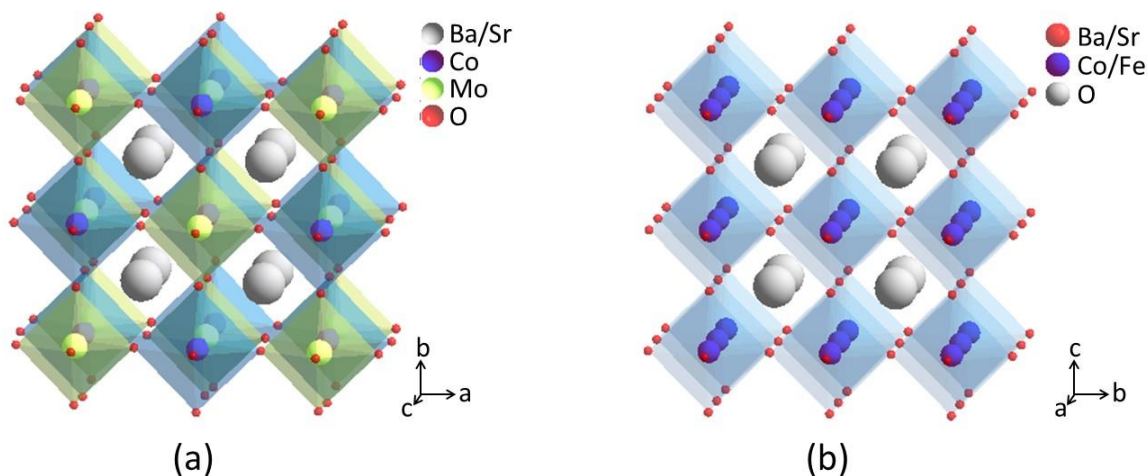
Figure 12.1: (a) Crystal structure of $Ba_{0.5}Sr_{0.5}Co_{0.5}Mo_{0.5}O_3$ (BaSrCoMoO$_6$). Note the ordering of Co and Mo. (b) Crystal structure of $Ba_{0.5}Sr_{0.5}Co_{0.8}Fe_{0.2}O_{3-\delta}$.

Table 12.1: The refined structural parameters of BaSrCoMoO$_6$ using PXRD data. Space group: *Fm-3m* (#225) a = 7.9913(1) Å, R_p = 0.0400, wR_p = 0.0557, χ^2 = 3.00%.

Element	x	y	z	Occupancy	Uiso	Multiplicity
Ba1/Sr1	0.25	0.25	0.25	0.5	0.017(6)	8
Co1	0.5	0.5	0.5	1	0.013(2)	4
Mo1	0	0	0	1	0.014(1)	4
O1	0.2428(7)	0	0	1	0.014(2)	24

Table 12.2: The refined structural parameters of $Ba_{0.5}Sr_{0.5}Co_{0.8}Fe_{0.2}O_{3-\delta}$ (BSCF) using PXRD data. Space group: *Pm-3m* (#221) a = 3.99413(24) Å, R_p = 0.0175, wR_p = 0.0260, χ^2 = 1.45%.

Element	x	y	z	Occupancy	Uiso	Multiplicity
Ba1/Sr1	0.5	0.5	0.5	0.5/0.5	0.0210(5)	1
Co1/Fe1	0	0	0	0.8/0.2	0.0300(7)	1
O1	0.5	0	0	1	0.071(2)	3
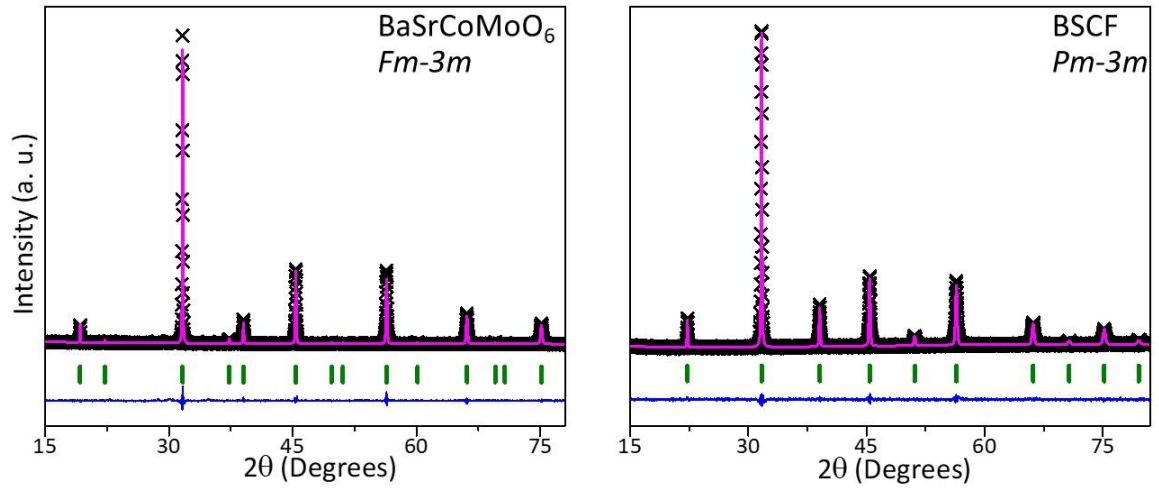
Figure 12.2: Rietveld refinement profiles using powder X-ray diffraction data. The black cross symbols, magenta solid curve, olive vertical tick marks, and the lower blue curve correspond to the experimental data, the calculated pattern for the cubic models, the Bragg peak positions, and the difference plot, respectively.
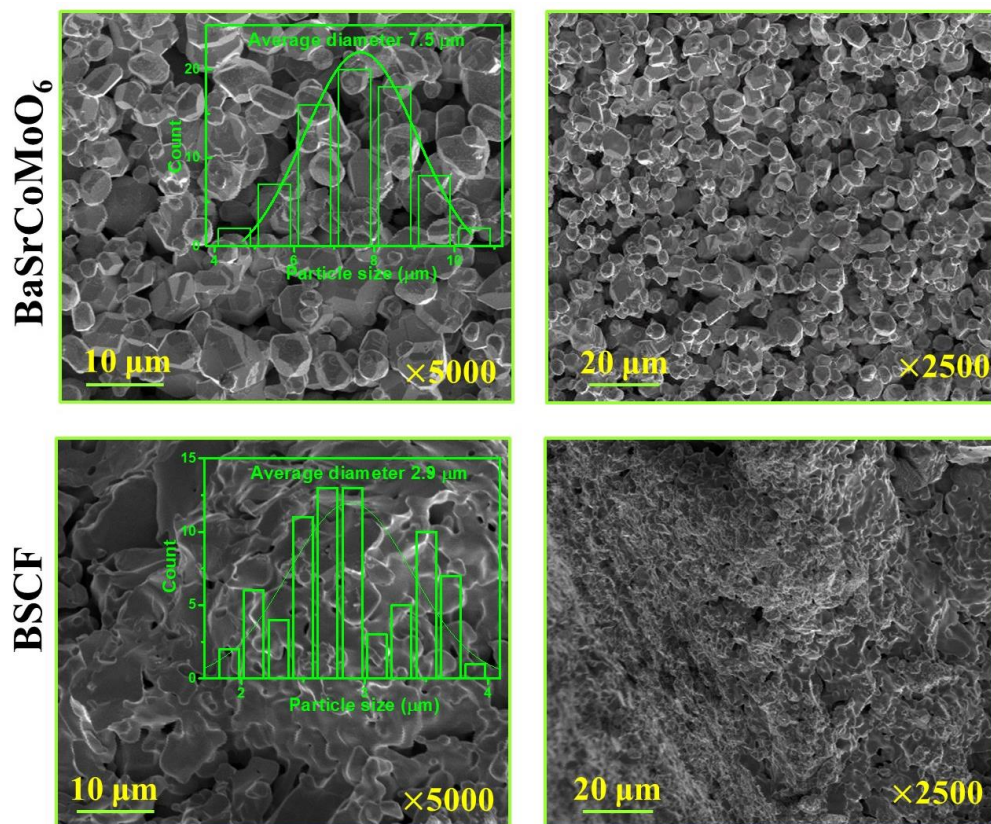
Figure 12.3: SEM images of both compound showing the crystallite size and porosity. The insets on the left panel show the histograms and gaussian fit analysis for the average diameter.

12.2 HYDROGEN AND OXYGEN EVOLUTION ACTIVITIES

The variations in composition and structure have a significant impact on HER and OER activities. As shown in Figures 12.4a, HER experiments in 1 M KOH show the enhanced electrocatalytic performance of $BaSrCoMoO_6$ over BSCF. The overpotential (η_{10}) values required to deliver a current density of 10 mA/cm^2 are 325 mV and 470 mV, respectively. The current density of 10mA/cm^2 is typically adopted as a reference in such studies, as desired for 10% solar-to-fuel conversion efficiency.[284] The observed overpotential for BSCF is close to that of a previous report, η_{10} = 430 mV.[284] The overpotential of $BaSrCoMoO_6$ is significantly lower than that of BSCF. It is also lower

than the values reported for some other highly active perovskite-based electrocatalysts such as $Ba_{0.95}Co_{0.4}Fe_{0.4}Zr_{0.1}Y_{0.1}O_{3-\delta}$ ($\eta_{10} = 360$ mV)[284] and $SrCo_{0.7}Fe_{0.25}Mo_{0.05}O_{3-\delta}$ ($\eta_{10} = 378$ mV).[363] In addition, $BaSrCoMoO_6$ is very stable, as evident from the nearly constant chronopotentiometry response, shown in the inset of Figure 12.4a.
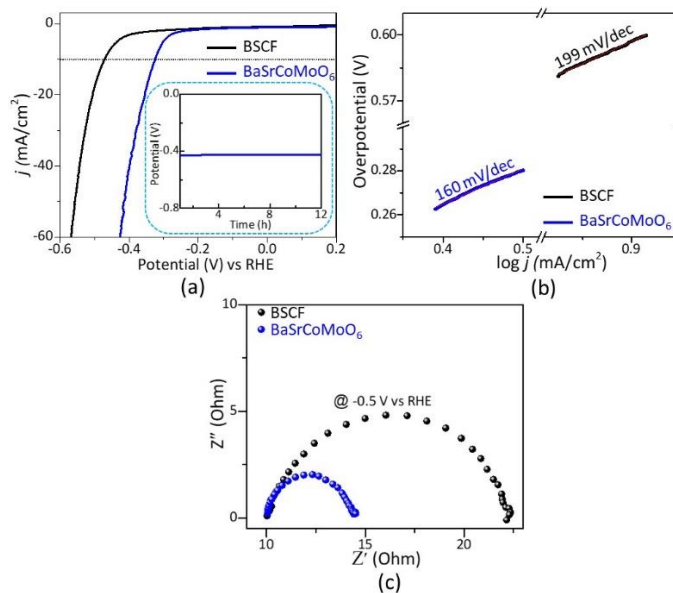
Figure 12.4: (a) HER polarization curves in 1 M KOH. The inset shows the chronopotentiometry data of $BaSrCoMoO_6$ at a current density of 10 mA/cm^2. (b) The Tafel plot showing Tafel slopes. (c) The Nyquist plot recorded in the HER potential region, −0.5 V vs the RHE, indicating lower charge transfer resistance for $BaSrCoMoO_6$.

To examine the kinetics of the reaction, the Tafel equation, $\eta = a + b \log j$, was used where η is the overpotential, and j is the current density. The Tafel slope, *i.e.,* the slope of η versus $\log j$, indicates the kinetics of the reaction.[184, 285] Tafel plot is influenced by the conductivity and mass transport of the catalyst.[245, 246, 406] In general, a smaller Tafel slope indicates a faster reaction. As shown in Figure 12.4b, $BaSrCoMoO_6$ shows a smaller value of Tafel slope, 142 mV/dec, compared to BSCF, 174 mV/dec, indicating the faster electron transfer in $BaSrCoMoO_6$ during the HER. This catalyst also shows smaller charge

transfer resistance[70] in the HER region (-0.5 V vs RHE), as evident from the lower real axis intercept of the semi-circle in Nyquist plot as compared to BSCF (Figure 12,4c).

BaSrCoMoO$_6$ also shows an enhanced performance for OER electrocatalysis compared with BSCF.[290, 295, 407] As shown in Figure 12.5a, the overpotential (η10) at 10 mA/cm2 is 400 mV for BaSrCoMoO6, as compared to that of BSCF, 500 mV, in 0.1 M KOH. The overpotential for BSCF is in line with previous reports.[290, 295, 407] We note that the OER activity of BaSrCoMoO$_6$ is comparable to that of the precious metal catalyst, RuO$_2$ (η_{10} = 420 mV).[81, 248]

The kinetics of the OER for BaSrCoMoO$_6$ is faster than that of BSCF, as evident from the Tafel plots[184, 185, 285] shown in Figure 12.5b, giving Tafel slopes of 93 mV/dec for BaSrCoMoO$_6$, as compared to 81 mV/dec for BSCF. The lower Tafel slope value for the former is indicative of faster reaction, consistent with its greater OER activity. In addition, the charge transfer resistance in the OER region (1.7 V vs RHE) is smaller for BaSrCoMoO$_6$ than BSCF (Figure 12.5c), which indicates an enhanced charge transfer for BaSrCoMoO$_6$, consistent with its superior catalytic activity. This catalyst is also very stable, as evident from the stable chronopotentiometry response in OER conditions, shown in the inset of Figure 12.5a.
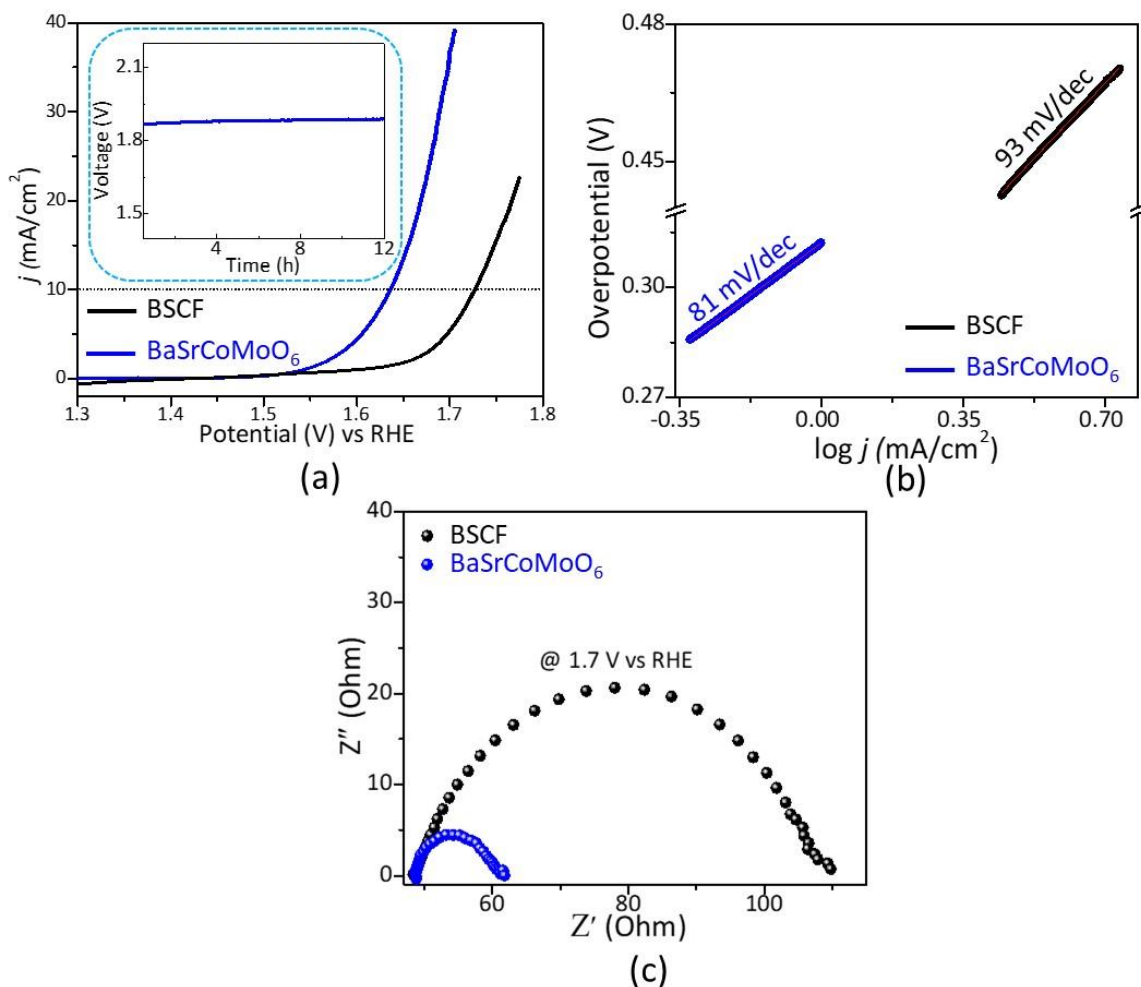
Figure 12.5: (a) OER polarization curves in 0.1 M KOH. The inset shows the chronopotentiometry data for $BaSrCoMoO_6$ at a current density of 10 mA/cm^2. (b) The Tafel plot showing Tafel slopes. (c) The Nyquist plot recorded in the OER potential region, 1.7 V vs the RHE, indicating lower charge transfer resistance for $BaSrCoMoO_6$.

Another important advantage of $BaSrCoMoO_6$ is that it can be used in bulk without the need for nanofabrication or composite formation. Even the addition of carbon black, which is routinely added in OER or HER studies, is not needed. Carbon black is often mixed with the catalyst to enhance the change transfer.[343, 408, 409] The electrocatalytic experiments for $BaSrCoMoO_6$ with or without carbon black lead to similar overpotentials (Figure 12.6). This indicates the outstanding intrinsic catalytic activity of $BaSrCoMoO_6$. On the other hand, for BSCF, the absence of carbon black leads to low catalytic

performance, where the current response does not even reach 10 mA/cm^2, as shown in Figure 12.6.
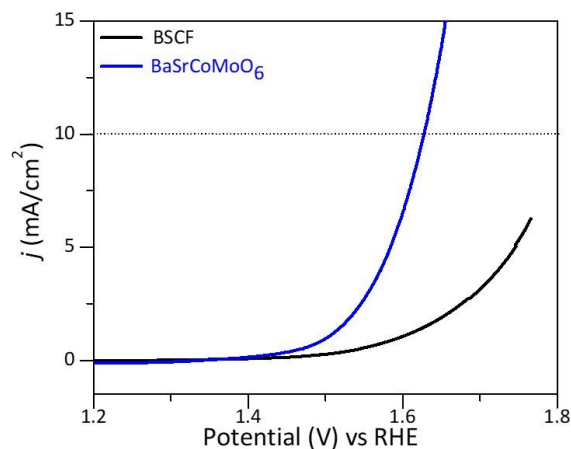
Figure 12.6: Representative polarization curve showing the OER activity without the addition of carbon black for BaSrCoMoO$_6$ and BSCF.

Importantly, BaSrCoMoO$_6$ retains its structural integrity, as evident from X-ray diffraction data before and after 1000 cycles of OER and HER. As shown in Figure 12.7, the X-ray diffraction pattern remains unchanged, indicating the catalyst structure is intact.
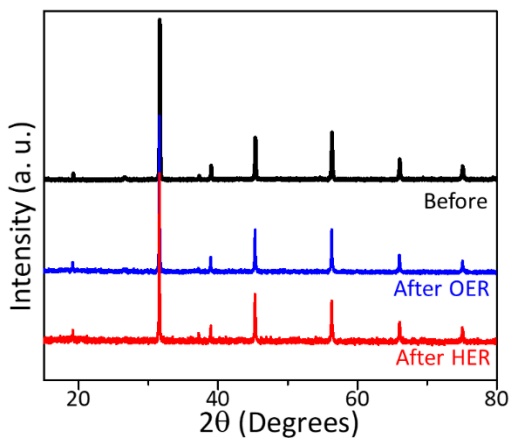
Figure 12.7: X-ray diffraction data before and after 1000 cycles of OER and HER.

11.3 DENSITY FUNCTIONAL THEORY AND METHODS

The *ab initio* calculations were performed within the density functional theory (DFT) at the level of the spin polarized generalized gradient approximation (SGGA) and the Perdew-Burke-Ernzerhof (PBE)[266] level of approximation augmented by including Hubbard-U corrections[267] based on Dudarev's approach,[268] as implemented in the Vienna Ab-initio Simulation Package (VASP).[269-271] The projected augmented wave (PAW) potential [270, 271] was used to describe the core electrons. The Hubbard-U parameter was applied as a many-body correction to overcome the underestimation of electronic correlation due to the approximate nature of the exchange-correlation functionals in the traditional single particle Kohn-Sham DFT. It partially corrects the electronic self-interaction error inherent in DFT and leads to better gap estimations. Hubbard parameters were used only for the d-orbitals of the transition metal (TM) atoms. After testing a range of U values, $U(d,TM) = 3$ eV was selected for Co, Mo and Fe. This value is very close to other DFT/SGGA + U studies reported on similar systems.[272, 336, 410-414] We note that the use of DFT/SGGA+U has been shown to work very well for ternary alloys of the type ABO_3 by producing correct total energies and band gap values.[279]

The ABO_3 perovskite-type $BaSrCoMoO_6$ and $Ba_{0.5}Sr_{0.5}Co_{0.8}Fe_{0.2}O_{3-\delta}$ ($\delta = 0.4$) systems were simulated by supercells periodically repeated along the x, y and z-directions. The supercells for $BaSrCoMoO_6$ were obtained by extending a $BaSrCoMoO_6$ unit cell with *Fm*-3*m* symmetry. Supercells of several sizes were considered. Positions of Ba and Sr atoms were randomly selected, while ordering was maintained for the Co and Mo atoms, consistent with the experimentally determined structure. Among various supercells considered with 20, 40, or 80 atoms, a 40 atom supercell with $P4_222$ symmetry was found

to have the optimal energetics (lowest energy per atom). Similarly, for $Ba_{0.5}Sr_{0.5}Co_{0.8}Fe_{0.2}O_{3-\delta}$, different sizes of supercells with 46 and 92 atoms were considered. They were obtained by extending the $BaCoO_3$ unit cell with *Pm-3m* symmetry. In each of the supercells, the placing of Ba and Sr atoms were random. This was also the case for Co and Fe atoms, consistent with the experimentally determined structure. The oxygen vacancy sites were also chosen randomly. A 92 atom supercell with *P*1 symmetry was found to have the optimal energetics. A Monkhorst- Pack 4x4x4 k-point mesh was used in all calculations.[337] All structures were subjected to full symmetry unconstrained geometric relaxation of all atom positions and cell parameters. We note that the relaxation of the cell volume is extremely critical for an accurate estimation of the ground state. The lowest energy structures obtained in the two cases were used in the calculation of band structures and densities of states (DOS).
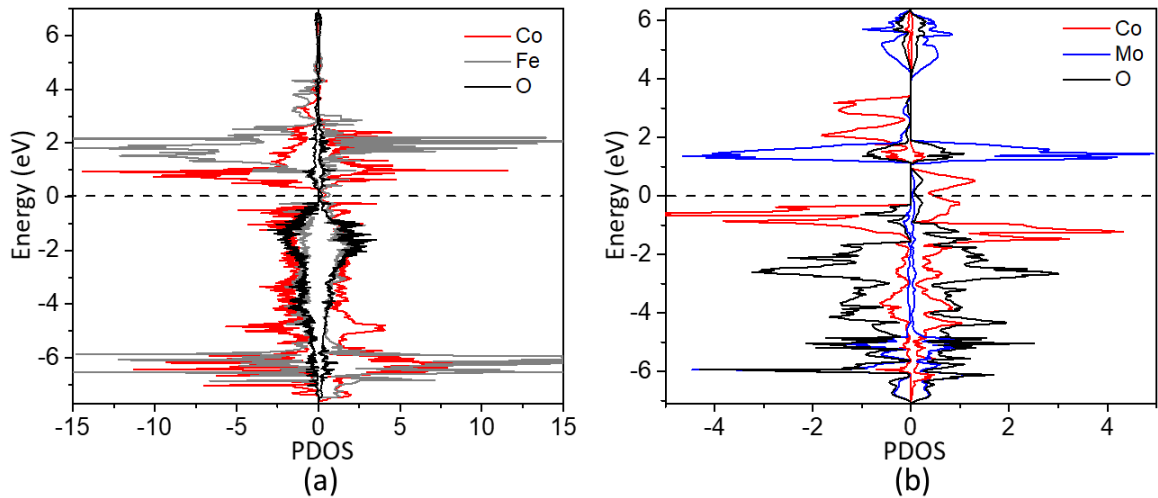
Figure 12.8: Density of States (DOS) from DFT calculations for (a) BSCF, and (b) $BaSrCoMoO_6$.

Further insight into the properties of these materials is obtained using density functional theory (DFT) calculations. These calculations (Figure 12.8) indicate that, for

191

BaSrCoMoO$_6$, the center of the Co d-band is considerably closer to the Femi level, compared to that of BSCF. This is important because cobalt in BSCF is considered the active site,[74] and its electronic configuration is thought to be responsible for the high electrocatalytic activity of BSCF.[74] Therefore, the shift in the Co d-band center can have a direct impact on the electrocatalytic performance.

It has been previously proposed[299, 300] that the proximity of the d-band center to the Fermi level is correlated with the electrocatalytic activity due to the improved bonding with the adsorbates during the reaction.[299, 300] The average center of the Co d-band (from both spin up and spin down) for BSCF is -3.796 eV, as compared to that of BaSrCoMoO$_6$, -1.852 eV, indicating a significant shift toward the Fermi level. The average center of the Mo d-band in BaSrCoMoO$_6$ is -5.204 eV, while that of the Fe d-band for BSCF is -4.193 eV. The difference in the d-band centers of Mo and Fe is expected. However, the magnitude of this difference is about half the difference between the centers of Co d-bands of the two materials. The enhanced electrocatalytic performance of BaSrCoMoO$_6$ is consistent with the considerable shift of the Co d-band closer to the Fermi level compared to that of BSCF.

11.4 CONCLUSIONS

The double perovskite BaSrCoMoO$_6$ is a promising functional electrocatalyst to catalyze both hydrogen evolution reaction (HER) and oxygen evolution reaction (OER) for water splitting in both acidic and alkaline media. Experimental results show that the double perovskite outperforms both HER and OER activity of the state-of-the-art Ba$_{0.5}$Sr$_{0.5}$Co$_{0.8}$Fe$_{0.2}$O$_{3-\delta}$ (BSCF) and commercial RuO$_2$ catalysts in 1 M KOH electrolyte. BaSrCoMoO$_6$ has very low OER and HER overpotentials of 340 mV and 325 mV,

respectively. This is a remarkable finding in the field of energy conversion by water splitting process.

CHAPTER 13

BIFUNCTIONAL WATER-SPLITTING ELECTROCATALYSIS, BROUGHT ABOUT

BY STRUCTURAL ORDER

In this chapter, the significant enhancement of HER and OER activities upon topotactic reduction of $LaCoO_3$ to achieve an oxygen-deficient system $LaCoO_{2.67}$ ($La_3Co_3O_8$), has been studied. Detailed electrochemical studies show the important effect of oxygen-deficiency, resulting in the improvements of overpotential and kinetics for both OER and HER processes.

13.1 CRYSTAL STRUCTURE AND OXYGEN CONTENT

The occurrence of oxygen vacancies (δ) results in the formation of oxygen-deficient perovskites (ODP) with the general formula, $ABO_{3-\delta}$. While typical perovskites (ABO_3) only contain AO_{12} and BO_6 polyhedra, ODPs can contain several types of coordination geometries around A and B-site metals, such as AO_{12}, AO_8, BO_4, and BO_6, depending upon the ordering scheme of oxygen vacancies.

The crystal structures were examined by Rietveld refinements using powder X-ray diffraction (PXRD). The Rietveld refinement profile and the refined structural parameters for $LaCoO_3$ are presented in Figure 13.1a and Table 13.1, respectively. This compound has a trigonal structure with *R-3c* space group, as also reported previously.[415, 416] The crystal structure (Figure 13.1b) contains corner-sharing 6-coordinated CoO_6 and edge-sharing 9-

coordinated LaO_9 polyhedra. Using iodometric titration, the amount of oxygen vacancies

(δ) per formula for this material was confirmed to be ~0.02 (1), indicating an almost

stoichiometric $LaCoO_3$ formula, consistent with a previous report.[417]
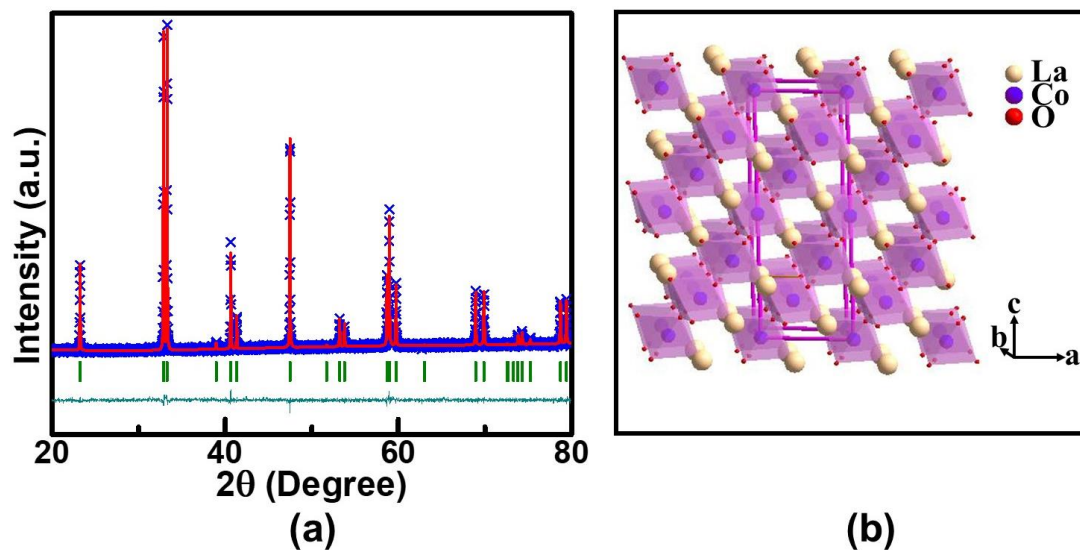
Figure 13.1: (a) Rietveld refinement profile for PXRD data of $LaCoO_3$ with *R-3c* space group. The blue crosses, red solid curve, olive vertical tick marks, and dark cyan curve correspond to the experimental data, calculated model, Bragg peak positions, and difference plot, respectively. (b) Crystal structure of $LaCoO_3$, showing the corner-sharing CoO_6 octahedral units.

Table 13.1: Refined structural parameters of lacoo₃ at room temperature using pxrd data. space group: *r-3c*, a = 5.44660(6) å, c = 13.1005(1)å, r_p = 0.0283, wr_p = 0.0361, χ^2 = 1.324%.

Atom	x	y	z	Multiplicity	Occupancy	Uiso
La1	0	0	0.25	6	1.0	0.0271(5)
Co1	0	0	0	6	1.0	0.0265(8)
O1	0.451(1)	0	0.25	18	1.0	0.031(2)

The reduction of $LaCoO_3$ in 5% H_2 gas leads to the creation of $LaCoO_{2.67}$ ($\delta = 0.33$)

with a significant level of oxygen-vacancies that are arranged in an ordered fashion. This

reduction method is a facile route for the synthesis of $La_3Co_3O_8$ at a lower temperature

(350 °C), without the need for more elaborate methods, such as reduction in a sealed silica glass ampoule containing Zr chip.[418] The results of the Rietveld refinement for this compound are shown in Figure 13.2a and Table 13.2. During the refinements, y positions were fixed at special positions except for Co1 and O1, consistent with a previous report.[418] Fixing the y positions of those two atoms results in an unstable refinement. The degree of oxygen deficeny, $\delta \approx 0.33$ (1), was confirmed using iodometric titration.
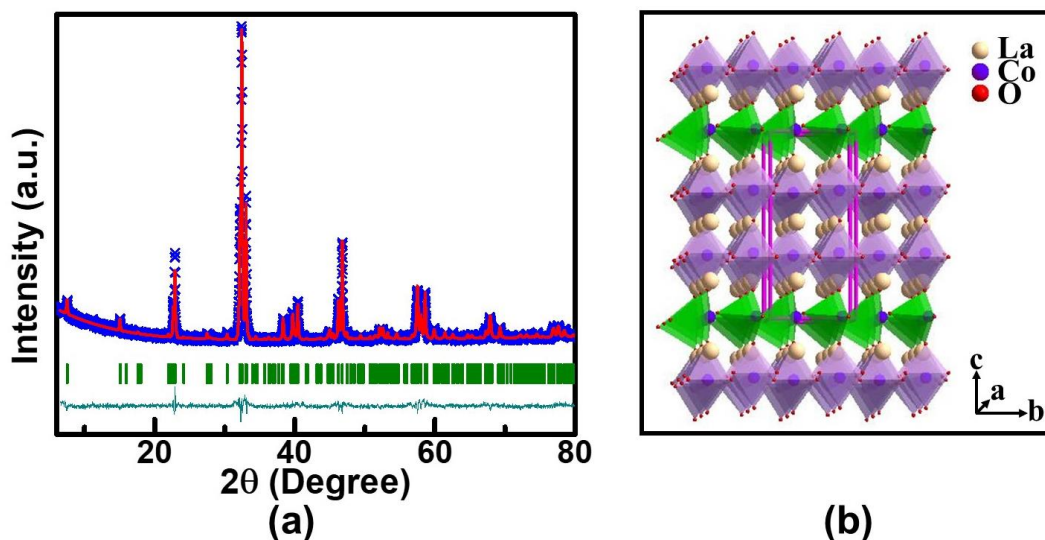
Figure 13.2: (a) Rietveld refinement profile for PXRD data of $La_3Co_3O_8$ with $P2_1$ space group. The blue crosses, red solid curve, olive vertical tick marks, and dark cyan curve correspond to the experimental data, calculated model, Bragg peak positions, and difference plot, respectively. (b) Crystal structure of $La_3Co_3O_8$, showing the corner-sharing CoO_4 tetrahedra located in between two layers of CoO_6 octahedra.

This material forms a crystal structure which is an intermediate between brownmillerite and perovskite structure. In this type of structure, the vacancies appear in every third layer, forming CoO_4 tetrahedra in between bilayer stacks of CoO_6 octahedra (Figure 13.2b). This bilayer brownmillerite structure type, is also known as Grenier phase.[13] It has six different positions for metal atoms; hence the formula $LaCoO_{2.67}$ is better described as $La_3Co_3O_8$.

Table 13.2: Refined structural parameters of la$_3$co$_3$o$_8$ at room temperature using pxrd data. space group: *p2$_1$*, a = 5.45645(2) å, b = 5.4212(2) å, c = 11.7760(5)å, r$_p$ = 0.0201, wr$_p$ = 0.0261, χ^2 = 2.483%.

Atom	x	y	z	Multiplicity	Occupancy	Uiso
La1	0.751(3)	0.25	0.811(2)	2	1.0	0.019(1)
La2	0.725(2)	0.25	0.186(2)	2	1.0	0.019(1)
La3	0.752(3)	0.25	0.500(2)	2	1.0	0.019(1)
Co1	0.201(5)	0.282(5)	0.004(4)	2	1.0	0.010(3)
Co2	0.232(7)	0.25	0.331(4)	2	1.0	0.010(3)
Co3	0.267(7)	0.25	0.665(4)	2	1.0	0.010(3)
O1	0.151(9)	0.826(9)	-0.012(9)	2	1.0	0.0150
O2	0.26(2)	0.25	0.15(1)	2	1.0	0.0150
O3	0.31(1)	0.25	0.863(1)	2	1.0	0.0150
O4	0.39(2)	0	0.338(4)	2	1.0	0.0150
O5	0.45(3)	0.5	0.338(4)	2	1.0	0.0150
O6	0.19(1)	0.25	0.49(1)	2	1.0	0.0150
O7	0.01(7)	0	0.309(3)	2	1.0	0.0150
O8	-0.01(7)	0.5	0.309(3)	2	1.0	0.0150

We note that the $A_3B_3O_8$ is reported to oxidize to $LaCoO_3$ upon heating at ~ 360 K in air.[418] As mentioned in the experimental seciton, this material was exposed to air at room temperature for at least 12 hours before being stored in a desiccator. This did not lead to any phase transformation at room temperature, as confirmed by X-ray diffraction. In addition, we did not observe any phase transformation after electrocatalysis experiments. However, prolonged storage (after about a month) in air leads to the oxidation into the coexistence of the parent phase with itself, as observed in XRD experiments.

It is also possible to achieve a higher degree of reduction if $La_3Co_3O_8$ pellet is heated at 350 °C in 5% H_2 for 36 hours. This leads to the formation of $La_2Co_2O_5$, which

has a regular brownmillerite-type structure, with alternating CoO_6 octahedra and CO_4 tetrahedra. This material is reported to crystallize in orthorhombic *Pnma* space group,[418-420] although there is still some debate about the space group of this material.[420] However, it often forms alongside the bilayer brownmillerite $La_3Co_3O_8$, leading to peak broadening as a result of the coexistence of two phases. [418, 420] It is also noteworthy that the highly reduced $La_2Co_2O_5$ is very prone to oxidation in air and starts converting into $La_3Co_3O_8$ after 8-10 hours in air at room temperature. It is also readily oxidized during electrocatalytic experiments if used as an electrocatalysts for HER or OER.
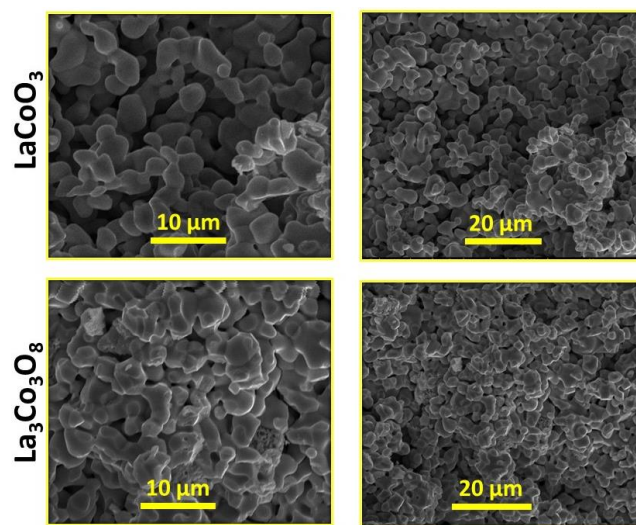
Figure 13.3: SEM images of both compounds showing smaller crystallite sizes for $La_3Co_3O_8$

13.2 HYDROGEN-EVOLUTION ACTIVITY

Numerous materials such as ruthenium nanoparticles,[306] CoS_2/MoS_2 heteronanosheet,[307] Ni-Mo electrode,[308], and nitrides[224] have been studied as HER electrocatalysts in basic medium. Recently, some perovskite-based multi-metal oxides, such as $Pr_{0.5}(Ba_{0.5}Sr_{0.5})_{0.5}Co_{0.8}Fe_{0.2}O_{3-\delta}$[183] and $NdBaMn_2O_{5.5-\delta}$,[70] have been studied as electrocatalysts for HER in alkaline electrolyte. Similarly, our group has reported several

perovskite oxides, such as $CaSrFeMnO_{6-\delta}$[81] and $CaMn_{0.67}Ga_{0.33}O_{2.67}$,[86] that are capable of catalyzing HER.
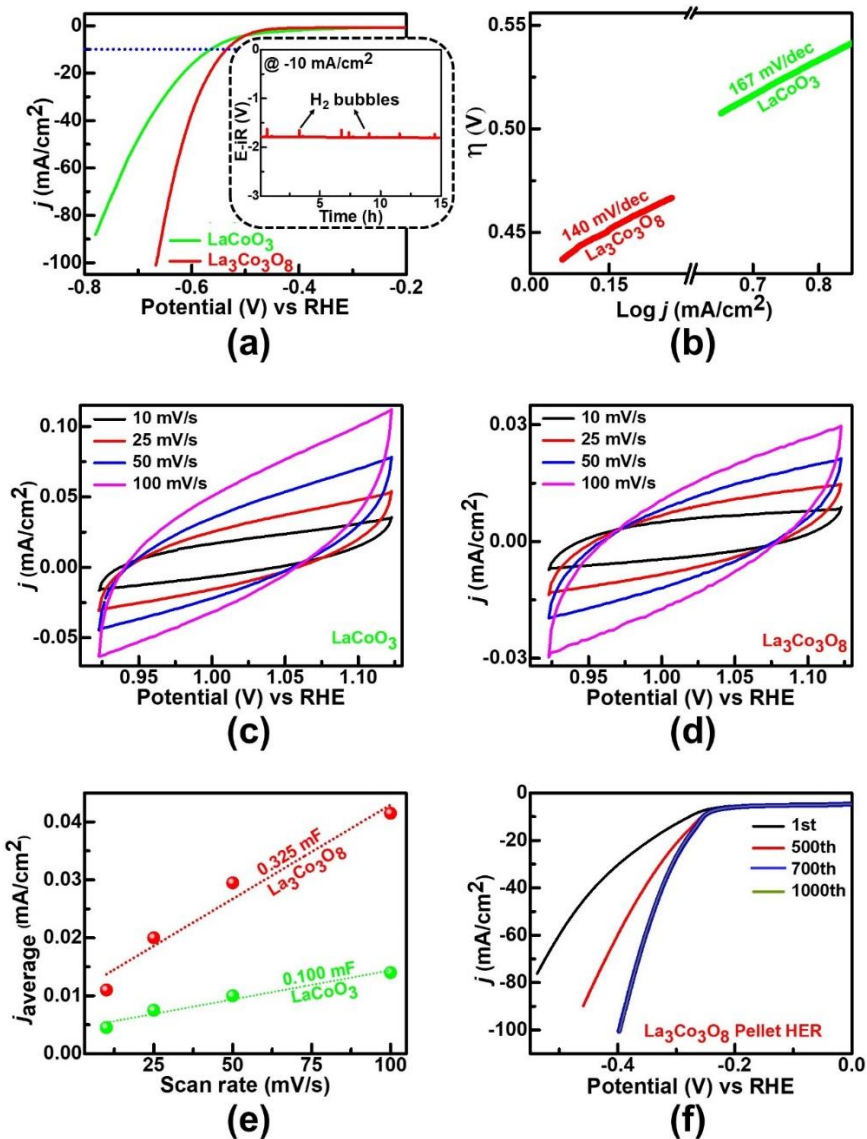
Figure 13.4: (a) HER polarization curves in 1M KOH. The inset shows chronopotentiometry data for $La_3Co_3O_8$. The noise is due to the formations of H_2 bubbles on the surface of the Ni-foam substrate. (b) Tafel slopes for HER. (c) and (d) CVs in the non-Faradaic regions. (e) C_{dl} values obtained from the slope of $j_{average}$ plotted against scan rate. (f) HER polarization curves on pure disk (pellet) of $La_3Co_3O_8$ over 1000 cycles.

The most utilized electrolyte, 1M KOH,[224, 306-308] was used to study the HER activities of $LaCoO_3$ and $La_3Co_3O_8$. The performance of an electrocatalyst is often

199

evaluated based on the onset potential and overpotential at 10 mA/cm^2.[234, 309] The current density of 10 mA/cm^2 is associated with the solar fuel synthesis[290] and has been adopted for comparison of water-splitting eletcrcatalysts. The catalytic activity toward HER is usually compared with a precious metal-based catalyst, Pt/C (20 wt. % Pt).[77, 183] The HER onset potential, where the the electrocatalytic reaction starts, is almost zero for the Pt/C catalyst.[77, 183]

For the two materials in this study, the catalytic activity toward HER is shown in Figure 13.4. The onset potential values for $LaCoO_3$ and $La_3Co_3O_8$ are –0.42V and –0.41V vs RHE in 1M KOH, respectively. These materials show the respective overpotential (η_{10}) values at 10 mA/cm^2 (marked by the blue dashed line in Figure 13.4a) of –563 mV and –533 mV. While these overpotential values are higher than those reported for several other perovskite oxide-based electrocatalysts such as $Pr_{0.5}(Ba_{0.5}Sr_{0.5})_{0.5}Co_{0.8}Fe_{0.2}O_{3-\delta}$, ($\eta_{10}$ = 237 mV),[183] $PrBaCo_2O_{5+\delta}$ (η_{10} = 356 mV),[69] $NdBaMn_2O_{5.5}$ (η_{10} = 290 mV),[70] and $CaSrFeMnO_{6-\delta}$ (η_{10} = 390 mV),[81] they are better than the overpotential obtained from another perovskite oxide $Ba(Fe_{0.7}Ta_{0.3})O_{3-\delta}$ (η_{10} = ≈700 mV)[374] in alkaline electrolyte. They are also comparable to the HER activities of some non-oxide catalysts, such as and MoS_2 [235] and Co-embedded nitrogen rich carbon nanotubes[421] in alkaline medium.

The kinetics of HER is often evaluated by utilizing the Tafel equation η = a + b log j,[86, 292, 310] where η is overpotential and j is current density. The rate of HER is determined from the slope of the plot of η versus log j (Figure 13.4b). Smaller values of Tafel slope indicate faster HER kinetics. The values of the Tafel slope can also be informative with regards to the HER mechanism. The expected Tafel slope values are 120 mV/dec, 40

mV/dec, and 30 mV/dec to indicate if the rate-determining reaction is Volmer, Heyrovsky, or Tafel, respectively.[237] However, more than one reaction mechanism may be operating, which yields a larger value, indicating mixed mechanism. As shown in Figure 13.4b, the Tafel slope values for $LaCoO_3$ and $La_3Co_3O_8$ are found to be 167 mV/dec, and 140 mV/dec, respectively. These Tafel slope values indicate that more than one reaction mechanism is operating during the electrocatalysis process

Another important parameter is the electrochemically active surface area (ECSA), which is evaluated using cyclic voltammograms (CVs) at a non-faradaic region where HER or OER do not take place. Figure 13.4c-d show CVs in the non-faradaic region to determine the double-layer capacitance (C_{dl}),[86, 291] which is directly proportional to ECSA,[185] and therefore is often taken as a measure of ECSA. The C_{dl} value is related to $j_{average}$ (the average of j_{anodic} and $j_{cathodic}$ absolute values at the middle potential of the CV) and the scan rate, v, based on the relation $C_{dl} \times v = j_{average}$.[295] Therefore, the C_{dl} value is obtained as the slope of the plot of $j_{average}$ versus v. As shown in Figure 13.4e, the C_{dl} values are 0.325 mF and 0.100 mF for $La_3Co_3O_8$ and $LaCoO_3$, respectivly, further confirming the better HER activity of the former compound.

The stability of HER catalyst can be examined by chronopotentiometry[323] or chronoamperometry.[422] The stability of the best performing catalyst $La_3Co_3O_8$ under HER condition was studied using chronopotentiometry experiment (inset of Figure 13.4a) by loading the catalyst ink on 1 cm^2 nickel foam. The catalyst showed a stable performance for at least 15 hours.

An additional experiment was also performed in an attempt to eliminate any possible contributions from glassy carbon, nafion and carbon black, which are often used in preparation of the catalyst ink. Removal of such additives allows the investigation of the intrinsic properties of an electrocatalyst by eliminating their interferences.[347, 423] Therefore, an experiment was conducted using a pure disk of $La_3Co_3O_8$ as the working electrode in the RDE setup. As shown in Figure 13.4f, the performance of the electrocatalyst disk improves significantly from the 1st to 500th cycle. Then, the performance remains almost unchanged between 700 and 1000th cycle, giving an excellent overpotential of $\eta_{10} \approx -253$ mV.

13.3 OXYGEN-EVOLUTION ACTIVITY

While OER activity is sometimes studied in acidic condition,[424] alkaline electrolyte using 1M KOH is very commonly used.[82, 317, 425] The OER electrocatalysis for both compounds (Figure 13.5) was assessed in 1 M KOH to directly compare the catalytic activity with previously reported catalysts. Both materials studied in this work, $LaCoO_3$ and $La_3Co_3O_8$, show excellent OER activities. However, the reduced compound that has a bilayer brownmillerite structure performs significantly better, which is the same trend observed for the HER activity. The onset potential, where the OER process begins, is found to be 1.37 V for $LaCoO_3$ and 1.24 V for $La_3Co_3O_8$ in 1 M KOH (Figure 13.5a). The overpotential (η_{10}), at 10 mA/cm^2,[293, 321] is obtained according to the formula: η (V) = E_{RHE} − 1.23 V, where 1.23 V is the ideal thermodynamic potential for OER. The overpotential improves from $\eta_{10} \approx 370$ mV for $LaCoO_3$[426], to $\eta_{10} \approx 360$ mV for RuO_2[287] to the remarkable $\eta_{10} \approx 210$ mV for $La_3Co_3O_8$.

Similar to HER, the kinetics of OER is examined using the Tafel equation, $\eta = a + b \log j$.[292, 310] The evaluation of kinetics provides information about electron and mass transport[246] of an electrocatalyst during the OER activity. A smaller value of Tafel slope,[81, 292] i.e., the slope of η vs $\log j$ (Figure 13.5b), indicates a faster electron transfer process. Larger values[422, 427] are often observed indicating the predominance of the surface species before or after the rate-determining step.[292] As shown in Figure 5b, the Tafel slopes for RuO_2, $LaCoO_3$, and $La_3Co_3O_8$ are 72 mV/dec, 71 mV/dec, and 53 mV/dec, respectively. The latter compound has significantly lower Tafel slope value than some oxides such as $LaCoO_3$[426] (82 mV/dec) and $LaCa_2Fe_3O_8$ (74 mV/dec),[82] indicating the facile electron transport. Tafel slopes close to 120 mV/dec may suggest that most of the surface species formed in the step just before the rate-determining step are predominant for the two compounds.[292] The Tafel slope value smaller than 120 mV/dec indicates predominant surface adsorbed species produced in the early stage of the OER.[292] However, these materials show significantly smaller Tafel slopes and improved OER kinetics compared to several other OER catalysts, such as $NiCo_2O_4$ nanoneedles (292 mV/dec), $NiCo_2O_4$ nanosheets (393 mV/dec), and CoPi (312 mV/dec) in alkaline electrolyte.[422]

The catalyst stability was evaluated using chronopotentiometry, as shown in the inset of Figure 13.5a, which indicates the stability of $La_3Co_3O_8$ under the same OER condition for at least 15 hours. X-ray diffraction experiment on the $La_3Co_3O_8$ catalyst after 1000 OER cycles indicates the remarkable retention of the structural integrity of this material (Figure 13.5c).
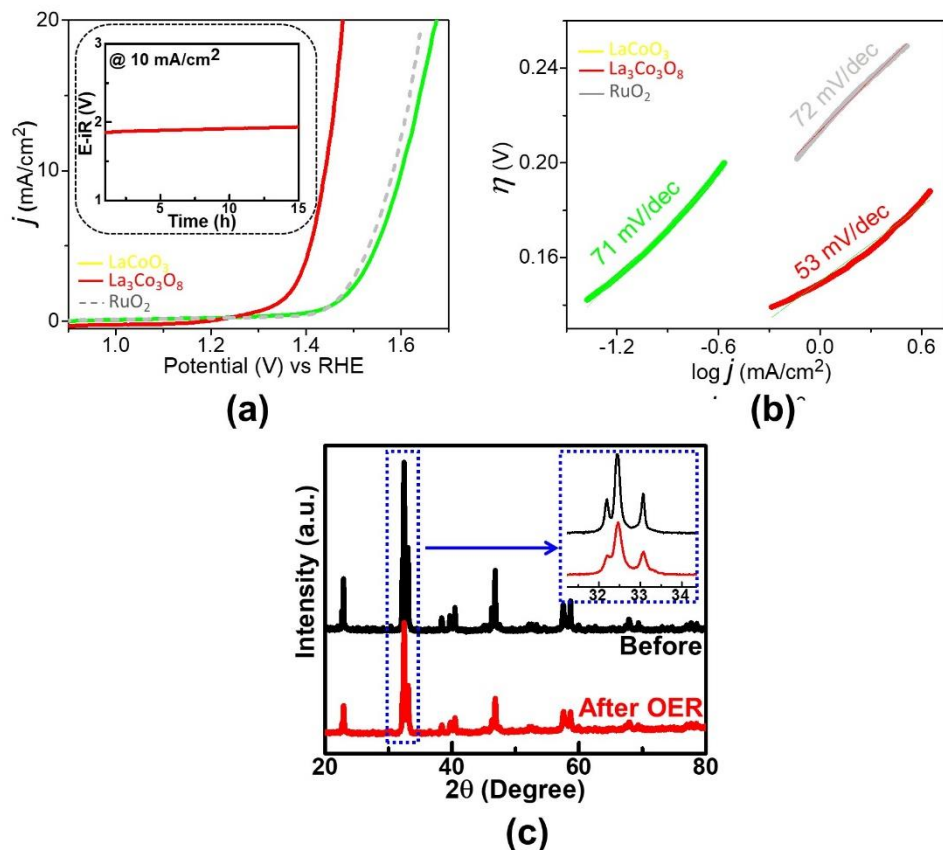
Figure 13.5: (a) OER polarization curves in 0.1M KOH with chronopotentiometry data for $La_3Co_3O_8$ in the inset. (b) Tafel slopes of OER. (c) PXRD data of $La_3Co_3O_8$ before and after the 1000 cycles of OER

In addition to the direct quantification of the oxygen defects by iodometry as mentioned in earlier section, we further demonstrate defect concentrations before and after 1000 OER CV scans uising XPS. As shown in Figure 13.6, XPS data for $La_3Co_3O_8$ before cyclcing could be fitted for Co^{2+} and Co^{3+} oxidation states with the corresponding binding energies of 779.45 eV and 780.50 eV.[12, 85] Additionally, a pronounced satellite peak appear at ≈ 9 eV higher than $2p_{3/2}$ peak is an indicative of Co^{3+}.[124] The XPS data after shows $2p_{3/2}$ for Co^{2+} and Co^{3+} around 779.51 eV and 780.80 eV respectively along with the satellite peaks. This indicates a negligible change in oxygen defects after the catalysis.
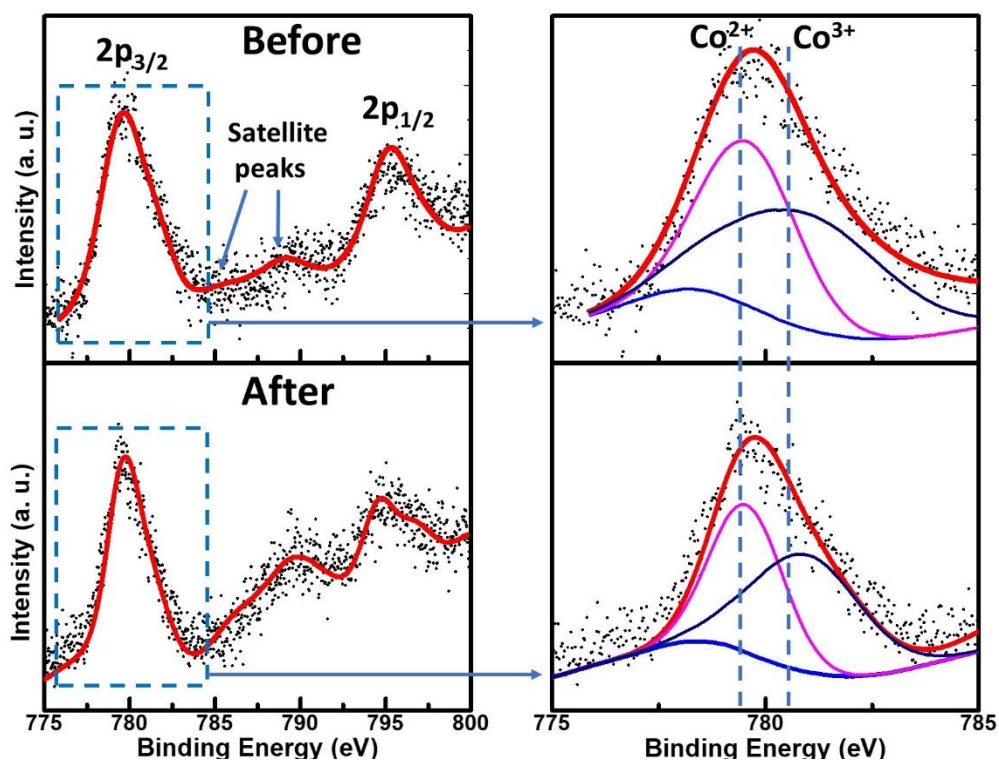
Figure 13.6: XPS data of $La_3Co_3O_8$ before and after 1000 OER cycles.

The outstanding OER activity of both compounds, especially the reduced material $La_3Co_3O_8$, becomes more evident when its overpotential ($\eta_{10} \approx 270$ mV) is compared to those of the precious metal catalysts IrO_2 ($\eta_{10} \approx 450$ mV)[290] and RuO_2 ($\eta_{10} \approx 420$ mV).[248] It also shows significantly enhanced performance compared to the previously reported perovskite-based oxide catalysts $CaSrFeMnO_{6-\delta}$ (370 mV),[81] $SrNb_{0.1}Co_{0.7}Fe_{0.2}O_{3-\delta}$ (420 mV),[290] and $Pr_{0.5}Ba_{0.3}Ca_{0.2}CoO_{3-\delta}$ (440 mV).[428] In addition, $La_3Co_3O_8$ has the ability to act as a water-splitting electrocatalyst as a single-phase bulk material, without requiring nanofabrication or elaborate multi-component composite preparation.

13.4 CONCLUSIONS

Outstanding bifunctional electrocatalytic activity can be achieved by inducing oxygen vacancies in a perovskite oxide structure. The electrocatalyst $La_3Co_3O_8$ featuring defect-order is synthesized via reduction of the parent compound $LaCoO_3$ under H_2 atmosphere. This results in the enhancement of the electrocatalytic activity toward both hydrogen evolution reaction (HER) and oxygen evolution reaction (OER). This outstanding structure-activity correlation is ascribed to the increased concentration of oxygen vacancies and their ordered arrangement in $La_3Co_3O_8$. In particular, this material shows very high OER activity, which exceeds that of precious metal catalysts. In addition, it is highly stable and retains its catalytic activity and structural integrity upon electrocatalytic process.

CHAPTER 14

CONCLUSION

Perovskite-related oxides exhibit interesting properties, such as magnetism, charge transport, gas sensing, pseudocapacitance, and electrocatalysis. The study of double perovskite series, $BaSrMMoO_6$ (M = Mn, Fe, Co, Ni), shows interesting trends of magnetic, electrical, and electrocatalytic properties. $BaSrMnMoO_6$, $BaSrCoMoO_6$, and $BaSrNiMoO_6$ possess contrasting properties as compared to their structural analog $BaSrFeMoO_6$. The latter compound has a metallic property and ferrimagnetic ordering of Fe moments, whereas the other three compounds have semiconducting property with antiferromagnetic ordering. Such properties can be particularly useful for electronic devices and magnetic memory devices. Therefore, the research on these materials is important for applications in those fields.

Our next aim was to create oxygen deficiencies in the double perovskite structures discussed above to obtain oxygen deficient phases. Utilizing 5 - 10% H_2 gas to reduce such compounds resulted in impure/mixture of phases. However, there are other perovskite phases, which can be designed to contain oxygen-deficiencies in their structures Such oxygen deficient perovskites (ODPs) are a versatile class of compounds to tune property, structure, and practical application in several devices such as gas sensors. The sensor studies of $Ca_2Fe_2O_5$, Ca_2FeMnO_5, $Sr_2Fe_2O_5$, and Sr_2FeMnO_5, lead to an important finding

that the structural stability of $Ca_2Fe_2O_5$ enhances oxygen, caron dioxide, and carbon monoxide gas sensing property at 700°C.

Other impactful property studies include the utilization of ODPs for energy storage and conversion. For pseudocapacitive energy storage, bilayer brownmillerite structures have been studied for the first time in literature, where $Ca_3GaMn_2O_8$ and $Sr_2CaGaMn_2O_8$ show hydroxide ion intercalation-based pseudocapacitance. For energy conversion process, our studies on electrochemical water splitting results in the discovery of remarkable electrocatalysts. Our materials improve the sluggish kinetics of both half reactions of water splitting. The overpotential (η) of both half reactions of water splitting namely OER and HER, is lowered significantly as compared to many reported catalysts in literature. Most importantly, our materials contain earth abundant metals, which can significantly reduce the cost and replace expensive catalysts such as platinum (Pt), ruthenium dioxide (RuO_2), and iridium dioxide (IrO_2).

We have systematically studied several factors to tune electrocatalytic properties. Among several approaches and strategies, our approach to synthetically control the amount of oxygen vacancy in the ODP structure or other related structures (Sr_3FeMnO_6 and $Sr_3Mn_2O_6$), has proven to be highly effective for lowering the overpotential. Compounds such as $Ca_3GaMn_2O_8$, $Sr_2CaGaMn_2O_8$, $Ca_3Fe_2MnO_8$, $Ca_3Fe_{1.5}Mn_{1.5}O_8$, $LaCa_2Fe_3O_8$, $LaBa_2Fe_3O_8$, $LaCaBaFe_3O_8$, $LaBaSrFe_3O_8$, $LaCaSrFe_3O8$, $LaSr_2F_{e3}O_8$, and $La_3Co_3O_8$, have similar degree of vacancies, $\delta = 1/3$ per $ABO_{3-\delta}$ formula. Strategies such as A- site and B-site modification/substitution are utilized to tune the oxygen content. This allows to screen materials for studying pseudocapacitance, magnetism, charge transport, and electrocatalytic properties. These materials also have activity toward HER for water

splitting process in acidic medium. Other compounds such as $LaCa_2Fe_3O_8$, $LaSr_2Fe_3O_8$, and $La_3Co_3O_8$ turn out to be remarkable electrocatalysts for overall water splitting process.

Another strategy to lower the overpotential is a less explored factor in literature, the structural factor. The structural ordering in $LaCa_2Fe_3O_8$ as compared to $LaSr_2Fe_3O_8$ leads to the enhanced activity. This is a thorough study that involves both experimental and computational methods (DFT calculations). The next remarkable finding related to the structural factor is observed in an ODP series, $Ca_2FeCoO_{6-\delta}$, $CaSrFeCoO_{6-\delta}$, and $Sr_2FeCoO_{6-\delta}$. The most structurally ordered brownmillerite structure $Ca_2FeCoO_{6-\delta}$, shows remarkable bifunctional OER and HER activities with an overpotential of 0.25 V in alkaline medium. Another versatile ODP electrocatalyst namely $CaSrFeMnO_{6-\delta}$ can catalyze OER and HER in both acidic and alkaline media with an overpotential lower than commercial electrocatalysts.

With the experimental and computational methods, our work leads to the discovery of a novel descriptor called free e_g carriers for both OER and HER processes. A large amount of free e_g carriers for facile charge transfer during HER and OER, is observed in $CaSrFe0_{.75}Co_{0.75}Mn_{0.5}O_{6-\delta}$ (CSFCM) compound. This project involved synthesizing 8 different ODP compositions, where Mn content was systematically varied. A thorough characterization such as electronic structure studies, XANES, XPS, and XRD have strongly given support for the discovery of the descriptor, which could be a universal descriptor for bifunctional catalysts.

Overall, this study has emphasized perovskite oxides can be very versatile materials for magnetic devices, water electrolyzers, pseudocapacitors, batteries, etc. There is much room in the structure to tune the properties. Our findings reveal that these materials have

outperformed the state-of-the-art catalysts such as RuO_2 in the field of electrocatalysis. These can be commercialized to replace expensive precious metal-based materials. Our research resulted in the development of remarkable, robust, and versatile materials for various applications. The new materials, innovative methods such as disk electrode catalysis, and novel descriptors such as free e_g carriers, will be a solid foundation for many researchers in the future.

REFERENCES

1.Tilley, R. J. D., *Perovskites: Structure-Property Relationships*. John Wiley & Sons, Ltd: 2016.

2.Pinacca, R. M.; Larrégola, S. A.; López, C. A.; Pedregosa, J. C.; Pomjakushin, V.; Sánchez, R. D.; Alonso, J. A., Cationic ordering and role of the B-site lanthanide(III) and molybdenum(V) cations on the structure and magnetism of double perovskites Sr_2LnMoO_6. *Mater. Res. Bull.* **2015,** *66*, 192-199.

3.Alexander, C. T.; Mefford, J. T.; Saunders, J.; Forslund, R. P.; Johnston, K. P.; Stevenson, K. J., Anion-Based Pseudocapacitance of the Perovskite Library $La_{1-x}Sr_xBO_{3-\delta}$ (B = Fe, Mn, Co). *ACS Appl. Mater. Interfaces* **2019,** *11*, 5084-5094.

4.Bukhari, S. M.; Giorgi, J. B., Ni doped $Sm_{0.95}Ce_{0.05}FeO_{3-\delta}$ perovskite based sensors for hydrogen detection. *Sens. Actuators B Chem.* **2013,** *181*, 153-158.

5.Mulmi, S.; Hona, R. K.; Jasinski, J. B.; Ramezanipour, F., Electrical conductivity of $Sr_{2-x}Ca_xFeMnO_5$ (x = 0, 1, 2). *J. Solid State Electrochem.* **2018,** *22*, 2329-2338.

6.Krumpelt, M.; Kumar, R.; Myles, K. M., Fundamentals of fuel cell system in integration. *J. Power Sources* **1994,** *49*, 37-51.

7.Goldschmidt, V. M., Die Gesetze der Krystallochemie. *Naturwissenschaften* **1926,** *14*, 477-485.

8.Megaw, H., Crystal Structure of Barium Titanate. *Nature* **1945,** *155*, 484-485.

9.Anderson, M. T.; Vaughey, J. T.; Poeppelmeier, K. R., Structural similarities among oxygen-deficient perovskites. *Chem. Mater.* **1993,** *5*, 151-165.

10.Hona, R. K.; Huq, A.; Mulmi, S.; Ramezanipour, F., Transformation of Structure, Electrical Conductivity, and Magnetism in $AA'Fe_2O_{6-\delta}$, A = Sr, Ca and A' = Sr. *Inorg. Chem.* **2017,** *56*, 9716-9724.

11.Hona, R. K.; Ramezanipour, F., Enhanced electrical properties in $BaSrFe_2O_{6-\delta}$ (δ = 0.5): A disordered defect-perovskite. *Polyhedron* **2019,** *167*, 69-74.

12.Hona, R. K.; Huq, A.; Ramezanipour, F., Unraveling the Role of Structural Order in the Transformation of Electrical Conductivity in $Ca_2FeCoO_{6-\delta}$, $CaSrFeCoO_{6-\delta}$, and $Sr_2FeCoO_{6-\delta}$. *Inorg. Chem.* **2017,** *56*, 14494-14505.

13.Grenier, J.-C.; Darriet, J.; Pouchard, M.; Hagenmuller, P., Mise en evidence d'une nouvelle famille de phases de type perovskite lacunaire ordonnee de formule $A_3M_3O_8$ ($AMO_{2,67}$). *Mater. Res. Bull.* **1976,** *11*, 1219-1225.

14.Hudspeth, J. M.; Goossens, D. J.; Studer, A. J.; Withers, R. L.; Norén, L., The crystal and magnetic structures of $LaCa_2Fe_3O_8$ and $NdCa_2Fe_3O_8$. *J. Phys. Condens. Matter* **2009,** *21*, 124206.

15.Luo, K.; Hayward, M. A., The synthesis and characterisation of $LaCa_2Fe_2GaO_8$. *J. Solid State Chem.* **2013,** *198*, 203-209.

16.Battle, P. D.; Gibb, T. C.; Lightfoot, P., The crystal and magnetic structures of $Sr_2LaFe_3O_8$. *J. Solid State Chem.* **1990,** *84*, 237-244.

17.Martínez de Irujo-Labalde, X.; Goto, M.; Urones-Garrote, E.; Amador, U.; Ritter, C.; Amano Patino, M. E.; Koedtruad, A.; Tan, Z.; Shimakawa, Y.; García-Martín, S., Multiferroism Induced by Spontaneous Structural Ordering in Antiferromagnetic Iron Perovskites. *Chem. Mater.* **2019,** *31*, 5993-6000.

18. Fanah, S. J.; Yu, M.; Ramezanipour, F., Experimental and theoretical investigation of lithium-ion conductivity in $Li_2LaNbTiO_7$. *Dalton Trans.* **2019,** *48*, 17281-17290.

19. Singh, Y., Electrical Resistivity Measurements: A Review. *Int. J. Mod. Phys.: Conf. Ser.* **2013,** *22*, 745-756.

20. Shaula, A. L.; Kolotygin, V. A.; Naumovich, E. N.; Pivak, Y. V.; Kharton, V. V., Oxygen Ionic Transport in Brownmillerite-Type and Calcium Ferrite-Based Composite Membranes. *Solid State Phenom.* **2013,** *200*, 286-292.

21. Patrakeev, M. V.; Kharton, V. V.; Bakhteeva, Y. A.; Shaula, A. L.; Leonidov, I. A.; Kozhevnikov, V. L.; Naumovich, E. N.; Yaremchenko, A. A.; Marques, F. M. B., Oxygen nonstoichiometry and mixed conductivity of $SrFe_{1-x}M_xO_{3-\delta}$ (M=Al, Ga): Effects of B-site doping. *Solid State Sci.* **2006,** *8*, 476-487.

22. Hona, R. K.; Huq, A.; Ramezanipour, F., Charge transport properties of $Ca_2FeGaO_{6-\delta}$ and $CaSrFeGaO_{6-\delta}$: The effect of defect-order. *Mater. Chem. Phys.* **2019,** *238*, 121924.

23. Hona, R. K.; Huq, A.; Mulmi, S.; Ramezanipour, F., Transformation of Structure, Electrical Conductivity, and Magnetism in $AA'Fe_2O_{6-\delta}$, A = Sr, Ca and A' = Sr. *Inorganic Chemistry* **2017,** *56* (16), 9716-9724.

24. Patrakeev, M. V.; Kharton, V. V.; Bakhteeva, Y. A.; Shaula, A. L.; Leonidov, I. A.; Kozhevnikov, V. L.; Naumovich, E. N.; Yaremchenko, A. A.; Marques, F. M. B., Oxygen nonstoichiometry and mixed conductivity of $SrFe_{1-x}M_xO_{3-\delta}$ (M=Al, Ga): Effects of B-site doping. *Solid State Sci.* **2006,** *8* (5), 476-487.

25. Mineshige, A.; Kobune, M.; Fujii, S.; Ogumi, Z.; Inaba, M.; Yao, T.; Kikuchi, K., Metal–Insulator Transition and Crystal Structure of $La_{1-x}Sr_xCoO_3$ as Functions of Sr-Content, Temperature, and Oxygen Partial Pressure. *J. Solid State Chem.* **1999,** *142*, 374-381.

26. Mineshige, A.; Inaba, M.; Yao, T.; Ogumi, Z.; Kikuchi, K.; Kawase, M., Crystal Structure and Metal–Insulator Transition of $La_{1-x}Sr_xCoO_3$. *J. Solid State Chem.* **1996,** *121*, 423-429.

27. Yamazoe, N.; Miura, N., Environmental gas sensing. *Sens. Actuators, B* **1994,** *20*, 95-102.

28. Takeuchi, T., Oxygen sensors. *Sens. Actuators, B* **1988,** *14*, 109-124.

29. Beie, H. J.; Gnörich, A., Oxygen gas sensors based on CeO_2 thick and thin films. *Sens. Actuators B Chem.* **1991,** *4*, 393-399.

30. Josepovits, V. K.; Krafcsik, O.; Kiss, G.; Perczel, I. V., Effect of gas adsorption on the surface structure of β-Ga_2O_3 studied by XPS and conductivity measurements. *Sens. Actuators B Chem.* **1998,** *48*, 373-375.

31. Zhu, J.; Ren, C.; Chen, G.; Yu, C.; Wu, J.; Mu, H., A new automotive air/fuel sensor based on TiO_2-doped Nb_2O_5 thin film by ion-beam-enhanced deposition. *Sensors and Actuators B: Chemical* **1996,** *32*, 209-213.

32. Mulmi, S.; Thangadurai, V., Semiconducting SnO_2-TiO_2 (S-T) composites for detection of SO_2 gas. *Ionics* **2016,** *22*, 1927-1935.

33. Meixner, H.; Lampe, U., Metal oxide sensors. *Sens. Actuators B Chem.* **1996,** *33*, 198-202.

34. Nisar, J.; Topalian, Z.; De Sarkar, A.; Österlund, L.; Ahuja, R., TiO_2-Based Gas Sensor: A Possible Application to SO_2. *ACS Appl. Mater. Interfaces* **2013,** *5*, 8516-8522.

35. Morrison, S. R., Semiconductor gas sensors. *Sens. Actuators* **1981,** *2*, 329-341.

36. Chen, M.; Wang, Z.; Han, D.; Gu, F.; Guo, G., Porous ZnO Polygonal Nanoflakes: Synthesis, Use in High-Sensitivity NO_2 Gas Sensor, and Proposed Mechanism of Gas Sensing. *J. Phys. Chem. C* **2011,** *115*, 12763-12773.

37. Chiu, C. M.; Chang, Y. H., The structure, electrical and sensing properties for CO of the $La_{0.8}Sr_{0.2}Co_{1-x}Ni_xO_{3-\delta}$ system. *Mater. Sci. Eng., A* **1999,** *266*, 93-98.

38.Zhang, Y.; Yang, G.; Chen, G.; Ran, R.; Zhou, W.; Shao, Z., Evaluation of the CO_2 Poisoning Effect on a Highly Active Cathode $SrSc_{0.175}Nb_{0.025}Co_{0.8}O_{3-\delta}$ in the Oxygen Reduction Reaction. *ACS Appl. Mater. Interfaces* **2016,** *8*, 3003-3011.

39.Bartolomeo, E.; Grilli, M. L.; Yoon, J. W.; Traversa, E., Zirconia-Based Electrochemical NO_x Sensors with Semiconducting Oxide Electrodes. *J. Am. Ceram. Soc.* **2004,** *87*, 1883-1889.

40.Riegel, J.; Neumann, H.; Wiedenmann, H. M., Exhaust gas sensors for automotive emission control. *Solid State Ion.* **2002,** *152-153*, 783-800.

41.Bektas, M.; Schönauer-Kamin, D.; Hagen, G.; Mergner, A.; Bojer, C.; Lippert, S.; Milius, W.; Breu, J.; Moos, R., $BaFe_{1-x}Ta_xO_{3-\delta}$ – A material for temperature independent resistive oxygen sensors. *Sens. Actuators B Chem.* **2014,** *190*, 208-213.

42.Lin, Q.; Greenblatt, M.; Caspi, E. a. N.; Avdeev, M., Crystallographic and magnetic properties of $CaLaMnMoO_6$ double perovskite. *J. Solid State Chem.* **2006,** *179*, 2086-2092.

43.Jeng, H.-T.; Guo, G.-Y., First-principles investigations of orbital magnetic moments and electronic structures of the double perovskites Sr_2FeMoO_6, Sr_2FeReO_6, and Sr_2CrWO_6. *Phys. Rev. B* **2003,** *67*, 94438.

44.Mefford, J. T.; Hardin, W. G.; Dai, S.; Johnston, K. P.; Stevenson, K. J., Anion charge storage through oxygen intercalation in $LaMnO_3$ perovskite pseudocapacitor electrodes. *Nat. Mater.* **2014,** *13*, 726.

45.Kudo, T.; Obayashi, H.; Gejo, T., Electrochemical Behavior of the Perovskite-Type $Nd_{1-x}Sr_x CoO_3$ in an Aqueous Alkaline Solution. *J. Electrochem. Soc. 1* **1975,** *122*, 159-163.

46.Lang, X.; Mo, H.; Hu, X.; Tian, H., Supercapacitor performance of perovskite $La_{1-x}Sr_xMnO_3$. *Dalton Trans.* **2017,** *46*, 13720-13730.

47.Mo, H.; Nan, H.; Lang, X.; Liu, S.; Qiao, L.; Hu, X.; Tian, H., Influence of calcium doping on performance of $LaMnO_3$ supercapacitors. *Ceram. Int.* **2018,** *44*, 9733-9741.

48.Zhu, L.; Liu, Y.; Su, C.; Zhou, W.; Liu, M.; Shao, Z., Perovskite $SrCo_{0.9}Nb_{0.1}O_{3-\delta}$ as an Anion-Intercalated Electrode Material for Supercapacitors with Ultrahigh Volumetric Energy Density. *Angew. Chem., Int. Ed.* **2016,** *55*, 9576-9579.

49.Alexander, C. T.; Forslund, R. P.; Johnston, K. P.; Stevenson, K. J., Tuning Redox Transitions via the Inductive Effect in $LaNi_{1-x}Fe_xO_{3-\delta}$ Perovskites for High-Power Asymmetric and Symmetric Pseudocapacitors. *ACS Appl. Energy Mater.* **2019,** *2*, 6558-6568.

50.Ma, T. Y.; Dai, S.; Jaroniec, M.; Qiao, S. Z., Metal–Organic Framework Derived Hybrid Co_3O_4-Carbon Porous Nanowire Arrays as Reversible Oxygen Evolution Electrodes. *J. Amer. Chem. Soc.* **2014,** *136*, 13925-13931.

51.Mahmood, J.; Li, F.; Jung, S.-M.; Okyay, M. S.; Ahmad, I.; Kim, S.-J.; Park, N.; Jeong, H. Y.; Baek, J.-B., An efficient and pH-universal ruthenium-based catalyst for the hydrogen evolution reaction. *Nat. Nanotechnol.* **2017,** *12*, 441-446.

52.Subbaraman, R.; Tripkovic, D.; Chang, K.-C.; Strmcnik, D.; Paulikas, A. P.; Hirunsit, P.; Chan, M.; Greeley, J.; Stamenkovic, V.; Markovic, N. M., Trends in activity for the water electrolyser reactions on 3d M(Ni,Co,Fe,Mn) hydr(oxy)oxide catalysts. *Nat. Mater.* **2012,** *11*, 550-557.

53.Hamdani, M.; Singh, R. N.; Chartier, P., Co_3O_4 and Co- Based Spinel Oxides Bifunctional Oxygen Electrodes *Int. J. Electrochem. Sci.* **2010,** *5*, 556 - 577.

54.Li, Y.; Gong, M.; Liang, Y.; Feng, J.; Kim, J.-E.; Wang, H.; Hong, G.; Zhang, B.; Dai, H., Advanced zinc-air batteries based on high-performance hybrid electrocatalysts. *Nat. Commun.* **2013,** *4*, 1805.

55.Shinagawa, T.; Garcia-Esparza, A. T.; Takanabe, K., Insight on Tafel slopes from a microkinetic analysis of aqueous electrocatalysis for energy conversion. *Sci. Rep.* **2015,** *5*, 13801.

56. Zhu, J.; Hu, L.; Zhao, P.; Lee, L. Y. S.; Wong, K.-Y., Recent Advances in Electrocatalytic Hydrogen Evolution Using Nanoparticles. *Chem. Rev.* **2020,** *120*, 851-918.

57. Wang, C.; Zeng, L.; Guo, W.; Gong, C.; Yang, J., Enhancing oxygen and hydrogen evolution activities of perovskite oxide $LaCoO_3$ via effective doping of platinum. *RSC Adv.* **2019,** *9*, 35646-35654.

58. Kananke-Gamage, C. C. W.; Ramezanipour, F., Variation of Electrocatalytic Activity of Isostructural Oxides $Sr_2LaFeMnO_7$ and $Sr_2LaCoMnO_7$ for Hydrogen and Oxygen-Evolution Reactions. *Dalton Trans.* **2021**, 50, 14196-14206.

59. Chi, J.-Q.; Xie, J.-Y.; Zhang, W.-W.; Dong, B.; Qin, J.-F.; Zhang, X.-Y.; Lin, J.-H.; Chai, Y.-M.; Liu, C.-G., N-Doped Sandwich-Structured $Mo_2C@C@Pt$ Interface with Ultralow Pt Loading for pH-Universal Hydrogen Evolution Reaction. *ACS Appl. Mater. Interfaces* **2019,** *11*, 4047-4056.

60. Lee, Y.; Suntivich, J.; May, K. J.; Perry, E. E.; Shao-Horn, Y., Synthesis and activities of rutile IrO_2 and RuO_2 nanoparticles for oxygen evolution in acid and alkaline solutions. *J. Phys. Chem. Lett.* **2012,** *3*, 399-404.

61. Luo, Y.; Wang, Z.; Fu, Y.; Jin, C.; Wei, Q.; Yang, R., In situ preparation of hollow $Mo_2C–C$ hybrid microspheres as bifunctional electrocatalysts for oxygen reduction and evolution reactions. *J. Mater. Chem. A* **2016,** *4*, 12583-12590.

62. Lee, J. W.; Hall, A. S.; Kim, J.-D.; Mallouk, T. E., A Facile and Template-Free Hydrothermal Synthesis of Mn_3O_4 Nanorods on Graphene Sheets for Supercapacitor Electrodes with Long Cycle Stability. *Chem. Mater.* **2012,** *24*, 1158-1164.

63. Escudero-Escribano, M.; Pedersen, A. F.; Paoli, E. A.; Frydendal, R.; Friebel, D.; Malacrida, P.; Rossmeisl, J.; Stephens, I. E. L.; Chorkendorff, I., Importance of Surface IrO_x in Stabilizing RuO_2 for Oxygen Evolution. *J. Phys. Chem. B* **2018,** *122*, 947-955.

64. He, D.; He, G.; Jiang, H.; Chen, Z.; Huang, M., Enhanced durability and activity of the perovskite electrocatalyst $Pr_{0.5}Ba_{0.5}CoO_{3-\delta}$ by Ca doping for the oxygen evolution reaction at room temperature. *Chem. Commun.* **2017,** *53*, 5132-5135.

65. Chen, G.; Zhou, W.; Guan, D.; Sunarso, J.; Zhu, Y.; Hu, X.; Zhang, W.; Shao, Z., Two orders of magnitude enhancement in oxygen evolution reactivity on amorphous $Ba_{(0.5)}Sr_{(0.5)}Co_{(0.8)}Fe_{(0.2)}O_{(3-\delta)}$ nanofilms with tunable oxidation state. *Sci. Adv.* **2017,** *3*, e1603206.

66. Zhu, Y.; Zhou, W.; Chen, Z. G.; Chen, Y.; Su, C.; Tadé Moses, O.; Shao, Z., $SrNb_{0.1}Co_{0.7}Fe_{0.2}O_{3-\delta}$ perovskite as a next-generation electrocatalyst for oxygen evolution in alkaline solution. *Angew. Chem. Int. Ed.* **2015,** *54*, 3897-3901.

67. Li, J.; Wen, Z.; Hui, Z. X.; Chen, Z. W.; Yang, C. C.; Jiang, Q., Graphene-MoS_2 vertically anchored on an MXene-derived accordion-like TiO_2/C skeleton: an ultrastable HER catalyst. *J. Mater. Chem.y A* **2020,** *8*, 14223-14233.

68. Chen, D.; Chen, C.; Baiyee, Z. M.; Shao, Z.; Ciucci, F., Nonstoichiometric Oxides as Low-Cost and Highly-Efficient Oxygen Reduction/Evolution Catalysts for Low-Temperature Electrochemical Devices. *Chem. Rev.* **2015,** *115*, 9869-9921.

69. Sun, Q.; Dai, Z.; Zhang, Z.; Chen, Z.; Lin, H.; Gao, Y.; Chen, D., Double perovskite $PrBaCo_2O_{5.5}$: An efficient and stable electrocatalyst for hydrogen evolution reaction. *J. Power Sources* **2019,** *427*, 194-200.

70. Wang, J.; Gao, Y.; Chen, D.; Liu, J.; Zhang, Z.; Shao, Z.; Ciucci, F., Water Splitting with an Enhanced Bifunctional Double Perovskite. *ACS Catal.* **2018,** *8*, 364-371.

71. Su, C.; Wang, W.; Chen, Y.; Yang, G.; Xu, X.; Tadé, M. O.; Shao, Z., $SrCo_{0.9}Ti_{0.1}O_{3-\delta}$ as a new electrocatalyst for the oxygen evolution reaction in alkaline electrolyte with stable performance. *ACS Appl. Mater. Interfaces* **2015,** *7*, 17663-17670.

72.Park, H. W.; Lee, D. U.; Zamani, P.; Seo, M. H.; Nazar, L. F.; Chen, Z., Electrospun porous nanorod perovskite oxide/nitrogen-doped graphene composite as a bi-functional catalyst for metal air batteries. *Nano Energy* **2014,** *10*, 192-200.

73.Jung, J.-I.; Risch, M.; Park, S.; Kim, M. G.; Nam, G.; Jeong, H.-Y.; Shao-Horn, Y.; Cho, J., Optimizing nanoparticle perovskite for bifunctional oxygen electrocatalysis. *Energy Environ. Sci.* **2016,** *9*, 176-183.

74.Suntivich, J.; May, K. J.; Gasteiger, H. A.; Goodenough, J. B.; Shao-Horn, Y., A Perovskite Oxide Optimized for Oxygen Evolution Catalysis from Molecular Orbital Principles. *Science* **2011,** *334*, 1383.

75.Guan, D.; Zhou, J.; Huang, Y.-C.; Dong, C.-L.; Wang, J.-Q.; Zhou, W.; Shao, Z., Screening highly active perovskites for hydrogen-evolving reaction via unifying ionic electronegativity descriptor. *Nature Communications* **2019,** *10*, 3755.

76.Tian, S.; He, J.; Huang, H.; Song, T.-s.; Wu, X.; Xie, J.; Zhou, W., Perovskite-Based Multifunctional Cathode with Simultaneous Supplementation of Substrates and Electrons for Enhanced Microbial Electrosynthesis of Organics. *ACS Appl. Mater. Interfaces* **2020,** *12*, 30449-30456.

77.Zhu, Y.; Zhou, W.; Zhong, Y.; Bu, Y.; Chen, X.; Zhong, Q.; Liu, M.; Shao, Z., A Perovskite Nanorod as Bifunctional Electrocatalyst for Overall Water Splitting. *Adv. Energy Mater.* **2017,** *7*, 1602122.

78.Hu, C.; Hong, J.; Huang, J.; Chen, W.; Segre, C. U.; Suenaga, K.; Zhao, W.; Huang, F.; Wang, J., Surface decoration accelerates the hydrogen evolution kinetics of a perovskite oxide in alkaline solution. *Energy Environ. Sci.* **2020,** *13*, 4249-4257.

79.West, A. R., *Solid state chemistry and its applications*. Second edition, student edition. ed.; Wiley: 2014.

80.Hona, R. K.; Karki, S. B.; Cao, T.; Mishra, R.; Sterbinsky, G. E.; Ramezanipour, F., Sustainable Oxide Electrocatalyst for Hydrogen and Oxygen-Evolution Reactions. *ACS Catal.* **2021,** *11*, 14605–14614.

81.Hona, R. K.; Karki, S. B.; Ramezanipour, F., Oxide Electrocatalysts Based on Earth-Abundant Metals for Both Hydrogen- and Oxygen-Evolution Reactions. *ACS Susttain. Chem. Eng.* **2020,** *8*, 11549-11557.

82.Karki, S. B.; Andriotis, A. N.; Menon, M.; Ramezanipour, F., Bifunctional Water-Splitting Electrocatalysis Achieved by Defect-Order in $LaA_2Fe_3O_8$ (A = Ca, Sr). *ACS Appl. Energy Mater.* **2021,** *4*, 12063–12066.

83.Karki, S. B.; Hona, R. K.; Ramezanipour, F., Effect of Structure on Sensor Properties of Oxygen-Deficient Perovskites, $A_2BB'O_5$ (A = Ca, Sr; B = Fe; B' = Fe, Mn) for Oxygen, Carbon Dioxide and Carbon Monoxide Sensing. *J. Electron. Mater.* **2020,** *49*, 1557-1567.

84.Karki, S. B.; Hona, R. K.; Ramezanipour, F., Electrocatalytic activity and structural transformation of $Ca_2Sr_2Mn_2MO_{10-\delta}$ (M = Fe, Co). *Ionics* **2021,** *28*, 397-406.

85.Karki, S. B.; Ramezanipour, F., Magnetic and electrical properties of $BaSrMMoO_6$ (M = Mn, Fe, Co, and Ni). *Mater. Today Chem.* **2019,** *13*, 25-33.

86.Karki, S. B.; Ramezanipour, F., Pseudocapacitive Energy Storage and Electrocatalytic Hydrogen-Evolution Activity of Defect-Ordered Perovskites $Sr_xCa_{3-x}GaMn_2O_8$ (x = 0 and 1). *ACS Appl. Energy Mater.* **2020,** *3*, 10983–10992.

87.Karki, S. B.; Hona, R. K.; Ramezanipour, F., Sr3Mn2O6 and Sr3FeMnO6 for oxygen and hydrogen evolution electrocatalysis. *Journal of Solid State Electrochemistry* **2022,** *DOI: 10.1007/s10008-022-05167-1*.

88. Navas, D.; Fuentes, S.; Castro-Alvarez, A.; Chavez-Angel, E., Review on Sol-Gel Synthesis of Perovskite and Oxide Nanomaterials. *Gels* **2021,** *7*, 275.

89. Danks, A. E.; Hall, S. R.; Schnepp, Z., The evolution of 'sol–gel' chemistry as a technique for materials synthesis. *Mater. Horiz.* **2016,** *3*, 91-112.

90. Znaidi, L., Sol–gel-deposited ZnO thin films: A review. *Mater. Sci. Eng. B* **2010,** *174*, 18-30.

91. Cheetham, A. K.; Day, P., *Solid-State Chemistry: Techniques*. Oxford University Press: 1987; Vol. 1.

92. Larson, A. C.; Von Dreele, A. C. *General Structure Analysis System (GSAS)*; Los Alamos National Laboratory: 2004; pp 86 - 748.

93. Toby, B. H., EXPGUI, a graphical user interface for GSAS. *J. Appl. Crystallogr.* **2001,** *34*, 210–213.

94. Macdonald, J. R., *Impedance spectroscopy : emphasizing solid materials and systems*. New York : Wiley: 1987; Vol. 346.

95. Chen, W. M.; Hong, W.; Geng, J. F.; Wu, X. S.; Ji, W.; Li, L. Y.; Qui, L.; Jin, X., Iodometric titration for determining the oxygen content of samples doped with Fe and Co. *Physica C Supercond.* **1996,** *270*, 349-353.

96. Shen, Q.; Li, S.; Yang, G.; Sunden, B.; Yuan, J., Effect of A-/B-site Doping on Oxygen Non-Stoichiometry, Structure characteristics, and O_2 Releasing Behavior of $La_{1-x}Ca_xCo_{1-y}Fe_yO_{3-\delta}$ Perovskites. *Energies* **2019,** *12*, 410.

97. Vazhayil, A.; Vazhayal, L.; Thomas, J.; Ashok C, S.; Thomas, N., A comprehensive review on the recent developments in transition metal-based electrocatalysts for oxygen evolution reaction. *Appl. Surf. Sci. Adv.* **2021,** *6*, 100184.

98. Jeerage, K. M.; Candelaria, S. L.; Stavis, S. M., Rapid Synthesis and Correlative Measurements of Electrocatalytic Nickel/Iron Oxide Nanoparticles. *Sci. Rep.* **2018,** *8* (1), 4584.

99. Zhu, Y.; Zhou, W.; Chen, Z. G.; Chen, Y.; Su, C.; Tadé, M. O.; Shao, Z., $SrNb_{0.1}Co_{0.7}Fe_{0.2}O_{3-\delta}$ perovskite as a next-generation electrocatalyst for oxygen evolution in alkaline solution. *Angew. Chem. Int. Ed.* **2015,** *54*, 3897-3901.

100. Wu, W.; Niu, C.; Wei, C.; Jia, Y.; Li, C.; Xu, Q., Activation of MoS_2 Basal Planes for Hydrogen Evolution by Zinc. *Angew. Chem. Int. Ed.* **2019,** *58*, 2029-2033.

101. Zhu, J.; Wang, Z.-C.; Dai, H.; Wang, Q.; Yang, R.; Yu, H.; Liao, M.; Zhang, J.; Chen, W.; Wei, Z.; Li, N.; Du, L.; Shi, D.; Wang, W.; Zhang, L.; Jiang, Y.; Zhang, G., Boundary activated hydrogen evolution reaction on monolayer MoS_2. *Nat. Commun.* **2019,** *10*, 1348.

102. McGlynn, J. C.; Dankwort, T.; Kienle, L.; Bandeira, N. A. G.; Fraser, J. P.; Gibson, E. K.; Cascallana-Matías, I.; Kamarás, K.; Symes, M. D.; Miras, H. N.; Ganin, A. Y., The rapid electrochemical activation of $MoTe_2$ for the hydrogen evolution reaction. *Nat. Commun.* **2019,** *10*, 4916.

103. Yang, W.; Kim, J. H.; Hutter, O. S.; Phillips, L. J.; Tan, J.; Park, J.; Lee, H.; Major, J. D.; Lee, J. S.; Moon, J., Benchmark performance of low-cost Sb_2Se_3 photocathodes for unassisted solar overall water splitting. *Nat. Commun.* **2020,** *11*, 861.

104. Ritter, C.; Ibarra, M. R.; Morellón, L.; Blasco, J.; García, J.; De Teresa, J. M., Structural and magnetic properties of double perovskites AA'FeMoO$_6$ (AA' = Ba$_2$, BaSr, Sr$_2$ and Ca$_2$). *J. Phys.: Condens. Matter* **2000,** *12*, 8295–8308.

105. Zheng, K.; Świerczek, K.; Zając, W.; Klimkowicz, A., Rock salt ordered-type double perovskite anode materials for solid oxide fuel cells. *Solid State Ionics* **2014,** *257*, 9-16.

106. Zheng, K.; Świerczek, K., A- and B-site doping effect on physicochemical properties of $Sr_{2-x}Ba_xMMoO_6$ (M = Mg, Mn, Fe) double perovskites - candidate anode materials for SOFCs. **2016,** *9*, 1641002.

107.Poddar, A.; Das, S.; Chattopadhyay, B., Effect of alkaline-earth and transition metals on the electrical transport of double perovskites. *J. Appl. Phys.* **2004,** *95*, 6261-6267.

108.Zheng, K.; Świerczek, K., Physicochemical properties of rock salt-type ordered Sr_2MMoO_6 (M=Mg, Mn, Fe, Co, Ni) double perovskites. *J. Eur. Ceram. Soc* **2014,** *34*, 4273-4284.

109.Chan, T. S.; Liu, R. S.; Guo, G. Y.; Hu, S. F.; Lin, J. G.; Chen, J. M.; Attfield, J. P., Chemical Tuning of Structure, Magnetization, and Conductivity in the Self-doped Double-Perovskite ($Sr_{2-x}Ca_x$)$FeMoO_6$ ($0 \leq x \leq 2.0$) System. *Chem. Mater.* **2003,** *15*, 425-432.

110.Teraoka, Y.; Wei, M.-D.; Kagawa, S., Double perovskites containing hexavalent molybdenum and tungsten: synthesis, structural investigation and proposal of a fitness factor to discriminate the crystal symmetry. *J. Mater. Chem.* **1998,** *8*, 2323-2325.

111.Pagnier, T.; Rosman, N.; Galven, C.; Suard, E.; Fourquet, J. L.; Le Berre, F.; Crosnier-Lopez, M. P., Phase transition in the Ruddlesden–Popper layered perovskite $Li_2SrTa_2O_7$. *Journal of Solid State Chemistry* **2009,** *182* (2), 317-326.

112.Li, Q.; Thangadurai, V., A comparative 2 and 4-probe DC and 2-probe AC electrical conductivity of novel co-doped $Ce_{0.9-x}RE_xMo_{0.1}O_{2.1-0.5x}$ (RE = Y, Sm, Gd; x = 0.2, 0.3). *J. Mater. Chem.* **2010,** *20*, 7970-7983.

113.Ghaffari, M.; Liu, T.; Huang, H.; Tan, O. K.; Shannon, M., Investigation of local structure effect and X-ray absorption characteristics (EXAFS) of Fe (Ti) K-edge on photocatalyst properties of $SrTi_{(1-x)}FexO_{(3-\delta)}$. *Mater. Chem. Phys* **2012,** *136*, 347-357.

114.Yamashita, T.; Hayes, P., Analysis of XPS spectra of Fe^{2+} and Fe^{3+} ions in oxide materials. *Appl. Surf. Sci.* **2008,** *254*, 2441-2449.

115.Hona, R. K.; Ramezanipour, F., Disparity in electrical and magnetic properties of isostructural oxygen-deficient perovskites $BaSrCo_2O_{6-\delta}$ and $BaSrCoFeO_{6-\delta}$. *J. Mater. Sci. Mater. Electron* **2018,** *29*, 13464-13473.

116.Morales, J.; Sánchez, L.; Martín, F.; Berry, F.; Ren, X., Synthesis and Characterization of Nanometric Iron and Iron-Titanium Oxides by Mechanical Milling: Electrochemical Properties as Anodic Materials in Lithium Cells. *J. Electrochem. Soc.* **2005,** *152*, A1748-A1754.

117.Doi, A.; Nomura, M.; Obukuro, Y.; Maeda, R.; Obata, K.; Matsushima, S.; Kobayashi, K., Characterization of Ti-doped $CaFe_2O_4$ prepared from a malic acid complex. *J. Ceram. Soc. Jpn.* **2014,** *122*, 175-178.

118.Li, C.; Wang, W.; Zhao, N.; Liu, Y.; He, B.; Hu, F.; Chen, C., Structure properties and catalytic performance in methane combustion of double perovskites $Sr_2Mg_{1-x}Mn_xMoO_{6-\delta}$. *Appl. Catal. B-Environ.* **2011,** *102*, 78-84.

119.Zhang, L.; Zhou, Q.; He, Q.; He, T., Double-perovskites $A_2FeMoO_{6-\delta}$ (A=Ca, Sr, Ba) as anodes for solid oxide fuel cells. *J. Power Sources* **2010,** *195*, 6356-6366.

120.Zhang, W.; Meng, J.; Zhang, X.; Zhang, L.; Liu, X.; Meng, J., Co-incorporating enhancement on oxygen vacancy formation energy and electrochemical property of $Sr_2Co_{1+x}Mo_{1-x}O_{6-\delta}$ cathode for intermediate-temperature solid oxide fuel cell. *Solid State Ion.* **2018,** *316*, 20-28.

121.Moulder, J. F.; Stickle, W. F.; Sobol, P. E.; Bomben, K. B., *Handbook of X-Ray Photoelectron Spectroscopy*. Perkin-Elmer Corporation: 1992.

122.Biesinger, M. C.; Payne, B. P.; Grosvenor, A. P.; Lau, L. W. M.; Gerson, A. R.; Smart, R. S. C., Resolving surface chemical states in XPS analysis of first row transition metals, oxides and hydroxides: Cr, Mn, Fe, Co and Ni. *ppl. Surf. Sci.* **2011,** *257*, 2717-2730.

123.Davison, N.; McWhinnie, W. R., X-ray Photoelectron Spectroscopic Study of Cobalt(II) and Nickel(II) Sorbed on Hectorite and Montmorillonite. *Clays and Clay Minerals* **1991,** *39*, 22-27.

124. Dupin, J. C.; Gonbeau, D.; Benqlilou-Moudden, H.; Vinatier, P.; Levasseur, A., XPS analysis of new lithium cobalt oxide thin-films before and after lithium deintercalation. *Thin Solid Films* **2001,** *384*, 23-32.

125. Zhang, G.; Zhang, J.; Zhang, Y.; Zhou, P.; Wei, C.; Li, W.; Liang, T., Degradation of dimethyl phthalate by peroxomonosulfate ion activated by Zn–NiO$_x$ catalyst. *Reac Kinet Mech Cat.* **2017,** *122*, 1175-1192.

126. Ren, Y.; Dong, Q.; Feng, J.; Ma, J.; Wen, Q.; Zhang, M., Magnetic porous ferrospinel NiFe$_2$O$_4$: A novel ozonation catalyst with strong catalytic property for degradation of di-n-butyl phthalate and convenient separation from water. *J. Colloid Interface Sci.* **2012,** *382*, 90-96.

127. Feng, J.; Yang, G.; Dai, N.; Wang, Z.; Sun, W.; Rooney, D.; Qiao, J.; Sun, K., Investigation into the effect of Fe-site substitution on the performance of Sr$_2$Fe$_{1.5}$Mo$_{0.5}$O$_{6−\delta}$ anodes for SOFCs. *J. Mater. Chem. A* **2014,** *2*, 17628-17634.

128. Liu, K.; Zhang, Q.; Dai, S.; Li, W.; Liu, X.; Ding, F.; Zhang, J., Synergistic Effect of F-Doping and LiF Coating on Improving the High-Voltage Cycling Stability and Rate Capacity of LiNi$_{0.5}$Co$_{0.2}$Mn$_{0.3}$O$_2$ Cathode Materials for Lithium-Ion Batteries. *ACS Appl. Mater. Interfaces* **2018,** *10*, 34153-34162.

129. Martínez-Lope, María J.; Alonso, José A.; Casais, María T.; Fernández-Díaz, María T., Preparation, Crystal and Magnetic Structure of the Double Perovskites Ba$_2$CoBO$_6$ (B = Mo, W). *Eur. J. Inorg. Chem.* **2002,** *2002*, 2463-2469.

130. Ramezanipour, F.; Greedan, J. E.; Cranswick, L. M. D.; Garlea, V. O.; Donaberger, R. L.; Siewenie, J., Systematic Study of Compositional and Synthetic Control of Vacancy and Magnetic Ordering in Oxygen-Deficient Perovskites Ca$_2$Fe$_{2−x}$Mn$_x$O$_{5+y}$and CaSrFe$_{2−x}$Mn$_x$O$_{5+y}$ (x = 1/2, 2/3, and 1; y = 0–1/2). *J. Am. Chem. Soc.* **2012,** *134*, 3215-3227.

131. Ramezanipour, F.; Greedan, J. E.; Siewenie, J.; Proffen, T.; Ryan, D. H.; Grosvenor, A. P.; Donaberger, R. L., Local and Average Structures and Magnetic Properties of Sr$_2$FeMnO$_{5+y}$, y = 0.0, 0.5. Comparisons with Ca$_2$FeMnO$_5$ and the Effect of the A-Site Cation. *Inorg. Chem.* **2011,** *50*, 7779-7791.

132. Ramezanipour, F.; Cowie, B.; Derakhshan, S.; Greedan, J. E.; Cranswick, L. M. D., Crystal and magnetic structures of the brownmillerite compound Ca$_2$Fe$_{1.039(8)}$Mn$_{0.962(8)}$O$_5$. *J. Solid State Chem.* **2009,** *182*, 153-159.

133. Kagomiya, I.; Hirota, Y.; Kakimoto, K.-i.; Fujii, K.; Shiraiwa, M.; Yashima, M.; Fuwa, A.; Nakamura, S., Weak ferromagnetic ordering in brownmillerite Ca$_2$Fe$_2$O$_5$ and its effect on electric field gradients. *Phys. Chem. Chem. Phys.* **2017,** *19*, 31194-31201.

134. Nakahara, Y.; Kato, S.; Sugai, M.; Ohshima, Y.; Makino, K., Synthesis and crystal structure of (Sr$_{1−x}$Ca$_x$)$_2$FeMnO$_y$ (x = 0–1.0). *Mater. Lett.* **1997,** *30*, 163-167.

135. Mulmi, S.; Hona, R. K.; Jasinski, J. B.; Ramezanipour, F., Electrical conductivity of Sr$_{2−x}$Ca$_x$FeMnO$_5$ (x = 0, 1, 2). *J. Solid State Electrochem.* **2018,** *22*, 2329-2338.

136. D'Hondt, H.; Abakumov, A. M.; Hadermann, J.; Kalyuzhnaya, A. S.; Rozova, M. G.; Antipov, E. V.; Van Tendeloo, G., Tetrahedral Chain Order in the Sr$_2$Fe$_2$O$_5$ Brownmillerite. *Chem. Mater.* **2008,** *20*, 7188-7194.

137. Berggren, J., Refinement of the crystal tructure of dicalcium ferrite, Ca$_2$Fe$_2$O$_5$. *Acta Chem. Scand.* **1975,** *25*, 3616-3624.

138. Ramamoorthy, R.; Dutta, P. K.; Akbar, S. A., Oxygen sensors: Materials, methods, designs and applications. *J. Mater. Sci.* **2003,** *38*, 4271-4282.

139. Akbar, S.; Dutta, P.; Lee, C., High-Temperature Ceramic Gas Sensors: A Review. *Int. J. Appl. Ceram. Technol.* **2006,** *3*, 302-311.

218

140. Yo, C. H.; Jung, I. Y.; Ryu, K. H.; Ryu, K. S.; Choy, J. H., A Study of the Nonstoichiometry and Physical Properties of the Perovskite $Nd_{1-x}Ca_xFeO_{3-y}$ System. *J. Solid State Chem.* **1995,** *114*, 265-270.

141. Hona, R. K.; Ramezanipour, F., Variation in electrical conductivity of $A_2Fe_2O_5$ (A = Sr, Ba): the role of structural order. *Mater. Res. Express.* **2018,** *5*, 076307.

142. Menesklou, W.; Schreiner, H.-J.; Härdtl, K. H.; Ivers-Tiffée, E., High temperature oxygen sensors based on doped $SrTiO_3$. *Sens. Actuators B Chem.* **1999,** *59*, 184-189.

143. Liu, Y.; Parisi, J.; Sun, X.; Lei, Y., Solid-state gas sensors for high temperature applications - a review. *J. Mater. Chem. A* **2014,** *2*, 9919-9943.

144. Bartic, M.; Ogita, M.; Isai, M.; Baban, C.-L.; Suzuki, H., Oxygen sensing properties at high temperatures of β-Ga_2O_3 thin films deposited by the chemical solution deposition method. *J. Appl. Phys.* **2007,** *102*, 023709.

145. Post, M. L.; Tunney, J. J.; Yang, D.; Du, X.; Singleton, D. L., Material chemistry of perovskite compounds as chemical sensors. *Sens. Actuators B Chem.* **1999,** *59*, 190-194.

146. Hodges, J. P.; Short, S.; Jorgensen, J. D.; Xiong, X.; Dabrowski, B.; Mini, S. M.; Kimball, C. W., Evolution of Oxygen-Vacancy Ordered Crystal Structures in the Perovskite Series $Sr_nFe_nO_{3n-1}$ (n=2, 4, 8, and ∞), and the Relationship to Electronic and Magnetic Properties. *J. Solid State Chem.* **2000,** *151*, 190-209.

147. Hosaka, Y.; Ichikawa, N.; Saito, T.; Mizumaki, M.; Shimakawa, Y., A Layered Double Perovskite Ca_2FeMnO_6 with Unusually High Valence Fe^{4+} Obtained by Low-Temperature Topotactic Oxidation. *J. Jpn. Soc. Powder Powder Metallurgy* **2016,** *63*, 605-608.

148. Thangadurai, V.; Weppner, W., $Ce_{0.8}Sm_{0.2}O_{1.9}$: characterization of electronic charge carriers and application in limiting current oxygen sensors. *Electrochim. Acta* **2004,** *49*, 1577-1585.

149. Chowdhury, A. K. M. S.; Akbar, S. A.; Kapileshwar, S.; Schorr, J. R., A Rugged Oxygen Gas Sensor with Solid Reference for High Temperature Applications. *J. Electrochem. Soc.* **2001,** *148*, G91-G94.

150. Mulmi, S.; Hassan, A.; Pereira-Almao, P.; Thangadurai, V., Detecting CO_2 at ppm level in synthetic air using mixed conducting double perovskite-type metal oxides. *Sens. Actuators B Chem.* **2013,** *178*, 598-605.

151. Liao, M.; Liu, J.; Sang, L.; Coathup, D.; Li, J.; Imura, M.; Koide, Y.; Ye, H., Impedance analysis of Al_2O_3/H-terminated diamond metal-oxide-semiconductor structures. *Appl. Phys. Lett.* **2015,** *106*, 083506.

152. Zhou, X.; Toft Sørensen, O.; Xu, Y., Defect structure and oxygen sensing properties of Mg-doped $SrTiO_3$ thick film sensors. *Sens. Actuators B Chem.* **1997,** *41*, 177-182.

153. Zhu, J.; Ren, C.; Chen, G.; Yu, C.; Wu, J.; Mu, H., A new automotive air/fuel sensor based on TiO_2-doped Nb_2O_5 thin film by ion-beam-enhanced deposition. *Sens. Actuators B Chem.* **1996,** *32*, 209-213.

154. Schwebel, T.; Fleischer, M.; Meixner, H., A selective, temperature compensated O_2 sensor based on Ga_2O_3 thin films. *Sens. Actuators B Chem.* **2000,** *65*, 176-180.

155. Manorama, S. V.; Izu, N.; Shin, W.; Matsubara, I.; Murayama, N., On the platinum sensitization of nanosized cerium dioxide oxygen sensors. *Sens. Actuators B Chem.* **2003,** *89*, 299-304.

156. Xu, Y.; Zhou, X.; Sorensen, O. T., Oxygen sensors based on semiconducting metal oxides: an overview. *Sens. Actuators B Chem.* **2000,** *65*, 2-4.

157. Motohashi, T.; Hirano, Y.; Masubuchi, Y.; Oshima, K.; Setoyama, T.; Kikkawa, S., Oxygen Storage Capability of Brownmillerite-type $Ca_2AlMnO_{5+\delta}$ and Its Application to Oxygen Enrichment. *Chem. Mater.* **2013,** *25*, 372-377.

158. Orr, F. M.; Taber, J. J., Use of Carbon Dioxide in Enhanced Oil Recovery. *Science* **1984,** *224*, 563-569.

159. Gerard, D.; Wilson, E. J., Environmental bonds and the challenge of long-term carbon sequestration. *J. Environ. Econ. Manag.* **2009,** *90*, 1097-1105.

160. Lang, A. C.; Fleischer, M.; Meixner, H., Surface modifications of Ga_2O_3 thin film sensors with Rh, Ru and Ir clusters. *Sens. Actuators B Chem.* **2000,** *66*, 80-84.

161. Schwebel, T.; Fleischer, M.; Meixner, H.; Kohl, C. D., CO-Sensor for domestic use based on high temperature stable Ga_2O_3 thin films. *Sens. Actuators B Chem.* **1998,** *49*, 46-51.

162. Mulmi, S.; Thangadurai, V., Preparation, Structure and CO_2 Sensor Studies of $BaCa_{0.33}Nb_{0.67-x}Fe_xO_{3-\delta}$. *J. Electrochem. Soc.* **2013,** *160*, B95-B101.

163. Lampe, U.; Gerblinger, J.; Meixner, H., Carbon-monoxide sensors based on thin films of $BaSnO_3$. *Sens. Actuators B Chem.* **1995,** *25*, 657-660.

164. Sahay, P. P.; Tewari, S.; Jha, S.; Shamsuddin, M., Sprayed ZnO thin films for ethanol sensors. *J. Mater. Sci.* **2005,** *40*, 4791-4793.

165. Wetchakun, K.; Samerjai, T.; Tamaekong, N.; Liewhiran, C.; Siriwong, C.; Kruefu, V.; Wisitsoraat, A.; Tuantranont, A.; Phanichphant, S., Semiconducting metal oxides as sensors for environmentally hazardous gases. *Sens. Actuators B Chem.* **2011,** *160*, 580-591.

166. Fan, K.; Qin, H.; Wang, L.; Ju, L.; Hu, J., CO_2 gas sensors based on $La_{1-x}Sr_xFeO_3$ nanocrystalline powders. *Sens. Actuator B-Chem.* **2013,** *177*, 265-269.

167. Zhang, P.; Qin, H.; Zhang, H.; LÜ, W.; Hu, J., CO_2 gas sensors based on $Yb_{1-x}Ca_xFeO_3$ nanocrystalline powders. *J. Rare Earths* **2017,** *35*, 602-609.

168. Zhou, Z.-G.; Tang, Z.-L.; Zhang, Z.-T., Studies on grain-boundary chemistry of perovskite ceramics as CO gas sensors. *Sens. Actuators B Chem.* **2003,** *93*, 356-361.

169. Belysheva, T. V.; Gromov, V. F.; Gerasimov, G. N.; Spiridonova, E. Y.; Bondarenko, S. A.; Trakhtenberg, L. I., Sensors based on $SnO_2 + In_2O_3$ composite films for detecting CO in air. *Russ. J. Phys. Chem. A* **2011,** *85*, 1021.

170. Mädler, L.; Sahm, T.; Gurlo, A.; Grunwaldt, J.-D.; Barsan, N.; Weimar, U.; Pratsinis, S. E., Sensing low concentrations of CO using flame-spray-made Pt/SnO_2 nanoparticles. *J. Nanoparticle Res.* **2006,** *8*, 783-796.

171. Zhou, Z. G.; Tang, Z. L.; Zhang, Z. T.; Wlodarski, W., Perovskite oxide of PTCR ceramics as chemical sensors. *Sens. Actuators B Chem.* **2001,** *77*, 22-26.

172. Mulmi, S.; Kannan, R.; Thangadurai, V., CO_2 and SO_2 tolerant Fe-doped metal oxides for solid state gas sensors. *Solid State Ion.* **2014,** *262*, 274-278.

173. Sun, F.; Li, X.; Liu, L.; Wang, J., Novel Zn–M–O (M=Sn, Co) sensing electrodes for selective mixed potential CO/C_3H_8 sensors. *Sens. Actuators B Chem.* **2013,** *184*, 220-227.

174. Chevallier, L.; Di Bartolomeo, E.; Grilli, M. L.; Mainas, M.; White, B.; Wachsman, E. D.; Traversa, E., Non-Nernstian planar sensors based on YSZ with a Nb_2O_5 electrode. *Sens. Actuators B Chem.* **2008,** *129*, 591-598.

175. Battle, P. D.; Blundell, S. J.; Santhosh, P. N.; Rosseinsky, M. J.; Steer, C., Electronic phase transitions and magnetoresistance in a new bilayer manganate, $Ca_{2.5}Sr_{0.5}GaMn_2O_8$. *J. Phys. Condens. Matter* **2002,** *14*, 13569-13577.

176. Asenath-Smith, E.; Lokuhewa, I. N.; Misture, S. T.; Edwards, D. D., p-Type thermoelectric properties of the oxygen-deficient perovskite $Ca_2Fe_2O_5$ in the brownmillerite structure. *J. Solid State Chem.* **2010,** *183*, 1670-1677.

177. Patrakeev, M. V.; Leonidov, I. A.; Kozhevnikov, V. L.; Poeppelmeier, K. R., p-Type electron transport in $La_{1-x}Sr_xFeO_{3-\delta}$ at high temperatures. *J. Solid State Chem.* **2005,** *178*, 921-927.

178. Larson, A. C.; Von Dreele, R. B. *General Structure Analysis System (GSAS)*; Los Alamos National Laboratory: Los Alamos, NM: 1994.

179. Sheptyakov, D. V.; Abakumov, A. M.; Antipov, E. V.; Balagurov, A. M.; Billinge, S. J. L.; Fischer, P.; Keller, L.; Lobanov, M. V.; Pavlyuk, B. P.; Pomjakushin, V. Y.; Rozova, M. G., Crystal and magnetic structures of new layered oxides A_2GaMnO_{5+y} (A=Ca, Sr). *Appl. Phys. A* **2002,** *74*, s1734-s1736.

180. Battle, P. D.; Bell, A. M. T.; Blundell, S. J.; Coldea, A. I.; Gallon, D. J.; Pratt, F. L.; Rosseinsky, M. J.; Steer, C. A., Crystal Structure and Magnetic Properties of $SrCaMnGaO_{5+\delta}$. *J. Solid State Chem.* **2002,** *167*, 188-195.

181. Wright, A. J.; Palmer, H. M.; Anderson, P. A.; Greaves, C., Structures and magnetic ordering in the brownmillerite phases, Sr_2MnGaO_5 and Ca_2MnAlO_5. *J. Mater. Chem.* **2002,** *12*, 978-982.

182. Li, M.-R.; Hodges, J. P.; Retuerto, M.; Deng, Z.; Stephens, P. W.; Croft, M. C.; Deng, X.; Kotliar, G.; Sánchez-Benítez, J.; Walker, D.; Greenblatt, M., Mn_2MnReO_6: Synthesis and Magnetic Structure Determination of a New Transition-Metal-Only Double Perovskite Canted Antiferromagnet. *Chem. Mater.* **2016,** *28*, 3148-3158.

183. Xu, X.; Chen, Y.; Zhou, W.; Zhu, Z.; Su, C.; Liu, M.; Shao, Z., A Perovskite Electrocatalyst for Efficient Hydrogen Evolution Reaction. *Adv. Mater.* **2016,** *28*, 6442-6448.

184. Oh, S.; Kim, H.; Kwon, Y.; Kim, M.; Cho, E.; Kwon, H., Porous Co–P foam as an efficient bifunctional electrocatalyst for hydrogen and oxygen evolution reactions. *J. Mater. Chem. A* **2016,** *4*, 18272-18277.

185. Pan, Y.; Chen, Y.; Li, X.; Liu, Y.; Liu, C., Nanostructured nickel sulfides: phase evolution, characterization and electrocatalytic properties for the hydrogen evolution reaction. *RSC Adv.* **2015,** *5*, 104740-104749.

186. Zheng, T.; Sang, W.; He, Z.; Wei, Q.; Chen, B.; Li, H.; Cao, C.; Huang, R.; Yan, X.; Pan, B.; Zhou, S.; Zeng, J., Conductive Tungsten Oxide Nanosheets for Highly Efficient Hydrogen Evolution. *Nano Lett.* **2017,** *17*, 7968-7973.

187. Zhang, W.; Li, H.; Firby, C. J.; Al-Hussein, M.; Elezzabi, A. Y., Oxygen-Vacancy-Tunable Electrochemical Properties of Electrodeposited Molybdenum Oxide Films. *ACS Appl. Mater. Interfaces* **2019,** *11*, 20378-20385.

188. Han, H.; Nayak, A. K.; Choi, H.; Ali, G.; Kwon, J.; Choi, S.; Paik, U.; Song, T., Partial Dehydration in Hydrated Tungsten Oxide Nanoplates Leads to Excellent and Robust Bifunctional Oxygen Reduction and Hydrogen Evolution Reactions in Acidic Media. *ACS Sustainable Chem. Eng.* **2020,** *8*, 9507-9518.

189. Hona, R. K.; Karki, S. B.; Ramezanipour, F., Oxide Electrocatalysts Based on Earth-Abundant Metals for Both Hydrogen- and Oxygen-Evolution Reactions. *ACS Sustainable Chem. Eng.* **2020,** *8*, 11549-11557.

190. Guo, X.; Tong, X.; Wang, Y.; Chen, C.; Jin, G.; Guo, X.-Y., High photoelectrocatalytic performance of a MoS_2–SiC hybrid structure for hydrogen evolution reaction. *J. Mater. Chem. A* **2013,** *1*, 4657-4661.

191. Uosaki, K.; Elumalai, G.; Dinh, H. C.; Lyalin, A.; Taketsugu, T.; Noguchi, H., Highly Efficient Electrochemical Hydrogen Evolution Reaction at Insulating Boron Nitride Nanosheet on Inert Gold Substrate. *Sci. Rep.* **2016,** *6*, 32217.

192. Li, Y. H.; Liu, P. F.; Pan, L. F.; Wang, H. F.; Yang, Z. Z.; Zheng, L. R.; Hu, P.; Zhao, H. J.; Gu, L.; Yang, H. G., Local atomic structure modulations activate metal oxide as electrocatalyst for hydrogen evolution in acidic water. *Nat. Commun.* **2015,** *6*, 8064.

193. Hona, R. K.; Ramezanipour, F., Remarkable Oxygen-Evolution Activity of a Perovskite Oxide from the $Ca_{2-x}Sr_xFe_2O_{6-\delta}$ Series. *Angew. Chem.* **2019,** *58*, 2060-2063.

194. Vellacheri, R.; Al-Haddad, A.; Zhao, H.; Wang, W.; Wang, C.; Lei, Y., High performance supercapacitor for efficient energy storage under extreme environmental temperatures. *Nano Energy* **2014,** *8*, 231-237.

195. Che, W.; Wei, M.; Sang, Z.; Ou, Y.; Liu, Y.; Liu, J., Perovskite $LaNiO_{3-\delta}$ oxide as an anion-intercalated pseudocapacitor electrode. *J. Alloys Compd.* **2018,** *731*, 381-388.

196. Cao, Y.; Lin, B.; Sun, Y.; Yang, H.; Zhang, X., Synthesis, structure and electrochemical properties of lanthanum manganese nanofibers doped with Sr and Cu. *J. Alloys Compd.* **2015,** *638*, 204-213.

197. Forslund, R. P.; Pender, J.; Alexander, C. T.; Johnston, K. P.; Stevenson, K. J., Comparison of perovskite and perovskite derivatives for use in anion-based pseudocapacitor applications. *J. Mater. Chem. A* **2019,** *7*, 21222-21231.

198. Yan, J.; Fan, Z.; Sun, W.; Ning, G.; Wei, T.; Zhang, Q.; Zhang, R.; Zhi, L.; Wei, F., Advanced Asymmetric Supercapacitors Based on $Ni(OH)_2$/Graphene and Porous Graphene Electrodes with High Energy Density. *Adv. Funct. Mater.* **2012,** *22*, 2632-2641.

199. Zhang, J.; Liu, H.; Shi, P.; Li, Y.; Huang, L.; Mai, W.; Tan, S.; Cai, X., Growth of nickel (111) plane: The key role in nickel for further improving the electrochemical property of hexagonal nickel hydroxide-nickel & reduced graphene oxide composite. *J. Power Sources* **2014,** *267*, 356-365.

200. Guo, D.; Zhang, H.; Yu, X.; Zhang, M.; Zhang, P.; Li, Q.; Wang, T., Facile synthesis and excellent electrochemical properties of $CoMoO_4$ nanoplate arrays as supercapacitors. *J. Mater. Chem. A* **2013,** *1*, 7247-7254.

201. Béguin, F.; Presser, V.; Balducci, A.; Frackowiak, E., Carbons and Electrolytes for Advanced Supercapacitors. *Adv. Mater.* **2014,** *26*, 2219-2251.

202. Stoller, M. D.; Ruoff, R. S., Best practice methods for determining an electrode material's performance for ultracapacitors. *Energy Environ. Sci.* **2010,** *3*, 1294-1301.

203. Zhang, J.; Zhao, X. S., On the Configuration of Supercapacitors for Maximizing Electrochemical Performance. *ChemSusChem* **2012,** *5*, 818-841.

204. Wang, G.; Kim, S.-K.; Wang, M. C.; Zhai, T.; Munukutla, S.; Girolami, G. S.; Sempsrott, P. J.; Nam, S.; Braun, P. V.; Lyding, J. W., Enhanced Electrical and Mechanical Properties of Chemically Cross-Linked Carbon-Nanotube-Based Fibers and Their Application in High-Performance Supercapacitors. *ACS Nano* **2020,** *14*, 632-639.

205. Kshetri, T.; Tran, D. T.; Nguyen, D. C.; Kim, N. H.; Lau, K.-t.; Lee, J. H., Ternary graphene-carbon nanofibers-carbon nanotubes structure for hybrid supercapacitor. *Chem. Eng. J.* **2020,** *380*, 122543.

206. Balamurugan, J.; Thanh, T. D.; Kim, N. H.; Lee, J. H., Facile synthesis of 3D hierarchical N-doped graphene nanosheet/cobalt encapsulated carbon nanotubes for high energy density asymmetric supercapacitors. *J. Mater. Chem. A* **2016,** *4*, 9555-9565.

207. da Silva, R. J.; Lima, R. M. A. P.; de Oliveira, M. C. A.; Alcaraz-Espinoza, J. J.; de Melo, C. P.; de Oliveira, H. P., Supercapacitors based on (carbon nanostructure)/PEDOT/(eggshell membrane) electrodes. *J. Electroanal. Chem.* **2020,** *856*, 113658.

208. Alcaraz-Espinoza, J. J.; de Oliveira, H. P., Flexible supercapacitors based on a ternary composite of polyaniline/polypyrrole/graphite on gold coated sandpaper. *Electrochim. Acta* **2018,** *274*, 200-207.

209. Yu, D.; Goh, K.; Wang, H.; Wei, L.; Jiang, W.; Zhang, Q.; Dai, L.; Chen, Y., Scalable synthesis of hierarchically structured carbon nanotube–graphene fibres for capacitive energy storage. *Nat. Nanotechnol.* **2014,** *9*, 555-562.

210. Kim, B. K.; Sy, S.; Yu, A.; Zhang, J., Electrochemical Supercapacitors for Energy Storage and Conversion. In *Handbook of Clean Energy Systems*, Wiley, 2015: pp 1-25.

211. Bag, S.; Raj, C. R., Facile shape-controlled growth of hierarchical mesoporous δ-MnO_2 for the development of asymmetric supercapacitors. *J. Mater. Chem. A* **2016,** *4*, 8384-8394.

212. Wei, C.; Rao, R. R.; Peng, J.; Huang, B.; Stephens, I. E. L.; Risch, M.; Xu, Z. J.; Shao-Horn, Y., Recommended Practices and Benchmark Activity for Hydrogen and Oxygen Electrocatalysis in Water Splitting and Fuel Cells. *Adv. Mater.* **2019,** *31*, 1806296.

213. Ramezanipour, F.; Greedan, J. E.; Siewenie, J.; Proffen, T.; Ryan, D. H.; Grosvenor, A. P.; Donaberger, R. L., Local and average structures and magnetic properties of Sr_2FeMnO_{5+y}, y = 0.0, 0.5. Comparisons with Ca_2FeMnO_5 and the effect of the A-site cation. *Inorg.Chem.* **2011,** *50*, 7779-7791.

214. Ramezanipour, F.; Greedan, J. E.; Siewenie, J.; Proffen, T.; Ryan, D. H.; Grosvenor, A. P.; Donaberger, R. L., Local and Average Structures and Magnetic Properties of Sr_2FeMnO_{5+y}, y=0.0, 0.5. Comparisons with Ca_2FeMnO_5 and the Effect of the A-Site Cation. *Inorg. Chem.* **2011,** *50*, 7779-7791.

215. King, G.; Ramezanipour, F.; Llobet, A.; Greedan, J. E., Local structures of Sr_2FeMnO_{5+y} (y=0, 0.5) and $Sr_2Fe_{1.5}Cr_{0.5}O_5$ from reverse Monte Carlo modeling of pair distribution function data and implications for magnetic order. *J. Solid State Chem.* **2013,** *198*, 407-415.

216. Andreola, F.; Leonelli, C.; Romagnoli, M.; Miselli, P., Techniques Used to Determine Porosity. *Am. Cer. Soc. Bull.* **2000,** *79*, 49-52.

217. Lu, C.-H.; Bai, J.-H.; Chen, H., Preparation, sintering, and microstructures of strontium barium bismuth tantalate layered perovskite ceramics. *J. Mater. Sci.* **2004,** *39*, 3079-3083.

218. Kim, J.; Yin, X.; Tsao, K. C.; Fang, S.; Yang, H., $Ca_2Mn_2O_5$ as oxygen-deficient perovskite electrocatalyst for oxygen evolution reaction. *J. Am. Chem. Soc.* **2014,** *136*, 14646-14649.

219. Hona, R. K.; Ramezanipour, F., Remarkable Oxygen-Evolution Activity of a Perovskite Oxide from the $Ca_{2-x}Sr_xFe_2O_{6-\delta}$ Series. *Angew. Chem. Int. Ed.* **2019,** *58*, 2060-2063.

220. Choi, S.; Park, Y.; Yang, H.; Jin, H.; Tomboc, G. M.; Lee, K., Vacancy-engineered catalysts for water electrolysis. *CrystEngComm* **2020,** *22*, 1500-1513.

221. Sun, H.; Xu, X.; Hu, Z.; Tjeng, L. H.; Zhao, J.; Zhang, Q.; Lin, H.-J.; Chen, C.-T.; Chan, T.-S.; Zhou, W.; Shao, Z., Boosting the oxygen evolution reaction activity of a perovskite through introducing multi-element synergy and building an ordered structure. *J. Mater. Chem. A* **2019,** *7*, 9924-9932.

222. Zhang, C.; Wang, Z.; Bhoyate, S.; Morey, T.; Neria, B. L.; Vasiraju, V.; Gupta, G.; Palchoudhury, S.; Kahol, P. K.; Mishra, S. R.; Perez, F.; Gupta, R. K., MoS_2 Decorated Carbon Nanofibers as Efficient and Durable Electrocatalyst for Hydrogen Evolution Reaction. *J. Carbon Res.* **2017,** *3*, 33.

223. Benson, J.; Li, M.; Wang, S.; Wang, P.; Papakonstantinou, P., Electrocatalytic Hydrogen Evolution Reaction on Edges of a Few Layer Molybdenum Disulfide Nanodots. *ACS Appl. Mater. Interfaces* **2015,** *7*, 14113-14122.

224. Ma, L.; Ting, L. R. L.; Molinari, V.; Giordano, C.; Yeo, B. S., Efficient hydrogen evolution reaction catalyzed by molybdenum carbide and molybdenum nitride nanocatalysts synthesized via the urea glass route. *J. Mater. Chem. A* **2015,** *3*, 8361-8368.

225. Yang, X.; Zhao, Z.; Yu, X.; Feng, L., Electrochemical hydrogen evolution reaction boosted by constructing Ru nanoparticles assembled as a shell over semimetal Te nanorod surfaces in acid electrolyte. *Chem. Commun.* **2019,** *55*, 1490-1493.

226. He, J.; Song, L.; Yan, J.; Kang, N.; Zhang, Y.; Wang, W., Hydrogen Evolution Reaction Property in Alkaline Solution of Molybdenum Disulfide Modified by Surface Anchor of Nickel–Phosphorus Coating. *Metals* **2017,** *7*, 211.

227. Yang, F.; Kang, N.; Yan, J.; Wang, X.; He, J.; Huo, S.; Song, L., Hydrogen Evolution Reaction Property of Molybdenum Disulfide/Nickel Phosphide Hybrids in Alkaline Solution. *Metals* **2018,** *8*, 359.

228. Nayak, A. K.; Verma, M.; Sohn, Y.; Deshpande, P. A.; Pradhan, D., Highly Active Tungsten Oxide Nanoplate Electrocatalysts for the Hydrogen Evolution Reaction in Acidic and Near Neutral Electrolytes. **2017,** *2*, 7039-7047.

229. Hao, Z.; Yang, S.; Niu, J.; Fang, Z.; Liu, L.; Dong, Q.; Song, S.; Zhao, Y., A bimetallic oxide $Fe_{1.89}Mo_{4.11}O_7$ electrocatalyst with highly efficient hydrogen evolution reaction activity in alkaline and acidic media. *Chem. Sci.* **2018,** *9*, 5640-5645.

230. Galal, A.; Atta, N. F.; Ali, S. M., Investigation of the catalytic activity of $LaBO_3$ (B=Ni, Co, Fe or Mn) prepared by the microwave-assisted method for hydrogen evolution in acidic medium. *Electrochim. Acta* **2011,** *56*, 5722-5730.

231. Jia, Y.; Zhang, L.; Du, A.; Gao, G.; Chen, J.; Yan, X.; Brown, C. L.; Yao, X., Defect Graphene as a Trifunctional Catalyst for Electrochemical Reactions. *Adv. Mater.* **2016,** *28*, 9532-9538.

232. Chai, L.; Yuan, W.; Cui, X.; Jiang, H.; Tang, J.; Guo, X., Surface engineering-modulated porous N-doped rod-like molybdenum phosphide catalysts: towards high activity and stability for hydrogen evolution reaction over a wide pH range. *RSC Adv.* **2018,** *8*, 26871-26879.

233. Hwang, B.-J.; Chen, H.-C.; Mai, F.-D.; Tsai, H.-Y.; Yang, C.-P.; Rick, J.; Liu, Y.-C., Innovative Strategy on Hydrogen Evolution Reaction Utilizing Activated Liquid Water. *Sci. Rep.* **2015,** *5*, 16263.

234. Mohammed-Ibrahim, J.; Sun, X., Recent progress on earth abundant electrocatalysts for hydrogen evolution reaction (HER) in alkaline medium to achieve efficient water splitting – A review. *J. Energy Chem.* **2019,** *34*, 111-160.

235. Song, X.; Chen, G.; Guan, L.; Zhang, H.; Tao, J., Interfacial engineering of MoS_2/TiO_2 hybrids for enhanced electrocatalytic hydrogen evolution reaction. *Appl. Phys. Express* **2016,** *9*, 095801.

236. Li, A.; Sun, Y.; Yao, T.; Han, H., Earth-Abundant Transition-Metal-Based Electrocatalysts for Water Electrolysis to Produce Renewable Hydrogen. *Chem.: Eur. J.* **2018,** *24*, 18334-18355.

237. Chaitoglou, S.; Giannakopoulou, T.; Speliotis, T.; Vavouliotis, A.; Trapalis, C.; Dimoulas, A., Mo_2C/graphene heterostructures: low temperature chemical vapor deposition on liquid bimetallic Sn–Cu and hydrogen evolution reaction electrocatalytic properties. *Nanotechnology* **2019,** *30*, 125401.

238. Zhang, X.; Zhang, M.; Tian, Y.; You, J.; Yang, C.; Su, J.; Li, Y.; Gao, Y.; Gu, H., In situ synthesis of MoS_2/graphene nanosheets as free-standing and flexible electrode paper for high-efficiency hydrogen evolution reaction. *RSC Adv.* **2018,** *8*, 10698-10705.

239. Lai, B.; Singh, S. C.; Bindra, J. K.; Saraj, C. S.; Shukla, A.; Yadav, T. P.; Wu, W.; McGill, S. A.; Dalal, N. S.; Srivastava, A.; Guo, C., Hydrogen evolution reaction from bare and surface-functionalized few-layered MoS_2 nanosheets in acidic and alkaline electrolytes. *Mater. Today Chem.* **2019,** *14*, 100207.

240. Xi, W.; Yan, G.; Tan, H.; Xiao, L.; Cheng, S.; Khan, S. U.; Wang, Y.; Li, Y., Superaerophobic P-doped $Ni(OH)_2/NiMoO_4$ hierarchical nanosheet arrays grown on Ni foam for electrocatalytic overall water splitting. *Dalton Trans.* **2018,** *47*, 8787-8793.

241. Liu, M.-R.; Hong, Q.-L.; Li, Q.-H.; Du, Y.; Zhang, H.-X.; Chen, S.; Zhou, T.; Zhang, J., Cobalt Boron Imidazolate Framework Derived Cobalt Nanoparticles Encapsulated in B/N Codoped Nanocarbon as Efficient Bifunctional Electrocatalysts for Overall Water Splitting. *Adv. Func. Mater.* **2018,** *28*, 1801136.

242. Tavakkoli, M.; Kallio, T.; Reynaud, O.; Nasibulin, A. G.; Sainio, J.; Jiang, H.; Kauppinen, E. I.; Laasonen, K., Maghemite nanoparticles decorated on carbon nanotubes as efficient electrocatalysts for the oxygen evolution reaction. *J. Mater. Chem. A* **2016,** *4*, 5216-5222.

243. Lv, X.; Zhu, Y.; Jiang, H.; Yang, X.; Liu, Y.; Su, Y.; Huang, J.; Yao, Y.; Li, C., Hollow mesoporous $NiCo_2O_4$ nanocages as efficient electrocatalysts for oxygen evolution reaction. *Dalton Trans.* **2015,** *44*, 4148-4154.

244. Oh, S.; Kim, H.; Kwon, Y.; Kim, M.; Cho, E.; Kwon, H., Porous Co–P foam as an efficient bifunctional electrocatalyst for hydrogen and oxygen evolution reactions. *J. Mater.Chem. A* **2016,** *4*, 18272-18277.

245. Song, F.; Hu, X., Ultrathin Cobalt–Manganese Layered Double Hydroxide Is an Efficient Oxygen Evolution Catalyst. *J. Am. Chem. Soc.* **2014,** *136*, 16481-16484.

246. Moir, J.; Soheilnia, N.; O'Brien, P.; Jelle, A.; Grozea, C. M.; Faulkner, D.; Helander, M. G.; Ozin, G. A., Enhanced Hematite Water Electrolysis Using a 3D Antimony-Doped Tin Oxide Electrode. *ACS Nano* **2013,** *7*, 4261-4274.

247. Zhu, Y.; Zhou, W.; Chen, Z. G.; Chen, Y.; Su, C.; Tade, M. O.; Shao, Z., $SrNb_{0.1}Co_{0.7}Fe_{0.2}O_{3-\delta}$ Perovskite as a Next-Generation Electrocatalyst for Oxygen Evolution in Alkaline Solution. *Angew. Chem., Int. Ed.* **2015,** *54*, 3897.

248. Das, D.; Das, A.; Reghunath, M.; Nanda, K. K., Phosphine-free avenue to Co_2P nanoparticle encapsulated N,P co-doped CNTs: a novel non-enzymatic glucose sensor and an efficient electrocatalyst for oxygen evolution reaction. *Green Chem.* **2017,** *19*, 1327-1335.

249. Shaula, A. L.; Kharton, V. V.; Patrakeev, M. V.; Waerenborgh, J. C.; Rojas, D. P.; Marques, F. M. B., Defect formation and transport in $SrFe_{1-x}Al_xO_{3-\delta}$. *Ionics* **2004,** *10*, 378-384.

250. Asenath-Smith, E.; Misture, S. T.; Edwards, D. D., Structural behavior and thermoelectric properties of the brownmillerite system $Ca_2(Zn_xFe_{2-x})O_5$. *J. Solid State Chem.* **2011,** *184*, 2167-2177.

251. Pommier, A.; Leinenweber, K. D., Electrical cell assembly for reproducible conductivity experiments in the multi-anvil. *Am. Mineral.* **2018,** *103*, 1298–1305.

252. Achary, P. G. R.; Munisha, B.; Singh, D. S.; Parida, K. S., Study of Electrical Properties of Nickel Doped Polyurethane Nanocomposites. *Polym. Sci.* **2018,** *4*, No.1:7.

253. Singh, Y., Electrical Resistivity Measurements: a Review. *Int. J. Modern Phys.: Conference Series* **2013,** *22*, 745–756.

254. Tao; Canales-Vázquez, J.; Irvine, J. T. S., Structural and Electrical Properties of the Perovskite Oxide Sr_2FeNbO_6. *Chem. Mater.* **2004,** *16*, 2309-2316.

255.Zhang, Q.; Xu, Z. F.; Wang, L. F.; Gao, S. H.; Yuan, S. J., Structural and electromagnetic properties driven by oxygen vacancy in $Sr_2FeMoO_{6-\delta}$ double perovskite. *J. Alloys Compd.* **2015,** *649*, 1151-1155.

256.Mineshige, A.; Inaba, M.; Yao, T.; Ogumi, Z.; Kikuchi, K.; Kawase, M., Crystal Structure and Metal–Insulator Transition of $La_{1-x}Sr_xCoO_3$. *J.Solid State Chem.* **1996,** *121*, 423-429.

257.Cheng, X.; Fabbri, E.; Nachtegaal, M.; Castelli, I. E.; El Kazzi, M.; Haumont, R.; Marzari, N.; Schmidt, T. J., Oxygen evolution reaction on $La_{1-x}Sr_xCoO_3$ perovskites: a combined experimental and theoretical study of their structural, electronic, and electrochemical properties. *Chem. Mater.* **2015,** *27*, 7662-7672.

258.Pizzini, S., Physical chemistry of semiconductor materials and processes *John Wiley & Sons Ltd, West Sussex, United Kingdom* **2015**.

259.Andoulsi, R.; Horchani-Naifer, K.; Férid, M., Electrical conductivity of $La_{1-x}Ca_xFeO_{3-\delta}$ solid solutions. *Ceram. Int.* **2013,** *39*, 6527-6531.

260.Jain, S. D.; Sahasrabudhe, G. G., *Engineering physics*. 1 ed.; Universities Press: *2010*, p-365.

261.Kim, Y. T.; Lopes, P. P.; Park, S. A.; Lee, A. Y.; Lim, J.; Lee, H.; Back, S.; Jung, Y.; Danilovic, N.; Stamenkovic, V.; Erlebacher, J.; Snyder, J.; Markovic, N. M., Balancing activity, stability and conductivity of nanoporous core-shell iridium/iridium oxide oxygen evolution catalysts. *Nat. Commun.* **2017,** *8*, 1449.

262.Pramana, S. S.; Cavallaro, A.; Li, C.; Handoko, A. D.; Chan, K. W.; Walker, R. J.; Regoutz, A.; Herrin, J. S.; Yeo, B. S.; Payne, D. J.; Kilner, J. A.; Ryan, M. P.; Skinner, S. J., Crystal structure and surface characteristics of Sr-doped $GdBaCo_2O_{6-\delta}$ double perovskites: oxygen evolution reaction and conductivity. *J. Mater. Chem. A* **2018,** *6*, 5335-5345.

263.Lee, D. G.; Gwon, O.; Park, H. S.; Kim, S. H.; Yang, J.; Kwak, S. K.; Kim, G.; Song, H. K., Conductivity-dependent completion of oxygen reduction on oxide catalysts. *Angew. Chem., Int. Ed.* **2015,** *54*, 15730–15733.

264.Zou, S.; Burke, M. S.; Kast, M. G.; Fan, J.; Danilovic, N.; Boettcher, S. W., Fe (Oxy)hydroxide Oxygen Evolution Reaction Electrocatalysis: Intrinsic Activity and the Roles of Electrical Conductivity, Substrate, and Dissolution. *Chem. Mater.* **2015,** *27*, 8011-8020.

265.Viswanathan, V.; Pickrahn, K. L.; Luntz, A. C.; Bent, S. F.; Nørskov, J. K., Nanoscale Limitations in Metal Oxide Electrocatalysts for Oxygen Evolution. *Nano Lett.* **2014,** *14*, 5853-5857.

266.Perdew, J. P.; Burke, K.; Ernzerhof, M., Generalized Gradient Approximation Made Simple. *Phys. Rev. Lett.* **1996,** *77*, 3865-3868.

267.Andriotis, A. N.; Mpourmpakis, G.; Lisenkov, S.; Sheetz, R. M.; Menon, M., U-calculation of the LSDA + U functional using the hybrid B3LYP and HSE functionals. *Phys. Status Solidi B* **2013,** *250*, 356-363.

268.Dudarev, S. L.; Botton, G. A.; Savrasov, S. Y.; Humphreys, C. J.; Sutton, A. P., Electron-energy-loss spectra and the structural stability of nickel oxide: An LSDA+U study. *Phys. Rev. B* **1998,** *57*, 1505-1509.

269.Kresse, G.; Hafner, J., Ab initio molecular dynamics for liquid metals. *Phys. Rev. B* **1993,** *47*, 558-561.

270.Kresse, G.; Joubert, D., From ultrasoft pseudopotentials to the projector augmented-wave method. *Phys. Rev. B* **1999,** *59*, 1758-1775.

271.Blöchl, P. E., Projector augmented-wave method. *Phys. Rev. B* **1994,** *50*, 17953-17979.

272.Andriotis, A. N.; Sheetz, R. M.; Menon, M., LSDA+U method: A calculation of the U values at the Hartree-Fock level of approximation. *Phys. Rev. B* **2010,** *81*, 245103.

273.Andriotis, A. N.; Menon, M., Coupled and Implicit Relationships of the d-Band Center of the Magnetic Dopants in Diluted Magnetic Semiconductors and Transition Metal Oxides. *J. Phys. Chem. C* **2017,** *121*, 21713-21719.

274.Andriotis, A. N.; Menon, M., Universal features underlying the magnetism in diluted magnetic semiconductors. *J. Phys. Condens. Matter* **2018,** *30*, 135803.

275.Sanyal, B.; Grånäs, O.; Knut, R.; Coleman, V. A.; Thunström, P.; Iuşan, D. M.; Karis, O.; Eriksson, O.; Westin, G., Electronic structure of Co doped ZnO: Theory and experiment. *J. Appl. Phys.* **2008,** *103*, 07D130.

276.Donati, F.; Dubout, Q.; Autès, G.; Patthey, F.; Calleja, F.; Gambardella, P.; Yazyev, O. V.; Brune, H., Magnetic Moment and Anisotropy of Individual Co Atoms on Graphene. *Phys. Rev. Lett.* **2013,** *111*, 236801.

277.Gopal, P.; Spaldin, N. A., Magnetic interactions in transition-metal-doped ZnO: An ab initio study. *Phys. Rev. B* **2006,** *74*, 094418.

278.Baniecki, J. D.; Ishii, M.; Aso, H.; Kurihara, K.; Ricinschi, D., Density functional theory and experimental study of the electronic structure and transport properties of La, V, Nb, and Ta doped $SrTiO_3$. *J. Appl. Phys.* **2013,** *113*, 013701.

279.Varignon, J.; Bibes, M.; Zunger, A., Origin of band gaps in 3d perovskite oxides. *Nat. Commun.* **2019,** *10*, 1658.

280.Hona, R. K.; Ramezanipour, F., Structure-dependence of electrical conductivity and electrocatalytic properties of $Sr_2Mn_2O_6$ and $CaSrMn_2O_6$. *J. Chem. Sci.* **2019,** *131* (11), 109.

281.Hona, R. K.; Ramezanipour, F., Effect of the Oxygen Vacancies and Structural Order on the Oxygen Evolution Activity: A Case Study of $SrMnO_{3-\delta}$ Featuring Four Different Structure Types. *Inorg. Chem.* **2020,** *59*, 4685-4692.

282.Alom, M. S.; Ramezanipour, F., Layered Oxides $SrLaFe_{1-x}Co_xO_{4-\delta}$ (x=0–1) as Bifunctional Electrocatalysts for Water-Splitting. *ChemCatChem* **2021,** *13*, 3510-3516.

283.Guo, H.; Hosaka, Y.; Romero, F. D.; Saito, T.; Ichikawa, N.; Shimakawa, Y., Two Charge Ordering Patterns in the Topochemically Synthesized Layer-Structured Perovskite $LaCa_2Fe_3O_9$ with Unusually High Valence $Fe^{3.67+}$. *Inorg. Chem.* **2017,** *56*, 3695–3701.

284.Li, X.; He, L.; Zhong, X.; Zhang, J.; Luo, S.; Yi, W.; Zhang, L.; Hu, M.; Tang, J.; Zhou, X.; Zhao, X.; Xu, B., Evaluation of A-Site Ba^{2+}-Deficient $Ba_{1-x}Co_{0.4}Fe_{0.4}Zr_{0.1}Y_{0.1}O_{3-\delta}$ Oxides as Electrocatalysts for Efficient Hydrogen Evolution Reaction. *Scanning* **2018,** *2018*, 1341608-1341608.

285.Bard, A. J.; Faulkner, L. R., *Electrochemical Methods: Fundamentals and Applications*. Wiley: 2000.

286.Tahir, M.; Pan, L.; Zhang, R.; Wang, Y.-C.; Shen, G.; Aslam, I.; Qadeer, M. A.; Mahmood, N.; Xu, W.; Wang, L.; Zhang, X.; Zou, J.-J., High-Valence-State NiO/Co_3O_4 Nanoparticles on Nitrogen-Doped Carbon for Oxygen Evolution at Low Overpotential. *ACS Energy Lett.* **2017,** *2*, 2177-2182.

287.Fan, Z.; Liao, F.; Shi, H.; Liu, Y.; Shao, M.; Kang, Z., Highly efficient water splitting over a RuO_2/F-doped graphene electrocatalyst with ultra-low ruthenium content. *Inorg. Chem. Front.* **2020,** *7*, 2188-2194.

288.Das, D.; Nanda, K. K., One-step, integrated fabrication of Co_2P nanoparticles encapsulated N, P dual-doped CNTs for highly advanced total water splitting. *Nano Energy* **2016,** *30*, 303-311.

289.Lee, Y.; Suntivich, J.; May, K. J.; Perry, E. E.; Shao-Horn, Y., Synthesis and Activities of Rutile IrO_2 and RuO_2 Nanoparticles for Oxygen Evolution in Acid and Alkaline Solutions. *J. Phys. Chem. Lett* **2012,** *3*, 399-404.

227

290.Zhu, Y.; Zhou, W.; Chen, Z.-G.; Chen, Y.; Su, C.; Tadé, M. O.; Shao, Z., SrNb$_{0.1}$Co$_{0.7}$Fe$_{0.2}$O$_{3-\delta}$ Perovskite as a Next-Generation Electrocatalyst for Oxygen Evolution in Alkaline Solution. *Angew. Chem* **2015,** *54*, 3897-3901.

291.Li, L.; Qin, Z.; Ries, L.; Hong, S.; Michel, T.; Yang, J.; Salameh, C.; Bechelany, M.; Miele, P.; Kaplan, D.; Chhowalla, M.; Voiry, D., Role of Sulfur Vacancies and Undercoordinated Mo Regions in MoS$_2$ Nanosheets toward the Evolution of Hydrogen. *ACS Nano* **2019,** *13*, 6824-6834.

292.Shinagawa, T.; Garcia-Esparza, A. T.; Takanabe, K., Insight on Tafel slopes from a microkinetic analysis of aqueous electrocatalysis for energy conversion. *Sci. Rep.* **2015,** *5*, 13801-13801.

293.McCrory, C. C. L.; Jung, S.; Peters, J. C.; Jaramillo, T. F., Benchmarking Heterogeneous Electrocatalysts for the Oxygen Evolution Reaction. *J. Am. Chem. Soc.* **2013,** *135*, 16977-16987.

294.Zhang, B.; Lui, Y. H.; Zhou, L.; Tang, X.; Hu, S., An alkaline electro-activated Fe–Ni phosphide nanoparticle-stack array for high-performance oxygen evolution under alkaline and neutral conditions. *J. Mater. Chem. A* **2017,** *5*, 13329-13335.

295.Zhu, Y.; Zhou, W.; Sunarso, J.; Zhong, Y.; Shao, Z., Phosphorus-Doped Perovskite Oxide as Highly Efficient Water Oxidation Electrocatalyst in Alkaline Solution. *Adv. Funct. Mater* **2016,** *26*, 5862-5872.

296.Petrie, J. R.; Cooper, V. R.; Freeland, J. W.; Meyer, T. L.; Zhang, Z.; Lutterman, D. A.; Lee, H. N., Enhanced Bifunctional Oxygen Catalysis in Strained LaNiO$_3$ Perovskites. *J. Am. Chem. Soc.* **2016,** *138*, 2488-2491.

297.Song, J.; Wei, C.; Huang, Z.-F.; Liu, C.; Zeng, L.; Wang, X.; Xu, Z. J., A review on fundamentals for designing oxygen evolution electrocatalysts. *Chem. Soc. Rev.* **2020,** *49*, 2196-2214.

298.Li, H.; Sun, S.; Xi, S.; Chen, Y.; Wang, T.; Du, Y.; Sherburne, M.; Ager, J. W.; Fisher, A. C.; Xu, Z. J., Metal–Oxygen Hybridization Determined Activity in Spinel-Based Oxygen Evolution Catalysts: A Case Study of ZnFe$_{2-x}$Cr$_x$O$_4$. *Chem. Mater.* **2018,** *30*, 6839-6848.

299.Sun, Y.; Zhao, Z.; Wu, S.; Li, W.; Wu, B.; Liu, G.; Chen, G.; Xu, B.; Kang, B.; Li, Y.; Li, C., Engineering of the d-Band Center of Perovskite Cobaltite for Enhanced Electrocatalytic Oxygen Evolution. *ChemSusChem* **2020,** *13*, 2671-2676.

300.Sun, S.; Zhou, X.; Cong, B.; Hong, W.; Chen, G., Tailoring the d-Band Centers Endows (Ni$_x$Fe$_{1-x}$)$_2$P Nanosheets with Efficient Oxygen Evolution Catalysis. *ACS Catal.* **2020,** *10*, 9086-9097.

301.Mpourmpakis, G.; Andriotis, A. N.; Vlachos, D. G., Identification of Descriptors for the CO Interaction with Metal Nanoparticles. *Nano Lett.* **2010,** *10*, 1041-1045.

302.Seikh, M. M.; Caignaert, V.; Perez, O.; Raveau, B.; Hardy, V., Interplay between single-ion magnetism, single-chain magnetism and long-range ordering in the spin chain oxides Sr$_{4-x}$Ca$_x$Mn$_2$CoO$_9$. *J. Mater.Chem. C* **2018,** *6*, 3362-3372.

303.Battle, P. D.; Branford, W. R.; Mihut, A.; Rosseinsky, M. J.; Singleton, J.; Sloan, J.; Spring, L. E.; Vente, J. F., Structural Chemistry and Electronic Properties of the n = 3 Ruddlesden–Popper Phases Ca$_4$Mn$_2$FeO$_{9.75}$ and Sr$_4$Mn$_2$FeO$_{9.80}$. *Chem. Mater.* **1999,** *11*, 674-683.

304.Boulahya, K.; Parras, M.; González-Calbet, J. M.; Martínez, J. L., Synthesis, Structural Characterization, and Magnetic Study of Sr$_4$Mn$_2$CoO$_9$. *Chem. Mater.* **2003,** *15*, 3537-3542.

305.Chung, Y. S.; Kim, T.; Shin, T. H.; Yoon, H.; Park, S.; Sammes, N. M.; Kim, W. B.; Chung, J. S., In situ preparation of a La$_{1.2}$Sr$_{0.8}$Mn$_{0.4}$Fe$_{0.6}$O$_4$ Ruddlesden–Popper phase with exsolved Fe nanoparticles as an anode for SOFCs. *J. Mater. Chem. A* **2017,** *5*, 6437-6446.

306.Li, J.-S.; Huang, M.-J.; Kong, L.-X.; Chen, X.-N.; Zhou, Y.-W.; Li, J.-L.; Wang, M.-Y., Ruthenium Nanoparticles Anchored on Graphene Hollow Nanospheres Superior to Platinum for the Hydrogen Evolution Reaction in Alkaline Media. *Inorg. Chem.* **2020,** *59*, 930-936.

307. Shi, M.; Zhang, Y.; Zhu, Y.; Wang, W.; Wang, C.; Yu, A.; Pu, X.; Zhai, J., A flower-like CoS_2/MoS_2 heteronanosheet array as an active and stable electrocatalyst toward the hydrogen evolution reaction in alkaline media. *RSC Adv.* **2020,** *10*, 8973-8981.

308. Razmjooei, F.; Liu, T.; Azevedo, D. A.; Hadjixenophontos, E.; Reissner, R.; Schiller, G.; Ansar, S. A.; Friedrich, K. A., Improving plasma sprayed Raney-type nickel–molybdenum electrodes towards high-performance hydrogen evolution in alkaline medium. *Sci. Rep.* **2020,** *10*, 10948.

309. Hwang, B. J.; Chen, H. C.; Mai, F. D.; Tsai, H. Y.; Yang, C. P.; Rick, J.; Liu, Y. C., Innovative Strategy on Hydrogen Evolution Reaction Utilizing Activated Liquid Water. *Sci Rep* **2015,** *5*, 16263.

310. Allen J. Bard, L. R. F., *Electrochemical Methods: Fundamentals and Applications*. 2, illustrated ed.; Wiley, 2000.

311. Liu, S.; Sun, C.; Chen, J.; Xiao, J.; Luo, J.-L., A High-Performance Ruddlesden–Popper Perovskite for Bifunctional Oxygen Electrocatalysis. *ACS Catal.* **2020,** *10*, 13437-13444.

312. Liu, S.; Luo, H.; Li, Y.; Liu, Q.; Luo, J.-L., Structure-engineered electrocatalyst enables highly active and stable oxygen evolution reaction over layered perovskite $LaSr_3Co_{1.5}Fe_{1.5}O_{10-\delta}$. *Nano Energy* **2017,** *40*, 115-121.

313. Forslund, R. P.; Hardin, W. G.; Rong, X.; Abakumov, A. M.; Filimonov, D.; Alexander, C. T.; Mefford, J. T.; Iyer, H.; Kolpak, A. M.; Johnston, K. P.; Stevenson, K. J., Exceptional electrocatalytic oxygen evolution via tunable charge transfer interactions in $La_{0.5}Sr_{1.5}Ni_{1-x}Fe_xO_{4\pm\delta}$ Ruddlesden-Popper oxides. *Nat. Commun.* **2018,** *9*, 3150.

314. Zhu, Y.; Tahini, H. A.; Hu, Z.; Yin, Y.; Lin, Q.; Sun, H.; Zhong, Y.; Chen, Y.; Zhang, F.; Lin, H.-J.; Chen, C.-T.; Zhou, W.; Zhang, X.; Smith, S. C.; Shao, Z.; Wang, H., Boosting oxygen evolution reaction by activation of lattice-oxygen sites in layered Ruddlesden-Popper oxide. *EcoMat.* **2020,** *2*, e12021.

315. Jung, K.-N.; Jung, J.-H.; Im, W. B.; Yoon, S.; Shin, K.-H.; Lee, J.-W., Doped Lanthanum Nickelates with a Layered Perovskite Structure as Bifunctional Cathode Catalysts for Rechargeable Metal–Air Batteries. *ACS Appl. Mater. Interfaces* **2013,** *5*, 9902-9907.

316. Zhu, Y.; Tahini, H. A.; Hu, Z.; Dai, J.; Chen, Y.; Sun, H.; Zhou, W.; Liu, M.; Smith, S. C.; Wang, H.; Shao, Z., Unusual synergistic effect in layered Ruddlesden–Popper oxide enables ultrafast hydrogen evolution. *Nat. Commun.* **2019,** *10*, 149.

317. Kumar, N.; Kumar, M.; Nagaiah, T. C.; Siruguri, V.; Rayaprol, S.; Yadav, A. K.; Jha, S. N.; Bhattacharyya, D.; Paul, A. K., Investigation of New B-Site-Disordered Perovskite Oxide $CaLaScRuO_{6+\delta}$: An Efficient Oxygen Bifunctional Electrocatalyst in a Highly Alkaline Medium. *ACS Appl. Mater. Interfaces* **2020,** *12*, 9190-9200.

318. Xu, W.; Apodaca, N.; Wang, H.; Yan, L.; Chen, G.; Zhou, M.; Ding, D.; Choudhury, P.; Luo, H., A-site Excessive $(La_{0.8}Sr_{0.2})_{1+x}MnO_3$ Perovskite Oxides for Bifunctional Oxygen Catalyst in Alkaline Media. *ACS Catal.* **2019,** *9*, 5074-5083.

319. Chen, G.; Zhou, W.; Guan, D.; Sunarso, J.; Zhu, Y.; Hu, X.; Zhang, W.; Shao, Z., Two orders of magnitude enhancement in oxygen evolution reactivity on amorphous $Ba_{0.5}Sr_{0.5}Co_{0.8}Fe_{0.2}O_{3-\delta}$ nanofilms with tunable oxidation state. *Sci. Adv.* **2017,** *3*, e1603206.

320. Chaitoglou, S.; Bertran, E., Effect of temperature on graphene grown by chemical vapor deposition. *J. Mater. Sci.* **2017,** *52*, 8348-8356.

321. Chang, C.; Zhu, S.; Liu, X.; Chen, Y.; Sun, Y.; Tang, Y.; Wan, P.; Pan, J., One-Step Electrodeposition Synthesis of Bimetal Fe- and Co-Doped NiPi/P for Highly Efficient Overall Water Splitting. *Ind. Eng. Chem. Res.* **2021,** *60*, 2070-2078.

322.Tong, X.; Yang, P.; Wang, Y.; Qin, Y.; Guo, X., Enhanced photoelectrochemical water splitting performance of TiO_2 nanotube arrays coated with an ultrathin nitrogen-doped carbon film by molecular layer deposition. *Nanoscale* **2014,** *6*, 6692-6700.

323.Lee, J. G.; Hwang, J.; Hwang, H. J.; Jeon, O. S.; Jang, J.; Kwon, O.; Lee, Y.; Han, B.; Shul, Y.-G., A New Family of Perovskite Catalysts for Oxygen-Evolution Reaction in Alkaline Media: $BaNiO_3$ and $BaNi_{0.83}O_{2.5}$. *J. Am. Chem. Soc.* **2016,** *138*, 3541-3547.

324.Hona, R. K.; Ramezanipour, F., Structure-dependence of electrical conductivity and electrocatalytic properties of $Sr_2Mn_2O_6$ and $CaSrMn_2O_6$. *J. Chem. Sci.* **2019,** *131*, 109.

325.Kim, J.; Yin, X.; Tsao, K.-C.; Fang, S.; Yang, H., $Ca_2Mn_2O_5$ as Oxygen-Deficient Perovskite Electrocatalyst for Oxygen Evolution Reaction. *J. Am. Chem. Soc.* **2014,** *136*, 14646-14649.

326.Suntivich, J.; May, K. J.; Gasteiger, H. A.; Goodenough, J. B.; Shao-Horn, Y., A perovskite oxide optimized for oxygen evolution catalysis from molecular orbital principles. *Science* **2011,** *334*, 1383-1385.

327.Wilke, M.; Farges, F. o.; Petit, P.-E.; Brown, G. E., Jr.; Martin, F. o., Oxidation state and coordination of Fe in minerals: An Fe K-XANES spectroscopic study. *Am. Mineral.* **2001,** *86*, 714-730.

328.Westre, T. E.; Kennepohl, P.; DeWitt, J. G.; Hedman, B.; Hodgson, K. O.; Solomon, E. I., A Multiplet Analysis of Fe K-Edge 1s → 3d Pre-Edge Features of Iron Complexes. *J. Am. Chem. Soc.* **1997,** *119*, 6297-6314.

329.Dau, H.; Liebisch, P.; Haumann, M., X-ray absorption spectroscopy to analyze nuclear geometry and electronic structure of biological metal centers--potential and questions examined with special focus on the tetra-nuclear manganese complex of oxygenic photosynthesis. *Anal. Bioanal. Chem.* **2003,** *376*, 562-583.

330.Kresse, G.; Furthmüller, J., Efficiency of ab-initio total energy calculations for metals and semiconductors using a plane-wave basis set. *Comput. Mater. Sci.* **1996,** *6*, 15-50.

331.Zunger, A.; Wei, S. H.; Ferreira, L. G.; Bernard, J. E., Special quasirandom structures. *Phys. Rev. Lett.* **1990,** *65*, 353-356.

332.van de Walle, A.; Tiwary, P.; de Jong, M.; Olmsted, D. L.; Asta, M.; Dick, A.; Shin, D.; Wang, Y.; Chen, L. Q.; Liu, Z. K., Efficient stochastic generation of special quasirandom structures. *Calphad* **2013,** *42*, 13-18.

333.Trimarchi, G.; Wang, Z.; Zunger, A., Polymorphous band structure model of gapping in the antiferromagnetic and paramagnetic phases of the Mott insulators MnO, FeO, CoO, and NiO. *Phys. Rev. B* **2018,** *97*, 035107.

334.Stokes, H. T.; Kisi, E. H.; Hatch, D. M.; Howard, C. J., Group-theoretical analysis of octahedral tilting in ferroelectric perovskites. *Acta Cryst. B* **2002,** *58*, 934-938.

335.Dorado, B.; Garcia, P., First-principles DFT + U modeling of actinide-based alloys: Application to paramagnetic phases of UO_2 and (U,Pu) mixed oxides. *Phys. Rev. B* **2013,** *87*, 195139.

336.Wang, L.; Maxisch, T.; Ceder, G., Oxidation energies of transition metal oxides within the GGA+U framework. *Phys. Review B* **2006,** *73*, 195107.

337.Monkhorst, H. J.; Pack, J. D., Special points for Brillouin-zone integrations. *Phys. Rev. B* **1976,** *13*, 5188-5192.

338.Kim, N. I.; Afzal, R. A.; Choi, S. R.; Lee, S. W.; Ahn, D.; Bhattacharjee, S.; Lee, S. C.; Kim, J. H.; Park, J. Y., Highly active and durable nitrogen doped-reduced graphene oxide/double perovskite bifunctional hybrid catalysts. *J. Mater. Chem. A* **2017,** *5*, 13019-13031.

339.Du, J.; Zhang, T.; Cheng, F.; Chu, W.; Wu, Z.; Chen, J., Nonstoichiometric perovskite $CaMnO_{3-\delta}$ for oxygen electrocatalysis with high activity. *Inorg. Chem.* **2014,** *53*, 9106-9114.

340.Šljukić, B.; Vujković, M.; Amaral, L.; Santos, D. M. F.; Rocha, R. P.; Sequeira, C. A. C.; Figueiredo, J. L., Carbon-supported Mo_2C electrocatalysts for hydrogen evolution reaction. *J. Mater. Chem. A* **2015,** *3*, 15505-15512.

341.Malkhandi, S.; Trinh, P.; Manohar, A. K.; Jayachandrababu, K. C.; Kindler, A.; Surya Prakash, G. K.; Narayanan, S. R., Electrocatalytic activity of transition metal oxide-carbon composites for oxygen reduction in alkaline batteries and fuel cells. *J. Electrochem. Soc.* **2013,** *160*, 943-952.

342.May, K. J.; Carlton, C. E.; Stoerzinger, K. A.; Risch, M.; Suntivich, J.; Lee, Y. L.; Grimaud, A.; Shao Horn, Y., Influence of oxygen evolution during water oxidation on the surface of perovskite oxide catalysts. *J. Phys. Chem. Lett.* **2012,** *3*, 3264-3270.

343.Jin, C.; Cao, X.; Zhang, L.; Zhang, C.; Yang, R., Preparation and electrochemical properties of urchin-like $La_{0.8}Sr_{0.2}MnO_3$ perovskite oxide as a bifunctional catalyst for oxygen reduction and oxygen evolution reaction. *J. Power Sources* **2013,** *241*, 225-230.

344.Mohamed, R.; Cheng, X.; Fabbri, E.; Levecque, P.; Kötz, R.; Conrad, O.; Schmidt, T. J., Electrocatalysis of perovskites: the influence of carbon on the oxygen evolution activity. *J. Electrochem. Soc.* **2015,** *162*, 579-586.

345.Liang, Y.; Li, Y.; Wang, H.; Zhou, J.; Wang, J.; Regier, T.; Dai, H., Co_3O_4 nanocrystals on graphene as a synergistic catalyst for oxygen reduction reaction. *Nat. Mater.* **2011,** *10*, 780-786.

346.Fabbri, E.; Nachtegaal, M.; Cheng, X.; Schmidt Thomas, J., Superior bifunctional electrocatalytic activity of $Ba_{0.5}Sr_{0.5}Co_{0.8}Fe_{0.2}O_{3-\delta}$/carbon composite electrodes: insight into the local electronic structure. *Adv. Energy Mater.* **2015,** *5*, 1402033.

347.Chen, Y.; Yu, G.; Chen, W.; Liu, Y.; Li, G.-D.; Zhu, P.; Tao, Q.; Li, Q.; Liu, J.; Shen, X.; Li, H.; Huang, X.; Wang, D.; Asefa, T.; Zou, X., Highly Active, Nonprecious Electrocatalyst Comprising Borophene Subunits for the Hydrogen Evolution Reaction. *J. Am. Chem. Soc.* **2017,** *139*, 12370-12373.

348.Adolphsen, J. Q.; Sudireddy, B. R.; Gil, V.; Chatzichristodoulou, C., Oxygen Evolution Activity and Chemical Stability of Ni and Fe Based Perovskites in Alkaline Media. *J. Electrochem. Soc.* **2018,** *165*, 827-835.

349.Xu, X.; Pan, Y.; Zhou, W.; Chen, Y.; Zhang, Z.; Shao, Z., Toward Enhanced Oxygen Evolution on Perovskite Oxides Synthesized from Different Approaches: A Case Study of $Ba_{0.5}Sr_{0.5}Co_{0.8}Fe_{0.2}O_{3-\delta}$. *Electrochim.Acta* **2016,** *219*, 553-559.

350.Retuerto, M.; Pascual, L.; Calle-Vallejo, F.; Ferrer, P.; Gianolio, D.; Pereira, A. G.; García, Á.; Torrero, J.; Fernández-Díaz, M. T.; Bencok, P.; Peña, M. A.; Fierro, J. L. G.; Rojas, S., Na-doped ruthenium perovskite electrocatalysts with improved oxygen evolution activity and durability in acidic media. *Nat. Commun.* **2019,** *10*, 2041.

351.Yao, R.-Q.; Shi, H.; Wan, W.-B.; Wen, Z.; Lang, X.-Y.; Jiang, Q., Flexible Co–Mo–N/Au Electrodes with a Hierarchical Nanoporous Architecture as Highly Efficient Electrocatalysts for Oxygen Evolution Reaction. *Adv. Materi.* **2020,** *32*, 1907214.

352.Jung, S.; McCrory, C. C. L.; Ferrer, I. M.; Peters, J. C.; Jaramillo, T. F., Benchmarking nanoparticulate metal oxide electrocatalysts for the alkaline water oxidation reaction. *J. Mater.Chem. A* **2016,** *4*, 3068-3076.

353.Lu, B.; Cao, D.; Wang, P.; Wang, G.; Gao, Y., Oxygen evolution reaction on Ni-substituted Co_3O_4 nanowire array electrodes. *Int. J. Hydrogen Energy* **2011,** *36*, 72-78.

354.Lee, J. G.; Hwang, J.; Hwang, H. J.; Jeon, O. S.; Jang, J.; Kwon, O.; Lee, Y.; Han, B.; Shul, Y.-G., A new family of perovskite catalysts for oxygen-evolution reaction in alkaline media: $BaNiO_3$ and $BaNi_{0.83}O_{2.5}$. *J. Am.Chem. Soc.* **2016,** *138*, 3541-3547.

355.Petrie, J. R.; Cooper, V. R.; Freeland, J. W.; Meyer, T. L.; Zhang, Z.; Lutterman, D. A.; Lee, H. N., Enhanced bifunctional oxygen catalysis in strained LaNiO₃ perovskites. *J. Am. Chem.Soc.* **2016,** *138*, 2488-2491.

356.Zhang, B.; Lui, Y. H.; Zhou, L.; Tang, X.; Hu, S., An alkaline electro-activated Fe-Ni phosphide nanoparticle-stack array for high-performance oxygen evolution under alkaline and neutral conditions. *J. Mater. Chem. A* **2017,** *5*, 13329-13335.

357.Pan, Y.; Chen, Y.; Li, X.; Liu, Y.; Liu, C., Nanostructured nickel sulfides: phase evolution, characterization and electrocatalytic properties for the hydrogen evolution reaction. *RSC Advances* **2015,** *5*, 104740-104749.

358.Konkena, B.; junge Puring, K.; Sinev, I.; Piontek, S.; Khavryuchenko, O.; Dürholt, J. P.; Schmid, R.; Tüysüz, H.; Muhler, M.; Schuhmann, W.; Apfel, U.-P., Pentlandite rocks as sustainable and stable efficient electrocatalysts for hydrogen generation. *Nat. Commun.* **2016,** *7*, 12269.

359.Zhu, Y.; Zhou, W.; Sunarso, J.; Zhong, Y.; Shao, Z., Phosphorus-doped perovskite oxide as highly efficient water oxidation electrocatalyst in alkaline solution. *Adv. funct. mater.* **2016,** *26*, 5862-5872.

360.Zhou, H.; Zhai, H.-J., A highly flexible solid-state supercapacitor based on the carbon nanotube doped graphene oxide/polypyrrole composites with superior electrochemical performances. *Org. Electron.* **2016,** *37*, 197-206.

361.Grimaud, A.; May, K. J.; Carlton, C. E.; Lee, Y. L.; Risch, M.; Hong, W. T.; Zhou, J.; Shao-Horn, Y., Double Perovskites as a Family of Highly Active Catalysts for Oxygen Evolution in Alkaline Solution. *Nat. Commun.* **2013,** *4*, 2439.

362.Suntivich, J.; Gasteiger, H. A.; Yabuuchi, N.; Nakanishi, H.; Goodenough, J. B.; Shao-Horn, Y., Design principles for oxygen-reduction activity on perovskite oxide catalysts for fuel cells and metal–air batteries. *Nat. Chem.* **2011,** *3*, 546.

363.Zhang, Z.; Chen, Y.; Dai, Z.; Tan, S.; Chen, D., Promoting hydrogen-evolution activity and stability of perovskite oxides via effectively lattice doping of molybdenum. *Electrochim. Acta* **2019,** *312*, 128-136.

364.Sun, W.; Song, Y.; Gong, X.-Q.; Cao, L.-m.; Yang, J., An efficiently tuned d-orbital occupation of IrO₂ by doping with Cu for enhancing the oxygen evolution reaction activity. *Chem. Sci.* **2015,** *6*, 4993-4999.

365.Guedes, I.; Mitchell, J. F.; Argyriou, D.; Grimsditch, M., Oxygen stoichiometry in Sr₃Mn₂O₇₋δ: A Raman scattering investigation. *Phys. Rev. B* **2000,** *62*, 13809-13811.

366.MIin-Seok Song; Suk-Young Kim; Lee, J.-Y., Synthesis and physical properties of Ruddlesden-Popper phase Sr₃Mn₂₋ₓFexO₇₋δ (x = 0.15 ∼ 1.0). *Ceramics – Silikáty* **2004,** *48*, 175-179.

367.Dann, S. E.; Weller, M. T., Structure and Oxygen Stoichiometry in Sr₃Co₂O₇₋ᵧ (0.94 ≤ y ≤ 1.22). *J. Solid State Chem.* **1995,** *115*, 499-507.

368.Dann, S. E.; Weller, M. T.; Currie, D. B., Structure and oxygen stoichiometry in Sr₃Fe₂O₇₋ᵧ, 0 ≤ y ≤ 1.0. *J. Solid State Chem.* **1992,** *97*, 179-185.

369.Cava, R. J.; Santoro, A.; Krajewski, J. J.; Fleming, R. M.; Waszczak, J. V.; Peck, W. F.; Marsh, P., The crystal structure of the La₁.₆Sr₀.₄CaCu₂O₆±δ superconductor. *Physica C Supercond.* **1990,** *172*, 138-142.

370.Itoh, M.; Shikano, M.; Kawaji, H.; Nakamura, T., Structural aspects on the variations of electric and magnetic properties of the layered compound system Srₙ₊₁VₙO₃ₙ₊₁₋δ(n = 1, 2, 3 ∞). *Solid State Commun.* **1991,** *80*, 545-548.

371.Wu, A.; Gu, Y.; Xie, Y.; Tian, C.; Yan, H.; Wang, D.; Zhang, X.; Cai, Z.; Fu, H., Effective Electrocatalytic Hydrogen Evolution in Neutral Medium Based on 2D MoP/MoS$_2$ Heterostructure Nanosheets. *ACS Appl. Mater. Interfaces* **2019,** *11*, 25986-25995.

372.Jiang, L.; Ji, S.-J.; Xue, H.-G.; Suen, N.-T., HER activity of M$_x$Ni$_{1-x}$ (M = Cr, Mo and W; x ≈ 0.2) alloy in acid and alkaline media. *Int. J. Hydrog. Energy* **2020,** *45*, 17533-17539.

373.McCrory, C. C. L.; Jung, S.; Ferrer, I. M.; Chatman, S. M.; Peters, J. C.; Jaramillo, T. F., Benchmarking Hydrogen Evolving Reaction and Oxygen Evolving Reaction Electrocatalysts for Solar Water Splitting Devices. *J. Am. Chem. Soc.* **2015,** *137*, 4347-4357.

374.Ramana, C. V.; Bandi, M.; N Nair, A.; Manciu, F. S.; Sreenivasan, S.; Shutthanandan, V., Electronic Structure, Chemical Bonding, and Electrocatalytic Activity of Ba(Fe$_{0.7}$Ta$_{0.3}$)O$_{3-\delta}$ Compounds. *ACS Appl. Energy Mater.* **2021**.

375.Ma, Z.; Zhang, Y.; Liu, S.; Xu, W.; Wu, L.; Hsieh, Y.-C.; Liu, P.; Zhu, Y.; Sasaki, K.; Renner, J. N.; Ayers, K. E.; Adzic, R. R.; Wang, J. X., Reaction mechanism for oxygen evolution on RuO$_2$, IrO$_2$, and RuO$_2$@IrO$_2$ core-shell nanocatalysts. *J. Electroanal. Chem.* **2018,** *819*, 296-305.

376.Baeumer, C.; Li, J.; Lu, Q.; Liang, A. Y.-L.; Jin, L.; Martins, H. P.; Duchoň, T.; Glöß, M.; Gericke, S. M.; Wohlgemuth, M. A.; Giesen, M.; Penn, E. E.; Dittmann, R.; Gunkel, F.; Waser, R.; Bajdich, M.; Nemšák, S.; Mefford, J. T.; Chueh, W. C., Tuning electrochemically driven surface transformation in atomically flat LaNiO3 thin films for enhanced water electrolysis. *Nat. Mater.* **2021,** *20*, 674-682.

377.Retuerto, M.; Calle-Vallejo, F.; Pascual, L.; Lumbeeck, G.; Fernandez-Diaz, M. T.; Croft, M.; Gopalakrishnan, J.; Peña, M. A.; Hadermann, J.; Greenblatt, M.; Rojas, S., La$_{1.5}$Sr$_{0.5}$NiMn$_{0.5}$Ru$_{0.5}$O$_6$ Double Perovskite with Enhanced ORR/OER Bifunctional Catalytic Activity. *ACS Appl. Mater. Interfaces* **2019,** *11*, 21454-21464.

378.Maitra, S.; Mitra, R.; Nath, T. K., Sol-gel derived MgCr$_2$O$_4$ nanoparticles for aqueous supercapacitor and alkaline OER and HER bi-functional electrocatalyst applications. *J. Alloys Compd.* **2021,** *858*, 157679.

379.Tahira, A.; Ibupoto, Z. H.; Willander, M.; Nur, O., Advanced Co$_3$O$_4$–CuO nano-composite based electrocatalyst for efficient hydrogen evolution reaction in alkaline media. *Int. J. Hydrog. Energy* **2019,** *44*, 26148-26157.

380.Grimaud, A.; May, K. J.; Carlton, C. E.; Lee, Y.-L.; Risch, M.; Hong, W. T.; Zhou, J.; Shao-Horn, Y., Double perovskites as a family of highly active catalysts for oxygen evolution in alkaline solution. *Nat. Commun.* **2013,** *4*, 2439.

381.Suen, N.-T.; Hung, S.-F.; Quan, Q.; Zhang, N.; Xu, Y.-J.; Chen, H. M., Electrocatalysis for the oxygen evolution reaction: recent development and future perspectives. *Chem. Soc. Rev.* **2017,** *46*, 337-365.

382.Dong, C.; Yuan, X.; Wang, X.; Liu, X.; Dong, W.; Wang, R.; Duan, Y.; Huang, F., Rational design of cobalt–chromium layered double hydroxide as a highly efficient electrocatalyst for water oxidation. *J. Mater. Chem. A* **2016,** *4*, 11292-11298.

383.Li, M.; Xiong, Y.; Liu, X.; Bo, X.; Zhang, Y.; Han, C.; Guo, L., Facile synthesis of electrospun MFe2O4 (M = Co, Ni, Cu, Mn) spinel nanofibers with excellent electrocatalytic properties for oxygen evolution and hydrogen peroxide reduction. *Nanoscale* **2015,** *7*, 8920-8930.

384.Connor, P.; Schuch, J.; Kaiser, B.; Jaegermann, W., The Determination of Electrochemical Active Surface Area and Specific Capacity Revisited for the System MnO$_x$ as an Oxygen Evolution Catalyst. *Z. Phys. Chem.* **2020,** *234*, 979-994.

385.Bocquet, A. E.; Mizokawa, T.; Saitoh, T.; Namatame, H.; Fujimori, A., Electronic structure of 3d-transition-metal compounds by analysis of the 2p core-level photoemission spectra. *Phys. Rev. B* **1992,** *46*, 3771-3784.

386.Suntivich, J.; Hong, W. T.; Lee, Y.-L.; Rondinelli, J. M.; Yang, W.; Goodenough, J. B.; Dabrowski, B.; Freeland, J. W.; Shao-Horn, Y., Estimating Hybridization of Transition Metal and Oxygen States in Perovskites from O K-edge X-ray Absorption Spectroscopy. *J. Phys. Chem. C* **2014,** *118*, 1856-1863.

387.Yagi, S.; Yamada, I.; Tsukasaki, H.; Seno, A.; Murakami, M.; Fujii, H.; Chen, H.; Umezawa, N.; Abe, H.; Nishiyama, N.; Mori, S., Covalency-reinforced oxygen evolution reaction catalyst. *Nat. Commun.* **2015,** *6*, 8249.

388.Matsumoto, Y.; Sato, E., Electrocatalytic properties of transition metal oxides for oxygen evolution reaction. *Mater. Chem. Phys.* **1986,** *14*, 397-426.

389.Ji, D.; Liu, C.; Yao, Y.; Luo, L.; Wang, W.; Chen, Z., Cerium substitution in $LaCoO_3$ perovskite oxide as bifunctional electrocatalysts for hydrogen and oxygen evolution reactions. *Nanoscale* **2021,** *13*, 9952-9959.

390.Tang, L.; Fan, T.; Chen, Z.; Tian, J.; Guo, H.; Peng, M.; Zuo, F.; Fu, X.; Li, M.; Bu, Y.; Luo, Y.; Li, J.; Sun, Y., Binary-dopant promoted lattice oxygen participation in OER on cobaltate electrocatalyst. *Chem. Eng. J.* **2021,** *417*, 129324.

391.Miao, X.; Wu, L.; Lin, Y.; Yuan, X.; Zhao, J.; Yan, W.; Zhou, S.; Shi, L., The role of oxygen vacancies in water oxidation for perovskite cobalt oxide electrocatalysts: are more better? *Chem. Commun.* **2019,** *55*, 1442-1445.

392.Wu, Z.; Sun, L.-P.; Xia, T.; Huo, L.-H.; Zhao, H.; Rougier, A.; Grenier, J.-C., Effect of Sr doping on the electrochemical properties of bi-functional oxygen electrode $PrBa_{1-x}Sr_xCo_2O_{5+\delta}$. *J. Power Sources* **2016,** *334*, 86-93.

393.Guo, Q.; Li, X.; Wei, H.; Liu, Y.; Li, L.; Yang, X.; Zhang, X.; Liu, H.; Lu, Z., Sr, Fe Co-doped Perovskite Oxides With High Performance for Oxygen Evolution Reaction. *Front. Chem.* **2019,** *7*, 224.

394.Wang, X.; Yu, L.; Guan, B. Y.; Song, S.; Lou, X. W., Metal–Organic Framework Hybrid-Assisted Formation of Co_3O_4/Co-Fe Oxide Double-Shelled Nanoboxes for Enhanced Oxygen Evolution. *Adv. Mater.* **2018,** *30*, 1801211.

395.Lu, X.-F.; Gu, L.-F.; Wang, J.-W.; Wu, J.-X.; Liao, P.-Q.; Li, G.-R., Bimetal-Organic Framework Derived $CoFe_2O_4$/C Porous Hybrid Nanorod Arrays as High-Performance Electrocatalysts for Oxygen Evolution Reaction. *Adv. Mater.* **2017,** *29*, 1604437.

396.Peng, S.; Gong, F.; Li, L.; Yu, D.; Ji, D.; Zhang, T.; Hu, Z.; Zhang, Z.; Chou, S.; Du, Y.; Ramakrishna, S., Necklace-like Multishelled Hollow Spinel Oxides with Oxygen Vacancies for Efficient Water Electrolysis. *J. Am. Chem. Soc.* **2018,** *140*, 13644-13653.

397.Hohenberg, P.; Kohn, W., Inhomogeneous Electron Gas. *Phys. Rev.* **1964,** *136*, B864-B871.

398.Kohn, W.; Sham, L. J., Self-Consistent Equations Including Exchange and Correlation Effects. *Phys. Rev.* **1965,** *140*, A1133-A1138.

399.Kresse, G.; Furthmüller, J., Efficient iterative schemes for ab initio total-energy calculations using a plane-wave basis set. *Phys. Rev. B* **1996,** *54*, 11169-11186.

400.Blöchl, P. E., Projector augmented-wave method. *Phys. Rev. B* **1994,** *50* (24), 17953-17979.

401.Perdew, J. P.; Chevary, J. A.; Vosko, S. H.; Jackson, K. A.; Pederson, M. R.; Singh, D. J.; Fiolhais, C., Atoms, molecules, solids, and surfaces: Applications of the generalized gradient approximation for exchange and correlation. *Phys. Rev. B* **1992,** *46*, 6671-6687.

402.Perdew, J. P.; Burke, K.; Ernzerhof, M., Generalized Gradient Approximation Made Simple. *Phys. Rev. Lett.* **1996,** *77*, 3865-3868.

403.Gonze, X., First-principles responses of solids to atomic displacements and homogeneous electric fields: Implementation of a conjugate-gradient algorithm. *Phys. Rev. B* **1997,** *55*, 10337-10354.

404.Monkhorst, H. J.; Pack, J. D., Special points for Brillouin-zone integrations. *Phys. Rev. B* **1976,** *13*, 5188-5192.

405.Pavarini, E.; Koch, E.; Anders, F.; Jarrell, M., *Correlated Electrons: From Models to Materials Modeling and Simulation Vol. 2*. Forschungszentrum Jülich, 2012.

406.Song, F.; Bai, L.; Moysiadou, A.; Lee, S.; Hu, C.; Liardet, L.; Hu, X., Transition Metal Oxides as Electrocatalysts for the Oxygen Evolution Reaction in Alkaline Solutions: An Application-Inspired Renaissance. *J. Am. Chem. Soc.* **2018,** *140*, 7748-7759.

407.Xu, X.; Pan, Y.; Zhou, W.; Chen, Y.; Zhang, Z.; Shao, Z., Toward Enhanced Oxygen Evolution on Perovskite Oxides Synthesized from Different Approaches: A Case Study of $Ba_{0.5}Sr_{0.5}Co_{0.8}Fe_{0.2}O_{3-\delta}$. *Electrochim. Acta* **2016,** *219*, 553-559.

408.Müller, S.; Striebel, K.; Haas, O., $La_{0.6}Ca_{0.4}CoO_3$: a stable and powerful catalyst for bifunctional air electrodes. *Electrochim. Acta* **1994,** *39*, 1661-1668.

409.Weidenkaff, A.; Ebbinghaus, S. G.; Lippert, T., $Ln_{1-x}A_xCoO_3$ (Ln = Er, La; A = Ca, Sr)/Carbon Nanotube Composite Materials Applied for Rechargeable Zn/Air Batteries. *Chem. Mater.* **2002,** *14*, 1797-1805.

410.Ding, H.; Virkar, A. V.; Liu, M.; Liu, F., Suppression of Sr surface segregation in $La_{1-x}Sr_xCo_{1-y}Fe_yO_{3-\delta}$: a first principles study. *Phys. Chem. Chem. Phys.* **2013,** *15*, 489-496.

411.Cai, Z.; Kuru, Y.; Han, J. W.; Chen, Y.; Yildiz, B., Surface Electronic Structure Transitions at High Temperature on Perovskite Oxides: The Case of Strained $La_{0.8}Sr_{0.2}CoO_3$ Thin Films. *J. Am. Chem. Soc.* **2011,** *133*, 17696-17704.

412.Rollmann, G.; Rohrbach, A.; Entel, P.; Hafner, J., First-principles calculation of the structure and magnetic phases of hematite. *Phys. Rev. B* **2004,** *69* (16), 165107.

413.Han, J. W.; Yildiz, B., Enhanced one dimensional mobility of oxygen on strained $LaCoO_3$(001) surface. *J. Mater. Chem.* **2011,** *21*, 18983-18990.

414.Andriotis, A. N.; Fthenakis, Z. G.; Menon, M., Successive spin polarizations underlying a new magnetic coupling contribution in diluted magnetic semiconductors. *J. Phys.: Condens. Matter.* **2015,** *27*, 052202.

415.Thornton, G.; Tofield, B. C.; Hewat, A. W., A neutron diffraction study of $LaCoO_3$ in the temperature range 4.2 < T < 1248 K. *J. Solid State Chem.* **1986,** *61*, 301-307.

416.Haas, O.; Struis, R. P. W. J.; McBreen, J. M., Synchrotron X-ray absorption of $LaCoO_3$ perovskite. *J. Solid State Chem.* **2004,** *177*, 1000-1010.

417.Schmidt, R.; Wu, J.; Leighton, C.; Terry, I., Dielectric response to the low-temperature magnetic defect structure and spin state transition in polycrystalline $LaCoO_3$. *Phys. Rev. B* **2009,** *79*, 125105.

418.Hansteen, O. H.; Fjellvåg, H.; Hauback, B. C., Crystal structure, thermal and magnetic properties of $La_3Co_3O_8$. Phase relations for $LaCoO_{3-\delta}$ ($0.00 \le \delta \le 0.50$) at 673 K. *J. Mater. Chem.* **1998,** *8*, 2081-2088.

419.Vidyasagar, K.; Reller, A.; Gopalakrishnan, J.; Rao, C. N. R., Oxygen vacancy ordering in superlatives of the two novel oxides, $La_2Ni_2O_5$ and $La_2Co_2O_5$, prepared by low temperature reduction of the parent perovskites. *J. Chem. Soc., Chem. Commun.* **1985**, 7-8.

420.Hansteen, O. H.; Fjellvåg, H.; Hauback, B. C., Crystal Structure and Magnetic Properties of La$_2$Co$_2$O$_5$. *J. Solid State Chem.* **1998,** *141*, 411-417.

421.Zou, X.; Huang, X.; Goswami, A.; Silva, R.; Sathe, B. R.; Mikmeková, E.; Asefa, T., Cobalt-Embedded Nitrogen-Rich Carbon Nanotubes Efficiently Catalyze Hydrogen Evolution Reaction at All pH Values. *Angew. Chem. Int. Ed.* **2014,** *53*, 4372-4376.

422.Shi, H.; Zhao, G., Water Oxidation on Spinel NiCo$_2$O$_4$ Nanoneedles Anode: Microstructures, Specific Surface Character, and the Enhanced Electrocatalytic Performance. *J. Phys. Chem. C* **2014,** *118*, 25939-25946.

423.Adolphsen, J. Q.; Sudireddy, B. R.; Gil, V.; Chatzichristodoulou, C., Oxygen Evolution Activity and Chemical Stability of Ni and Fe Based Perovskites in Alkaline Media. *J. Electrochem. Soc.* **2018,** *165*, F827-F835.

424.Yang, L.; Yu, G.; Ai, X.; Yan, W.; Duan, H.; Chen, W.; Li, X.; Wang, T.; Zhang, C.; Huang, X.; Chen, J.-S.; Zou, X., Efficient oxygen evolution electrocatalysis in acid by a perovskite with face-sharing IrO$_6$ octahedral dimers. *Nature Commun.* **2018,** *9*, 5236.

425.Luo, Q.; Lin, D.; Zhan, W.; Zhang, W.; Tang, L.; Luo, J.; Gao, Z.; Jiang, P.; Wang, M.; Hao, L.; Tang, K., Hexagonal Perovskite Ba$_{0.9}$Sr$_{0.1}$Co$_{0.8}$Fe$_{0.1}$Ir$_{0.1}$O$_{3-\delta}$ as an Efficient Electrocatalyst towards the Oxygen Evolution Reaction. *ACS Appl. Energy Mater.* **2020,** *3*, 7149-7158.

426.Nguyen, T. X.; Liao, Y.-C.; Lin, C.-C.; Su, Y.-H.; Ting, J.-M., Advanced High Entropy Perovskite Oxide Electrocatalyst for Oxygen Evolution Reaction. *Adv. Funct. Mater.* **2021,** *31*, 2101632.

427.Miles, M. H.; Klaus, E. A.; Gunn, B. P.; Locker, J. R.; Serafin, W. E.; Srinivasan, S., The oxygen evolution reaction on platinum, iridium, ruthenium and their alloys at 80°C in acid solutions. *Electrochim. Acta* **1978,** *23*, 521-526.

428.He, D.; He, G.; Jiang, H.; Chen, Z.; Huang, M., Enhanced durability and activity of the perovskite electrocatalyst Pr$_{0.5}$Ba$_{0.5}$CoO$_{3-\delta}$ by Ca doping for the oxygen evolution reaction at room temperature. *Chem. Commun.* **2017,** *53*, 5132-5135.

CURRICULUM VITAE

Surendra B. Karki

Email: sbkarki2020@gmail.com, surendra.karki@louisville.edu

Google Scholar Link: https://scholar.google.com/citations?user=TjLt3FkAAAAJ&hl=en

EDUCATION

- **<u>PhD Chemistry</u>**　　University of Louisville　　May 2022　　GPA – 3.80

  Research: Solid-state and materials chemistry

- **<u>MS Chemistry</u>**　　University of South Carolina　　December 2016

  Research: Functionalization of carboranes

- **<u>MSc Chemistry</u>**　　Tribhuvan University, Nepal　　May 2009

- **<u>BSc Chemistry</u>**　　Tribhuvan University, Nepal　　May 2006

PATENT

1. Hona, R. K.; Karki, S. B.; Ramezanipour, F., Catalyst for Water Splitting Reactions. United States Patent No. 20210046453, Issued: February 18, 2021.

PEER REVIEWED PUBLICATIONS

1. **Karki, S. B**.; Hona, R. K.; Ramezanipour, F., Two-Dimensional Oxides, $Sr_3Mn_2O_6$ And Sr_3FeMnO_6 For Oxygen And Hydrogen Evolution Electrocatalysis (Just accepted in Journal of Solid State Electrochemistry).
2. Hona, R. K.; **Karki, S. B.**; Cao, T.; Mishra, M.; Sterbinsky, G. E.; Ramezanipour, F., A Sustainable Oxide Electrocatalyst with Unprecedented Hydrogen and Oxygen-Evolution Activity., *ACS Catal. 2021,* 11, 14605−14614. **(journal cover)**
3. **Karki, S. B**.; Hona, R. K.; Ramezanipour, F., Electrocatalytic Activity and Structural Transformation of $Ca_2Sr_2Mn_2MO_{10\text{-}\delta}$ (M = Fe, Co)., *Ionics*, 2021, 28, 396−406
4. **Karki, S. B.**; Andritios, A. N.; Menon, M.; Ramezanipour, F.,Bifunctional Water-Splitting Electrocatalysis Achieved by Defect-Order in $LaA_2Fe_3O_8$ (A = Ca, Sr)., *ACS Appl. Energy Mater.* 2021, 4, 12063−12066. **(journal cover)**
5. **Karki, S. B**.; Ramezanipour, F., Pseudocapacitive Energy Storage and Electrocatalytic Hydrogen-Evolution Activity of Defect-Ordered Perovskites $Sr_xCa_{3-x}GaMn_2O_8$ (x = 0 and 1)., *ACS Appl. Energy Mater. 2020,* 3, 10983−10992.

6. Hona, R. K.; **Karki, S. B.**; Ramezanipour, F., Oxide Electrocatalysts Based on Earth-Abundant Metals for Both Hydrogen- and Oxygen-Evolution Reactions. *ACS Sustainable Chem. Eng.* 2020, 8, 11549−11557. **(Journal cover)**
7. **Karki, S. B.**; Hona, R. K.; Ramezanipour, F**.,** Effect of Structure on Sensor Properties of Oxygen-Deficient Perovskites, $A_2BB'O_5$ (A = Ca, Sr; B = Fe; B' = Fe, Mn) for Oxygen, Carbon Dioxide and Carbon Monoxide Sensing. *J. Electron. Mater.* 2020, *49*, 1557-1567.
8. **Karki, S. B.**; Ramezanipour, F. Magnetic and electrical properties of $BaSrMMoO_6$ (M = Mn, Fe, Co, and Ni). *Mater. Today Chem.* 2019, *13*, 25-33.

MANUSCRIPTS UNDER REVIEW
1. **Karki, S. B**.; Hona, R. K.; Ming, Y.; Ramezanipour, F., Systematic Enhancement Of Electrocatalytic Activity As A Function Of Structural Order In Perovskite Oxides (Under Review in Nature Communication).
2. **Karki, S. B.**; Ramezanipour, F. Electrocatalytic CO_2 reduction of Two Compounds $Ba_2Fe_2O_5$ and $Sr_2Fe_2O_5$ (Under Review).
3. **Karki, S. B.**; Ramezanipour, F. Bifunctional Water-Splitting Electrocatalysis, Brought About By Structural Order in $La_3Co_3O_8$ Compound (Under Review).
4. **Karki, S. B.**; Andritios, A. N.; Menon, M.; Ramezanipour, F., An Enhanced Bifunctional Activity Of $BaSrCoMoO_6$ For Catalyzing Hydrogen And Oxygen Evolution Reactions Of Water Splitting In Alkaline Medium (Under Review).

TECHNICAL SKILLS
1. Powder X-ray Diffraction: Data analysis and resolving instrumental issues such as replacing tube, alignment, etc
2. Physical Property Measurement System: Data collection, analysis, and fixing issues.
3. Powder Neutron diffraction: Data Analysis, refinement, and solve magnetic structure
4. X-ray Photoelectron Spectroscopy (XPS): Sample loading, data acquisition, analysis, and fitting.
5. AC Impedance Spectroscopy: Data acquisition, analysis, and fitting
6. Electrocatalysis: Data acquisition, analysis, and fixing issues for rotating disk electrode setup and potentiostats.
7. Nuclear Magnetic Resonance (NMR)
8. Raman Spectroscopy, Mass Spectroscopy, Photo Luminescence, IR, UV-vis, BET, SEM

SERVICE/TEACHING
1. Served as reviewer for Journal of Inorganic and Organometallic Polymers, Journal of Physics and Chemistry of Solids, and New Journal of Glass and Ceramics.
2. Research Assistant, University of Louisville, August 2021- Present.
3. Teaching Assistant, University of Louisville, August 2017- July 2021.
4. Vice President, Nepalese Student Association, University of Louisville, August 2018 – July 2020.
5. High School Science Teacher, 2006 – 2009.
6. Chemistry Lecturer, 2009 – 2013.

AWARDS
1. Graduate Dean's Citation Award, Spring 2022.
2. Graduate Research Grant, Fall 2021.
3. UofL Mentored Undergraduate Research and Creative Activities Grant, Summer 2021.
4. UofL Graduate Network in A&S (GNAS) Grant, Spring 2021.
5. Chemistry Department Travel Award, Summer, 2019.

CONFERENCE PRESENTATIONS
1. *__Karki, S. B.__*; Ramezanipour, F., Steady-state Chronoamperometry Technique for the Tafel Slope Analysis of OER/HER Kinetics during the Water Splitting, Graduate Student Regional Research Conference, Louisville, KY,March 2022 – *__Oral talk__*.
2. *__Karki, S. B.__*; Andritios, A. N.; Menon, M.; Ramezanipour, F., Electrocatalysis of Water Splitting in Alkaline condition brought by Defect-Order in $LaCa_2Fe_3O_8$, ACS Spring 2022- San Diego – *__Oral talk__*.
3. *__Karki, S. B.__*; Ramezanipour, F., The A-site cation effect on variable-temperature electrical charge transport, magnetism, and electrocatalytic activity of $A'A_2GaMn_2O_8$ (A'= Sr, A = Ca), ACS Fall 2021 – Resilience of Chemistry, Atlanta, Georgia, August 2021 – *__Oral talk__*.
4. *__Karki, S. B.__*; Ramezanipour, F., Electrocatalytic Activity, Charge Mobility and Magnetism of Highly Ordered Oxides with Oxygen Vacancies, North American Solid-State Chemistry Conference, University of South California, July 2021 – *__Poster presentation__*.
5. __Karki, S. B.__; Hona, R. K.; Ramezanipour, F., Effect of A-Site Cation on Gas Sensing Properties of Oxygen Deficient Perovskites, $AA'Fe_2O_{6-\delta}$ (A =Ca, Sr; A'= Sr), Graduate Student Regional Research Conference, Louisville, KY, February 2020 – *__Oral talk__*.
6. __Karki, S. B.__; Hona, R. K.; Ramezanipour, F., Oxygen, Carbon Dioxide and Carbon Monoxide Sensing Properties of Oxygen-Deficient Perovskites, $AA'BB'O_{6-\delta}$ (A =Ca, Sr; B=Fe; B'=Fe, Mn), 71st Southeastern Regional Meeting of the American Chemical Society, Savannah, GA, October 2019 – *__Oral talk__*.
7. *__Karki, S. B.__*; Ramezanipour, F., A Study on the Electrical and Magnetic Properties of $BaSrMMoO_6$ (M = Mn, Fe, Co, Ni), Graduate Student Regional Research Conference, Louisville, KY, February 2019 – *__Oral talk__*.
8. *__Karki, S. B.__*; Ramezanipour, F., Comparative Investigation on the Structural and Magnetic Properties of the Double Perovskites $BaSrMMoO_6$ (M= Mn, Co, Ni), Glass city Chemistry Conference, Toledo, OH, June 2018 – *__Poster presentation__*.